# Advanced Wind Turbine Operational Modelling for Evaluating and Improving Power Electronics Reliability

A thesis submitted to The University of Manchester for the degree of

**Doctor of Philosophy**

in the Faculty of Science and Engineering

**2022**

**Arsim Ahmedi**

**Department of Electrical and Electronic Engineering**

(Blank Page)

# Table of Contents

**Word count: Main body 37435; Total 45638**

# List of Figures

# List of Tables

# List of Abbreviations

BJT – Bipolar Junction Transistor

BVSC – Back-to-back Voltage Source Converter

CF – Capacity Factor

COE – Cost of Energy

CTE – Coefficient of Thermal Expansion

DC – Direct Current

DFIG – Doubly-Fed Induction Generator

FACTS – Flexible AC Transmission System

FBG – Fibre Bragg Grating

FMEA – Failure Mode, Effects, and Analysis

Fraunhofer IWES – Frauhofer Institute of Wind Energy Systems

GSC – Grid Side Converter

HAWT – Horizontal Axis Wind Turbine

HVDC – High Voltage Direct Current

IGBT – Insulated-Gate Bipolar Transistor

IGCT – Integrated Gate Commutated Thyristor

LTI – Linear Time Invariant

LVRT – Low Voltage Ride-through

MIMO – Multiple Input Multiple Output

MMC – Modular Multilevel Converter

MOSFET – Metal-Oxide-Semiconductor Field-Effect Transistor

MPPT – Maximum Power Point Tracking

MSC – Machine Side Converter

MTBF – Mean Time Between Failures

MW – Mega Watt

NREL – National Renewable Energy Laboratory

ODE – Ordinary Differential Equation

O&M – Operations and Maintenance

ORE Catapult – Offshore Renewable Energy Catapult

OTC – Optimal Torque Control

OTSR – Optimal Tip Speed Ratio

PBA – Production Based Availability

PC – Power Cycling

PE – Power Electronics

PID – Proportional Integral Derivative

PLL – Phase Locked Loop

PM – Permanent Magnet

PMSG – Permanent Magnet Synchronous Generator

PoC – Point of Connection

PoF – Physics of Failure

PWM – Pulse Width Modulation

SCADA – Supervisory Control and Data Acquisition

SCIG – Squirrel Cage Induction Generator

SISO – Single Input Single Output

SPARTA – System Performance, Availability and Reliability Trend Analysis

STATCOM – Static Synchronous Compensator

TC – Temperature Cycling

TF – Transfer Function

VSC – Voltage Source Converter

WF – Wind Farm

WinD-Pool – Wind-energy-Information-Data-Pool

WRIG – Wound Rotor Induction Generator

WRSGE – Wound rotor synchronous generator with electrical excitation

WT – Wind Turbine

# Abstract

There is a reliability concern for wind turbines (WTs) installed in offshore wind farms, where the harsh environment not only has a potential to lead to more failures, but could also increase the time and cost of intervention. Such unreliability problems can cause downtime and losses, which would be reflected at the cost of energy and affect all involved parties, including the customers. The work undertaken in this thesis focuses on the reliability of power electronic systems which represent a crucial element in the operation of the majority of modern WTs. One particular reliability concern in WT power converters is the early aging and degradation. To analyse the degradation of power electronic converters, there is a need for advanced simulation models that combine wind turbine operation and mission profile with the specific failure mechanisms.

The focus of the thesis is the modelling and evaluation of the thermo-mechanical stress of the power electronic unit, which is believed to be the source of one of the most important failure and aging mechanisms in converter modules. A methodology for calculating the converter thermal stress and consumed lifetime for a specific design, failure mechanism, and operational profile of a WT has been developed. This methodology allows for evaluating WT operational transients that have been overlooked by similar models in the literature. The developed approach and model can be used to evaluate different design and operational aspects of WTs in the design phase while also having potential to be used to predict the lifetime and failures during operation. Such evaluation has been undertaken in this thesis using several case studies and operational scenarios: comparing machine side and grid side converters, different generator control strategies, as well as the reliability impact of reactive power transfer to the grid. The most thermally stressed part of converter is identified to be the diode on the machine side converter, and it is concluded that the dynamic transients and the response associated with the torque control of the generator significantly impact the converter lifetime. From the generator control, the strategies that deliver closer maximum power point tracking bring higher stress on the converter. After undertaking model order reduction and optimisation of the simulation, the converter aging is analysed for longer WT operational time and two days with different wind speed profile are compared using measured wind speed data.

# Declaration

No portion of the work referred to in the thesis has been submitted in support of an application for another degree or qualification of this or any other university or other institute of learning.

# Copyright Statement

# Acknowledgements

Doing the PhD has been a challenging but a very enjoyable time of my life. I am very grateful for the opportunity and the chance I got to spend three and a half years working around some brilliant human beings and academics. It has been a real privilege and I thank God and every friend or stranger whose big or small deed influenced me in some way so that I end up here.

I want to give a very special “Thank you!” to my supervisor, Professor Mike Barnes. Doing research and the skills gained working towards my PhD are only a small part of all the things that I have learned from him. Most importantly I thank him for the continuous support, kindness, and the trust he gave me since day one. Thank you Mike, I will really miss our coffee conversations.

I want to also thank my co-supervisor, Dr Victor Levi, who was always kind and willing to help. I also want to thank The University of Manchester and the Department of EEE for granting me a full scholarship for my studies. I thank ORE Catapult, especially Dr Chong Ng and Mr Paul McKeever for their support, technical input and discussions.

During the last five years, the city of Manchester and the University of Manchester became my home. This was true because I was lucky to meet and be surrounded by some amazing people who became my friends. I thank Vas, Theo, Andrea, Alberto, Iñaki, Vullnet, Jack, Zhao Jin, Jesus, Damian, Diego, and many others. I thank the academics, colleagues and staff in the Power Division group for their support and always being kind and helpful.

I thank my Arta for the great support, patience, and understanding. I thank my dear family, my parents Basri and Lumturije, and my sister Blerta. They have always been the ones who support me the most and celebrate my success the loudest. This has been certainly true during my PhD. They are my strength and I owe them so much.

# 1 Introduction

Wind energy development in the 21st Century has been colossal [1]. A record new wind capacity of 93.6 GW was installed in 2021 (only 1.8% less than in 2020 despite the impact and disruptions of the COVID-19 pandemic). This brought the total capacity to 837 GW and showed a year-over-year increase of 12% [1]. This was the best year ever for offshore wind with installation of 21.1 GW [1]. Annual wind installation numbers are expected to keep increasing and GWEC expects more than 110 GW of new installations each year until 2026 [1]. Each big step in this development has come with new challenges. When going offshore and increasing the size of turbines and wind farms, one significant challenge is ensuring a high reliability and availability of offshore wind generation units while maintaining reasonable operational costs. It is likely that the wind industry will keep battling against this challenge as larger wind farms are being built farther from shore and with the introduction of new concepts such as floating wind [1].

## 1.1 Aims and Objectives

The aim of this thesis is to provide an explanation and improvement of the methodology which calculates thermal stress and lifetime consumption in IGBT modules of WT converters. In the process of achieving this aim, the following objectives have been identified:

- Definition of an approach that enables linking wind turbine mission profile and operational aspects with the thermal stress and lifetime consumption of the converter module.
- Explanation of the analytical models that are used for building the WT operational model and the converter thermal loading models
- Building a time-series simulation model that combines the WT operation and the converter thermal stress.
- Adding an algorithm that counts the thermal cycles in the IGBT junction temperature and based on the number of counted cycles evaluates the lifetime consumption relevant to the bond-wire lift-off failure mode.

- Evaluating the lifetime consumptions of a range of case studies defined with properties such as different control strategies of the WT generator or different support to grid requirements for the WT.
- Considering the options to perform model order reduction on the fully-detailed methodology in order to be able to run converter lifetime analysis for longer period of WT operation.

## 1.2 Main Contributions

**Thesis**

- Development and explanation of a methodology for thermal stress analysis and lifetime assessment of IGBT power modules in WT systems.
- Analysis of operational and control aspects of the WT for their impact on the lifetime consumption of the IGBT converter module.
- Identification of the most important aspects in the WT and converter modelling when studying the converter thermal stress and lifetime consumption.

**Journal Papers**

- **A. Ahmedi**, M. Barnes, V. Levi, J. C. Sanchez, C. Ng, and P. Mckeever, ‘‘Modelling of wind turbine operation for enhanced power electronics reliability,’’ IEEE Transactions on Energy Conversion, vol. 37, no. 3, pp. 1764–1776, Sep. 2022

**Conference Papers**

- **Ahmedi, A.**, Barnes, M., Levi, V., Carmona-Sanchez, J., Madariaga, A., Ng, C., & Jia, C. (2020, December). Lifetime Estimation of IGBT Power Modules for Reliability Study of Wind Turbine Systems. In *The 10th International Conference on Power Electronics, Machines and Drives (PEMD 2020)* (Vol. 2020, pp. 729-734). IET.
- Vilchis-Rodriguez, D. S., **Ahmedi, A.,** Barnes, M., Shen, S., Wang, Z., & Gao, S. (2021, July). STATCOM+BESS Modelling and Harmonic Analysis. In *The 17th International Conference on AC and DC Power Transmission (ACDC 2021)* (Vol. 2021, pp. 73-78). IET.

**Additional**

- Report “Modelling of Thermal Aging in Wind Turbine Transformers” for ORE Catapult. The report covered reviewing the dominating technology and reliability challenges of WT transformers. Thermal behaviour and aging were analysed for case study transformers and using mission profile from a WT operational model. The work led to a new collaboration between ORE Catapult and transformer experts from the University of Manchester with a potential for a follow up project.
- Report “Grid Connected Converter Hardware and Software Options” as part of the Power Electronic Enhanced Transformer (PEET) Project.
- Report “Review of Generator Technologies in Offshore Wind Turbines” for HOME Offshore project and ORE Catapult. A review of offshore wind generator technology, and the implication into condition monitoring and maintenance aspects.

## 1.3 Thesis Structure

This subsection gives a short overview for all the upcoming chapters in this thesis.

**Chapter 2. Reliability in Wind Turbine Systems**

This chapter gives an overview and a discussion of the available information related to reliability and availability of wind farms, with a particular interest in the ones offshore. Next the discussion of reliability is focused on the wind turbine level. A thorough literature review on the state-of-the-art in converter thermal stress modelling and lifetime prediction is undertaken. In the end the main idea of the thesis, which is to develop a methodology for lifetime evaluation of IGBT power modules in WTs, is briefly presented.

**Chapter 3. Wind Turbine and Converter System Modelling**

In this chapter the converter and WT operational models are thoroughly explained. This involves control of the WT generator and converter, blade pitch control, electrical model of the converter, representation of the mechanical behaviour of the turbine. In the end, the behaviour of the simulation models for a step change of input wind speed as well as for a highly variable wind speed profile (measured from a real site) is demonstrated.

**Chapter 4. Thermo-Mechanical Failure of the Power Electronics Module**

This chapter describes in more detail the analytical modelling of the studied thermo-mechanical failure mechanism of the converter module. Additionally, context is given how this particular failure mechanism is used when developing the methodology for evaluation of the thermal stress and lifetime consumption in WT converters.

**Chapter 5. Lifetime Evaluation of the WT Converter Considering WT Control Transients and Grid Code Requirements**

In this chapter, the methodology for evaluation of thermal stress and lifetime consumption is applied to compare the impact of different control scenarios of the WT generator and the MSC and GSC converters. The results of the comparison show valuable information on the aspects that cause the most thermal stress and lifetime consumption on the converter.

**Chapter 6. Model Order Reduction: Converter Lifetime Estimation for Longer WT Operation Periods**

In this chapter are discussed the possibilities of undertaking a model order reduction at different parts of the lifetime estimation methodology. This is of interest in order to reduce the computational complexity as well as for simplifying the methodology – i.e. to make the model more convenient to parametrise and apply in different operational WTs. The lifetime consumption and accuracy for a number of reduced models based on these options is assessed. In the end, for a chosen reduced model, the lifetime consumption analysis is undertaken for a longer WT operating period: a 24 hour period of measured wind speed data.

# 2 Reliability in Wind Turbine Systems

Wind turbines (WTs) are a complex system comprised of a large number of subsystems, assemblies, subassemblies, and components [2]. This complex system can be a subject to different failure mechanisms and reliability issues which need to be managed and kept at minimum in order to maximise wind power generation and keep the levelized cost of energy (LCOE) low. Additionally, the unprecedented growth of wind energy makes the power supply of many consumers in the future, as well as the stability of the power system itself, rely more strongly on the availability of the power generated from wind. For these reasons, improving the reliability of WT systems is an ongoing challenge and a topic of high priority for the research community, industry, manufacturers, and operators. Improving the reliability covers aspects such as designing more robust components, advancements in materials used, development of better monitoring techniques, having a better understanding of the system operation, and understanding how certain failure mechanisms can be avoided or mitigated.

Experience has shown that even what are considered as minor and ‘quick fix’ faults in onshore WTs, in offshore WTs can cause longer downtime compared to onshore, mainly because of the difficulty of intervention [3]. Additionally, there are extra factors that are distinct for the harsh offshore environment that can make different WT components more susceptible to failure. These extra factors include humidity and salty environment which can accelerate some failure mechanisms such as corrosion [4]. The availability of offshore wind farms can still be improved: different sites report different availability (more on section 2.2 and 2.3); and although for specific sites it can be higher, some sources [5] have reported an average availability as low as 85%, which is considerably lower compared to onshore availability of over 97% [5]. In the process of improving the availability and reliability of WT systems, and reducing the failure frequency of its subassemblies, one major aspect of interest is to be able to predict and model different failures that occur during the operating lifetime.

## 2.1 WT Drivetrain Configurations

The components and structural configuration of the WT drivetrain can be of importance when considering maintenance and reliability aspects. The components comprising a WT

system can be classified into three general groups: mechanical (blades, gearbox, tower, nacelle, pitch drives, yaw drives, wind speed sensors, mechanical brakes), electrical (electric generator, power converter, harmonic filters, step-up transformer, grid or collection point), and control related components which are used and interlinked with both the mechanical and electrical systems [6].

For a better comparison, WT topologies are usually classified into different categories. Various classifications of WT configurations can be made depending on the aspect of consideration [4], [7]. One common categorisation of wind turbines is done with reference to the operational speed variability and the drivetrain configuration, and describes the four most commercially used WT types since the 1980s:

1. Type A – fixed speed and no converter control;
2. Type B – limited speed variation with variable resistance (limited) control;
3. Type C – variable speed operation with partially rated converter (DFIG);
4. Type D – variable speed operation with fully rated converter.

The four most common WT types considered for commercial installation are shown in Figure 2.1 and are briefly explained in this section [4], [7], [8]. The properties of the discussed drivetrain types are summarised in Table 1. The first two types, which have a limited speed variability and control, are part of an older technology and are not considered for installation in more recent and future larger WFs – although there are installed units that still remain operational. There are some other variations of the variable-speed concepts, but these have not yet been implemented at a large scale [3].

**Type A** is the oldest topology and dominated the industry in the 1980s. It is classified as a fixed speed concept because the generating speed of the WT varies only 1-2% above synchronous speed [9]. It was the standard concept among Danish manufacturers and that is why it is commonly referred as ‘The Danish Concept WT’. As illustrated in Figure 2.1 it consists of a geared connection between the turbine and the Squirrel Cage Induction Generator (SCIG). The SCIG power output is normally fed to the grid through a power transformer. The initial design was improved with the addition of a capacitor bank, for reactive power compensation; and a soft starter, for smoother grid connection and reduction of inrush current. The advantages of this concept are its simplicity, low cost, and

reliable operation. The advantages are outnumbered by several disadvantages including the large fatigue and mechanical stresses of the system, inability to support grid voltage, reactive power consumption, low efficiency of power conversion because of fixed speed operation [4], [7], [10]. Examples of Type A wind turbines: Vestas V82, 1.65 MW [11] and Siemens 2.3-101, 2.3 MW [12].

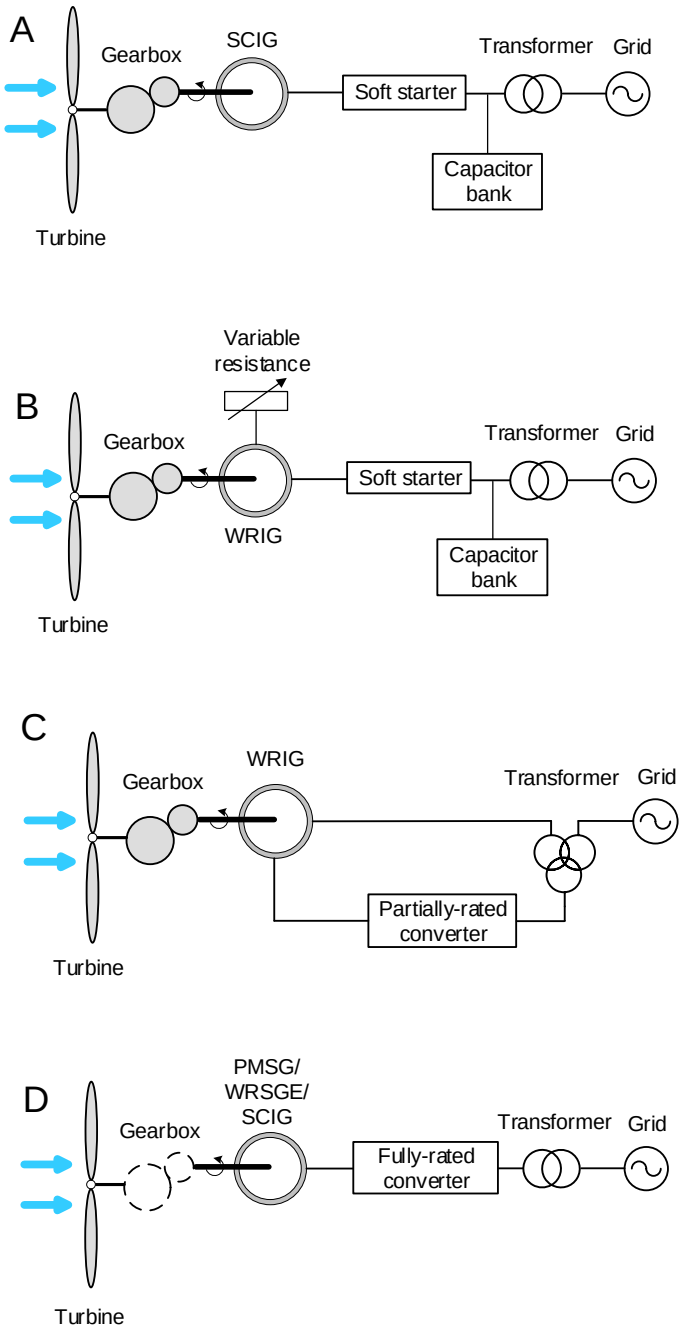


Figure 2.1: Layout of the four main types of WT concepts

**Type B** is a limited variable speed concept, also referred to as Optislip (Vestas). This was an upgrade from the Danish concept and introduced in 1990s. The difference is that it employs a Wound Rotor Induction Generator (WRIG) with variable resistance connected directly to the rotor winding. The variability in speed is achieved by controlling the energy of the WRIG rotor – dissipating energy in the external resistor as necessary. The advantages are the increased operating speed range to about +10% and the reduced mechanical stresses and fatigue compared to type A. The disadvantages are the inefficiency of dumping energy as heat loss in the external resistance, and as in Type A, reactive power consumption and an inability to support grid voltage. Commercial example: Suzlon Energy S88-2.1 MW [13].

**Type C** is a WT concept which uses a multi-stage gearbox and a WRIG as shown in Figure 2.1. The stator winding is connected directly (i.e. through a power transformer) to the grid. Meanwhile, the rotor winding terminals are connected to the grid through a partially-rated converter. The rating of the converter depends on the range of speed that the WRIG will generate at (usually ±30% of rated speed – so the converter rating is 30% of that of the WRIG). This WT topology is known as a Doubly-Fed Induction Generator (DFIG) system. As with the Optislip method, the speed is controlled by controlling the power in the rotor winding. However Type C does this more efficiently than Type B. Similar to type A and B, this topology also requires a gearbox but there is no need for a soft starter or reactive power compensation. The advantages of the DFIG are the ability to separately control active and reactive power output and therefore offer reactive power compensation and voltage support option, the option for wider operational speed range, and partial rating of converter which translates to lower capital cost compared to type D. The disadvantages include the necessary slip-ring system which requires regular maintenance and replacement (usual lifetime of 6-12 months [6]), necessity for additional control to ensure Low Voltage Ride-Through (LVRT) capability, and issues when operating under grid fault conditions [7]. Because of the good trade-off between cost and operational flexibility, this type has been the most installed turbine configuration in most onshore wind farms and has dominated the onshore market until now [6].

**Type D** is a variable-speed WT equipped with a fully rated converter. A crucial difference with Type C is that the rating of the converter, which connects the stator winding to the grid, is (at least) the same as the power rating of the generator. The gearbox

can be omitted in order to avoid unwanted drawbacks such as regular maintenance or heat dissipation. The generator is commonly a Permanent Magnet Synchronous Generator (PMSG) but it can also be other types such as a SCIG or a Wound Rotor Synchronous Generator with Electrical Excitation (WRSGE). The main advantage is the full controllability and the ability to provide reactive power support to the grid in a similar way as a STATCOM. As a disadvantage for early onshore WTs of this type was considered the increased cost because of the fully rated converter; however this diminishes for higher rated offshore WTs where the improved reliability and lower maintenance requirements make them a worthwhile investment. There is a wide range of commercial DFIG (Type C) and Type D turbines from different manufacturers and examples are given in Table 1.

***Table 1: Comparison of the characteristics for WT drivetrains of Types A to D*** [6]

| | Fixed Speed | Semi-Variable Speed | | Full-Variable Speed | |
|---|---|---|---|---|---|
| **Turbine type** | **Type A** | **Type B** | **Type C** | **Type D** | |
| **Generator** | SCIG | WRIG | DFIG | SCIG | PMSG/WRSG |
| **Power Converter** | None | Diode + Chopper | AC/DC+DC/AC (or) AC/AC | AC/DC+DC/AC (or) AC/AC | AC/DC+DC/AC (or) AC/AC (or) AC/DC+DC/DC+DC/AC |
| **Speed Range** | ±0 % | ±10 % | ±30 % | ±100 % | ±100 % |
| **Converter Capacity** | 0 % | 10 % | 30 % | 100 % | 100 % |
| **Soft Starter** | Required | Required | Not Required | Not Required | Not Required |
| **Gearbox** | 3-Stage | 3-Stage | 3-Stage | 3-Stage | 3/2/1/0-Stage |
| **Aero-Dynamic Power Control** | Active Stall, Stall, Pitch | Pitch | Pitch | Pitch | Pitch |
| **MPPT** | Not Possible | Limited | Achievable | Achievable | Achievable |
| **External Reactive Power Compensation** | Yes | Yes | No | No | No |
| **FRT Compliance** | By External Hardware | By External Hardware | By Power Converter | By Power Converter | By Power Converter |
| **Technology Status** | Outdated | Outdated | Highly Mature | Emerging | Mature |
| **Current Market Penetration** | Very low | Very low | ~50% Share | Low | Second Highest Share |
| **Example Commercial WT** | Vestas V82, 1.65 MW | Suzlon S88-2.1 MW | Repower 6M, 6.9 MW | Siemens SWT-3.6, 3.6 MW | Enercon E126, 7.5 MW |

## 2.2 Analysis of Reliability and Failure Data Surveys

The public access to availability and reliability data for offshore WTs is very limited and studies therefore have to rely and include onshore WT data as well. Additionally, the limited published data from different studies on onshore WTs are not consistent and employ different approaches and definitions. This can be misleading and conclusions need to be made with caution. Some of these surveys are dated and have considered turbines of different ages and sizes which might not be representative of modern WTs [14]. Although the available data is not sufficient and adequate for developing data driven statistical

models that would predict failures in a system, it is important for qualitative analysis and gives an insight on the field data and the industrial experience with wind turbine reliability.

There have been various initiatives and research projects to collect and discuss available data for performance and reliability of onshore and offshore WTs. A few of these initiatives are described in the rest of this subsection while the complete list of work (projects) related with WT performance databases is given in Table 2 [15]. A few very old databases have not been included in the table because their results are now too dated to help with the analysis for current or future WT technologies. Only the first four entries in Table 2 are for offshore WTs. In the next subsections a short description is given of a few of these initiatives which have been considered more relevant for offshore wind farms. More information can be found in the corresponding references in Table 2. Also, there are several published papers which provide more comprehensive comparisons of different initiatives that report on WT performance and reliability [15]–[20].

***Table 2: Data studies regarding performance and reliability of wind turbines***

| Survey | Country | End of study | Reference |
|---|---|---|---|
| **Round 1 offshore WFs** | UK | 2007 | [21] |
| **Strathclyde study** | UK | 2010 | [14], [22] |
| **WInD-Pool** | Germany/Europe | Ongoing/2019 | [23], [15]* |
| **SPARTA** | UK | Ongoing | [24], [25] |
| **Robert Gordon University** | UK | 2006 | [26] |
| **LWK** | Germany | 2006 | [27] |
| **WMEP** | Germany | 2008 | [28]–[30] |
| **Windstats** | Germany/Denmark | 2004 | [16], [27], [31] |
| **VTT** | Finland | Ongoing | [32], [33] |
| **MECAL** | Netherlands | 2010 | [34] |
| **Elforsk/Vindstat** | Sweden | 2005 | [20] |
| **CIRCE** | Spain | 2013 | [35], [36] |
| **ReliaWind** | Europe | 2010 | [2], [37], [38] |
| **Garrad Hassan** | Worldwide | 2007 | [15]* |
| **Nanjing University** | China | 2013 | [39] |
| **Huadian** | China | 2012 | [40] |
| **CWEA-Database** | China | 2012 | [41] |
| **CREW-Database** | USA | Ongoing | [42], [43] |
| **Muppandal** | India | 2004 | [44] |
| **NEDO** | Japan | 2005 | [15]* |

* - original reference analysing data from the study has not been found and the reference provided is a review paper

### 2.2.1 Round 1 Offshore WFs

Round 1 UK offshore wind farms had to publish operational reports for years 2004-2007 and these reports were meant to be used as experience for better operation of the

larger projects in the later rounds. Using the results from these reports, the performance of four offshore wind farms has been reviewed in reference [21]. This paper presents the issues that each wind farm faced in the reported years. The total data represents turbines totalling 300 MW and 270 turbine-years. The paper has included details about the nature of faults and fault modes in each wind farm, however no statistical analysis or record of the failures has been taken. Instead, the analysis and results have been presented in terms of the achieved availability, capacity factor (CF) and cost of energy (COE) from these wind farms.

The conclusion of the report was that the COE reached was satisfactory. However improvement was possible considering the lost energy which came as a result of the low availability achieved. Average availability was reported to be 80.2%, which was far lower than the average 97% which had been achieved by UK onshore WFs, and also lower than the 93.3% achieved by similar offshore wind farms in EU. The annual average CF was reported at 29.5%, which was higher than the onshore average of 27.3% at the time, but still not as high as those achieved by offshore farms in other countries.

### 2.2.2 Strathclyde Study

In [14] a different analysis on 350 offshore wind turbines from several offshore wind farms around Europe was made. This paper provides analysis of failure data from a large population of offshore wind turbines and also gives other information such as repair times, number of technicians required for repair and average cost of repair. This kind of information is very valuable for O&M cost models of offshore wind farms. Detailed analysis is given on three groups of common contributors to overall failure of offshore WTs as identified from this study: the pitch and hydraulics systems, the generator, and ‘other components’. In ‘other components’ group, this reference includes auxiliary components such as lifts, ladders, hatches, and door or nacelle seals. The empirical results are compared with figures from reference case studies in [45].

### 2.2.3 WInD-Pool

Wind-energy-Information-Data-Pool (WInD-Pool) is an ongoing initiative to share a common database of reliability data from different operators across Germany and Europe. It assesses the performance of both onshore and offshore wind farms. The data is managed

by a trusted body Fraunhofer IWES which ensures confidentiality for the data which is provided by different operators. The independent body analyses data and standardises benchmarks which are then reported back to all participants and the data providers i.e. operators. The initiative started to gather data in 2013, but because it is indirectly linked to other initiatives, it includes historic data from 2002 [15]. Publicly available reports on the results and conclusions coming from this initiative are limited.

### 2.2.4 SPARTA

System Performance, Availability and Reliability Trend Analysis (SPARTA) is an initiative created in 2013, sponsored by The Crown Estate and managed by ORE Catapult. All owners/operators with offshore wind in UK waters are involved in this project, with 19 participating offshore wind farms in UK waters reporting as of March 2019 [25], [46]. It collects operational data on 88 WT performance indicators which are reported monthly. The aim is to have a standard benchmark with monthly updates. This will allow owners and operators to make comparisons and improvements and will help achieve a continuous improvement on reliability, availability and performance of all wind farms. The benchmarking platform is an online database where Key Performance Indicators (KPI) are shared. The most recent published report is the portfolio review for 2018/2019 [46]. Production Based Availability (PBA) as defined in TS 61400 26-2 [47], is used as a main indicator to measure performance of the farms. For 2018/2019 average PBA was recorded to be 95.16%, an increase from 2017/2018 reported 94.5%, but still slightly lower value than the onshore 96.2% (in 2018) [25], [46].

### 2.2.5 Reliawind Project

EU FP7 Reliawind was a European Union project which involved 10 industrial and academic partners. It is the most extensive and most detailed publicly available failure reporting survey. Apart from analysing data for a number of 350 onshore WTs, its contribution includes also a sophisticated failure reporting and categorising taxonomy for WT systems. Around 35 000 downtime events have been organised using the proposed taxonomy and added to the database. The assessment included analysis of downtime events using 10 minute SCADA records and alarm logs [38]. Failure events were also rated in terms of maintenance requirement starting from the lowest (manual restart) up to the highest severity (major replacement). As part of the suggested taxonomy, a set of five

different tables for storing the fault events information have been developed. This standardised structure of information is then analysed using common reliability methods such as Pareto analysis. For different WT sub-categories (subsystems, assemblies, subassemblies, components) downtime and failure rates have been calculated. The average failure rate over the entire period has been calculated with the assumption that the reliability of sub-assemblies lies in the constant part of the bathtub curve [2], [38].

## 2.3 Results and Conclusions from the Reliability Initiatives

There are several reasons why the data reported in the described initiatives can be difficult to compare, including the fact that multiple initiatives report data on turbines with different ages, in different sites and consider different sizes of population. Furthermore, the reliability indicators that reports give do not follow the same taxonomy of WTs, and it is very difficult to differentiate and consistently designate reported failures to WT parts and subassemblies. In some cases the definitions of failures and downtimes is not the same, while in other cases a clear description of these concepts is not given. Authors in reference [15] have pointed out these issues and based on their experience have tried to organise the data and to come to reasonable conclusions. Nonetheless, a general comparison can still be made, mainly between performance indicators on wind farm level. Below, a comparison is made between two commonly reported performance indicators, the capacity factor and the availability of WTs studied in different initiatives.

The reported capacity factor (CF)[1] in different initiatives is given in Figure 2.2. The annual average CF from the UK Round 1 offshore wind farms in [21] was reported at 29.5%, which was higher than the onshore average of 27.3% at the time, but still not as high as the ones achieved by offshore farms in other countries. Note that as a result of higher average wind speeds in offshore sites, offshore wind farms usually tend to score higher capacity factors than onshore ones. Nevertheless, the 29.5% from early Round 1

[1] Capacity Factor (CF) is a common indicator of WT performance and is defined as the ratio between the average power output of the WT in a period of operating time and the rated power of the WT.

performance was low because of the low availability that these farms achieved in the early phase. The SPARTA portfolio in 2018/2019 [46] gave an annual average capacity factor of 36.05% for offshore wind farms in the UK. This value is slightly lower than the WInD-Pool achieved offshore capacity factor of 39% which is about the expected CF value in offshore WFs nowadays [15]. Modern offshore WFs can achieve a capacity factor between 40 and 50%, while the UK's best performing offshore wind farm is the floating Hywind Scotland which set a new record with an average 57.1% in 12 months until March 2020 [48].

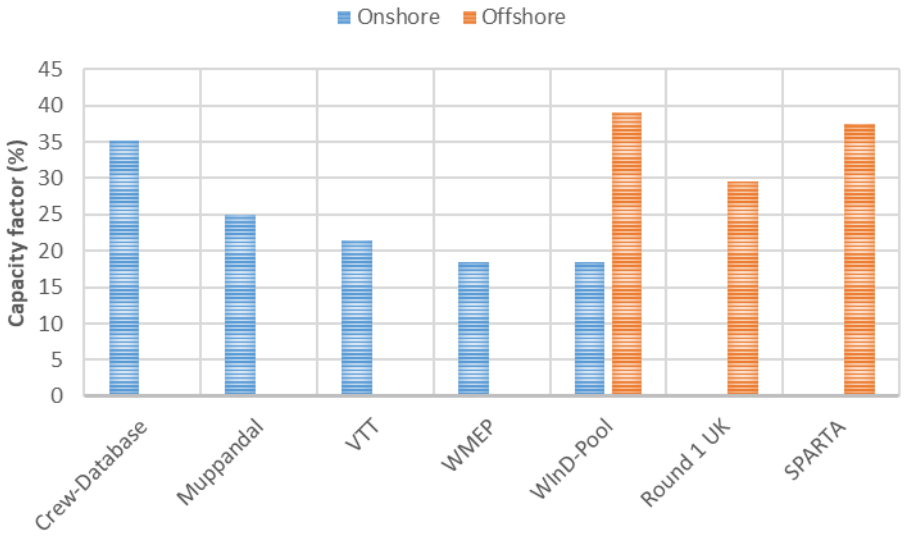


***Figure 2.2: Capacity factor of WFs reported in different initiatives*** [15]

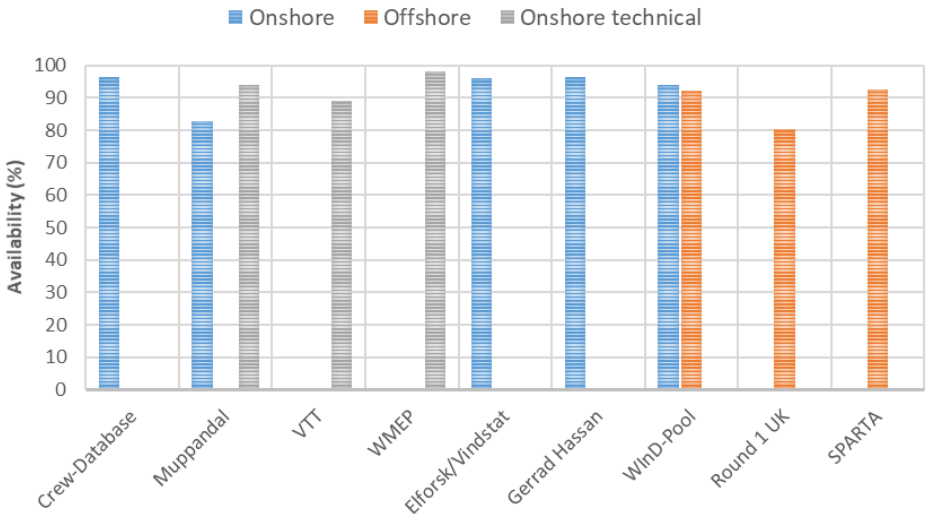


***Figure 2.3: Availability of WFs reported in different initiatives*** [15]

When comparing onshore to offshore wind farms using the results in the initiatives, as expected, the offshore ones report a higher capacity factor of up to 40% (Figure 2.2). The

onshore WFs usually have reported a capacity factor from 20 to 25%. An exception to this are the WFs in the USA, which in the CREW-Database report a CF of 35.2%. This high CF is likely to be a consequence of good site conditions with high average winds registered on the WFs that have been part of the study [15].

On the other hand, the onshore WFs report higher availability values (Figure 2.3). This is expected considering the harsh and difficult to access sites of offshore wind farms, which makes failures more likely as well as interventions and downtime last longer. Some high onshore time-based availabilities are reported from initiatives in Table 2: Gerrad Hassan 96.4%; WInD-Pool 94.1%; Crew-Database 96.5%.

In [21] a strong relation between the wind speed and availability of WFs is identified. The highest availability is reached in speeds between 7 m/s to 14 m/s. The reduction of availability above 14 m/s is because of failures that can be caused by the higher loads, while the reduction of availability that is observed for low speeds below 7 m/s is because of the scheduling of regular maintenance activities in periods of low wind. This is confirmed by [14] as well, where a trend of higher WT failures in areas with higher wind speeds is confirmed and it is concluded that this effect is more evident for offshore than for onshore sites.

In general, failure rates decline with time as WT models get more mature and industry gains experience [4], [29]. On the other hand, statistically failure rates increase as WT size increases [29]. Rapid increase in WT size has been common in the last two decades and especially emphasized when going offshore. Even though failure rates depend on the WT configuration, from results of different initiatives and studies it has been concluded that any current configuration can achieve a reasonable reliability provided sufficient experience has been gained and maintenance has been taken [4].

Depending on how a failure is defined, failure rates from 1 to 3 failures/turbine/year are common for onshore WTs [4]. In offshore wind turbines however, the reported failure rate is 8.3 failures/turbine/year, out of which 6.2 are minor repairs [14]. In [4] it is stated that for offshore WTs, a failure of 0.5 failures/turbine/year should be the goal so that, in average, the planned maintenance frequency will not be more than once per year.

Availability is a combination of failure frequency and downtime. Components which fail frequently may have a minimal impact on WT availability if they are rapidly repaired, compared with components which fail infrequently but have long repair times. For this reason, the usual approach of failure surveys is to give indicators about both the annual failure frequency and the downtime per failure for the studied component [4], [27], [49].

The ReliaWind study is one that gives very detailed results of the assemblies' contribution to failure rate and overall downtime. The results are still not detailed enough to build statistical models for failure prediction. However, the results can be considered as indicators to identify which assemblies have a potential for improved reliability. From the ReliaWind results it was concluded that the 'power module' sub-system (as classified in with the taxonomy of the study) contributed for the highest share in both downtime and failure rate of the WT. The assembly with highest impact in this reported low reliability of the 'power module' assembly was the converter [38]. The results showing the sub-system and assembly distribution of failure rate and downtime from this study are summarized in Figure 2.4 and Figure 2.5.

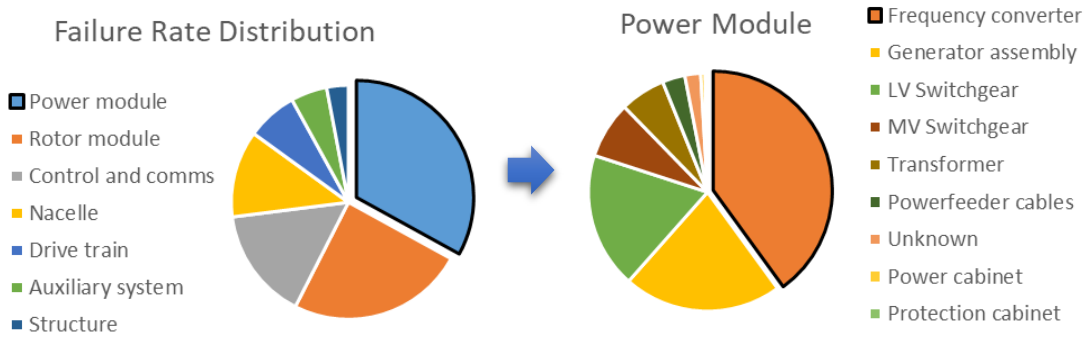


***Figure 2.4: Reliawind failure rate distribution for different sub-systems (left) and for different assemblies in Power Module sub-system (right)*** [38]

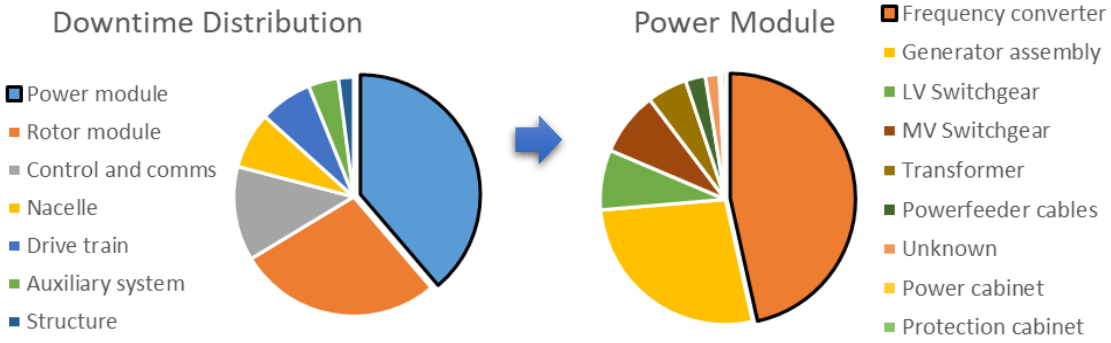


***Figure 2.5: Reliawind downtime contribution for different sub-systems (left) and for different assemblies in Power Module sub-system (right)*** [38]

It needs to be noted that the converter failures in the ReliaWind study shown in Figure 2.4 and Figure 2.5 are high. From the available data in the public, there is no way to distinguish between the different failure modes that are comprised in this number. Some of the failures are likely to have been 'infant mortality' which have been overcome while the technology has matured. Additionally, there are more than one failure causes and mechanisms which are related to converter aging and that can result in early degradation failures. These causes include humidity, temperature, and vibrations; while the failing components can be the converter phase module, capacitor, the converter control system, and so on. The methodology in this thesis is focused on the failure cause of temperature cycling, with particular attention to the failure mode of bond-wire lift-off, which are believed to dominate IGBT failures [56]–[62].

## 2.4 Physics of Failure – New Paradigm in Reliability Engineering

In the previous subsection, reliability indicators and results from large surveys were discussed. Such surveys and input from industrial experience are useful to identify WT assemblies of concern and direct the focus of reliability research towards components with high failure rate. On this basis, the power electronics is one of the most studied components of the WT in terms of reliability, given that it is a crucial part of the system and since there is potential for improvement when it comes to its reliability. To do this, there is a need to go a step further than creating data-driven reliability models and apply classical reliability methods, failure distributions, and statistical analysis on a fleet of already operating WTs. Even with access to more detailed and representative field data (which is not available publicly to the research community), for reliability/lifetime prediction, a model-based approach failures needs to be added. This model based approach, can be in the form of a digital twin of the WT, and can in real time show information on the lifetime consumption that is contributed by the operational properties of the system.

In the last two decades, the reliability evaluation of power electronic components as well as systems with a complex mission profile such as a WTs, has been considered to require a hybrid physics and statistics based approach [50]. The statistical only approach of calculating indices such as failure rates and Mean Time Between Failures (MTBF), assumes constant failures related to operating time or a number of identical missions. It

also depends a lot on the quality of data. Such analysis can be a historical observation and it does not necessarily provide information to predict or describe failures in other systems except the ones that are part of the analysed population. Reliability prediction and lifetime assessment need more in-depth analysis. Using approaches based on data and statistical analysis in reliability engineering for electronic components has been considered insufficient and not used since the 1990s, when 'military handbook' (MIL-HDBK-217F[2]) was withdrawn. Since then, hybrid methods and the Physics of Failure (PoF) approach have become widespread [50], [51]. PoF requires evaluation of the failure mechanisms that the studied component suffers as part of the system it comprises and the mission profile it encounters. This approach allows for more informed reliability calculations, eventually allowing to predict lifetime and failures in real applications.

## 2.5 Reliability and Lifetime Modelling of Power Electronic Systems

The PoF concept can be applied in different ways while assessing causes and mechanisms of failure. These ways vary from qualitative assessments such as Failure Mode, Effects and Analysis (FMEA) and up to detailed modelling of the device physics using advanced mathematical models and simulations [50]. One way that is convenient for evaluating the fatigue of systems depending on the mission profile and mechanical cycling degradation is the stress-strength approach.

In power electronic (PE) devices, one widely studied failure cause is the mechanism of thermo-mechanical strain. In this case, for more insight and useful reliability analysis, it is of high interest to apply PoF which is undertaken by a quantitative evaluation of two factors [50]:

a) the **stress** that the system imposes on the PE device – the quantity which manifests the mechanism that causes thermo-mechanical fatigue during operation. The stress indicator in this case can be the temperature cycling, which is an indirect representation of

[2] This was a handbook first developed in the '60s to predict and demonstrate reliability of electronic equipment. It was cancelled in 1995 and today is considered obsolete as a methodology/approach [51].

the mechanical load or strain that it causes (detailed explanation of the strain mechanism follows later in this chapter);

b) the **strength** of the studied device (power module of the converter) – this can be evaluated by a range of accelerated temperature and power testing of a number of devices to failure [50]. The evaluation is commonly done by manufacturers and information is provided in datasheets. That datasheet failure information is used to represent the strength of the power module (see 2.7.2 below for more explanation).

If the evaluated stress and strength can be quantified and compared, then an evaluation on consumed lifetime and failure prediction can be made: as the accumulated stress becomes larger and gets closer to the limits defined by the strength of the device, the failure probability increases. One of the challenging parts of the methodology is to bring both the stress and the strength to the same quantifiable failure criterion so that they can be compared. In the case of the power module, which is the component of focus in this study, this assessment is done based on evaluating the cycles of the temperature in the semiconductor device and its packaging.

## 2.6 A Review of Converter Lifetime Estimation Research

Extensive postoperative assessments of failures in operating turbines have been carried out in [52]–[54]. According to some studies, phase power semiconductor modules account for the highest percentage of failures in wind turbine power converters [54], [55]. Furthermore, thermal cycling has been recognised by previous models and research [55]–[62] as well as the industry [63], [64] as the dominant failure mechanism for IGBT power modules.

With the objective to create more sophisticated reliability analysis models, PoF-based reliability and lifetime studies of converters for different applications have attracted a significant interest in the last two decades [56]–[62], [64]–[69]. Advancements and new perspectives have been gained in the process, including new modelling techniques [58], [66], [70], [71], and a better understanding of the failure mechanisms [67], [72], [73]. Lifetime estimation models have been developed, including ones that focus on WT systems in particular [56], [58], [60], [74]. Particularly it was acknowledged that applying PE devices in WTs and other systems with less predictable mission profiles compared to

the mature traction applications can introduce new challenges in terms of reliability. Lifetime models for these systems could produce less useful and less accurate predictions [50].

Some models have attempted to solve the inaccuracy of the predictions by adding more detail in the thermal models of the converter or in the analytical stress and strength calculations [50], [73], [75]. All this work has been a great advancement in understanding and describing the failure mechanism on component level. However, when it comes to applying the methodology to the WT (or similar) system level and including longer term mission profiles, the approaches struggle to produce consistent and convincing results that can be compared to, and match with, observed failures and field data [53], [67]. This has left this area of research without the necessary progress that would allow the construction of models that can be used in real system scenarios, whether in the design or operational phases. There is a risk that the analysis will be reduced only to theoretical discussions and condensed into results and indices that are too distant from what they represent in the real world. In that case the whole analysis is counterproductive, providing false validation, which was the reason why the standard 'military handbook' approach for electronic components was cancelled [51]. For this not to happen, a systematic study which explains and models in detail the mechanisms that lead to failure needs to be developed. Using such a detailed model, dominating factors and transients need to be prioritised.

Field data for validation and error margin calculation of the complete methodology at the moment is limited and not publicly available because of commercial sensitivity and the pace of change of the technology [54], [55]. Parts of the methodology, such as the thermal modelling, have been validated in laboratory experiments and are feasible to be validated in field operation with further application of condition monitoring techniques and real time measurements of operational device temperature, using for example the attractive solution offered by Fiber Bragg Grating (FBG) sensors [76]. An attempt to validate a lifetime estimation model, validating the approach against an experimental setup with a range of assumptions, has been made in [77]. For the methodology developed in this thesis, attention has been paid to verify the model theoretically and against other simulations. A complete experimental validation of the methodology would be possible when it is applied to a WT system with a full scale digital twin. Building detailed digital twins is of high interest in order to operate most optimally the WTs in modern power systems; and the

methodology and analysis in this thesis contributes in building the lifetime estimation part of such models.

There is not enough data to calculate the error in similar converter lifetime and fatigue estimation approaches, whereas the error in mechanical systems from where this methodology was inspired, is assumed to be within 30 % [67], [78]. A particular benefit of converter lifetime estimation methods is the possibility to consider and compare different scenarios as well as hardware options [67]. Since in these cases, relative fatigue is compared between the different scenarios, useful conclusions can be drawn regardless of the fact that precise error margins of the calculations are not known. This has been done by several papers [59], [60], [79]–[81], however there is potential for much more to be explored. In this thesis, we consider one such comparison of control aspects in terms of converter reliability and derive from it some useful conclusions.

New challenges arise given the large range of resolutions and loading cycling of different nature when lifetime estimation based on PoF is applied on WT system level. It is of interest to run or extrapolate the analysis for longer periods of WT operation. To do this, some assumptions need to be made and it is unavoidable that some aspects need to be discounted when building the simulation. However, doing this model simplification needs to be done systematically so that the most important details are not overlooked and so that there is an idea of the error margin introduced by just the simplification itself. To contribute to this, one of the main objectives of this thesis is to undertake a systematic study of the relevant parameters in the mission profile. The importance of these parameters is assessed in terms of thermal stress and lifetime consumption, before attempting to simplify the model and run it for longer time periods.

One of the most extensive approaches for WT lifetime estimation in IGBT power modules is presented in [58]. It is a complete methodology that manages to account for fast AC frequency cycles as well as seasonal and longer term cycles introduced by the wind speed change. However, one major simplification is the consideration of different aspects of the cycling as separate, and as a superposition of a range of steady-state simulations. This overlooks the dynamic transients that are produced from the interaction between all the relevant aspects of the mission profile and the operation. These transients and the interaction are prioritised and evaluated in the methodology of this thesis.

The next step after evaluating and studying the lifetime power electronic devices is acting on the information and increasing reliability based on the evaluation. This can include more investment and research in design of the converters, redundancy, improved condition monitoring and maintenance scheduling, adapting control, and so on. Additionally, lifetime modelling can be very useful to actively improve reliability by real-time response when combined with techniques such as active thermal control. One such method is suggested in [82].

## 2.7 Proposed Methodology for Lifetime Estimation of Power Modules in WT Systems

The proposed methodology used to estimate lifetime consumption of IGBT power modules in wind turbine converters in this thesis is shown in Figure 2.6. It consists of three layers: the WT operational layer, the converter thermal loading layer, and the lifetime estimation layer. The first layer of the methodology in Figure 2.6, the WT operational layer will be described in more detail in the next chapter of the thesis. Meanwhile some of the key concepts from the other two layers are briefly described in the following subsections while also being revised and extended in the analyses in the other chapters.

The WT operational layer (model) is used to simulate the operation of the converter as a part of the WT system. This enables observation of the change of some quantities that are important for representing the mission profile. The level of detail included here defines the level of detail that can propagate and be perceived by the other two layers: the thermal loading and the lifetime estimation layer. The input of this layer and consequently of the whole methodology is the wind speed profile. The resolution of the wind profile time-series data is also important and can define which dynamic transients are included in the analysis. Ultimately, the variation of electrical quantities (currents, voltages, frequency) is attained as the output of this layer.

The second layer, the converter thermal loading model, uses as input the simulated electrical quantities from the first (WT operational) layer, and combined with other information (the converter topology, operation, applied devices, ambient temperature), the electrical loading and mission profile for the device itself are completed. This information is translated to thermal stress and temperature loading profile of the converter modules. This temperature profile is the basis of calculating the thermo-mechanical stress of the

device. Additionally, in order to make a quantifiable evaluation, an algorithm (the rain-flow counting block in Figure 2.6) is applied to count the number of cycles in the temperature profile. During this counting process, for the counted cycles, additional useful characteristic parameters which are relevant to the reliability and the failure mechanism of interest are recorded.

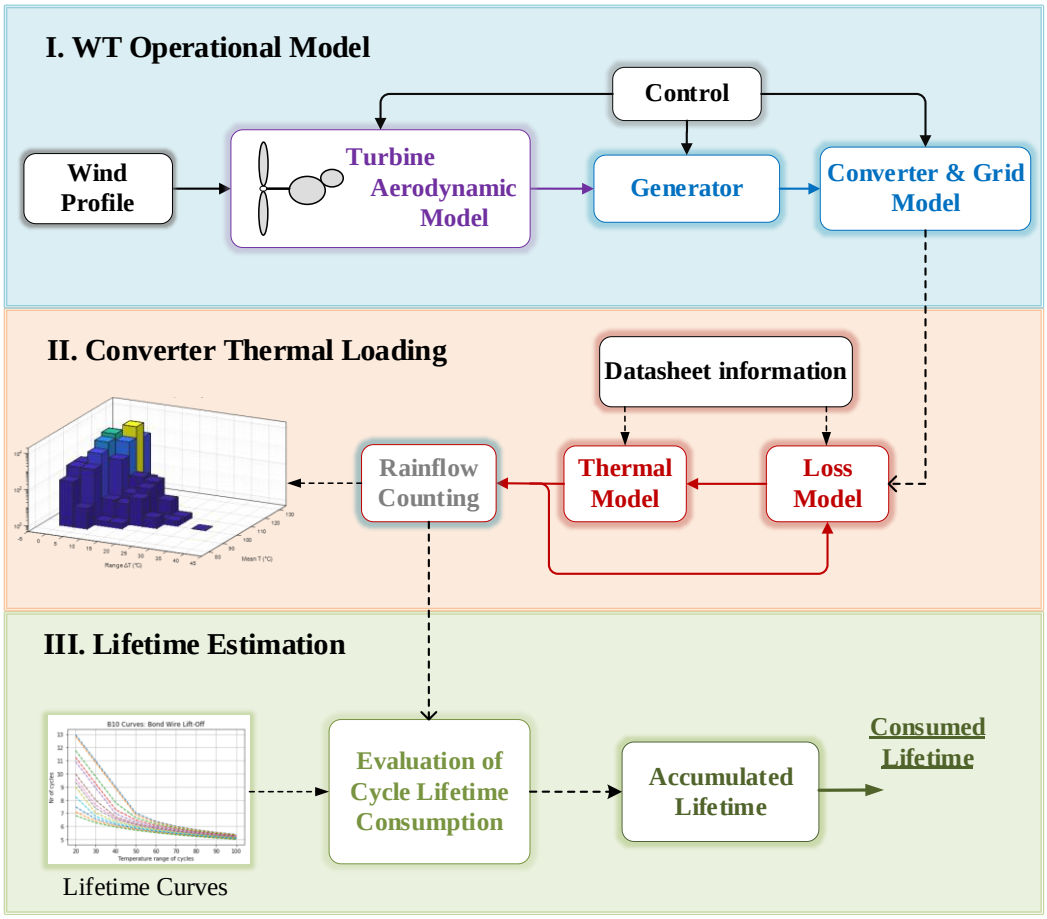


***Figure 2.6: Structure of lifetime estimation methodology***

The characteristics for the counted number of cycles in the temperature profile are analysed in the third layer, the lifetime estimation layer. This is where the observed (simulated) cycling, i.e. the **stress** in the power module as a result of the particular operation, is compared with the **strength** of the device translated from the available datasheet information. Processing of this information of stress and strength allows for evaluation of the consumed lifetime, which is the ultimate output of the third layer and the whole methodology.

This methodology is an adaptation of similar practices in research and industry [56], [58], [66], [67], [83]. The adaptation and advances are made to improve some of the

limitations of the methodology. Some of these limitations were discussed in subsection 2.6 and are extensively analysed in [67].

The improvements and the contributions in the methodology and analysis undertaken in this thesis are:

1. A consistent and systematic guide on the application of lifetime prediction models to WT converters;
2. More detailed aspects are considered in WT operational model compared to previous approaches;
3. The detailed model allows taking into account a window of transients in the converter operation that previous models have omitted;
4. A case study is performed: a comparison of WT generator control as well as grid integration aspects in terms of converter lifetime consumption.
5. Identification of best practices to minimise the margin of error in lifetime estimation when B10 curves are used;
6. Identification of the most important transients using the detailed model and undertaking a model order reduction approach in order to scale up the analysis to a larger (daily) time scale.

### 2.7.1 Cycle Counting Algorithm for Stress Evaluation

The so-called 'rain-flow' counting algorithm was initially proposed in the 60s [84] in mechanical fatigue systems and today is standardised and widely applied in lifetime analysis of different systems [85]. This is an algorithm that counts the reversals in a time-series waveform. It has also become part of the standard practice when evaluating the thermal fatigue of semiconductor power modules [86].

The rain-flow algorithm that has been applied in the methodology of this thesis is the one based on standard ASTM E1049 [85]. When applying the algorithm, a full cycle is counted when the stress load (in the case here this is the junction temperature) goes from one reversal value (valley or peak) to another and then comes back to the temperature of the first reversal value. The algorithm defined on the ASTM standard also counts half cycles for when the temperature does not return to the first value to complete the cycle, but another reversal happens in the meantime. Such half cycles are common for the loading profile of WTs because of the irregular wind speed change. Counting half cycles is also convenient for real-time application of the lifetime evaluation model, when cycles are

counted as they occur and not offline while looking at historical data [88]. The output of the rain-flow counting algorithm is a rain-flow matrix where each row consists the extracted information corresponding to every counted cycle. How this specific rain-flow algorithm is applied here when counting the reversals using a MATLAB function is described by the block diagram given in Figure 2.7.

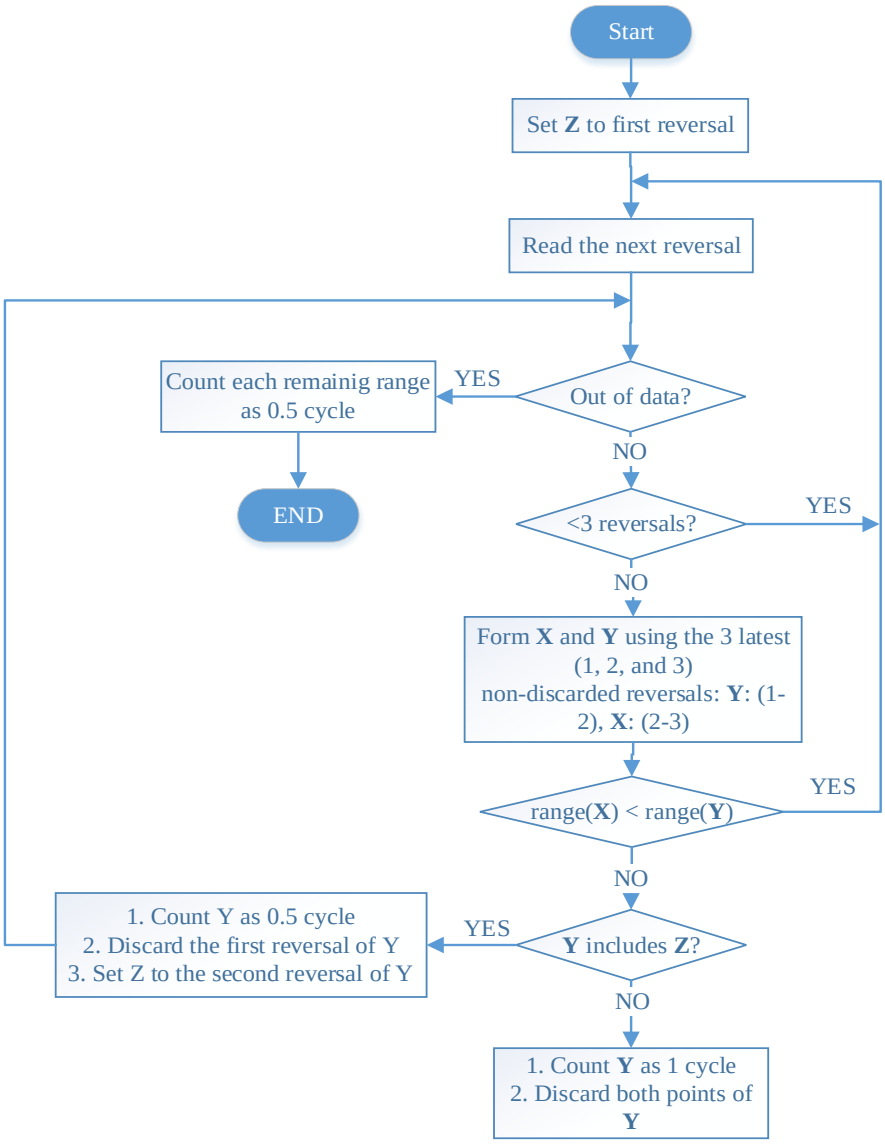


***Figure 2.7: Rain-flow counting algorithm for fatigue analysis based on ASTM E1049 standard as applied in MATLAB*** [87]

### 2.7.2 Strength Tests and Lifetime Models

Two of the most common experimental tests that are used to assess the strength of the device in terms of temperature cycling and accumulated damage are the accelerated tests: power cycling and temperature cycling (PC and TC respectively) [50]. These tests are

accelerated because the externally applied stress is exaggerated in order to bring the device to failure. For PC the external stress is conduction of power through the IGBT device which translates to losses and therefore temperature. On the other hand for TC, the temperature is raised directly using a thermal chamber. The testing results from a population of devices brought to failure are recorded and post-processed to create valuable degradation and stress-strength information. The results from these tests can be analysed, extrapolated to a range of temperatures, and fitted to statistical lifetime models [67]. Throughout the years, more complex lifetime models have been developed to represent more precisely the degradation. The more complex and precise the model, the more data and experiments needed to define it and its parameters. Some of the commonly used lifetime models with different complexity are shown in Table 3 below [57].

***Table 3: Lifetime analytical empirical models of different complexity***

| Lifetime Model | Variables considered | Equation |
|---|---|---|
| **Coffin-Manson** | $\Delta T_j$ | $N_f = a \cdot \left(\Delta T_j\right)^{-n}$ |
| **Coffin-Manson-Arrhenius** | $\Delta T_j$, $T_m$ | $N_f = a \cdot \left(\Delta T_j\right)^{-n} \cdot e^{E_a/(k \cdot T_m)}$ |
| **Norris-Landzberg** | $\Delta T_j$, $T_m$, $f$ | $N_f = A \cdot f^{n_2} \cdot \left(\Delta T_j\right)^{-n} \cdot e^{E_a/(k \cdot T_m)}$ |
| **Bayerer** | $\Delta T_j$, $T_{j-\max}$, $t_{on}$, $I$, $V$, $D$ | $N_f = K \cdot \left(\Delta T_j\right)^{\beta_1} \cdot e^{\beta_2/(T_{j-\max}+273\ K)} \cdot t_{on}^{\beta_3} \cdot I^{\beta_4} \cdot V^{\beta_5} \cdot D^{\beta_6}$ |

The equations in Table 3 show several forms of the so-called Coffin-Manson equation and describe the relation between the thermal cycling and the strength of materials: $\boldsymbol{\Delta T_j}$ is the junction temperature cycle range; $\boldsymbol{T_m}$ is the mean temperature of the cycle; $\boldsymbol{N_f}$ is the number of cycles to failure; $\boldsymbol{f}$ is the AC cycle frequency, $\boldsymbol{T_{j\text{-}max}}$ is the absolute maximum junction temperature, $\boldsymbol{a, n, \beta_{1\ldots6}}$ *are* constants; $\boldsymbol{E_a}$ is the activation energy value that characterizes the deformation process for the material, $\boldsymbol{k}$ is the Boltzman constant; $\boldsymbol{D}$ the diameter of wires, $\boldsymbol{t_{on}}$ the heating time; $\boldsymbol{V}$ is the chip voltage class (defined by blocking voltage); $\boldsymbol{I}$ is the current per wire bond [56]. More explanation and the impact of the lifetime model selection (from Table 3 and others) on the lifetime calculation has been analysed in [89] and [67].

Manufacturers undertake accelerated failure tests to power devices as part of fulfilling standard requirements. Then they do the statistical analysis of the devices tested to failure,

and extrapolate that information to construct the so-called $B_{10}$ lifetime curves to give an indication on expected device lifetime. The information in the curves represents number of cycles when 10 % of the tested devices have failed, extrapolated to other temperatures below the testing one. These curves show only a partial information from the performed experiments and from the actual reliability of the devices. The $B_{10}$ curves represent the number of cycles (Y-axis) at a certain temperature range i.e. cycle amplitude (X-axis) that a power module can withstand before it is expected to fail (Figure 2.8). The $B_{10}$ curves shown in Figure 2.8 are for the bond-wire lift-off failure mode which is the focus of the approach in this thesis (as a dominating failure in IGBT converter modules [65]) – for the complete discussion on the failure modes and mechanisms please refer to the literature review earlier in this chapter.

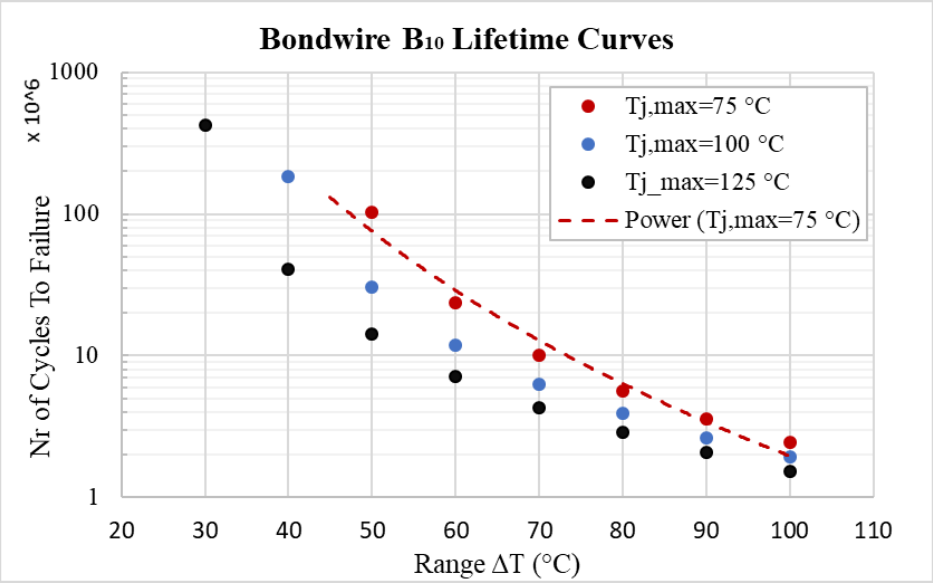


***Figure 2.8: B10 lifetime curves for wire bonds in HiPak modules: data-points and power-law fitted curve*** **[90]**

From the cycle counting, the range (magnitude) of the cycle and the mean temperature value of the counted cycles are the most important factors that the lifetime consumption calculation depends on. For this reason, to include the mean temperature dependency, several different curves can be constructed as in Figure 2.8. Scatter plots for different maximum values of the junction temperature are shown. This maximum value can be translated to the mean value for every cycle ($T_m = T_{j,max} - \Delta T_j/2$).

Reading the rated number of cycles to failure $N_f$ from the $B_{10}$ curve is an indirect application of equations in Table 3 for the situation where there is not enough information

to accurately evaluate the parameters and apply the equation. Curve fitting of $B_{10}$ data to evaluate parameters of the lifetime models does not give a satisfactory 'goodness of fit' because of the limited available data points. This can be seen in Figure 2.8 where the power law i.e. the Coffin-Manson equation from Table 3 has been fitted for the data with Tj,max = 75 °C. Applying the more complex models from the table may give a better fit but this is not always feasible depending on available information.

In this thesis, different approaches were tested and it was found that curve fitting the models to the $B_{10}$ lifetime data introduces a large inaccuracy and inconsistency of the results. It was found out that the best method to apply $B_{10}$ curves is by translating them to lookup tables, in which case the margin of error is consistent.

In this thesis, the lookup table is created by transforming the available data points from Nr. of Cycles to $\log_{10}$(Nr. of Cycles). In that case the logarithmic plot from Figure 2.8 becomes as in Figure 2.9 and linear extrapolation can be made between the data points as well as outside the defined range. When the curve in Figure 2.9 showing the $\log_{10}$(Nr. of Cycles) is reversed back to Nr. of Cycles, the linear extrapolation between each data point is a power function.

The limitations of lifetime information provided by $B_{10}$ lifetime curves is recognised in [55], [67]. Additionally, it should be noted that the models in Table 3 have an inherent inaccuracy themselves, given that they are only a statistical and empirical description of the link between the failure cause (temperature cycling) and the actual failure mechanism (the thermomechanical strain) observed in experiments. This link cannot be fully described because of the large number of influencing factors and the fact that a precise distinction between the portions of effect from every considered variable in the failure model cannot be resolved. Additionally, some of the factors such as the range and mean of temperature cycles can be interlinked [67]. There are some models which are used to analyse the actual mechanical strain in the semiconductor devices and not indirectly the thermal cycling as a cause of that strain. These models are potentially more accurate [50], [72], however applying them is a difficult and computationally expensive task given the requirements for detailed knowledge of the physical properties and structural characteristics of the semiconductor device and the package.

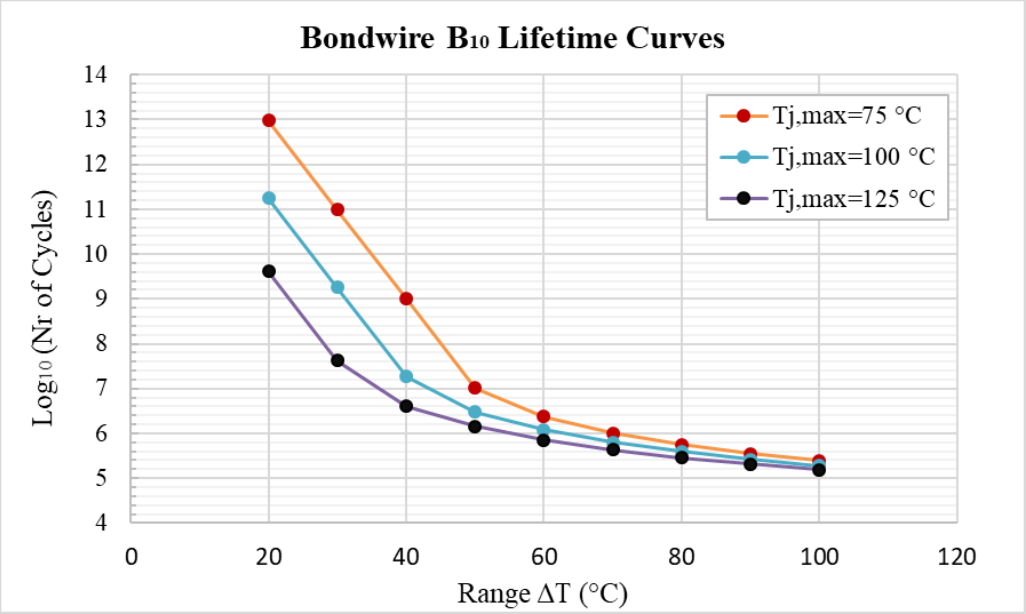


***Figure 2.9: Updated $B_{10}$ lifetime curves: linear extrapolation between $Log_{10}$(Nr. Cycles) data points***

### 2.7.3 Accumulated Lifetime

Combining the damage from all different cycles is done using Miner's rule for cumulative damage [91] described with the expression in (2.1).

$$D_{B10} = \sum_i \frac{n_i}{N_{f,i}} \tag{2.1}$$

$n_i$ - number of applied cycles $\Delta T_i$

$N_{f,i}$ - number of cycles to failure for $\Delta T_i$

Miner's rule gives as a result the percentage (share) of the module's lifetime, which has been consumed for all the cycles with different temperature ranges and mean values. As seen in (2.1) the effect of each cycle is calculated with the ratio between the counted cycles $n_i$ at a particular temperature and the rated cycles $N_{f,i}$ at that same temperature that the module has been tested and expected to withstand before failure. Therefore, the device will fail when the total lifetime $D_{B10}$ in (2.1) equals to one – meaning that 100% of the $B_{10}$ lifetime has been consumed. It is worth mentioning that one major assumption made in applying Miner's rule is treating this kind of fatigue mechanism in IGBT modules as linear – this premise needs further investigation [67].

## 2.8 Summary

In this chapter, a review and background on the reliability of wind turbine systems was given first. An extensive range of initiatives that report reliability and performance indicators on offshore wind turbines were presented. Based on these studies, a discussion on the performance of offshore and onshore wind turbines and wind farms was undertaken. Afterwards, the paradigm of physics of failure (PoF) as a reliability approach was introduced. The PoF and stress-strength lifetime evaluation approach in power electronic modules was described. Then the stress-strength methodology for lifetime evaluation of IGBT power modules in WT applications which is developed in this thesis was defined. The contributions of this methodology were outlined, supplemented with a thorough literature review of similar previous work. A brief description of the constituent layers of the methodology was undertaken. Parts of the methodology in each layer will be more extensively explained and applied in the other chapters.

# 3 Wind Turbine and Converter System Modelling

This chapter gives a detailed description of the structure and the modelling of the Wind Turbine (WT) operational layer which is essential in the lifetime estimation methodology that is developed and applied in this thesis. This description includes the modelling of the operation and the control aspects of the Wind Turbine system, with a focus on the aspects which are relevant for the intended study. The choices in the design and configuration of the WT system are explained. The design and tuning of the control loops are also elaborated.

## 3.1 Description of the System

The arrangement of the studied WT system and its connection to the grid is shown in Figure 3.1. The turbine is based on the NREL baseline 5 MW wind turbine [92], which is a reference WT that is widely applied in research.

The reference WT has been amended in a similar manner as in [93], [94]. The gearbox has been eliminated from the original design to adapt for a direct drive solution. Direct drive WT drive-trains are preferred over geared ones in current offshore multi-MW wind turbines, to reduce maintenance requirements [95]. Additionally, the turbine has been connected to a Permanent Magnet Synchronous Generator (PMSG). The PMSG has been adapted from reference [96].

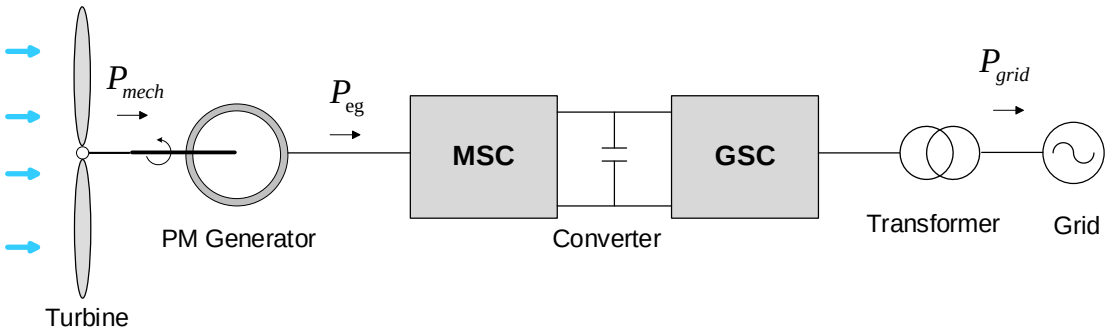


***Figure 3.1: PMSG gearless WT system layout***

To control the generator for variable speed operation while synchronising and injecting power to the grid at AC frequency, a Back-to-Back Voltage Source Converter (BVSC) is used. This topology belongs to Type D Variable Speed Full Scale Converter WT

topologies according to the classification described in Chapter 2. The main parameters of the WT system configuration are shown in Table 4.

***Table 4: Parameters of the WT system configuration***

| Parameter | Symbol | Value |
|---|---|---|
| **Rated power [MW]** | $P_{rated}$ | 5.08 |
| **Nominal torque [MNm]** | $T_{rated}$ | 4.02 |
| **Rated mech. rotor speed [rad/s]** | $\omega_{rated}$ | 1.256 |
| **PMSG pole pairs** | $p_p$ | 100 |
| **Generator mom. of inertia [kgm$^2$]** | $J_g$ | 534.166 |
| **Turbine moment of inertia [kgm$^2$]** | $J_w$ | 38.76 x10$^6$ |
| **Shaft stiffness [Nm/rad]** | $k_{wg}$ | 767.63 x10$^6$ |
| **Shaft damping [Nm/(rad/s)]** | $d_{wg}$ | 6.21 x10$^6$ |
| **Stator resistance [mΩ]** | $R_s$ | 50 |
| **Stator inductance (dq) [mH]** | $L_{sd} = L_{sq}$ | 7.8 |
| **DC link voltage [kV]** | $V_{DC}$ | 7.2 |
| **DC link capacitance [mF]** | $C_{DC}$ | 50 |
| **Generator side AC frequency [Hz]** | $f_{g,AC}$ | 20 |
| **PWM switching frequency [Hz]** | $f_{PWM}$ | 1750 |

## 3.2 The Back-to-Back Voltage Source Converter (BVSC)

The power electronics (PE) system is a fundamental part of the electrical system of the WT. In this case the PE is a combination of two Voltage Source Converters (VSCs), a Machine Side Converter (MSC) and a Grid Side Converter (GSC), with a DC link capacitor connecting the two. The MSC operates as a rectifier and transforms the AC power generated at the PMSG stator terminals to DC power on the DC link. The GSC then operates as an inverter, and 'feeds' the power from the DC link to the wind farm grid. This combination is called a Back-to-Back VSC (BVSC). This connection ensures decoupling of the grid and the PMSG. The former has a (nearly) constant frequency defined by the grid code, while the frequency of the latter is continuously changing with the changing wind speed. Accordingly, power generation at different and variable wind and rotor speeds is made possible by this decoupling.

## 3.3 VSC Topologies and Hardware Choice

There are different generations of the converter topologies that have been developed for power transmission applications (mainly in HVDC and FACTS technology development). One categorisation of these different topologies is in terms of the switching levels used to synthetize the desired output voltage – shown in Figure 3.2 [97]. Except for the number of

levels, two other main aspects in which the three generations of converters from Figure 3.2 differ are their design and control complexity, and the harmonic content of the output voltage waveform. The technology and experience with these topologies has been adapted and applied to converters used for grid connection of WT systems. Given the low voltage and power level of WTs as compared to HVDC systems, the two-level topology has had suitable operational characteristics and has been the standard used concept [98]. With the increase in WT size and power level, as well as the voltage level of the wind farm arrays, the three-level and multilevel concepts are becoming more attractive solutions for grid integration of WTs [99].

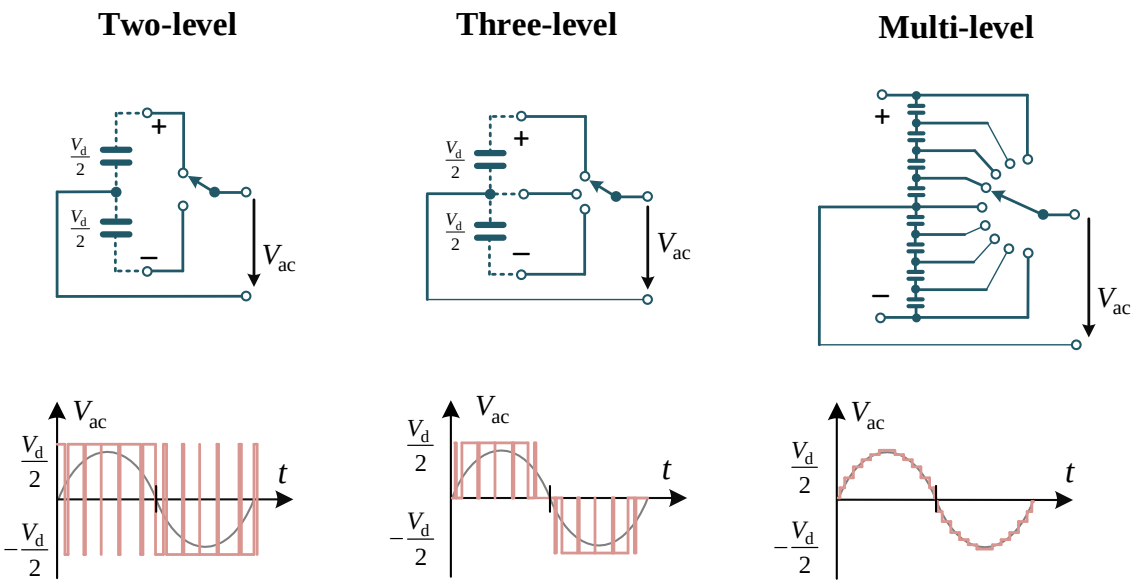


***Figure 3.2: Three main generations of VSC topologies depending on the number of levels in the output voltage. The representation of the semiconductor switch as an ideal switch is a simplification and the switching waveforms are a simplified illustration (redrawn from* [97]*)***

An important aspect when considering the choice of converter and topology is the harmonic content of the AC output voltage and the grid requirements. This choice is linked with both the hardware design and the software control of the specific converter. For topologies with different levels as in Figure 3.2, the harmonic content decreases with increasing number of steps in the synthetized voltage waveform. For the two-level and three-level topologies, usually an appropriate low-pass filter is designed to filter the high order harmonics. This filter is usually a network combination of inductors and capacitors on the AC connection side [100].

For the system simulated in this thesis, it is assumed that a two-level topology is applied for both converters in the BVSC. This simplifies some of the control aspects in the analysis of the power module losses and the lifetime consumption evaluation.

There are a number of semiconductor devices that are used in the industry for different applications. IGBTs with bond-wire technology are one of the most widely applied module technologies in WT systems [53], [100]. The choice of switching device for a certain application is dependent on the power level and device frequency as shown in Figure 3.3.

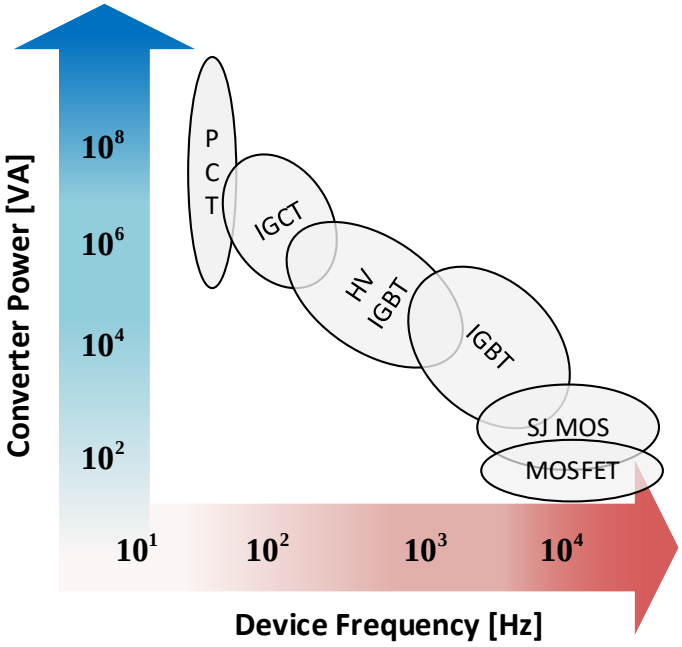


***Figure 3.3: Power level and switching frequency ranges for converters based on different power semiconductor switches (redrawn from* [101]*)***

The studied power semiconductor device (module) in this thesis is the IGBT in a two-level converter application. As illustrated in Figure 3.3, IGBT modules are the best choice for a kHz switching frequency and for kW active power output. For WTs rated higher than 3MW, two-level IGBT VSCs can suffer from high switching losses, and have a limitation coming from the current and voltage rating of modules. These additional challenges require special attention when designing multi-megawatt WTs. Alternative solutions have been considered. Such solutions include using IGCTs instead of IGBTs, using new technologies of press-pack IGBTs that eliminate the bond-wire connection, or going to multilevel converters. However, multilevel converters are yet to be applied widely in the wind industry [53]. Additionally, the majority of new WTs, including the Enercon E126-7.58, the MHI

Vestas V164-8.0, and the Siemens Gamesa SWT-7.0/SG-8.0, continue to apply standard IGBT modules [53].

The adaptation and design of the WT system simulated in this thesis have imposed operational requirements for the converter system. In this process it was concluded that the converter requires a power output capability higher than 5MVA, a BVSC DC link voltage of 7.2 kV, and a switching frequency of 1.75 kHz. These requirements can contribute to a large increase of the switching losses of the IGBT device and an increase of the junction temperature above the rated value (125 °C). The high switching frequency makes this a challenge even for highest rated IGBTs available on the market: the one chosen here is ABB HiPak 5SNA 0400J650100, which is rated for 6.5 kV blocking voltage and 400 A maximal current. In order to design the two-level IGBT BVSC topology with within these limitations, the assumption is that a certain number of modules are connected in parallel (13 modules) and in series (2 modules). It is assumed that suitable technology is used to allow voltage and current sharing. Similar technical and theoretical aspects have been respected in adapting the whole system. The connection of modules in series and parallel is not uncommon in commercial products [102]. However, the assumption here is that the IGBT devices are ideal and there is perfect current sharing between them when connected in parallel. More elegant solutions could be designed, but such a design ambition is outside the scope of this work.

Some other design aspects of the WT and converter system in this thesis might vary from the industrial design given that industrial practice is commercially sensitive and not fully public. If necessary, the approach can also be upgraded to consider a three-level or multilevel converter by changing the converter operational model, while the other parts of the lifetime methodology would remain identical.

## 3.4 Subsystem Description and Modelling

Modelling of the WT system is a central part in the work undertaken in this thesis. In this subsection the main characteristics and the modelling of separate subsystems that comprise the WT operational layer are described.

### 3.4.1 Aerodynamic Model

Starting from the left side in Figure 3.1, a fundamental part of the WT system is the rotor and its blades, which capture the kinetic energy of the wind. In this case the turbine is

Horizontal-Axis WT (HAWT) with three blades. The rotor system in the WT can be represented by a complex model if intended for aerodynamic studies [103], [104]. However, using an analytical aerodynamic model is sufficiently detailed for analysing the power conversion of the WT when coupled with its electrical system, [105], [106]. Such an analytical aerodynamic representation is used here and is described with equations (3.1) - (3.4). The analytical aerodynamic model equations describe the transformation of power: from the form of kinetic energy in the wind to rotational mechanical power in the turbine shaft. This aerodynamic model representation entails a number of assumptions and ignores effects such as drivetrain damping or variation in loads on the blades and the turbine tower.

The aerodynamic power $P_a$ extracted from the air [Watts] is given in (3.1) and it is proportional to the air density $\rho$ [kg/m$^3$], the rotor swept area $A_R$ [m$^2$], the power coefficient $c_p(\lambda,\beta)$, and the cubic power of wind speed $v_w$ [m/s]. The power coefficient $c_p(\lambda,\beta)$ is a function of the tip speed ratio $\lambda$, and the pitch angle of the rotor blades $\beta$ [degrees]. The $c_p(\lambda,\beta)$ is defined by the analytical approximation in (3.2) and (3.3). $T_w$ in (3.5) is the rotor torque [Nm], $\omega_m$ is the rotor mechanical speed [rad/s], $l$ is the radius of the rotor swept area [m]. As mentioned, the gearbox is emitted in this design, so the WT torque and mechanical speed are transferred to the generator side through the common shaft without any transformation (no stepping-up of the speed or stepping-down of the torque from the 'low-speed' side of the WT).

$$P_a = \frac{\rho}{2} A_R c_p(\lambda,\beta) v_w{}^3 \tag{3.1}$$

$$C_p = 0.5176\left(\frac{116}{\lambda_i} - 0.4\beta - 5\right)e^{\frac{-21}{\lambda_i}} + 0.0068\lambda \tag{3.2}$$

$$\frac{1}{\lambda_i} = \frac{1}{\lambda + 0.008\beta} - \frac{0.035}{\beta^3 + 1} \tag{3.3}$$

$$\lambda = \frac{l\omega_w}{v_w} \tag{3.4}$$

$$T_w = \frac{1}{2\omega_w}\rho\pi l^2 v_w{}^3 C_p \tag{3.5}$$

### 3.4.2 Drive Train Model

There are four types of shaft or drive train models that have been considered in literature: one-mass (lumped), two-mass, three-mass, and six-mass drive train model. Each of these models considers a particular number of mass inertias, with the six-mass being the most detailed. A two-mass model, shown in Figure 3.4, is considered suitable for the dynamics analysed in this thesis [9], [60], [94].

The two-mass model dynamics for the WT are described by the differential equations in (3.6) - (3.8). In these equations $J$ represents the moment of inertia [kg m$^2$]; $\omega$ is the mechanical speed [rad/s]; indexes *w* and *g* indicate turbine and generator quantities respectively; $k_{wg}$ is the shaft stiffness [Nm/rad]; $d_{wg}$ is the shaft mutual damping [Nm/(rad/s)]; $\theta_{wg}$ the twisting angle between the turbine and the generator; $T_w$ is the aerodynamic torque of turbine rotor [Nm]; and $T_{ge}$ is the electromagnetic torque of the generator [Nm].

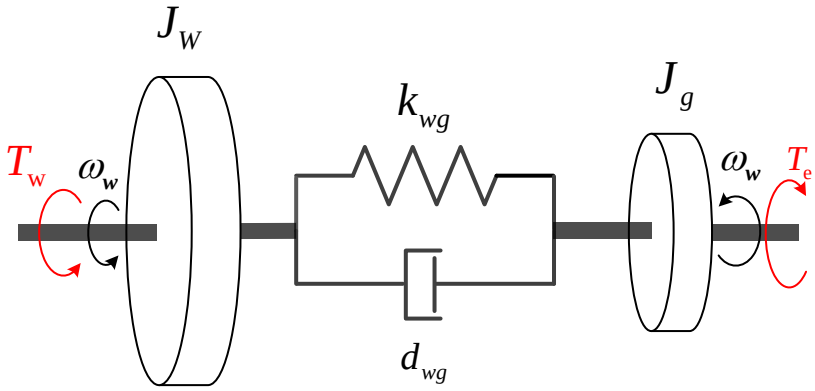


***Figure 3.4: Two-mass wind turbine drive train model (redrawn from*** [94]***)***

$$J_w \frac{d\omega_w}{dt} = T_w - k_{wg}\theta_{wg} - d_{wg}\frac{d\theta_{wg}}{dt} \tag{3.6}$$

$$J_g \frac{d\omega_{gm}}{dt} = k_{wg}\theta_{wg} + d_{wg}\frac{d\theta_{wg}}{dt} - T_{ge} \tag{3.7}$$

$$\frac{d\theta_{wg}}{dt} = \omega_w - \omega_{gm} \tag{3.8}$$

The differential equations in (3.6) - (3.8) are used to set up the transfer functions and build the time-series model that simulates the speed and torque change of the wind turbine and the generator.

### 3.4.3 Electrical Part

Connected to the mechanical part is the electrical part of the WT drivetrain, where the mechanical power from the rotor shaft is transformed to electrical power in the generator stator winding. The electrical part (model) of the system is represented by the dynamic equations which describe the relationship of voltages and currents in the generator and the network. These equations are used to build the time-series models in the simulation.

### *3.4.4* Generator Dynamic Equations

The behaviour of three phase electrical machines is described by differential equations of the voltages and currents. For such rotating machines the flux linkages and induced voltages change continuously as the machine rotor changes position over time and the electric circuit of the rotor is in motion relative to the stator winding. This creates a complex system where the flux linkage and the coefficients that define the differential equations are time varying. Usually the analysis is simplified by using mathematical transformations to decouple the variables and by referring to all variables in a common reference frame.

One widely used mathematical transformation is to the d-q (direct and quadrature axis) reference frame, which involves two steps (transformations):

a) transformation of the three phase electromagnetic field vector to two vector components $\alpha$ and $\beta$, which is known as the **Clarke transformation**; and

b) transformation from a stationary reference frame with vector components $\alpha$ and $\beta$ to a rotational reference frame with vector components d and q. This is known as the **Park Transformation.**

The Clarke and Park transformations are given in equations (3.9) and (3.10) respectively. There is another set of equations for the reverse transformation of the dq quantities to three-phase AC components. Different variants of these transformations can appear in the

literature depending on the applied conventions when they are derived. These conventions include the choice of alignment of the d and q axes, direction of rotation of the reference frame, and so on. Because transformations are made only in the control software and in the analysis, it makes no difference which version is used – as long as the assumptions are consistent in both directions of the transformation and for all the analysed quantities. The used convention in this thesis is that the q-axis is leading the d-axis in a counter-clockwise rotation. For the generator control the d-axis is aligned with the magnetic flux of the PM. A good overview and explanation of the Park and Clark transformations is given in [107]; for more extensive derivation and the background theory of d-q components, please refer to standard textbooks on electrical machines and drives.

$$\begin{bmatrix} v_\alpha \\ v_\beta \end{bmatrix} = \begin{bmatrix} 1 & -\frac{1}{2} & -\frac{1}{2} \\ 0 & \frac{\sqrt{3}}{2} & -\frac{\sqrt{3}}{2} \end{bmatrix} \begin{bmatrix} v_a \\ v_b \\ v_c \end{bmatrix} \tag{3.9}$$

$$\begin{bmatrix} v_d \\ v_q \end{bmatrix} = \begin{bmatrix} \cos\theta & \sin\theta \\ -\sin\theta & \cos\theta \end{bmatrix} \begin{bmatrix} v_\alpha \\ v_\beta \end{bmatrix} \tag{3.10}$$

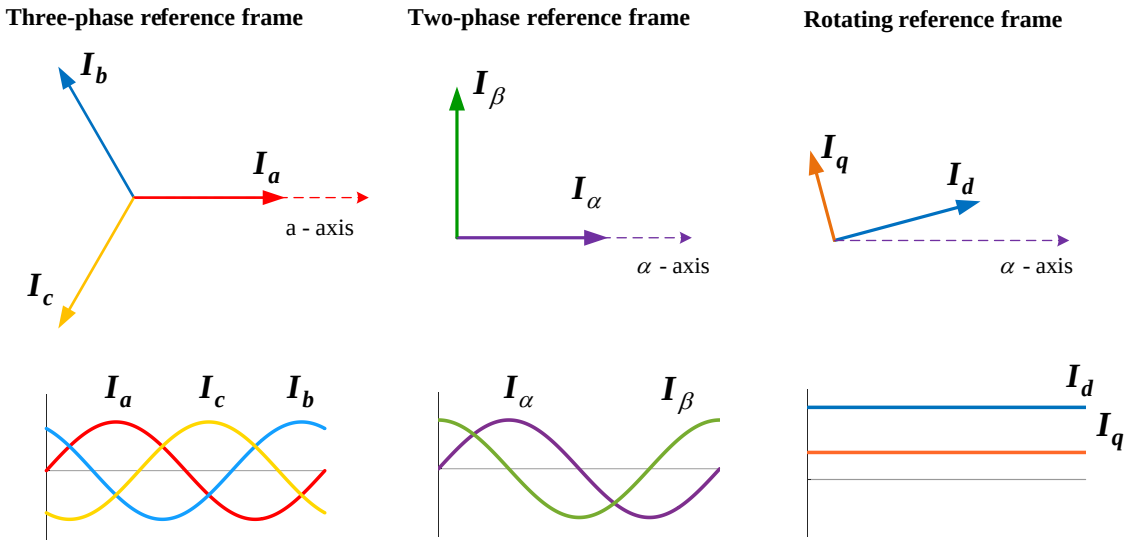


***Figure 3.5: Simplified steps of the three phase to dq reference frame transformations***

This transformation is originally derived from the spatial electromagnetic field distribution and applied to the resultant field flux vector in the machine. However, it is also valid and usually applied to the other quantities of a balanced three-phase system, such as currents and voltages. The steps of the transformation and the resulting waveforms when

applied to transform the three-phase sinusoidal AC current are shown in Figure 3.5. As seen in the figure, with the correct choice of reference frame, the transformation results in two DC components.

The transformation to dq components and the resulting DC quantities are attractive for applying control approaches such as PI controllers, which do not work as well with AC quantities. Similar to other drive applications, the control of WT generators is also commonly performed using field-oriented control where the machine equations are transformed in a d-q reference frame.

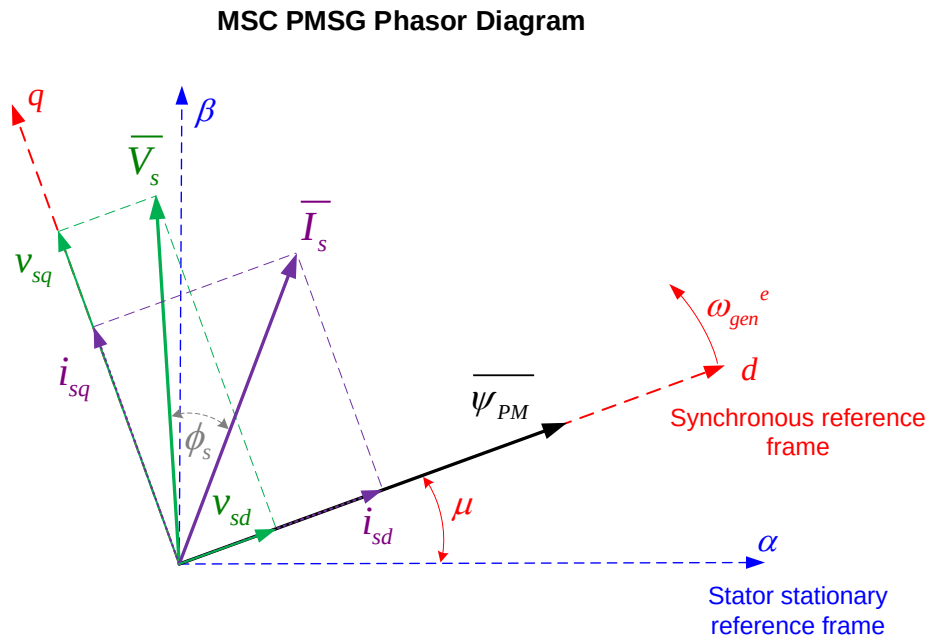


***Figure 3.6: PMSG Phasor Diagram in rotating reference frame***

For the PMSG voltages and currents, the choice is to transform to a reference frame that rotates at the electrical speed of the rotor $\omega_{\text{gen}}{}^{\text{e}}$, i.e. the speed of the electromagnetic field. Furthermore, the d-axis of the reference frame can be aligned with the PM magnetic flux of the rotor $\Psi_{\text{PM}}$ as shown in Figure 3.6 – in that case the PM flux vector has only the d-axis component $\bar{\psi}_{PM} = \bar{\psi}_{PM\_d}$ while the q-axis component is $\bar{\psi}_{PM\_q} = 0$. Such an alignment is usually referred to as 'field oriented', and the PM machine voltage equations in the dq reference frame take the form shown in equation (3.11) and (3.12).

$$v_{\text{sd}} = R_{\text{s}} i_{\text{sd}} + L_{\text{sd}} \frac{di_{\text{sd}}}{dt} - \omega_{\text{gen}}{}^{\text{e}} L_{\text{sq}} i_{\text{sq}} \tag{3.11}$$

$$v_{sq} = R_s i_{sq} + L_{sq}\frac{di_{sq}}{dt} + \omega_{gen}{}^{e}L_{sd}i_{sd} + \omega_{gen}{}^{e}\Psi_{PM} \qquad (3.12)$$

### 3.4.5 Network Dynamic Equations

Similar to the PMSG side, dynamic equations that describe the grid connection of the WT system can be derived. These equations form the network model which is another component of the electrical part of the WT operational layer. The network model is built similarly to the machine d-q representation, where the grid is analogous to a large synchronous generator. The grid model describes the grid voltage equations, i.e. the relation between the d-q components of the voltage drop and the current flowing between the GSC and the grid.

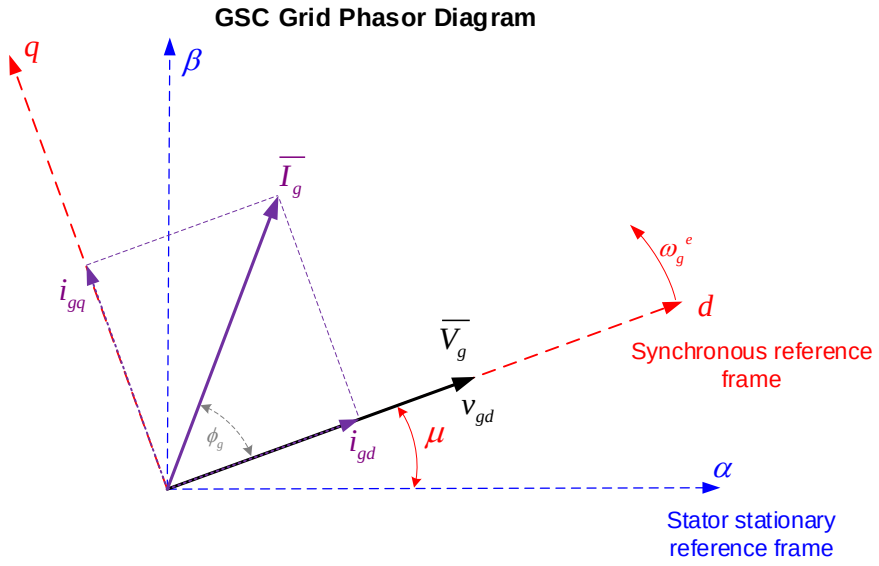


***Figure 3.7: Grid Phasor Diagram in synchronous reference frame***

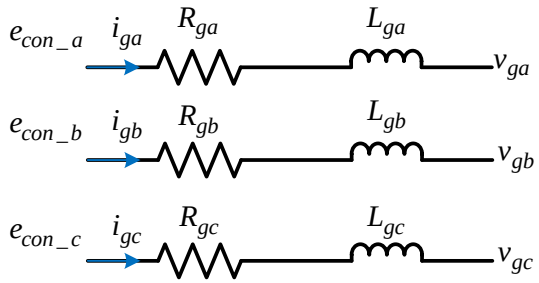


***Figure 3.8: Basic VSC and grid connection circuit*** [108]

The phasor diagram of the current and voltage components for the grid connection of the WT generated power is given in Figure 3.7. It is chosen that the dq reference frame in this case rotates at synchronous speed of the AC grid. While in the case of the PMSG, the

reference frame was oriented with the flux field of the generator (i.e. field oriented), in the case of the GSC the transformation is with voltage orientation – the voltage phasor is aligned with d-axis as in Figure 3.7. The equations are given in (3.13) and (3.14). The difference here is that the grid voltage at the point of connection (PoC) is set externally to be constant as defined by the grid code. The integration of power is realised by the GSC, governing the current flow between the output terminals of the converter and the PoC, while controlling the voltage difference $e_{con} - v_g$ between these two points (see Figure 3.8.).

Grid short circuit ratio here was assumed to be very high and the grid voltage magnitude and frequency are assumed to be kept constant (e.g. by being controlled by the HVDC MMC offshore converter). If there would be a connection to a "weak grid" with voltage variation, this would additionally change the current in the GSC and also the thermal cycling that is calculated. This scenario has not been studied here.

$$e_{con\_d} - v_{\mathrm{gd}} = R_{\mathrm{g}} i_{\mathrm{gd}} + L_{\mathrm{gd}} \frac{di_{\mathrm{gd}}}{dt} - \omega_{\mathrm{g}}{}^{\mathrm{e}} L_{\mathrm{gq}} i_{\mathrm{gq}} \tag{3.13}$$

$$e_{con\_q} - v_{\mathrm{gq}} = R_{\mathrm{g}} i_{\mathrm{gq}} + L_{\mathrm{gq}} \frac{di_{\mathrm{gq}}}{dt} + \omega_{\mathrm{g}}{}^{\mathrm{e}} L_{\mathrm{gd}} i_{\mathrm{gd}} \tag{3.14}$$

## 3.5 Control Levels of a PMSG Wind Turbine

The control of the PMSG WT used in this thesis can be separated in three levels as summarized in Figure 3.9. Note that this is a simplification and there are a number of other control aspects that are not illustrated because they are not considered in the modelling. The three levels of control illustrated in Figure 3.9 include several aspects:

**First level control**

c) **Converter switching (voltage) control** – includes the control of switches with the aim to synthetize the necessary voltage in the output terminals of the VSC. In the model here to control the IGBT switches, a sine-triangle PWM control is applied (explained below). The complete switching transients are not modelled – a switch-average model is applied instead. Nonetheless, the aspects of the PWM such as the duty-ratio and the switching frequency are still included and are important for the calculation of the losses and the thermal stress in the semiconductor devices. Even though in this thesis fast transients of current and

torque control change are modelled, the switching transients at 1.75 kHz were not included for simplification – because for the intended study here, they are too fast to cause significant thermal cycling in the IGBT. It is additionally assumed that the converter PWM control is designed to avoid any interference with the other control loops which are actually included in the simulation model.

d) **Converter current control** – for both the MSC and GSC controls, the necessary switching pattern of the devices is synthesized depending on the output voltage and current in the application. The current control loop is used to determine what this output voltage and current need to be and what voltage needs to be synthetized by the switching control. Usually the loop is designed to control the current while from the machine and grid dynamic equations the voltage is determined as well (the control design explained in the following subsections).

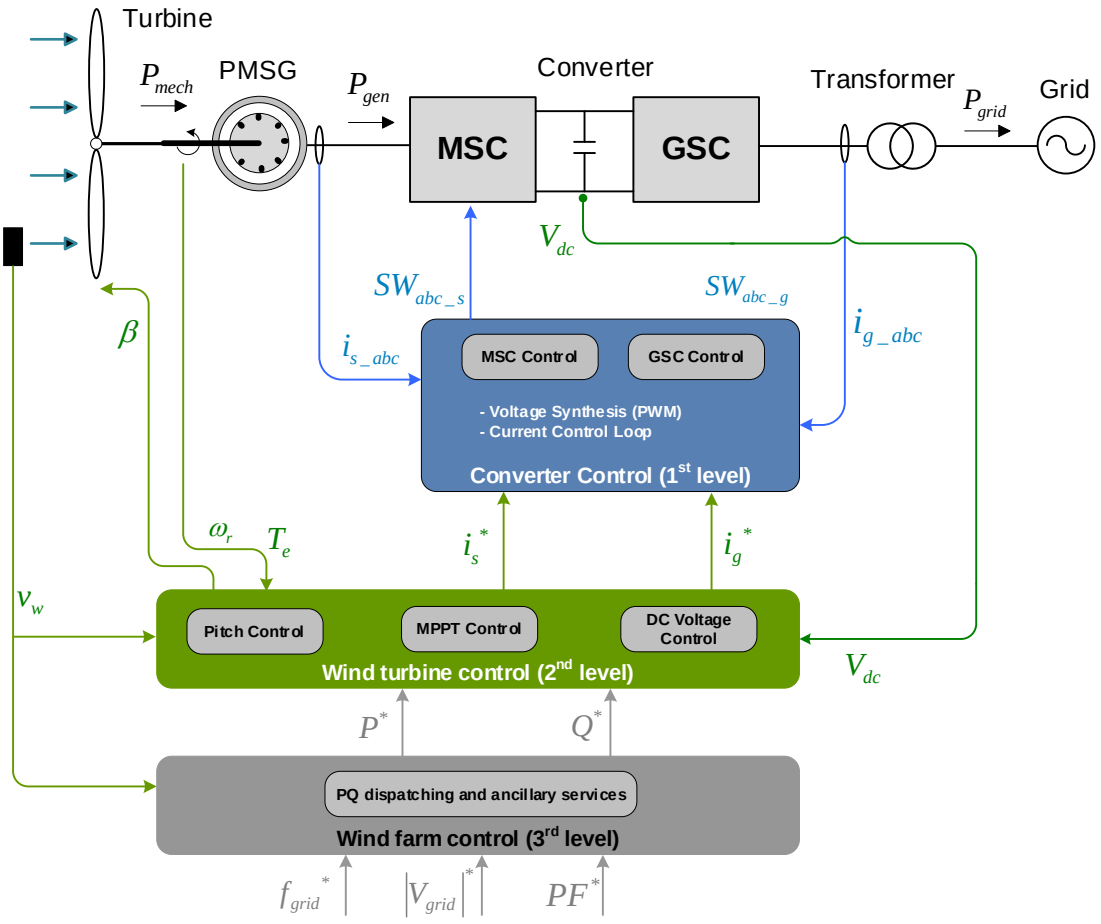


***Figure 3.9: Different levels of control for the PMSG wind turbine***

**Second level control**

e) Both the MSC and the GSC have outer loops on top of the loops which control the current. For the MSC this outer loop usually controls the Power/Torque/Speed of the generator. This is how the Maximum Power Point Tracking (MPPT) control is achieved.

f) For the GSC, on the other hand, the outer loop commonly controls the DC voltage in the DC link of the BVSC. Additionally, the reactive power output can be controlled independently (by utilising the d and q components of the currents independently, two independent outer loops can be applied).

g) Another control that here is incorporated in the second level and is considered in this thesis is the pitch control. This controller ensures that the turbine blades are pitched accordingly depending on the wind speed and the required active power capture of the turbine. This pitching of the blades is active and particularly important for operation above the rated wind speed of the turbine, where with the help of the pitch control the output power is limited to its rated value.

**Third level control**

The third level control in Figure 3.9 is included to indicate the commands coming from the wind farm level control towards the particular WT. These commands affect the other lower level controls and usually depend on the overall wind farm control design and operators commands. In the simulation here, the assumption is that the command for the WT is to output the maximum available power for the given wind speed hitting the rotor blades.

## 3.6 Converter Control and Software

The control of the VSCs is a sub-system of the WT control illustrated in Figure 3.9, and it also consists of several control loops: starting from the device-level voltage loop and up to the outer loops and the power control of the converter. These levels of the converter control are depicted in Figure 3.10, and are present in both the MSC and GSC.

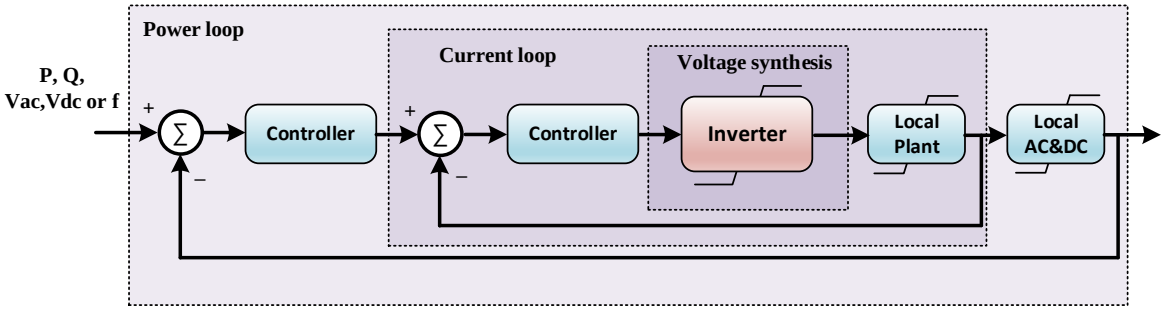


*Figure 3.10: Control loops of a VSC*

## 3.7 First Level VSC Control – Voltage Synthesis Loop

The innermost loop of the VSC is the voltage loop, which regardless of the converter topology, has a basic function to synthetize in its output the AC voltage waveform that is requested by the higher loop. Hence, it takes a voltage set-point reference signal and converts it to a physical output. This is done by converting the DC side voltage to the AC output by the suitable switching pattern of the VSC semiconductor switches.

The design of this loop is linked with the hardware properties of the converter, such as topology and switching frequency. The switching frequency is an important aspect, which is also related to the losses in the converter and the choice of the semiconductor device [100].

The response of the voltage loop is critical because it sets the speed of response of the overall system, given that it is the loop with the fastest bandwidth in the system. To avoid interference, a common practice is that each outer loop has to be 4 to 10 times slower than the previous inner one.

Essentially, this control consists of commanding and realising the correct ON and OFF switching of the devices in the VSC. Each switch is considered as a pulse with positive value when it is at ON state, and zero value when it is at OFF state. In that sense, this control is referred to as Pulse Width Modulation (PWM): by changing the width of the pulses, the magnitude of the fundamental harmonic and the desired output voltage waveform is synthetized. Depending on the required performance, both in terms of switching losses and harmonic elimination properties, most of the converters implement a type of a PWM switching pattern.

One widely used PWM technique is the sinusoidal (sine-triangle) PWM. This is the switching pattern that has been applied in the model in this thesis.

### 3.7.1 Sinusoidal PWM

Sinusoidal (sine-triangle) PWM switching control is designed by comparing a triangular (carrier) signal $v_{\text{tri}}$ with a sinusoidal control signal $v_{\text{control}}$. The reference sinusoidal control signal is the desired voltage at the VSC output. The common algorithm to realise the control is so that, separately for one phase leg of a two-level converter, when the control signal exceeds the carrier, the upper switch of the leg is turned ON and the phase terminal is connected to the positive DC voltage terminal. When the control signal is less than the carrier triangle waveform, the lower switch is turned ON and the terminal of the phase is connected to the negative DC voltage. The upper and lower switches of the same leg should never be ON at the same time because that would short circuit the DC source – to ensure this there is usually a dead-time during the transition when both of the switches are OFF.

The control signals for three phases and the triangle carrier waveform are shown in the top plot in Figure 3.11. For clarity of the illustration the switching frequency has been set to only 350 Hz, lower than 1750 Hz which is actually applied in the studied WT model. The corresponding switching signal of the upper switch of the first phase A is shown in the second plot of Figure 3.11, and the synthetized Phase-to-Phase Vab voltage in the output terminals is shown in the third plot in Figure 3.11.

With reference to the control signals, the PWM is defined by two variables, the amplitude modulation ratio i.e. modulation index $m_{a,}$ and the frequency modulation ratio $m_{f.}$

The definition of the modulation index $m_a$ is given in equation (3.15) as the ratio of the peak value of the control signal and the peak value of the triangular sampling signal. The magnitude of the output voltage waveform can be controlled by controlling $m_{a.}$

$$m_a = \frac{\hat{v}_{control}}{\hat{v}_{tri}} \tag{3.15}$$

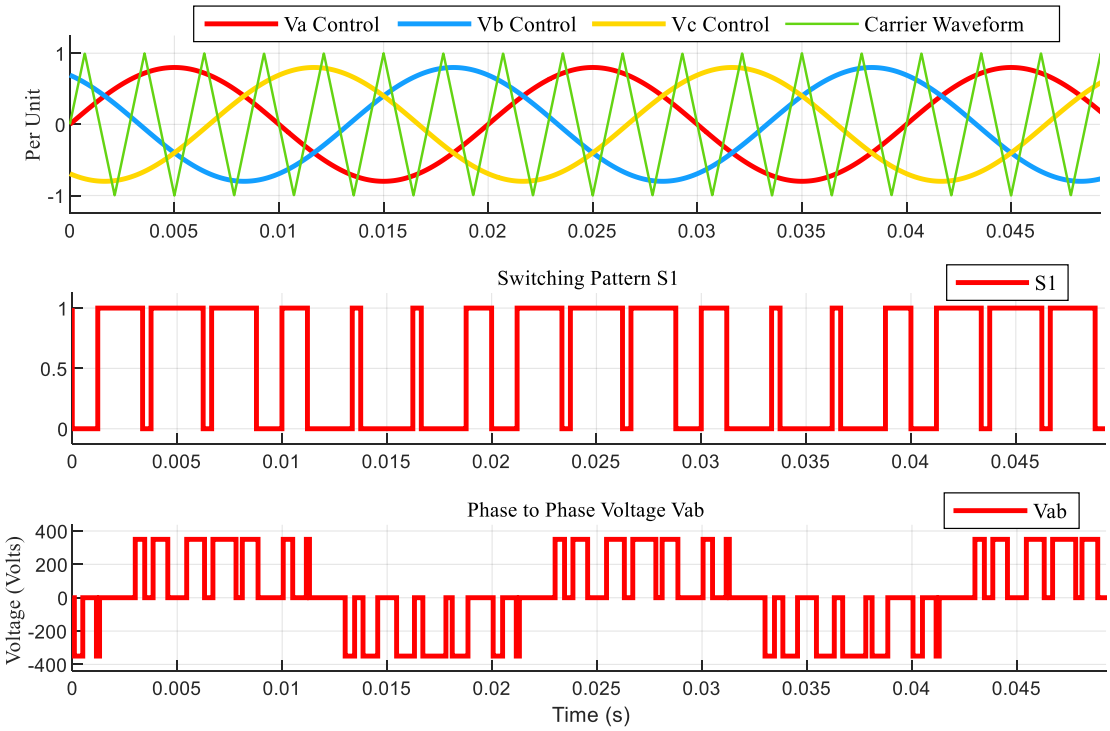


***Figure 3.11: Sinusoidal PWM for a two-level VSC: a) triangle i.e. carrier waveform and ABC voltage references; b) generated pulse switching signals for upper switch of phase A; c) phase-to-phase voltage waveform between two output terminals of phases a and b.***

Meanwhile, the frequency modulation ratio $m_f$ is given in equation (3.16) and is defined by the ratio of the switching frequency, i.e. triangle wave frequency $f_{sw}$, and the fundamental frequency i.e. control waveform frequency $f_1$ (which is identical to the fundamental harmonic of the desired output voltage – hence the index 1).

$$m_f = \frac{f_{sw}}{f_1} \tag{3.16}$$

The modulation index $m_a$ is usually from 0 to 1 – linear modulation. When $m_a$ >1, the peak of the reference signal exceeds the peak of the triangle and this leads to over-modulation. Operation in over-modulation is not desirable because it generates low order harmonics and no longer gives a linear relation between converter output voltage and reference control signal.

For two-level sine-triangle PWM, harmonics occur at frequencies ($f_h$) as given by the equation (3.17) and the harmonic spectrum is depicted in Figure 3.12.

$$f_h = \left( jm_f \pm k \right) f_1 \tag{3.17}$$

The frequency $f_1$ is the fundamental harmonic; $m_f$ is the frequency modulation index, i.e. the ratio between the switching frequency and $f_1$. Thus the product $m_f f_1$ equals the switching frequency, implying that the harmonic content is directly linked to the switching frequency. Lastly $j$ and $k$ are integers, with the condition that when $j$ is odd, $k$ is even – thus the 'sidebands' of harmonics occur in even offsets for odd multiples of $m_f$, and in odd offsets for even multiples of $m_f$ (Figure 3.12). For a higher quality of output waveform, $m_f$ should be an odd integer value greater than 21 and ideally a multiple of three [109]. In the studied WT system here, the switching frequency is 1750 Hz and $m_f = 35$.

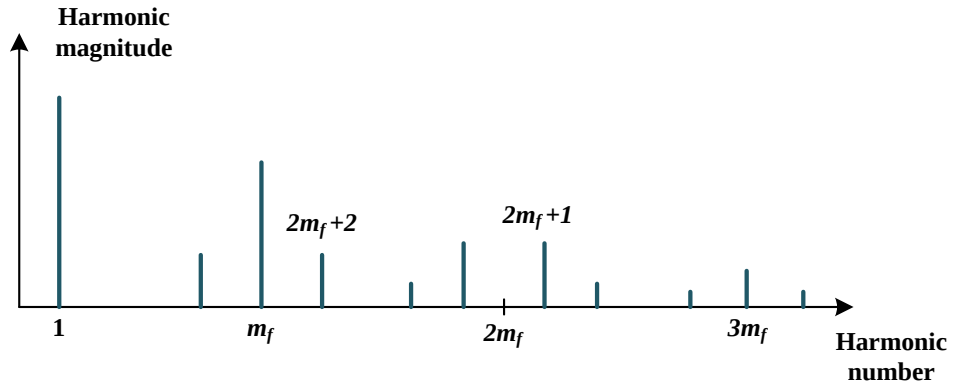


***Figure 3.12: Two level converter voltage harmonic spectrum – single phase output to DC link mid-point*** [110]

### 3.7.2 Current Control Loop

The current control of both the MSC and the GSC makes use of the dynamic equations from the generator and grid models introduced in sections 3.4.4 and 3.4.5. The simplified connection of the WT generator to the grid using the BVSC is shown in Figure 3.13. The voltage drops and currents of interest in both sides of the BVSC are depicted.

The voltage drops and currents annotated in Figure 3.13 are one-phase representations of a three-phase balanced system in stationary reference frame. For both the machine and the grid side, this three-phase system of voltages and currents can be transformed to their two-axis components in a d-q rotating reference frame. This transformation is done using the Clarke and Park transformations explained in subsection 3.4.4 and results in the equations (3.11) - (3.14) that were previously derived. Note that for non-salient machines as the PMSG applied here, $R_{sq}=R_{sd}=R_s$ and $L_{sq}=L_{sd}=L_s$ [111].

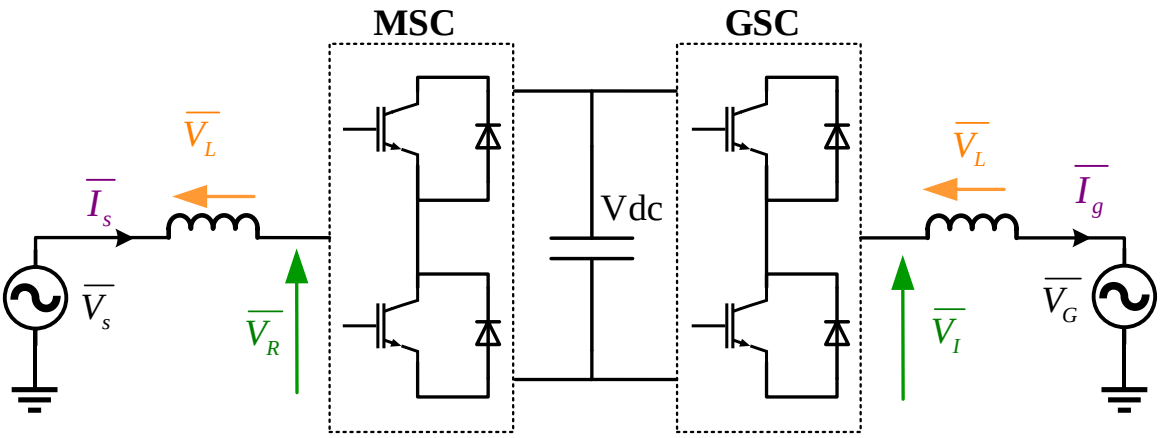


***Figure 3.13: Layout of the connection between the PMSG and WF AC grid (per phase representation)***

$$i_{sd} = \frac{1}{L_s}\int\left(v_{sd} - R_s i_{sd} + \overbrace{\omega_{gen}{}^{e} L_s i_{sq}}^{\text{Cross-coupling}}\right)dt \tag{3.18}$$

$$i_{sq} = \frac{1}{L_s}\int\left(v_{sq} - R_s i_{sq} - \omega_{gen}{}^{e}\Psi_{PM} - \overbrace{\omega_{gen}{}^{e} L_s i_{sd}}^{\text{Cross-coupling}}\right)dt \tag{3.19}$$

The PMSG dynamic equations from (3.11) and (3.12) are re-stated in (3.18) and (3.19) with re-arrangement to describe the change of current. In these equations, there is a cross coupling term, where the q-axis component of the current appears in the d-axis voltage equation and vice-versa, the d-axis current induces a voltage term in the q-axis voltage equation. The same is true for the equivalent dynamic equations describing the grid side dynamics. The block diagram representation of the plant which is represented by these equations can be constructed as in Figure 3.14.

Figure 3.14 shows the model for the PMSG which is controlled by the MSC. The grid side connection has an equivalent and similar model representation. The grid integration of the generated power from the wind is controlled by the GSC. Therefore, the PMSG model and the grid model represent the plants in the control realised by the MSC and GSC respectively.

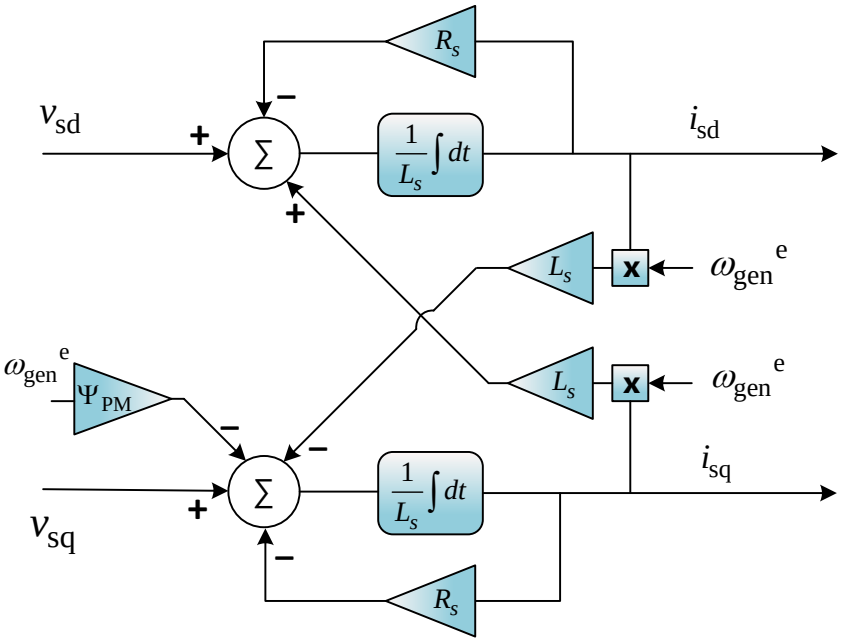


***Figure 3.14: State feedback block diagram for the PMSG dynamic model***

Controlling a system with cross-coupling terms as in Figure 3.14, entails designing a Multiple Input Multiple Output (MIMO) control algorithm, which is a complex task. One way this task can be simplified is to decouple the d and q voltage equations i.e. cancelling the cross-coupling terms. This decoupling (nulling) is done by subtracting (adding with an opposite sign) in the control, the same cross coupling terms that are present in the plant. As a result the initial cross-coupling terms that describe the system (plant) are cancelled (or in practice, reduced to sufficiently small values that may be ignored). This transformation is done analytically in the control of the system and no change is added to the actual plant. The block diagram of the control scheme for the PMSG with decoupling is shown in Figure 3.15. The final result is that the PI current control can be designed separately for the q-axis and d-axis component as a Single Input Single Output (SISO) system.

From the block diagram in Figure 3.15, the transfer function in Laplace domain for the current loop can be derived as in equation (3.20).

$$\frac{i_{sd}}{i_{sd}^{*}} = \frac{i_{sq}}{i_{sq}^{*}} = \frac{\frac{K_p}{L_s}s + \frac{K_i}{L_s}}{s^2 + \frac{K_p + R_s}{L_s}s + \frac{K_i}{L_s}} \tag{3.20}$$

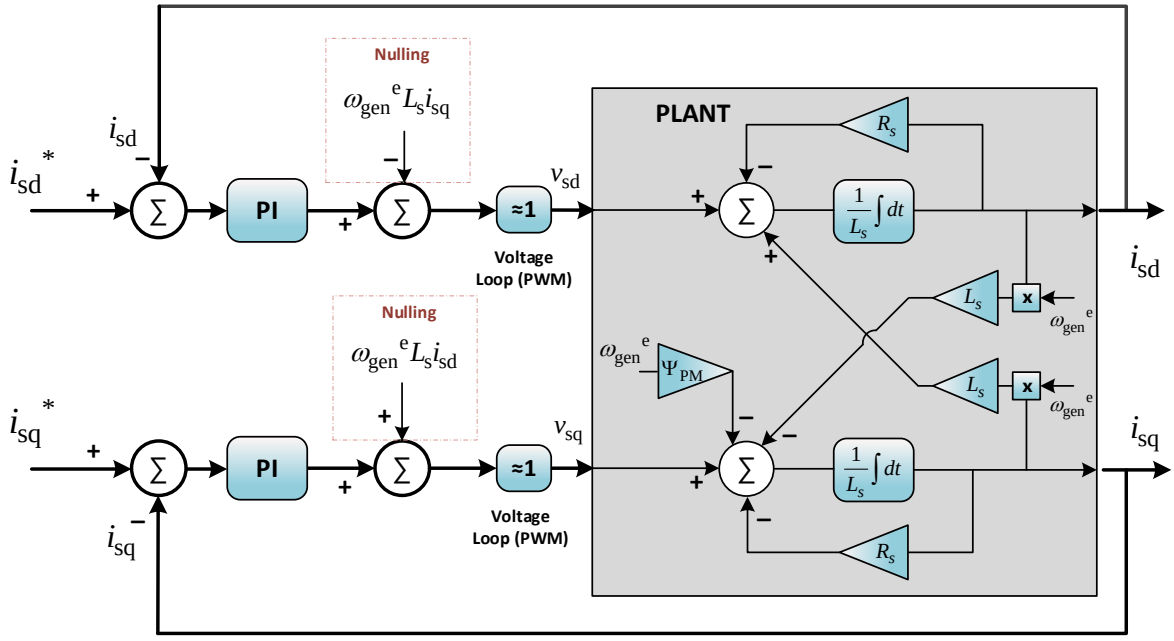


***Figure 3.15: Block diagram of the MSC current control loops with nulling of the cross-coupling terms***

The transfer function can be approximated as a 2nd order system, and the response can be tuned for the wanted damping ratio $\zeta$ and natural frequency $\omega_n$ of the response using the derived expressions for $K_p$ and $K_i$ as given in (3.21) and (3.22). For typical values of $\zeta$ in the range 0.7 to 1, it may further be assumed that $\omega_n$ is approximately equal to the bandwidth.

$$K_p = 2 \cdot \zeta \omega_n L_s - R_s \tag{3.21}$$

$$K_i = L_s \cdot \omega_n{}^{2} \tag{3.22}$$

Because of how the torque control is realised (explained in next subsection), the current has a q-axis component only. The q component of the current has a negative value (lags behind the flux vector for $\pi/2$) as represented in Figure 3.16 – this is specific for the convention used in the set of machine equations and for the assumed positive direction of the machine torque. In Figure 3.16 is shown the MSC phasor diagram for the field-oriented control applied here and the voltage drops of interest from Figure 3.13 have been annotated.

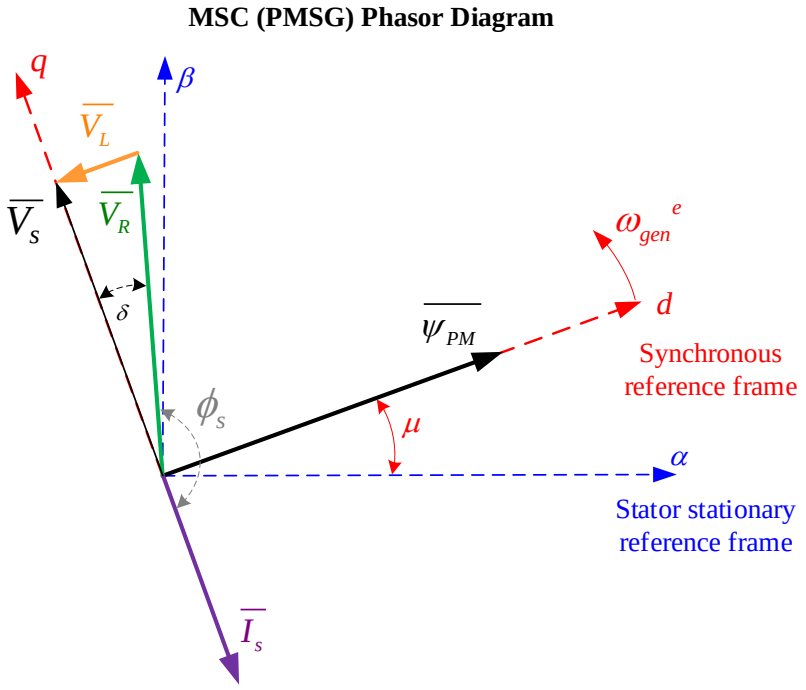


***Figure 3.16: Machine Side Converter phasor diagram for Field-oriented control and rectifier operation of the VSC.***

$$i_{gd} = \frac{1}{L_g}\int\left(e_{con\_d} - v_{gd} - R_g i_{gd} + \overbrace{\omega_g{}^{e} L_g i_{gq}}^{\text{Cross-coupling}}\right)dt \tag{3.23}$$

$$i_{gq} = \frac{1}{L_g}\int\left(e_{con\_q} - v_{gq} - R_g i_{gq} - \overbrace{\omega_g{}^{e} L_g i_{gd}}^{\text{Cross-coupling}}\right)dt \tag{3.24}$$

For the GSC side and the grid integration control, the approach taken to decouple the d and q-axis control loops is identical, while cancelling the corresponding cross-coupling terms. Here the grid voltage at the point of connection (PoC) is set externally to be constant as defined by the grid code and the control is realised by governing the current flow between the output terminals of the converter and the PoC, while synthetizing the voltage difference $e_{con}$ between these two points. To realize this, the d and q components of the constant grid voltage are also nulled in the control as seen in the block diagram of Figure 3.17.

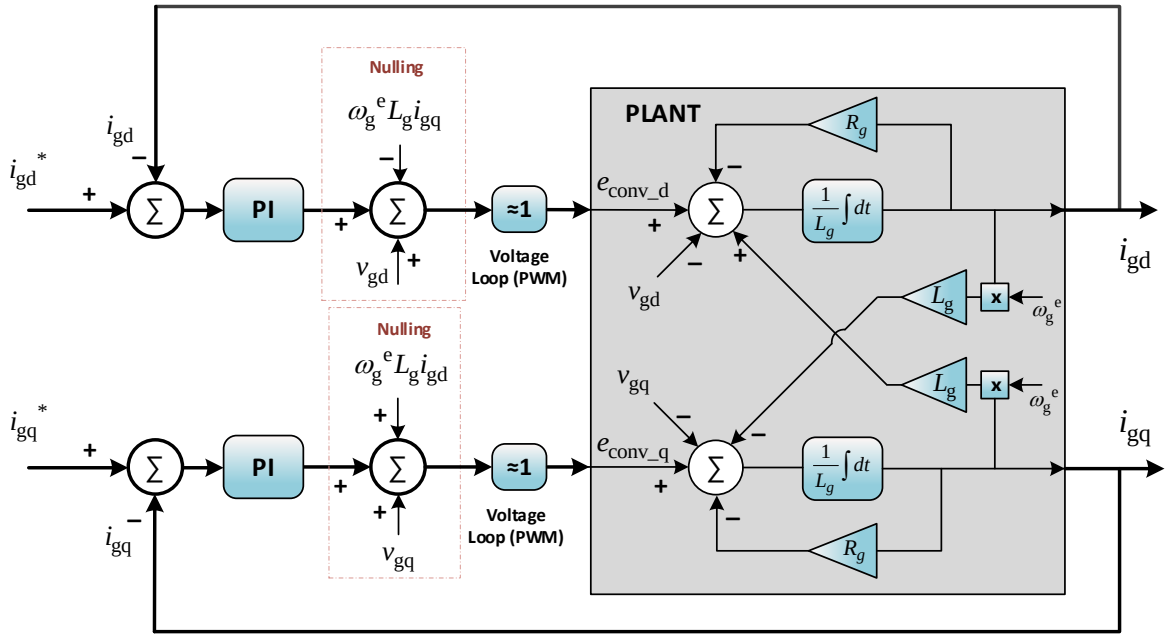


***Figure 3.17: Block diagram of the GSC current control loops with nulling of the cross-coupling terms***

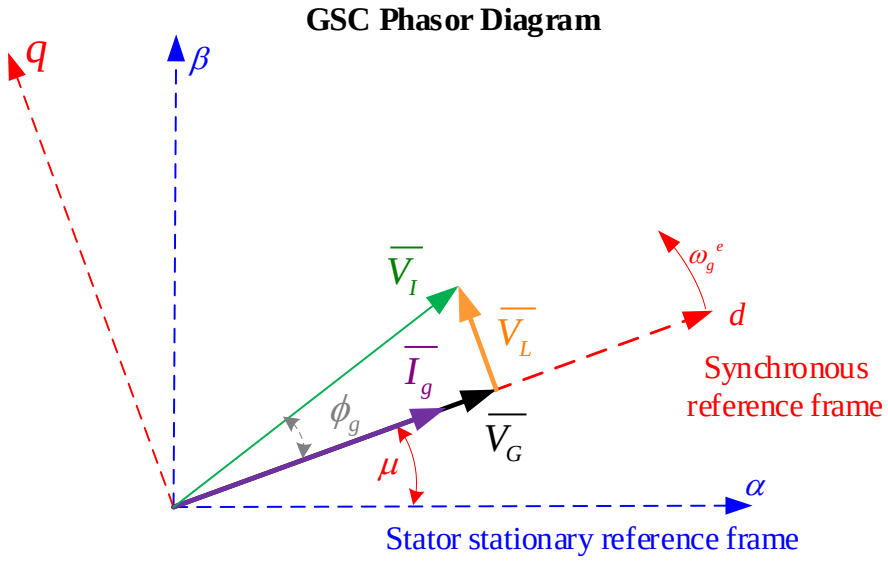


***Figure 3.18: Grid Side Converter phasor diagram for voltage oriented control and unity power factor connection with the grid.***

Similar to the previous case of the MSC, the transfer function can be derived and the PI parameters tuned for a desired response using a common technique (such as using a software like MATLAB or analytically approximating with a 2nd order system). The current equations and the block diagram of the GSC current loops are given in equations (3.23) - (3.24) and Figure 3.17 respectively, while the phasor diagram for unity power factor connection of the GSC with the grid is given in Figure 3.18.

## 3.8 Second Level Control

Both VSCs, the MSC and the GSC, on top of the current loop have other control requirements. This additional control enables the control of another system quantity by the VSC, such as active or reactive power, generator torque and speed, frequency, or DC link voltage. In this case, the MSC is utilised to control the torque of the PMSG. On the other hand, the GSC is utilised to control the DC link voltage – controlling the DC voltage is linked to controlling the active power flow into the grid (elaborated in the DC control dynamic in the following subsection).

### 3.8.1 PMSG Torque Control

The modelling is expanded with equations in (3.25) - (3.28). In (3.25) the relation between the electrical rotor speed $\omega_r^e$ and the mechanical rotor speed $\omega_r^m$ is described, using $p_p$ the number of pole pairs of the PMSG. In (3.26) is given the expression for the relation between the electrical torque $T_e$ and the stator current components, using the PM magnetic flux $\Psi_{PM}$, and the stator q and d axis inductance components $L_{sq}$ and $L_{sd}$. In (3.27) and (3.28) are given the expressions for calculating the real and reactive power using the dq components of the stator voltage and current. These expressions are valid for the 'amplitude invariant' abc to dq reference frame transformation (as opposed to the 'power invariant' – see reference [107] for definitions).

$$\omega_{\mathrm{r}}^{\mathrm{e}} = p_{\mathrm{p}} \cdot \omega_{\mathrm{r}} \tag{3.25}$$

$$T_{\mathrm{e}} = \left(\tfrac{3}{2}\right) p_{\mathrm{p}} \left[ \Psi_{\mathrm{PM}} i_{\mathrm{sq}} + \left(L_{\mathrm{sd}} - L_{\mathrm{sq}}\right) i_{\mathrm{sd}} i_{\mathrm{sq}} \right] \tag{3.26}$$

$$P_{\mathrm{e}} = \tfrac{3}{2} \left[ v_{\mathrm{sq}} i_{\mathrm{sq}} + v_{\mathrm{sd}} i_{\mathrm{sd}} \right] \tag{3.27}$$

$$Q_{\mathrm{e}} = \tfrac{3}{2} \left[ v_{\mathrm{sq}} i_{\mathrm{sd}} - v_{\mathrm{sd}} i_{\mathrm{sq}} \right] \tag{3.28}$$

The PMSG here is non-salient, and for non-salient machines $L_{sq}=L_{sd}=L_s$ [111]. Therefore, equation (3.26) is simplified to (3.29) from where the electromagnetic torque of the PMSG can be directly controlled by controlling only the q-axis component of the stator current.

$$T_e = \left(\frac{3}{2}\right) p_p \Psi_{PM} i_{sq} \tag{3.29}$$

The turbine mechanical torque from equation (3.5) can be written as in (3.30), where $K_{opt}$ is a constant calculated by (3.31). By equating the PMSG electric torque from (3.29) to the turbine optimal torque at different rotating mechanical speeds from (3.30), the so called Optimal Torque Control (OTC) of the WT can be achieved [92]. This is a fairly limited WT control where it does not allow for any flexibility and the dynamics of the response are set by the system inertias. The diagram of the implementation of this control, which is applied in the original reference of the WT used here, is given in Figure 3.19. Different and more advanced torque control methods can be applied which will introduce different dynamics of the WT and converter system (these will be analysed in Chapter 5).

$$T_w = K_{opt} \cdot \omega_r^{\,2} \tag{3.30}$$

$$K_{opt} = \frac{\pi \rho R^5 C_p}{2\lambda^3} \tag{3.31}$$

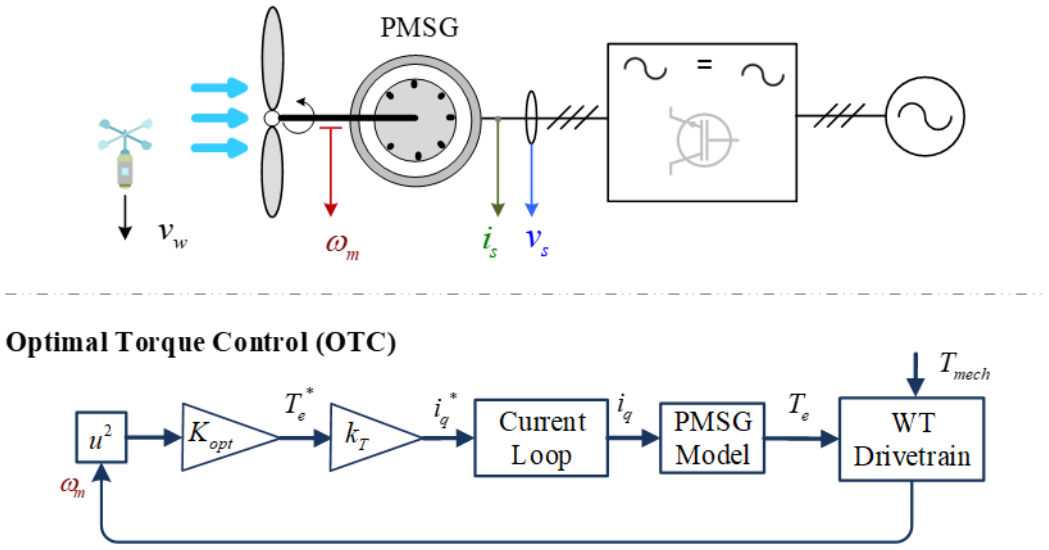


***Figure 3.19: Optimal Torque Control diagram for PMSG WT***

### 3.8.2 DC Link Model and Voltage Control

The model of the DC link of the BVSC can be built by modelling the voltage and power (current) flow dynamics of the DC link capacitor. A simplified diagram of the BVSC and the current flow in the DC link capacitor is shown in Figure 3.20. If the circuit losses are neglected, the DC power (DC current) that flows into the capacitor is equal to the

difference between the generated power on the DC side of the MSC and the network-injected power on the DC side of the GSC.

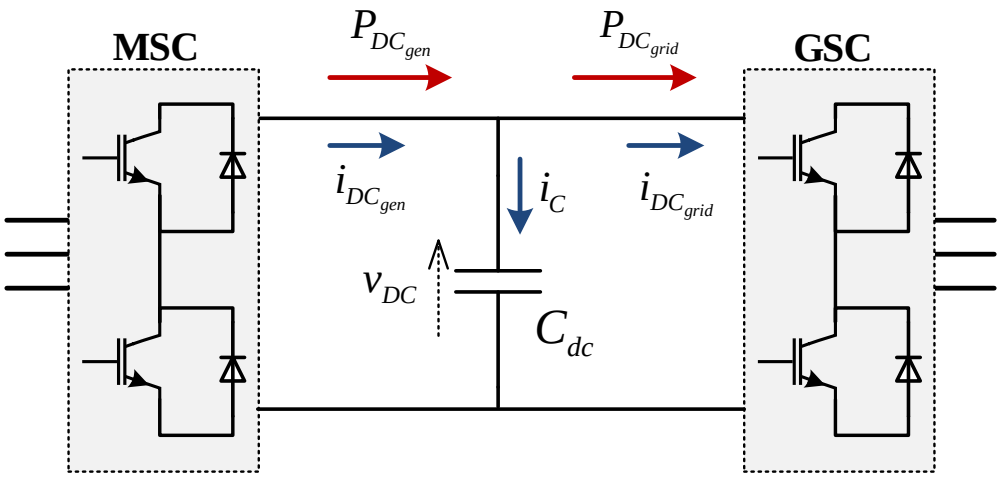


***Figure 3.20: BVSC block diagram with DC link current flow annotation***

The current that charges and discharges the capacitor is described with equation (3.32).

$$i_C = C_{dc}\frac{dV_{dc}}{dt} = i_{DC_{gen}} - i_{DC_{grid}} \tag{3.32}$$

The power balance equation can be written as described with (3.33) - (3.35). In (3.34) the minus sign is because of the definition of the electric torque to be positive when counteracting the turbine rotation, which is the opposite of the positive direction of the generated power as assumed in Figure 3.20. In (3.35), because of the application of voltage-oriented control for the GSC and alignment with d-axis, the q-axis component of the grid voltage is zero and the real power injected to the grid is proportional to the d-axis current and voltage value only. For both VSCs, in (3.34) and (3.35) is assumed that there are no losses and the real power is equal between the AC and DC sides. The DC link representation model is then built using equations (3.32) - (3.35) and is shown in Figure 3.21.

$$P_C = v_{DC}\cdot i_C = v_{DC}\cdot C_{dc}\frac{dv_{DC}}{dt} = P_{DC_{gen}} - P_{DC_{grid}} \tag{3.33}$$

$$P_{DC_{gen}} = v_{DC}\cdot i_{DC_{gen}} \approx P_{AC_{gen}} = -\frac{3}{2}\left[v_{sq}i_{sq} + v_{sd}i_{sd}\right] \tag{3.34}$$

$$P_{DC_{grid}} = v_{DC} \cdot i_{DC_{grid}} \approx P_{AC_{grid}} = \frac{3}{2} v_{gd} \cdot i_{gd} \tag{3.35}$$

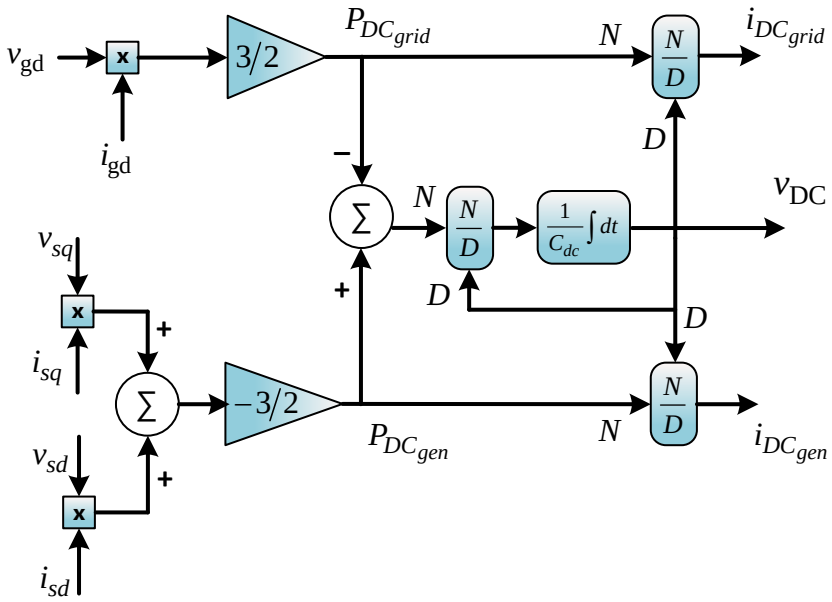


***Figure 3.21: DC link voltage dynamics model***

The control of the voltage of the DC link is undertaken by the GSC: by controlling the real power transferred to the grid, or particularly the current $i_{DC_{grid}}$ from equation (3.32). This control can be realised by designing a PI controller which determines the value of current $i_{gd}$ which is injected to the grid to appropriately control the discharge of the capacitor so that the DC voltage remains constant at the pre-set value. From (3.32) - (3.35), the differential equation for designing the control can be written as in (3.36).

$$C_{dc} \frac{dv_{DC}}{dt} = i_{DC_{gen}} - \frac{3}{2} \frac{v_{gd} \cdot i_{gd}}{v_{DC}} \tag{3.36}$$

The second term in the right side of the equation in (3.36), gives a non-linear relationship between $i_{gd}$, $v_{gd}$ and $v_{DC}$. Therefore, in order to design the controller, the equation needs to be linearized. The linearization is undertaken by small signal analysis around an operating point with $i_{gd_0}$, $v_{gd_0}$ and $v_{DC_0}$. The small signal model derived from equation (3.36) is described with (3.37) - (3.41).

$$C_{dc} \frac{d\Delta v_{DC}}{dt} = \Delta i_{DC_{gen}} - \frac{3}{2} \frac{i_{gd_0}}{v_{DC_0}} \Delta v_{gd} - \frac{3}{2} \frac{v_{gd_0}}{v_{DC_0}} \Delta i_{gd} - \left( -\frac{3}{2} \frac{v_{gd_0} i_{gd_0}}{{v_{DC_0}}^2} \right) \Delta v_{DC} \tag{3.37}$$

$$\Delta i_{DC_{gen}} = i_{DC_{gen}} - i_{DC_{gen_0}} \tag{3.38}$$

$$\Delta v_{gd} = v_{gd} - v_{gd_0} \tag{3.39}$$

$$\Delta i_{gd} = i_{gd} - i_{gd_0} \tag{3.40}$$

$$\Delta v_{DC} = v_{DC} - v_{DC_0} \tag{3.41}$$

Simplified, for design of the control loop, equation (3.37) is written as in (3.42), where $K_v$ and $K_G$ constants are as given in (3.43) and (3.44). The resulting diagram of the designed control loop is shown in Figure 3.22.

$$C_{dc}\frac{d\Delta v_{DC}}{dt} = \Delta i_{DC_{gen}} - 1.5K_G\Delta v_{gd} - 1.5K_v\Delta i_{gd} + 1.5K_vK_G\Delta v_{DC} \tag{3.42}$$

$$K_v = \frac{v_{gd_0}}{v_{DC_0}} \tag{3.43}$$

$$K_G = \frac{i_{gd_0}}{v_{DC_0}} \tag{3.44}$$

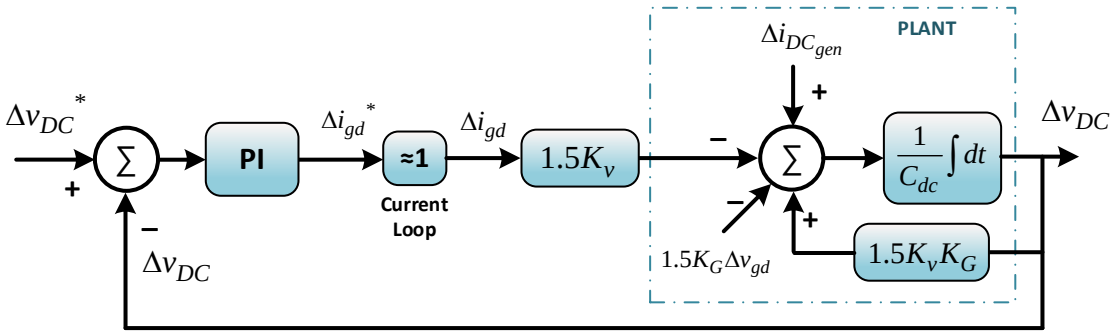


***Figure 3.22: DC link voltage control loop design***

Using the state feedback diagram and the differential equation, the transfer function describing the DC voltage change is derived in Laplace domain as in equation (3.45). The (-1) sign comes from the negative correlation between the error of the controlled DC voltage and the manipulated variable in the PI loop, which is the current injected to the grid. To simplify the transfer function, this negative sign can be cancelled if it is included in the PI coefficients, which will then have a negative value. Using the transfer function, the PI coefficients of the voltage loop can be determined for the desired response dynamics of the control.

$$TF = \frac{\Delta v_{DC}^{*}}{\Delta v_{DC}} = \frac{(-1)\left(K_{pdc} \cdot s + K_{idc}\right) \cdot 1.5K_v}{C_{dc} \cdot s^2 + 1.5K_v\left(K_G + (-1)K_{pdc}\right)s + (-1) \cdot 1.5K_v K_{idc}} \qquad (3.45)$$

### 3.8.3 The Phase-Locked Loop

To realise the Park transformation, especially for the GSC where the frequency is set externally by the grid, it is important to know the phase of the grid voltage. For the control to work, what is governed by the control in the d-q domain has to correspond exactly with the physical quantities in the abc domain. Consequently, the correct frequency $\omega$ needs to be known to synchronise the GSC with the grid frequency. To realise this, a key element is another loop, which measures the phase angle (and frequency) of the grid voltage – the Phase Locked Loop (PLL).

Different concepts of PLLs have been studied and considered. The PLL has been around since the 1930s and it is believed that it was first designed by Bellescize [112] to be used for synchronous reception of radio signals [113].

An example of a classic PLL which auto-tunes itself to the grid voltage d-axis is given in [114] and uses the same concept as the one shown in Figure 3.23. This PLL works by reducing the q-component to zero, which automatically aligns the reference frame with the d-axis network voltage. There are a number of issues faced when designing PLLs, such as dealing with imbalances and harmonics as well as managing the PLL during network faults. A comprehensive review of PLLs is given in [113] and [115]. Advantages and disadvantages are discussed, and a number of PLLs with different complexities as well as harmonic filtering techniques are described.

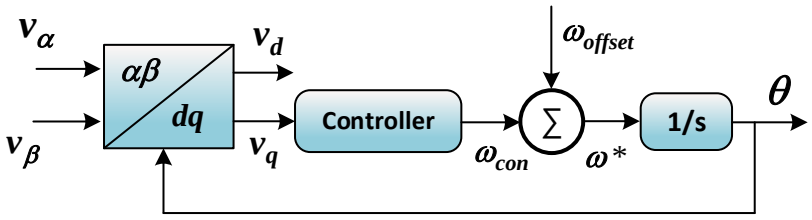


***Figure 3.23: Control Structure of a conventional Phase Locked Loop (redrawn from*** [116]***)***

PLL dynamics and control are not considered in the model that has been built in this thesis. In the model of the grid that is represented in the simulation, the frequency and voltage values of the grid are nominal. The WT is assumed to be connected to a large

modern offshore system, where the frequency is set by the offshore MMC VSC HVDC converter which is assumed to offer a stiff AC source as a 'grid forming' reference. Thus, apart from the short synchronizing instant when the WT connects to the system, the effect of the PLL in such a system is minor and can be neglected.

### 3.8.4 Pitch Control

Another control, that is one level higher than the previously discussed control loops and that is concerned with limiting the power that is extracted by the WT blades, is the pitch control. As the name suggests, this control is realised by ‘pitching’ the angle of the turbine blades in order to lower the amount of power captured from the wind by the WT rotor (see equation (3.1) describing WT power). In the actual WT, there is a separate pitch angle control and actuator for each blade. In simulations this is usually represented by a collective pitch angle.

The pitch control of the blades is primarily used in the ‘Power Limiting’ region of the WT operation. In this region, even with the wind speed exceeding the nominal value, the power that is captured from the wind by the WT is limited to the rated power. The pitching of the blades does this by lowering the aerodynamic efficiency when changing the blade angle.

The design of the pitch control in detail is explained in [92] – the same approach has been used and adapted for the controller here. In the power limiting region of operation, a gain-scheduled PI control is applied to control the speed of the generator and limit it to the rated speed (1.25 rad/s). The design of the controller and the derivation of the transfer function is based on the torque balance equation given in (3.46). Indexes *w* and *G* indicate the turbine and the generator respectively; *J* is the moment of inertia; $\Omega$ is the mechanical rotating speed of the turbine (and generator); while $\Omega_0$ is the rated turbine speed; $\Delta\Omega$ is the small perturbation of the rotational speed above the rated speed; $\Delta\dot{\Omega}$ is the turbine rotational acceleration. Because of the absence of a gearbox, the mechanical speed $\Omega$ as seen from the perspective of the pitch control, is equal to the mechanical speed of the PMSG previously notated as $\omega_r$ in (3.25).

Let’s assume that the power generation of the WT is kept at its rated value and the torque of the generator in the pitch controlling region $T_G(\Omega)$ is given in equation (3.47).

The mechanical torque of the turbine $T_w(\beta)$ is given in (3.48) and is a function of the pitch angle $\beta$. Consequently, because of the torque balance equation, the pitch angle $\beta$ is also used to control the rotational speed $\Omega$ and allows for limiting the generated power $P_0$. In type 4 WTs with fully rated converter, there is no explicit need to control the shaft speed i.e. the rotating frequency of the rotor. However this is one way of limiting the output power, and therefore the pitch control loop has been designed to have the shaft speed as a reference. Redesigning the loop to consider other methods of limiting output power is possible. However, attention needs to be paid to the design of the MPPT control loop so that there is no interference, especially in the transition region between MPPT and pitch control.

The equations (3.46) to (3.48) can be combined with a PID controller as in (3.49) to control the rotor speed perturbations $\Delta\Omega$. By using first-order Taylor series expansions of (3.47) and (3.48), combining and simplifying the expressions, and setting $\dot{\varphi} = \Delta\Omega$, the equation of motion for rotor-speed error of the form in (3.50) is derived [92]. Equation (3.50) has a form and will respond as a second order system with the natural frequency $\omega_{\varphi n}$ and damping ratio $\zeta_\varphi$ given in (3.51) and (3.52) respectively [92]. These can be used for tuning the pitch control loop.

$$T_w - T_G = (J_w + J_G)\frac{d}{dt}(\Omega_0 + \Delta\Omega) = J_{drivetrain}\Delta\dot{\Omega} \tag{3.46}$$

$$T_G(\Omega) = \frac{P_0}{\Omega} \tag{3.47}$$

$$T_w(\beta) = \frac{P(\beta, \Omega_0)}{\Omega_0} \tag{3.48}$$

$$\Delta\beta = K_p\Delta\Omega + K_i\int_0^t \Delta\Omega dt + K_D\Delta\Omega \tag{3.49}$$

$$\overbrace{\left[J_{drivetrain} + \frac{1}{\Omega_0}\left(-\frac{\partial P}{\partial\beta}\right)K_D\right]}^{M_\varphi}\ddot{\varphi} + \overbrace{\left[\frac{1}{\Omega_0}\left(-\frac{\partial P}{\partial\beta}\right)K_p - \frac{P_0}{{\Omega_0}^2}\right]}^{C_\varphi}\dot{\varphi} + \overbrace{\left[\frac{1}{\Omega_0}\left(-\frac{\partial P}{\partial\beta}\right)K_i\right]}^{K_\varphi}\varphi = 0 \tag{3.50}$$

$$\omega_{\varphi n} = \sqrt{\frac{K_\varphi}{M_\varphi}} \tag{3.51}$$

$$\zeta_\varphi = \frac{C_\varphi}{2\sqrt{K_\varphi M_\varphi}} \tag{3.52}$$

The derivative term of the controller can be neglected as recommended in [117]. Finally, the PI coefficients can be tuned using the expressions in (3.53) and (3.54) which are derived in [92] and can be used to directly tune the controller. To finish the tuning, the term $\left(-\frac{\partial P}{\partial \beta}\right)$, which represents the sensitivity of the aerodynamic power to the change in blade pitch angle, needs to be determined. This dependency is not linear and is different in different operating points (speeds) of the WT. Therefore, the PI gains $K_p$ and $K_i$ need to be set with gain scheduling in order to account for the difference around different operating points that depend on wind speed, rotor speed, and blade pitch angle. A linearization method that involves perturbation of the rotor collective-blade pitch angle at different operating points and measurement of the variation in aerodynamic power is undertaken. To determine the power-to-pitch sensitivity and the gain scheduling dependency for the WT system presented in this chapter, the WT simulation model has been used.

$$K_p = \frac{2 J_{drivetrain} \Omega_0 \zeta_\varphi \omega_{\varphi n}}{\left(-\frac{\partial P}{\partial \beta}\right)} \tag{3.53}$$

$$K_i = \frac{J_{drivetrain} \Omega_0 {\omega_{\varphi n}}^2}{\left(-\frac{\partial P}{\partial \beta}\right)} \tag{3.54}$$

The loop that uses blade pitch angle control to limit the rotational speed of the turbine and with that its power was added to the WT simulation model. The block diagram representation of this loop is shown in Figure 3.24. The tuning of the PI gains $K_p$ and $K_i$ was done using (3.53) and (3.54). The gain scheduling look-up table as well as the evaluated $\left(-\frac{\partial P}{\partial \beta}\right)$ for the analysed WT are given in the appendix.

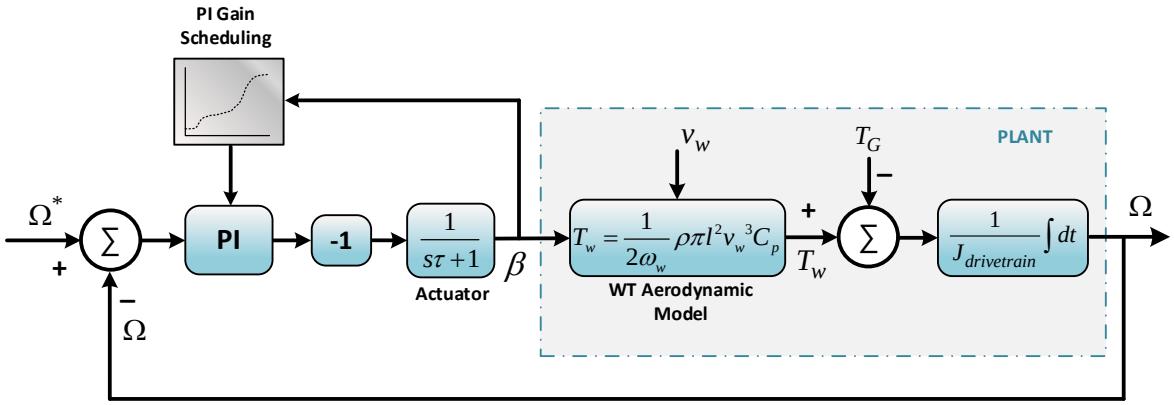


***Figure 3.24: Block diagram implementation for collective pitch control – limitation of the rotating speed of the WT (and hence power output) by varying the pitch angle of the blades.***

## 3.9 WT System Response

The control parameters of the WT system and the tuning of the control loops explained in the previous sections are summarized in Table 5. With this control setup, the response of the WT model was assessed in different scenarios with different wind speed inputs. Figure 3.25 shows the response for a step change in wind speed, from 11.4 m/s to 8.5 m/s.

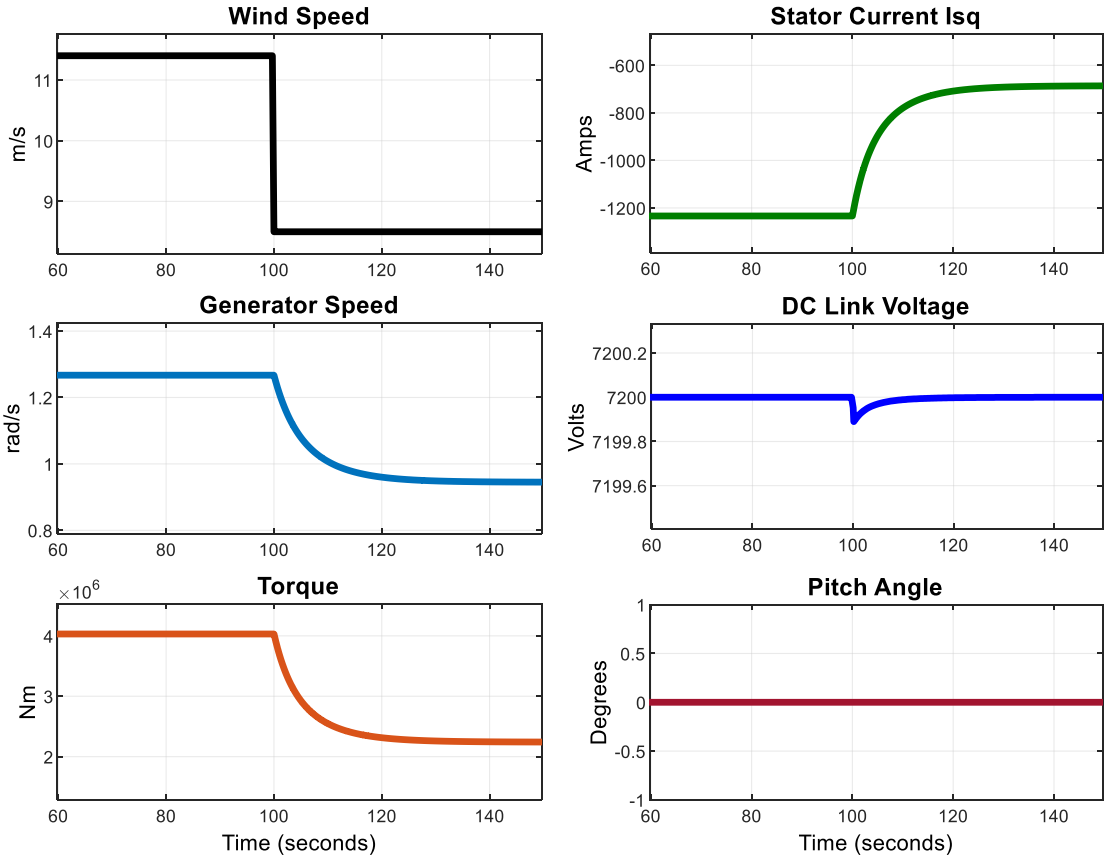


***Figure 3.25: System response for a wind speed step change from 11.4 m/s to 8.5 m/s in the second operating region of the WT (below rated speed)***

The response of the system as shown in Figure 3.25 closely matches the expectations from analytical calculations and the results in reference [94] where the same WT and PMSG have been analysed. Additionally, in Figure 3.26 is shown the response from 11.4 m/s to 12.4 m/s which is when the pitch control is regulating the WT rotating speed and the power output. Finally, in Figure 3.27 the response when operating with a realistic variable wind profile input that varies below and above the WT rated wind speed is shown. Note that the variation in DC link voltage is small, given the choice of large DC link capacitance and the applied fast DC link voltage control – in reality, for a more optimally designed system, the DC voltage spike is likely to be larger.

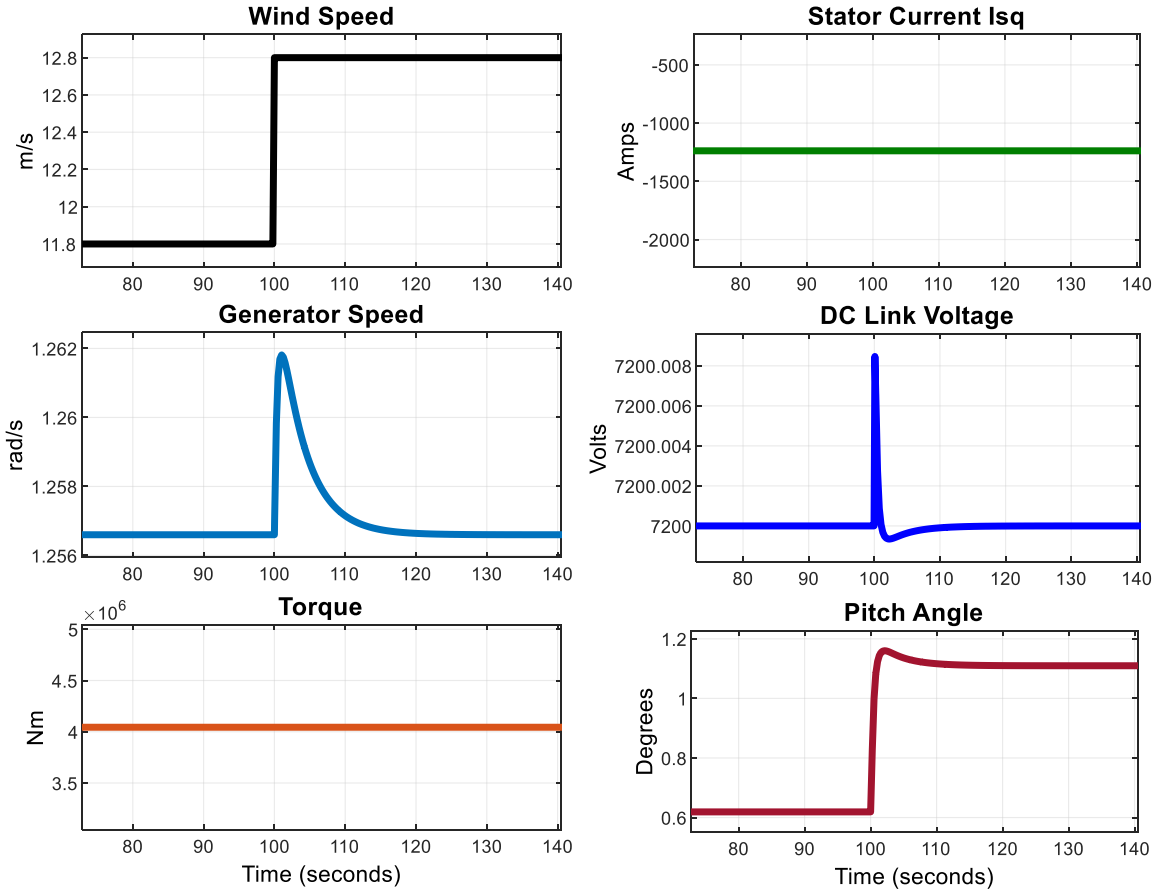


***Figure 3.26: System response for a wind speed step change from 11.8 m/s to 12.8 m/s in the third speed operating region of the WT (above rated speed)***

***Table 5: Control parameters for the converter current and power loops as well as collective blade pitch control[1]***

| | | Bandwidth $f_n$ (Hz) | Damping ratio ζ | Kp | Ki |
|---|---|---|---|---|---|
| **MSC** | Inner current loop | 10 | 0.7 | 0.64 | 30.8 |
| **GSC** | Inner current loop | 450 | 0.7 | 0.5 | 975 |
| | Outer DC link control | 10 | 1 | 6.5 | 200 |
| **3rd Level** | Pitch (Region 3) | 0.05 | 0.7 | [630 to 1150] | [140 to 250] |

[1]*For PI gain scheduling, the range in which the PI gains fall is given.*

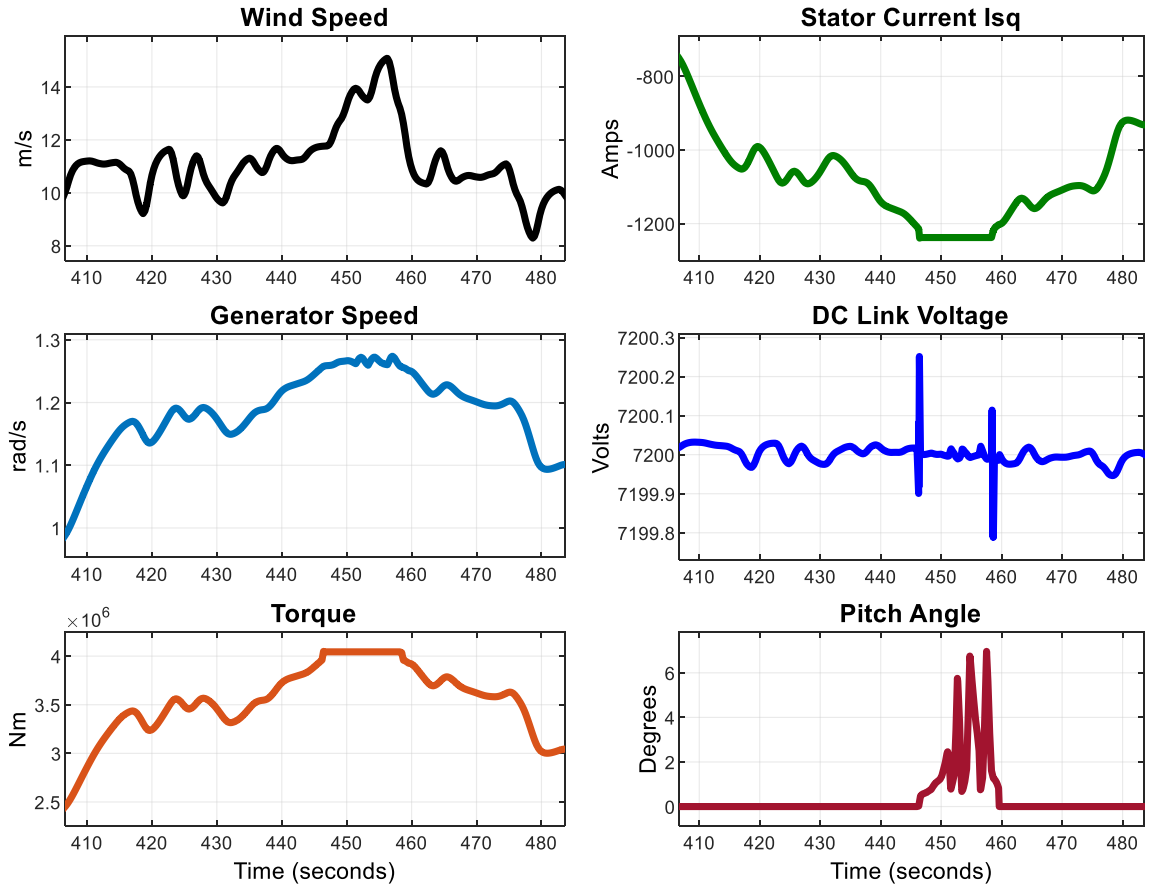


***Figure 3.27: System response for variable wind speed profile operation in the second and the third operating speed region of the WT (below and above rated speed)***

## 3.10 Summary

In this chapter a thorough explanation of the WT system configuration and its simulation model was given. Initially, the general structure and its comprising parts were introduced. The reasoning behind the choice of topology and comprising components was discussed while referring to the current research and available products on the market. The

assumptions and simplifications that have been made in the design of the simulated system were also stated.

Afterwards, the dynamic model and its implementation for the comprising subsystems of the WT were introduced. This included the aerodynamic and mechanical model of the turbine, as well as the electrical model of the converter and the generator.

A crucial part of the work analysed in this PhD is the operational and control aspects. Therefore, in the next stage in the chapter were explained the different control levels of the WT system that have been included in the modelling. The design, configuration, and tuning of the control loops was shortly presented. The explained control aspects include the PWM and the voltage synthetizing control, the current loops of the VSCs, the outer VSC control of torque and DC link voltage (power), the power (and speed) limiting control of the WT using collective blade pitch angle. In the end, the response of the WT system was shown for three scenarios: a wind speed step change in Region 2 of operation (below rated speed), a wind speed step change in Region 3 of operation (above rated speed), and a more realistic operation with a variable wind profile input that varies below and above the rated wind speed.

The WT operational system that was presented in this chapter is fundamental for the analysis undertaken in the other chapters of the thesis and for some of the most important conclusions.

# 4 Thermo-Mechanical Failure of the Power Electronics Module

This chapter describes in more detail the studied failure mechanism of the converter module. Additionally, context is given how this particular failure mechanism is used to develop the methodology for evaluation of the thermal stress and lifetime consumption in WT converters.

## 4.1 Bond Wire Lift-off Failure Mechanism

The power electronic (PE) converter is a crucial sub-assembly that enables the variable-speed operation of WT systems and their integration to the power grid. Consequently, the reliability of the PE converter is crucial for the availability and the continuous operation of the WT generating unit [50], [68], [118]. Considerable research has been undertaken on the topic of converter reliability over the last decades – especially as the reliance of the power system stability on power electronics-enabled generation is rising at an enormous pace – and the dominant failure mechanisms have been described and modelled [62], [69]. Particularly close attention has been paid to the modelling and mitigation of failure mechanisms that are a consequence of the loading profile, i.e. mission profile in the specific application, in this case WT systems.

IGBTs are one of the most widely applied devices for converters in current operating WTs, and are popular switching devices due to their property of combining the advantages of BJT and MOSFET devices: high current density from the former and controllability by voltage from the later [57]. In previous research, thermal cycling has been identified as the dominating failure mechanism for IGBT power modules [56]–[62]. The thermal stress cycling is considered as the most critical failure cause by the industry as well [63], [64]. One of the most studied and dominating failure modes for IGBT power modules manifested as a result from the thermal cycling, is the bond-wire lift-off failure mode [65]. Because of the dominance of this failure mode and its clear link to electrical operation, this is the reference failure mode which has been used when evaluating the converter lifetime in this thesis. The same failure mechanism is also applicable to other parts of the IGBT module packaging where there is an interface of different materials, such as the solder

layers – thus the same approach can be extended to consider the thermal fatigue in those parts as well, by relating the corresponding temperature change in the simulation to the layer (failure mode) of interest.

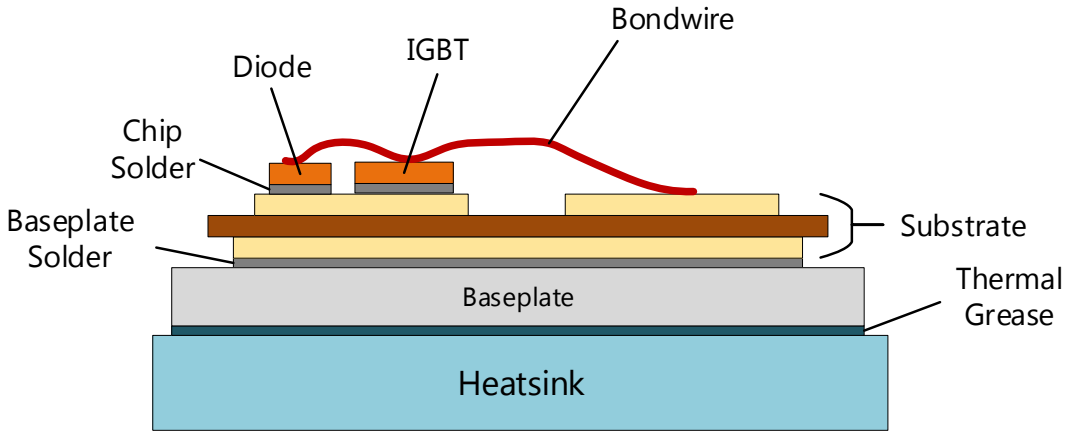


***Figure 4.1: Structure of IGBT module*** [69]

Figure 4.1 shows the standard structure of an IGBT module package. It consists of several layers made from different materials: silicon (Si), Copper (Cu), Ceramic (AlN or $Al_2O_3$). These materials have different Coefficients of Thermal Expansion (CTEs). During operation, i.e. conduction through the diode or IGBT, a significant amount of losses in the semiconductor devices is manifested as heat generation (with the sources being the IGBT and parallel diode chips). The generated temperature at the chips has a cyclical profile, affected by different factors of the mission profile. These factors include the converter operation and control of the switches, as well as the cycling resulting from the nature of the loading profile for the specific application. In the case of WT converters, the mission profile is highly variable because of the variable wind speed and this induces substantial temperature cycling. This continuous cycling between different temperatures in the power module structure, affects all the materials of the layers to a certain extent - thermo-mechanical strain (expansion and contraction) occurs according to the layer's corresponding CTE. A, usually small, portion of the expansion is plastic i.e. irreversible. Thus, after a considerable number of cycles, two interconnecting layers will have a distinct level of residual (plastic) expansion. This will result in stress and fatigue at the interconnection. Eventually, at some point after a number of cycles and a large enough difference in expansion, the contact between the two layers will be compromised. Usually, a failure by this mechanism is manifested with a crack propagation in one of the materials close to the interface. Commonly in the case of a bond wire and chip connection, the crack

propagation at the contact results in the failure mode bond wire lift-off. Other failures with such a mechanism can happen in the solder between chip and copper, solder between copper and substrate, etc.

## 4.2 Losses and Thermal Modelling

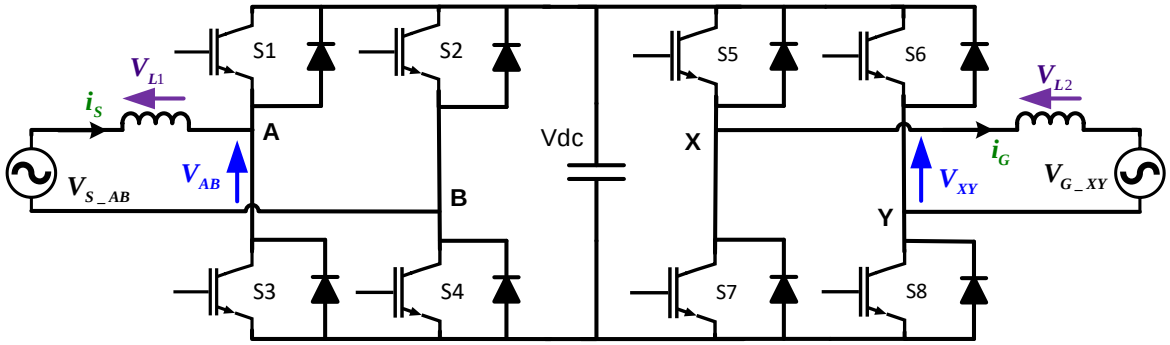


***Figure 4.2: Representation of a 2-level full-bridge back-to-back converter (both VSCs in inverter topology). Only two phases shown for simplification.***

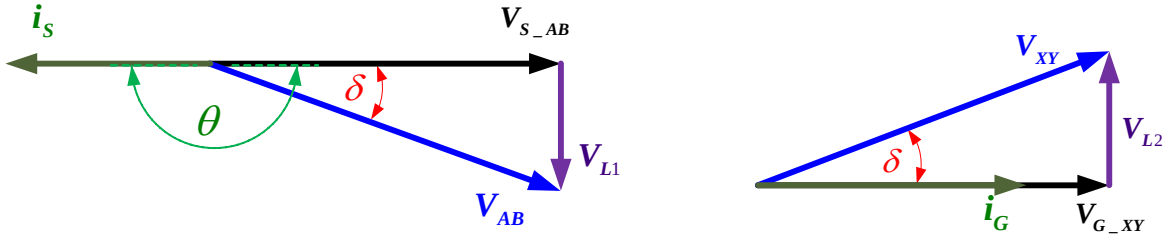


a) Rectifier (MSC) b) Inverter (GSC)

***Figure 4.3: Phasor diagram of current and voltages for the full bridge back-to-back configuration***

Design for reliability of PE converters is not the goal of this study, but rather building and examining a reliability evaluation tool. A standard high-power ABB HiPak [119] module is used as a basic unit and it is assumed that a suitable number of basic modules can be connected in parallel in order to keep the current and thermal profile within acceptable limits. The simplified two-phase connection diagram representing the grid integration of the WT using the back-to-back converter is shown in Figure 4.2. The phasor diagrams showing current and voltage of the Machine Side Converter (MSC) and Grid Side Converter (GSC) are shown in Figure 4.3. To simplify the calculations, a two-level PWM control is assumed for both VSCs. Actual integrated power modules, which may be designed for specific WT applications, may differ in terms of some construction and packaging aspects, as well as the control, but the thermal properties and phenomena

studied here, from the perspective of the IGBT module thermal cycling, are valid and can be applied and adapted for most of the converters in state-of-the-art WTs.

The temperature change and cycling inside of power semiconductor chips is primarily a consequence of the generated losses. Taking into account the thermo-mechanical phenomena described in the previous subsection, these losses are used to link the thermal stress and lifetime of the converter module to the WT operation and mission profile. Other factors such as the ambient temperature have an additional effect and can also be added to the thermal modelling by super-positioning them on the temperature generated by losses.

Commonly the losses $P_{loss}$ in a switching semiconductor device, including an IGBT, can be written as a sum of three components [120]:

$$P_{loss} = P_{conduction} + P_{switching} + P_{blocking}$$

The blocking losses are usually small and insignificant, and in such a system, together with the additional losses in the driver circuit, can be ignored [101]. In the case of the diode, instead of being externally switched on and off, its conduction state depends on the applied voltage and current flow imposed by the circuit. Consequently, the total losses in the diode instead of switching losses, contain the so-called reverse recovery losses. Therefore considering a standard high-power IGBT module that is commonly applied in WT converters – like ABB's HiPak series – the different losses in such a module for the different comprising semiconductor chips can be divided in IGBT losses (conduction and switching losses) and diode losses (conduction and reverse recovery losses) [121]. These losses are briefly described in the subsections below.

In this subsection, the analytical approach of evaluating the significant losses in an IGBT power module is described. This analytical model is built with several assumptions:

- Transistor and diode switching transients and dead times are neglected
- Control with linear modulation operation is assumed
- The switching frequency of the devices is significantly larger than the frequency of the AC waveform fsw >> $f_{AC}$ – for the PWM control applied here, the switching frequency is 35 times the AC grid frequency for the GSC, and more than 87 times for the MSC.

### 4.2.1 Conduction Losses

The conduction losses represent the power dissipated as a consequence of the current conducted through the semiconductor device and the on-state voltage. Using the device's current vs voltage characteristic, the dissipated power can also be described only as a function of current, as in (4.1).

$$\begin{aligned} V_{\mathrm{CE}}(t) &= \mathrm{V_{CE0}} + \mathrm{r_{CE}} \cdot i_{\mathrm{C}}(t) = \mathrm{V_{CE0}} + \mathrm{r_{CE}} \cdot \mathrm{I_1} \sin \omega t \\ P_{\mathrm{cond}}(t) &= V_{\mathrm{CE}}(t) \cdot i_{\mathrm{C}}(t) = \mathrm{V_{CE0}} \cdot i_{\mathrm{C}}(t) + \mathrm{r_{CE}} \cdot i_{\mathrm{C}}(t)^2 \end{aligned} \tag{4.1}$$

Where $V_{CE}$ and $r_{CE}$ are the collector-emitter on-state voltage and resistance respectively.

Conduction losses of the IGBT/diode can be written as in (4.2), where $i_c$ is the current through the chip, and $k_0$, $k_1$, $m_0$, $m_1$, are coefficients used to implement temperature-dependent calculation of losses using second-order dependence and curve fitting of datasheet information [122].

$$P_{con}(i_c, T_j) = \overbrace{(k_0 + k_1 \cdot T_j)}^{V_{CE0}(T_j)} \cdot i_c + \overbrace{(m_0 + m_1 \cdot T_j)}^{r_{CE}(T_j)} \cdot i_c^2 \tag{4.2}$$

Equation (4.2) gives the instantaneous power losses of the chip as a function of the instantaneous current, which can be calculated for devices in each of the phase legs of the back-to-back voltage source converter. For derivation of the instantaneous loading of the semiconductor devices, it is important to take note of the conduction period of each device in different phases and the direction of current in the converter. The four different current paths in the grid side inverter are shown in Figure 4.4, for a half-bridge configuration of one phase of the VSC with a reference connection to the virtual neutral point of the capacitor. By applying standard control approaches such as sine-wave PWM, the VSC current and voltage are controlled for the required power output.

The average conduction losses of the IGBT can be derived as in (4.3) by integrating (4.2) over the half-period where the device is conducting, i.e. when the current through the considered device is not zero, taking into account current direction from Figure 4.4.

$$P_{cond,av,IGBT} = \frac{1}{T_0} \int_0^{T_0/2} \left( P_{con}(i_c, T_j) \cdot \tau(t) \right) dt \tag{4.3}$$

Depending on the load and the mode of operation of the VSC, the voltage waveform can have a certain phase difference with the current waveform, and this will influence the calculation of the instantaneous losses on the devices. The waveforms of the phase current and converter terminal voltage for the phasor in Figure 4.3 b) (inverter mode) are shown in Figure 4.5 a). In Figure 4.5 b) is shown the transfer of current (state of conduction) in different half-periods between the upper IGBT switch S5 and its antiparallel diode D5 (switching transients and the conduction of the lower leg switches are not shown).

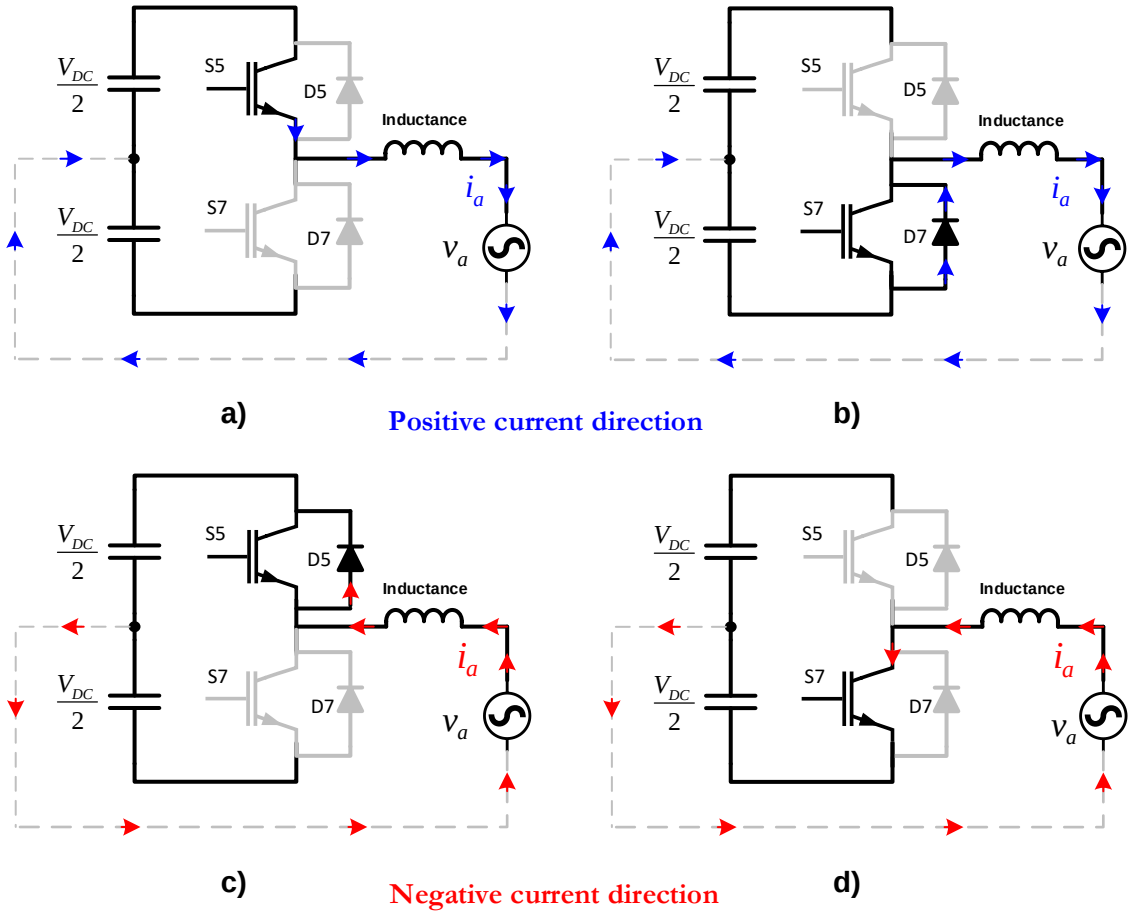


***Figure 4.4: Different current paths and transfer of current between the switching devices***

If the phase current $i_c$ is described as a function of time $t$ and frequency $\omega = 2\pi f$, as in (4.4), then the duty-variation (PWM pulse pattern) of the IGBT can be written as (4.5) (if a suitably fast switching frequency and bipolar switching with no dead-time is assumed). The inverter voltage leads the current by angle $\varphi$, which for unity grid power factor is $\varphi = \delta$, as shown in Figure 4.3 b) (inverter) and Figure 4.5 a) [123]. The duty-variation waveform of the S5 switch is in phase with the voltage waveform of phase A.

$$i_c(t) = \hat{I}_c \sin(\omega t) \tag{4.4}$$

$$\tau(t) = \frac{1}{2}\left(1 + m\sin(\omega t + \varphi)\right) \tag{4.5}$$

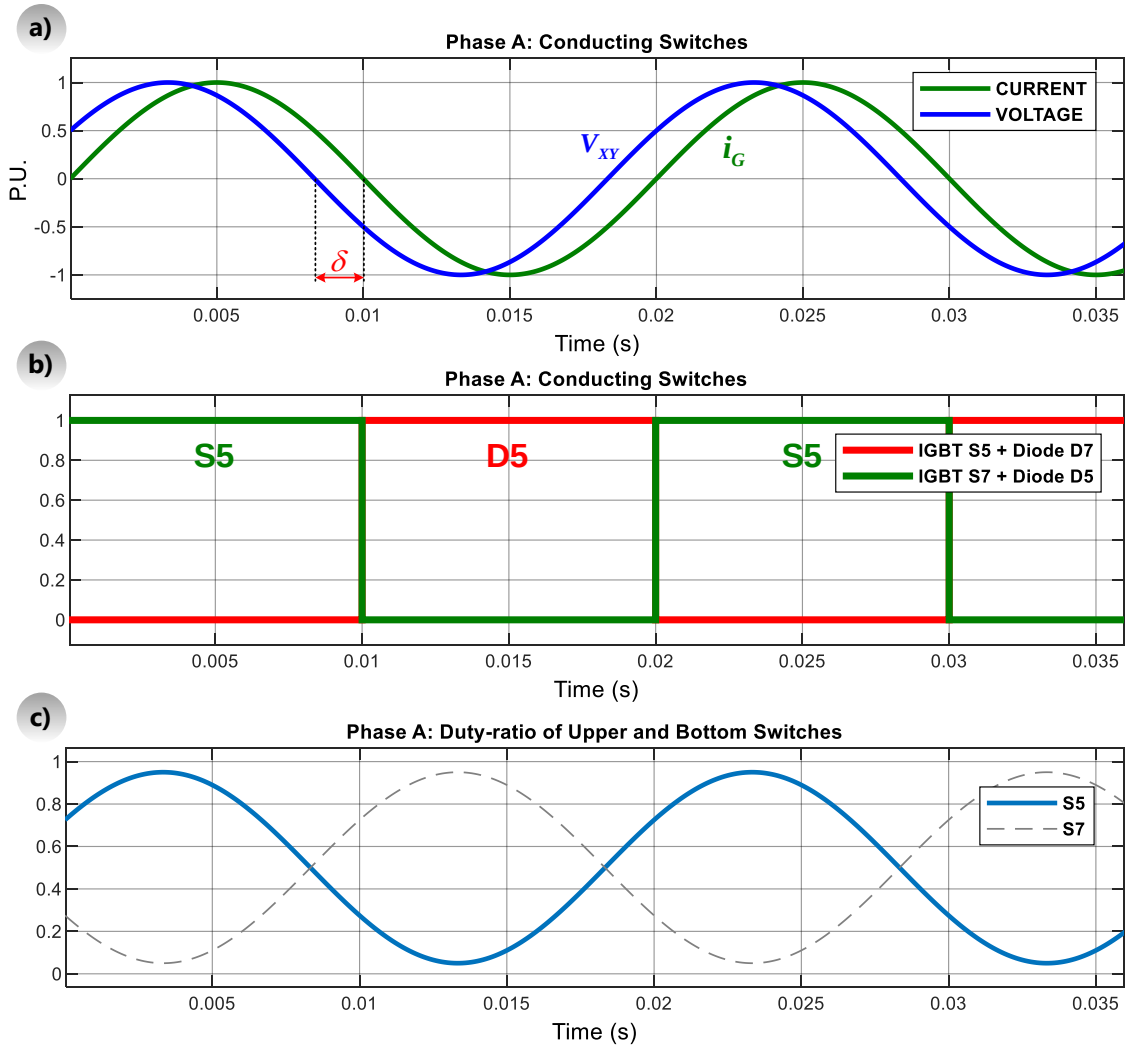


***Figure 4.5: GSC terminal output voltage and load current waveforms***

In (4.5), *m* is the modulation index which for a 2-level VSC equals to $(2V_{sine,peak})/V_{dc}$. Figure 4.5 b) has been annotated with the intention of analysing the upper switch – actual PWM frequency switching is in combination with the corresponding bottom switch. The duty ratio variations defined by (4.5) for upper and lower switches (S5 and S7) in phase leg A are given in Figure 4.5 c). In these waveforms the switching harmonics are ignored. The actual switching pattern for a 2-level PWM of S5 switch is shown in Figure 4.6; S7 will have a switching pattern and duty ratio that is the opposite of S5 (and any additional dead-time). The switching is happening continuously with a commutation between the upper and lower IGBTs, bringing the output voltage to +Vdc/2 or –Vdc/2. Meanwhile, the current

conduction is transferred between S5 and D7 or D5 and S7 – a) and b) or c) and d) in Figure 4.4 – depending if the current waveform is in a positive or negative half-period. The losses are symmetrical between the upper and lower switch in a 2-level VSC topology where the control of switches is symmetrical, so for reliability and lifetime analysis, only one IGBT module is studied.

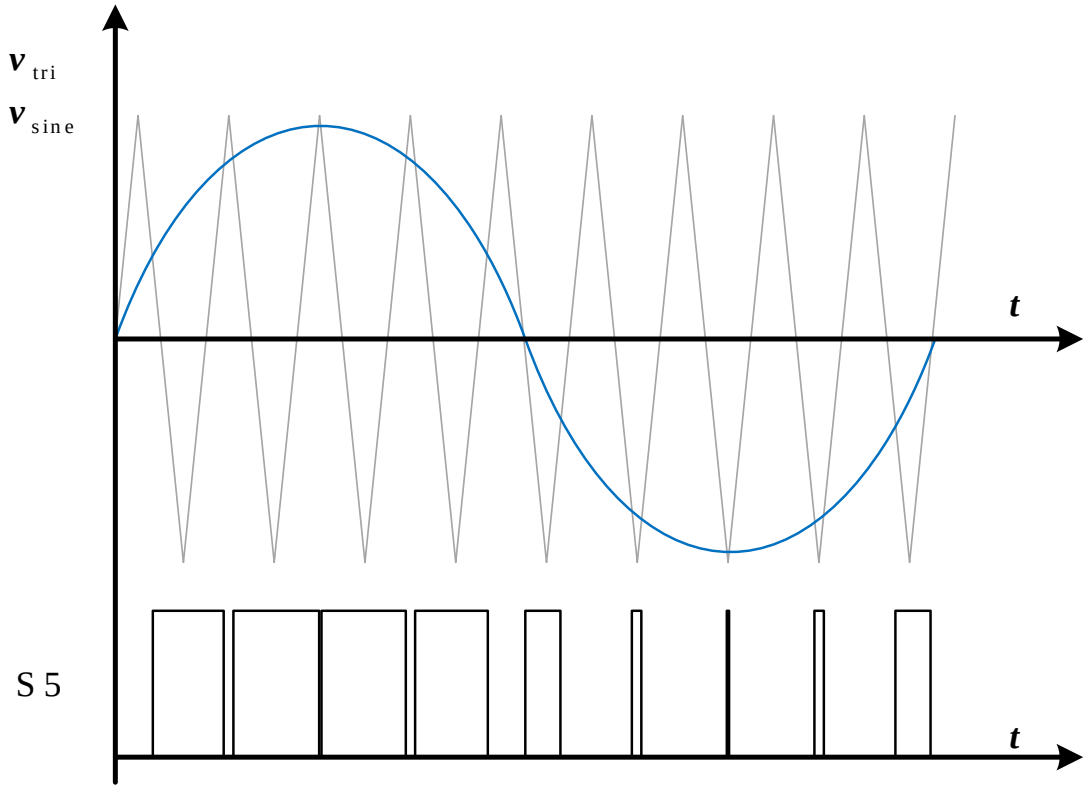


***Figure 4.6: Simplified sine-triangle PWM switching pattern of S5 switch***

Combining (4.3) - (4.5) and performing the integration, the expression (4.6) for the average IGBT conduction losses is derived. For full integration please refer to the Appendix 9.1.

$$P_{\text{av, cond}}\left(T_j\right)=\frac{1}{2}\left(V_{\text{CE0}}\left(T_j\right)\cdot\frac{\hat{\text{I}}_{\text{c}}}{\pi}+r_{\text{CE0}}\left(T_j\right)\cdot\frac{\hat{\text{I}}_{\text{c}}^{\,2}}{4}\right)+$$
$$+m\cdot\cos\varphi\cdot\left(V_{\text{CE0}}\left(T_j\right)\cdot\frac{\hat{\text{I}}_{\text{c}}}{8}+\frac{1}{3\pi}\cdot r_{\text{CE0}}\left(T_j\right)\cdot\hat{\text{I}}_{\text{c}}^{\,2}\right) \tag{4.6}$$

The diode conduction losses are calculated in a similar manner. The approximation of the on-state voltage and resistance is done as in [122] and the average conduction losses have the same form as (4.6). The difference in calculating the averaged conduction losses

for the diode is in the pulse pattern – a phase delay of π radians is used for the duty ratio in (4.5), because it conducts during the negative-current half cycle – which after the integration (Appendix 9.1) results in a negation in the second term of the equation as in (4.7).

$$P_{\text{av, cond}}\left(T_j\right)=\frac{1}{2}\left(V_{\text{F0}}\left(T_j\right)\cdot\frac{\hat{\text{I}}_{\text{c}}}{\pi}+r_{\text{T}}\left(T_j\right)\cdot\frac{\hat{\text{I}}_{\text{c}}^{\,2}}{4}\right)- \\ -m\cdot\cos\phi\cdot\left(V_{\text{F0}}\left(T_j\right)\cdot\frac{\hat{\text{I}}_{\text{c}}}{8}+\frac{1}{3\pi}\cdot r_{\text{T}}\left(T_j\right)\cdot\hat{\text{I}}_{\text{c}}^{\,2}\right) \tag{4.7}$$

### 4.2.2 Switching and Reverse Recovery Losses

The other device losses that cannot be neglected are the switching losses. These represent the power dissipation at the turn-on and turn-off instants during switching operations – occurring with the PWM switching frequency.

Switching losses in an IGBT are a consequence of the time ($t_{on}$ and $t_{off}$) it takes for the current and voltage between collector and emitter values to fall and rise to their steady-state (ON or OFF) values after the switching instants. Therefore, during that transient when both the voltage and current are non-zero (one rising and the other falling), their product results in on and off switching losses. In the case of the diode, the equivalent of the switching losses are the reverse recovery losses. These are losses manifested when the diode stops conducting and goes to a blocking state. In that instant, its internal storage charge has to be discharged. Therefore a reverse-direction current flows in the diode which causes the reverse recovery losses [101].

Switching and reverse recovery losses, for the IGBT and diode respectively, can be estimated starting from the energy loss for one switching operation which is given as information from manufacturers in datasheets. These reference switching IGBT and reverse recovery diode losses, $E_{on+off}^{ref}$ and $E_{rr}^{ref}$ respectively, are given in datasheets usually in the form of the polynomial function in (4.8), where $i_c$ is the current conducted through the device.

$$E_{sw}=E_{on+off}^{ref}=\left(\text{a}+\text{b}\cdot i_C+\text{c}\cdot i_C^{\,2}\right) \tag{4.8}$$

The energy losses are adapted for the particular application with the equations that are given in (4.9) and (4.10), where the subscript *ref* indicates the reference values from the datasheet information; $K_{v1}$ and $K_{v2}$ are factors for scaling to the operating DC voltage. Additionally, with the constants $K_{T,sw}$, and $K_{T,rr}$ is introduced the dependence of the losses to the junction temperature $T_j$, i.e. to account for different temperatures other than the reference datasheet value of $T_j^{ref}$ = 125 °C [101].

$$E_{on+off} = E_{on+off}^{ref} \cdot \left( \frac{V_{cc}}{V_{cc}^{ref}} \right)^{K_{v1}} \cdot \left(1 + K_{T,sw} \cdot \left(T_j - T_j^{ref}\right)\right) \tag{4.9}$$

$$E_{rr} = E_{rr}^{ref} \cdot \left( \frac{V_{cc}}{V_R^{ref}} \right)^{K_{v2}} \cdot \left(1 + K_{T,rr} \cdot \left(T_j - T_j^{ref}\right)\right) \tag{4.10}$$

Using (4.8), the sum of the energy loss of all the switching transients is given with the average switching losses in (4.11) as a function of the peak value of the collector-current $\hat{I}_c$. $T_0$ is the period of the waveform equal to 2π radians.

$$E_{sw,avg} = \frac{1}{T_0} \sum_n E_{sw}(i) = \left( \frac{a}{2} + \frac{b \cdot \hat{I}_c}{\pi} + \frac{c \cdot \hat{I}_c^{\,2}}{4} \right) \tag{4.11}$$

Multiplying the $E_{sw,avg}$ with the switching frequency $f_{sw}$, and scaling for the operating voltage and junction temperature, the average switching power losses for the IGBT are calculated as in (4.12) [101], [123]. In the same manner, instead of the average switching power losses, the instantaneous switching power losses can be calculated if (4.9) and (4.10) are multiplied with the switching frequency $f_{sw}$.

$$P_{sw,avg} = f_{sw} \cdot E_{sw,avg} \cdot \left( \frac{V_{cc}}{V_{cc}^{ref}} \right)^{K_{v1}} \cdot \left(1 + K_{T,sw} \cdot \left(T_j - T_j^{ref}\right)\right) \tag{4.12}$$

For the anti-parallel diode and the reverse recovery losses, the equations are similar to the IGBT, but attention needs to be paid in adjusting for the current direction and the conduction instants (Figure 4.7). A more extended explanation and derivation of these equations can be found in [100], [101], [123]. Furthermore, when the VSC of the same topology is operating in rectifier mode (in case of the MSC in Figure 4.2), the current and pulse pattern need to be adjusted with relation to how the converter is being controlled.

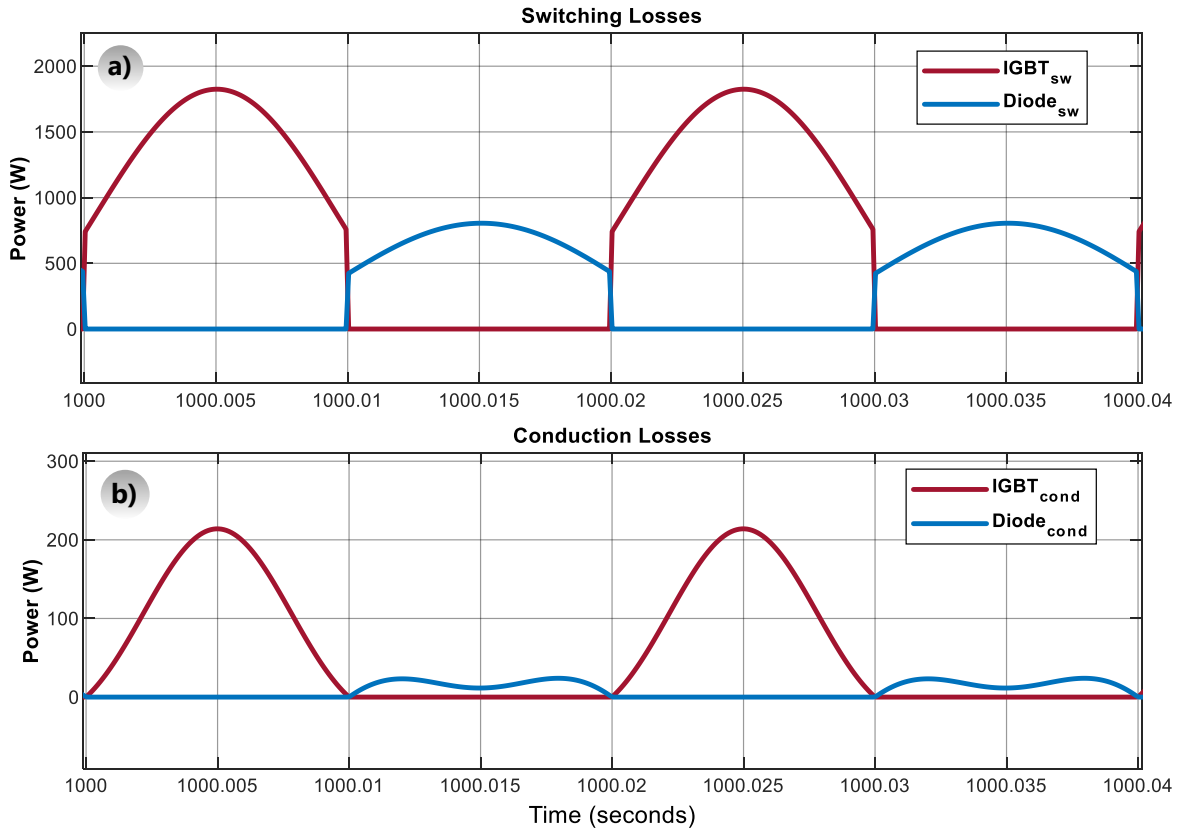


***Figure 4.7: Instantaneous switching and conduction losses for IGBT and diode chips for a steady-state operation of an inverter-mode VSC (grid side in WT converter)***

For inverter mode and steady-state WT power output, the waveforms of the instantaneous switching and conduction losses in the IGBT and diode of one phase module are shown in Figure 4.7. The switching of both phase devices (upper and lower) happens continuously independently of the current direction. However, even if a particular IGBT is switching to ON at a particular instant of the AC period, if the current direction is the opposite of the “forward direction” of the IGBT, it will flow through an antiparallel diode. Therefore, even though the IGBT is still switching as part of the PWM voltage synthesis; because there is no current flow through it, for that switching instant the losses are negligible. Instead, for that same instant, the losses are significant and manifested as reverse recovery losses for the antiparallel diode of the same module. For this reason, the switching (reverse recovery) losses are modelled while accounting for the current paths and the conduction for each studied semiconductor switch of the converter. In the plotted losses the presence of the diode and the IGBT losses can be seen distinctly for the different instants of conduction depending on current flow direction. Additionally it can be seen that the switching losses dominate and are approximately an order of magnitude larger than the conduction losses.

### 4.2.3 Thermal Model

The manufacturers give information about the thermal behaviour of a module in datasheets by giving an analytical function for the transient thermal impedance between junction and case, as in (4.13).

$$Z_{th(j-c)}(t) = \sum_{i=1}^{n} R_i \left(1 - e^{-t/\tau_i}\right) \tag{4.13}$$

Taking into account the analogous analysis of thermal and electrical networks, the given information is equivalent to a series connection of thermal impedances (parallel resistances and capacitances), which is known as a Foster thermal network. This representation is time dependent for the thermal behaviour of the whole module and does not give any information on the temperature distribution across the layers – thermal resistances and capacitances do not have a physical meaning [101]. Additionally, the Foster network does not model accurately the heat flow in the actual physical structure [124], [125]. In order to have a more accurate representation of the heat flow and the temperature distribution across the module, Foster networks can be transformed to Cauer networks (Figure 4.8). An additional factor is that because of the incorrect heat flow representation, when using Foster models it is difficult to derive the thermal model of a combined system: a combination of a module and a heatsink is not a series connection between module and heatsink Foster circuits. Cauer networks however solve this problem and simple series connections are a close enough representation of thermal interconnection between different materials [60], [124].

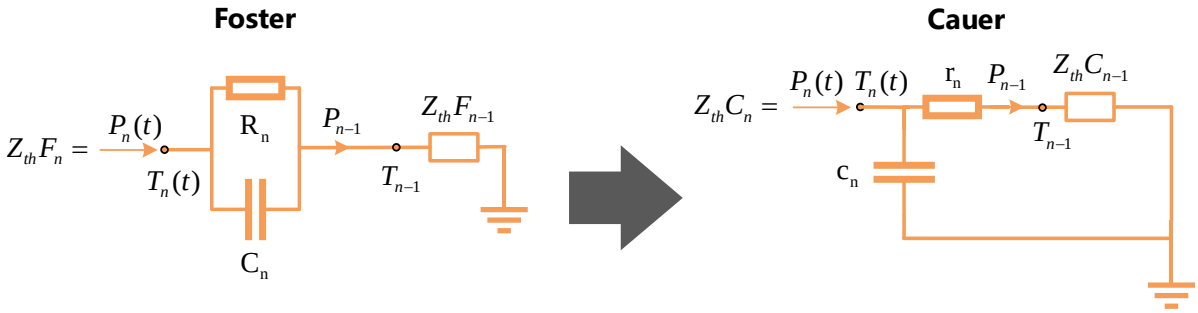


***Figure 4.8: Foster to Cauer transformation*** [124]

The Foster to Cauer transformation is done using the methodology derived in [124] utilising the impedance equations in the Laplace domain. The method encompasses writing the Foster network in the Laplace domain and in the recursive form given in (4.14), which

has been derived using the notation in Figure 4.8. $Z_{th}F_n$ is the total two-point Foster impedance of the module, from the junction to the case. The Cauer impedance is also represented as a recursive transfer function $Z_{th}C_n$ in (4.15) and in Figure 4.8. This method for Foster to Cauer transformation (and the other way around) is derived by finding the zeros of the transfer function in (4.14) and performing an analytical transformation to express the polynomial transfer function in the form of the type of network we want to transform to – from where each of the *n* thermal elements (capacitance and resistance) are obtained from the polynomial coefficients. For the applied HiPak IGBT module here, the Foster thermal elements are taken from datasheets and the Cauer elements are obtained using the transformation – the resulting elements are shown in Table 6 [119].

**Foster:** $$Z_{th}F_n(s) = \frac{T_n(s)}{P_n(s)} = \frac{1}{sC_n + \frac{1}{R_n}} + Z_{th}F_{n-1}(s) \tag{4.14}$$

**Cauer:** $$Z_{th}C_n(s) = \frac{T_n(s)}{P_n(s)} = \frac{1}{sc_n + \frac{1}{r_n + Z_{th}C_{n-1}(s)}} \tag{4.15}$$

***Table 6 Power module Foster and Cauer thermal network parameters***

| | **Foster** [119] | | **Cauer (transformed)** | |
|---|---|---|---|---|
| | IGBT | Diode | IGBT | Diode |
| **Thermal Resistance [K/kW]** | r1=12.75<br>r2=2.99 | r1=25.5<br>r2=6.3 | Rt(1) = 4<br>Rt(2) = 11.71 | Rd(1) = 8.47<br>Rd(2) = 23.32 |
| **Thermal Time Constant [ms]** | τ1=151<br>τ2=5.84 | τ1=144<br>τ2=5.83 | τ1 = 6.76<br>τ2 = 130.45 | τ1 = 6.74<br>τ2 = 124.5 |

The built thermal network, representing the temperature behaviour of one IGBT module connected to a heatsink, is shown in Figure 4.9. This thermal network enables a correct representation of the junction temperature change. Furthermore, here the simulated temperature is fed back to the loss model to add a dependence of IGBT and diode losses on the junction-temperature. The values of the thermal grease and heatsink elements which are added to complete the junction to ambient (or converter cabinet) thermal network are given in Table 7. The time constant of the thermal grease is negligible while the resistance is taken from [119]. The heatsink thermal parameters have been chosen referring to datasheets of commercial heatsink solutions for similar devices which employ forced air cooling [126]. In other real similar applications, such a low heatsink thermal resistance is also likely to be achieved using efficient forced air/liquid cooling.

The steady-state results calculated using the MATLAB/Simulink analytical model of the above-explained losses have been verified by comparison with the simulation tool SEMIS offered by the manufacturer of the IGBT module (Hitachi ABB Power Grids) [127]. The settings of the converter for the compared set-points are shown in Table 8, while the comparison of combined (switching/reverse recovery + conduction) losses for the IGBT and diode are plotted in Figure 4.10 and Figure 4.11 respectively. The comprehensive table containing the parameters and all the results of this comparison, for the different operation settings and operational set-points of the converter, is given in Appendix 9.3.

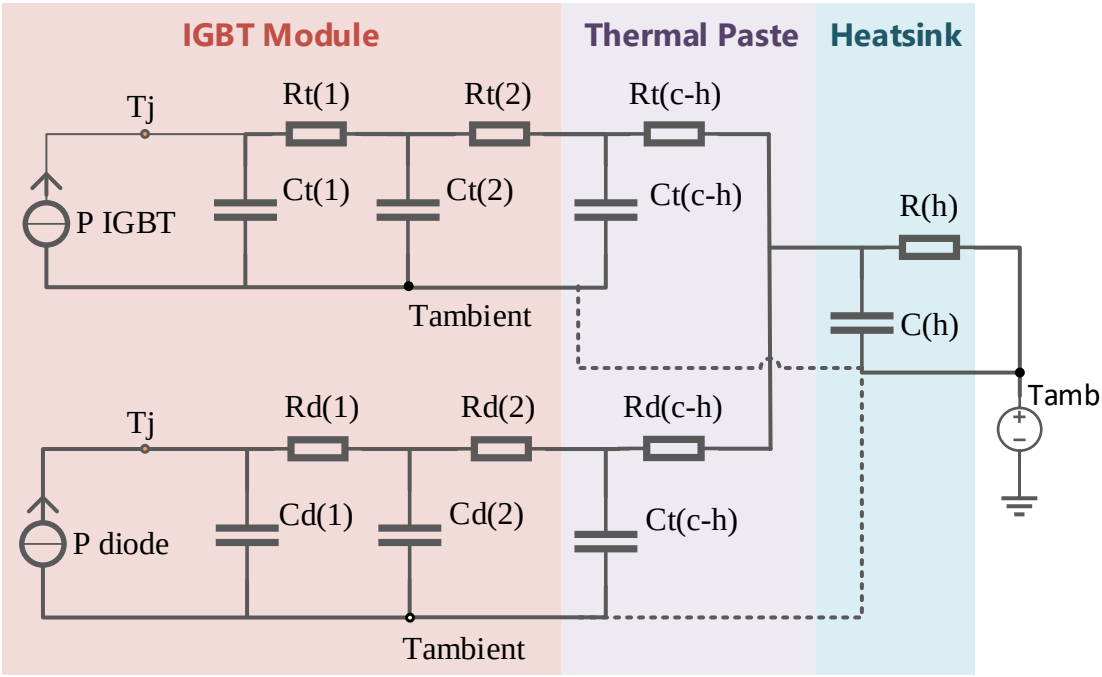


***Figure 4.9: Cauer thermal network for a single-chip IGBT module connected to a heatsink***

***Table 7: Additional thermal Network Parameters***

| | **Thermal Grease (case-heatsink)** | | **Heatsink** |
|---|---|---|---|
| | IGBT | Diode | |
| **Thermal Resistance [K/kW]** | 0.012 K/W | 0.024 K/W | 0.05 K/W |
| **Thermal Time Constant [ms]** | / | / | 100 s |

***Table 8: Converter set-points for validation of thermal and loss models***

| Setpoint | 1 | 2 | 3 | 4 | 5 | 6 |
|---|---|---|---|---|---|---|
| Real Power [kW] | 265.1 | 190.9 | 152.7 | 209 | 260.9 | -260.9 |
| Reactive Power [kVAR] | 0 | 0 | 74 | 68.5 | 147.9 | 147.9 |
| Phase Voltage RMS [V] | 354 | 354 | 283 | 318 | 250 | 250 |
| Phase Current RMS [A] | 250 | 180 | 200 | 230 | 400 | 400 |
| Output Frequency [Hz] | 50 | 50 | 50 | 50 | 50 | 50 |
| Power Factor | 1 | 1 | 0.9 | 0.95 | 0.87 | 0.87 |
| DC Power [kW] | 271.5 | 195.4 | 156.9 | 214 | 274.6 | -278.8 |
| DC Voltage [V] | 1000 | 1000 | 1000 | 1000 | 1000 | 1000 |
| Switching Frequency [Hz] | 1500 | 1700 | 1250 | 1450 | 1750 | 1750 |
| Modulation Index | 1 | 1 | 0.8 | 0.9 | 0.707 | 0.707 |

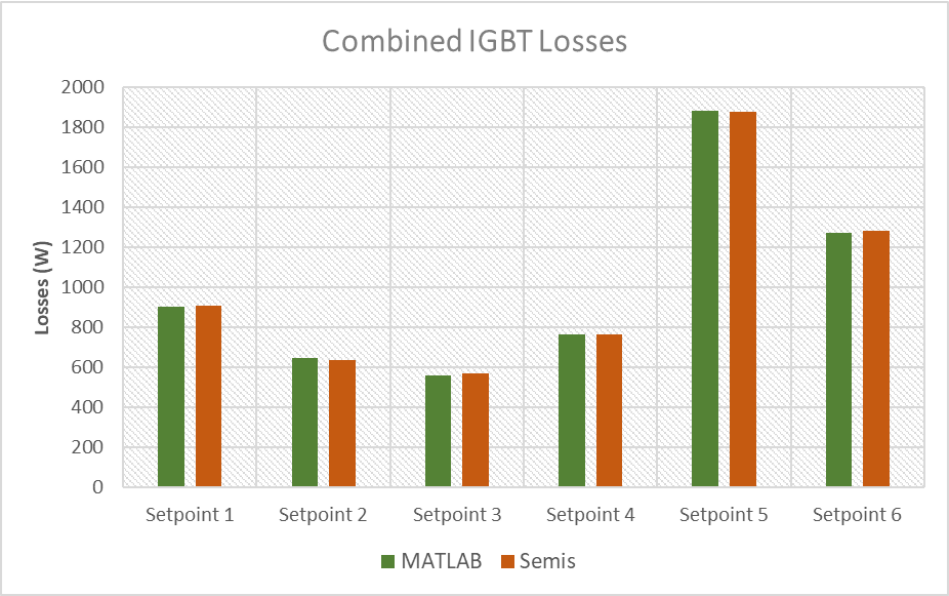


***Figure 4.10: IGBT total losses comparison between Semis tool and MATLAB/Simulink***

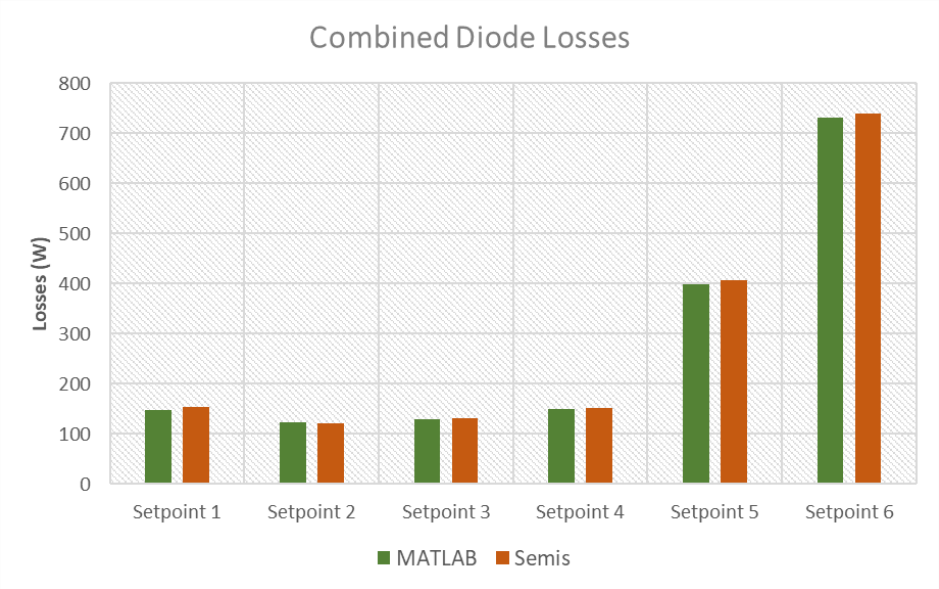


***Figure 4.11: Diode total losses comparison between Semis tool and MATLAB/Simulink***

## 4.3 Lifetime Evaluation – Bond-Wire Failure

In order to evaluate the consumption of lifetime and the development of fatigue in the bond-wire connection, the effect of counted junction temperature cycles i.e. the stress, is evaluated against the strength of the semiconductor module referenced to the device information from the manufacturer. This approach consists first of counting the cycles and then calculating the total lifetime consumption by adding the effect of each cycle.

A summary of the lifetime estimation model, containing the stress-strength evaluation and the calculation of the accumulated degradation is illustrated in Figure 4.12

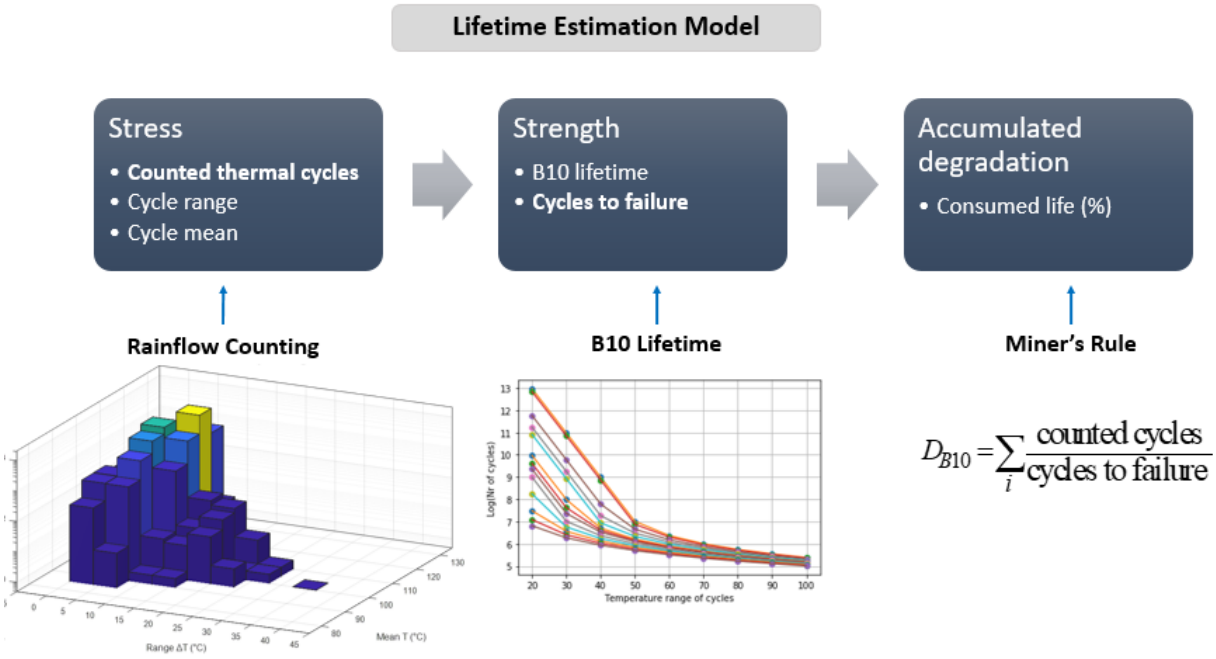


***Figure 4.12: Stress-Strength approach and Miner's rule for lifetime accumulation***

The applied algorithm for undertaking the lifetime evaluation based on counted cycles is shown in Figure 4.13. The counting of the cycles is done using the rain-flow counting algorithm. The output of the rain-flow counting algorithm is a matrix where each row consists of the necessary information for every one (or half) counted cycle in order to calculate the impact on the lifetime. After counting the reversals and using the rain-flow matrix, each of the counted cycles is evaluated against the expected lifetime (the strength) given from power module manufacturers (see illustrated in Figure 4.13).

The strength of the device, i.e. the expected lifetime, given with $B_{10}$ lifetime curves. The $B_{10}$ curves are produced by manufacturers using laboratory testing of the devices. A large

number of devices are brought to failure by undertaking failure testing using power and temperature accelerated tests [50]. The $B_{10}$ curves represent device strength information in terms of cycles-to-failure in the same way as Coffin-Mason based lifetime models of the form in (4.16). The actual value in the $B_{10}$ lifetime represents the number of cycles when 10 % of the tested devices have failed, from where the terminology $B_{10}$ comes. By lowering this margin from 10% to 5% or 1%, $B_5$ and $B_1$ lifetime can be calculated. For HiPak IGBT modules applied here and for the bond-wire failure mode, the $B_5$ and $B_1$ lifetimes can be calculated by multiplying the $B_{10}$ data with constants $k_5 = 0.82$ and $k_1 = 0.52$, respectively [90].

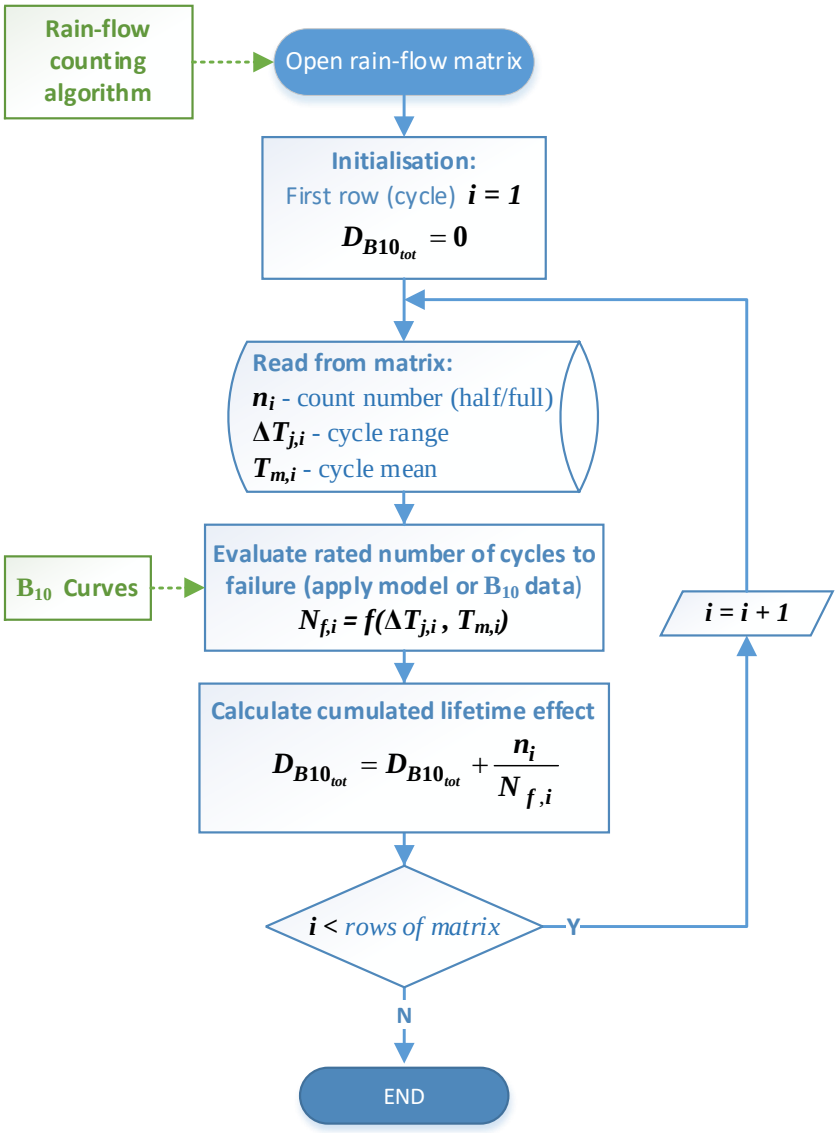


***Figure 4.13: Diagram of applying the function for lifetime estimation procedure***

$$N_f = a \cdot (\Delta T)^{-n} \cdot e^{E_a / (k \cdot T_m)} \tag{4.16}$$

One form of the Coffin-Manson equation that describes the relation between thermal cycling and the strength of materials is shown in (4.16): $N_f$ is the number of cycles to failure; *a*, *n* and *k are* constants; and $E_a$ is the activation energy value that characterizes the deformation process for the material [56]. Additional to the range (magnitude) of the cycle, the lifetime consumption also depends on the mean temperature value $T_m$ of the counted cycles. Calculating the rated number of cycles to failure $N_f$ , is done applying the $B_{10}$ curves directly as lookup tables, given that there is not enough information to accurately evaluate the parameters and apply the equation in (4.16) directly.

The evaluation of lifetime consumption for each of the counted cycles is undertaken relative to the expected lifetime from the datasheet information, while the lifetime consumption from all cycles is calculated as a total sum of the effect of each cycle, i.e. using the Miner's rule for lifetime accumulation given with the expression in (4.17).

$$D_{B10} = \sum_i \frac{n_i}{N_{f,i}}$$

$n_i$ - number of applied cycles $\Delta T_i$ (4.17)

$N_{f,i}$ - number of cycles to failure for $\Delta T_i$

Miner's rule gives as a result the percentage (share) of the module's lifetime, which has been consumed for all the cycles with different temperature ranges and mean values. As seen in (4.17) the effect of each cycle is calculated with the ratio between the counted cycles $n_i$ at a particular temperature and the expected (rated) cycles $N_{f,i}$ at that same temperature that the module is expected to withstand before failure (as indicated from previous tests). Therefore, the device will fail (have a probability of failure larger than 10%) when the total lifetime $D_{B10}$ in (4.17) and in Figure 4.13 equals one – meaning that 100% of the $B_{10}$ lifetime has been consumed.

## 4.4 Wind Turbine Converter Steady-State Thermal and Lifetime Evaluation

In this subsection, the results after running the complete set of the steps of the lifetime estimating methodology are shown for steady-state scenarios and different operating

speeds of the WT. Speeds from 5 m/s up to rated speed (11.4 m/s) have been applied to the WT rotor. For input speeds higher than rated, the steady-state losses and temperature remain at rated value because the turbine power is limited (equal to the power at rated wind speed) at that region of operation.

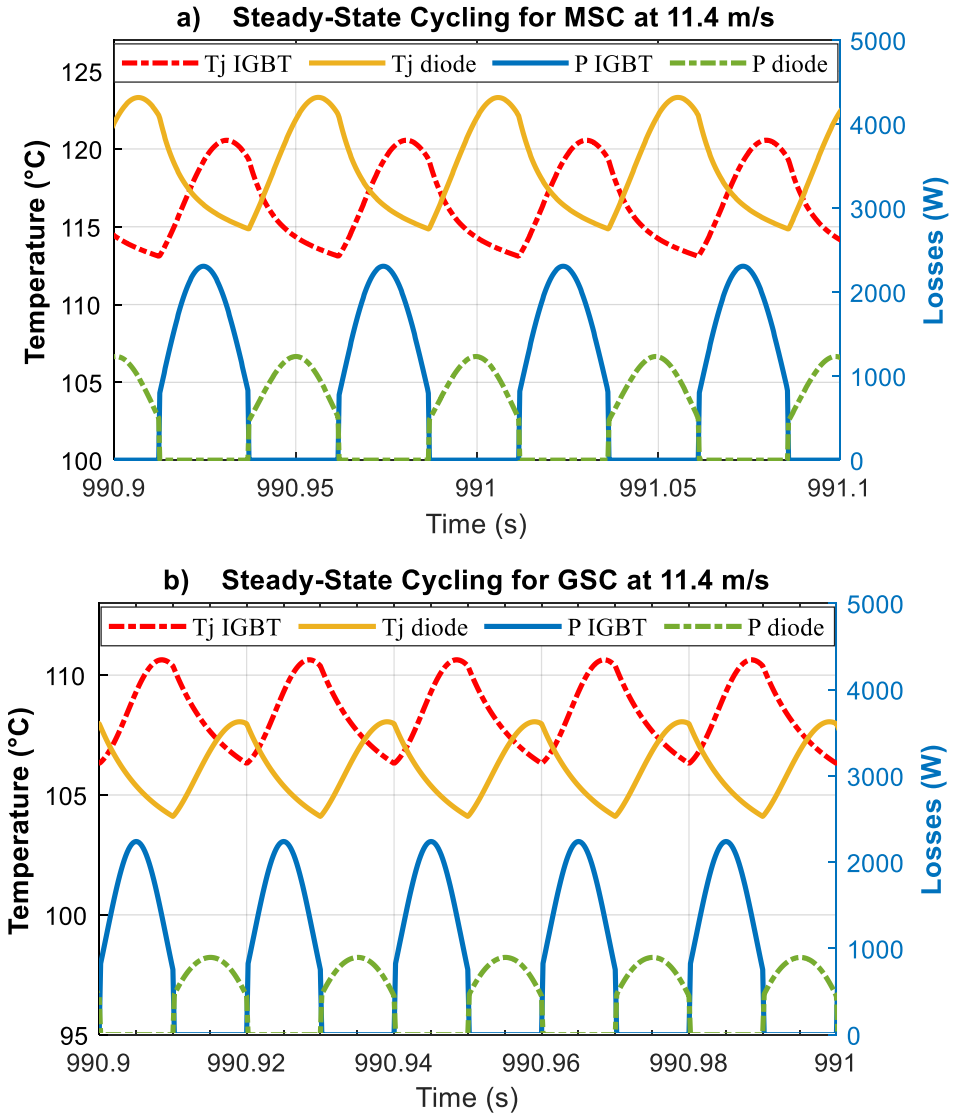


***Figure 4.14: Steady-state junction temperature cycling and losses of IGBT and diode for a) MSC and b) GSC***

The steady-state junction temperature cycling of the diode and the IGBT of the same module and the instantaneous losses causing that temperature change are given in Figure 4.14, for both MSC and GSC. The average losses and average temperature for steady-state operation at different wind speed inputs are shown in Figure 4.15.

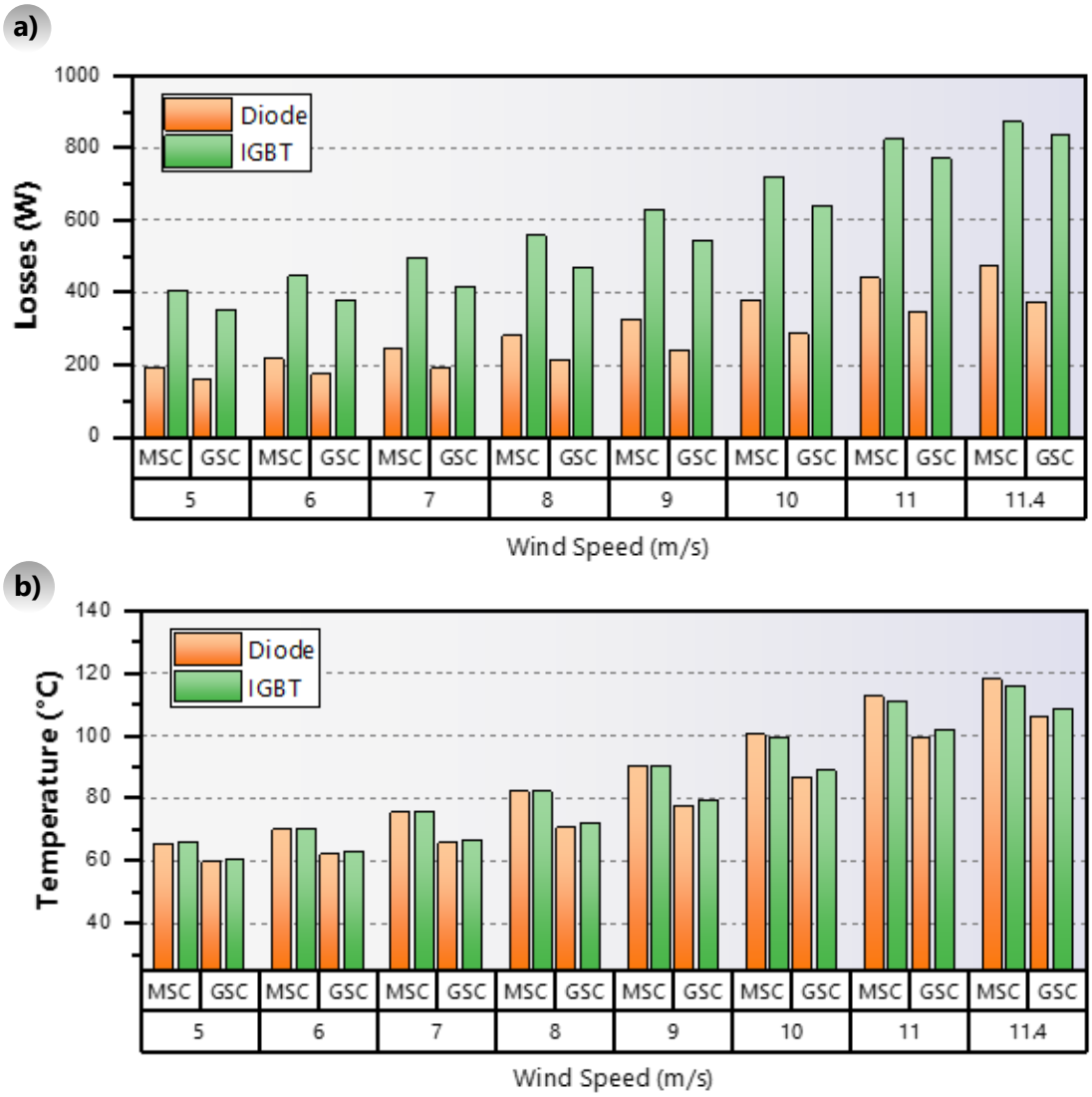


***Figure 4.15: Average losses (a) and junction temperature (b) against wind speed (m/s) at steady-state operation for phase-module diodes and IGBTs in MSC and GSC***

From analysing the results in steady-state operation, a few observations can be made. In Figure 4.14 the cycling which is the result of the transfer of conduction between the IGBT and antiparallel diode (depending on the current direction) can be seen. One difference in this cycling between the MSC and the GSC is the difference in frequency, which is related to the AC current frequency. For the GSC this is 50 Hz grid frequency, while for the MSC the frequency changes with rotor speed and at rated wind speed is 20 Hz. This difference makes the MSC cycling periods longer and as a consequence the temperature swings are larger than in the GSC junction temperature change. An additional difference is that in the MSC the more thermally stressed chip is the diode, while for the GSC it is the IGBT. This is because of the difference in operation, rectifier vs inverter, and the phase shift difference that comes with this (see Figure 4.3). The effect of that difference in operation is seen in

the losses in Figure 4.15 as well, where the share of losses that is manifested in the diode chip is more significant in the case of rectifier operation (i.e. in the MSC) than in the GSC. As a result of this, the diode junction temperature reaches a higher temperature than the IGBT for the MSC (seen in both Figure 4.14 and Figure 4.15). Note that this happens even though the absolute losses of the diode are still lower than those of the IGBT; the junction temperature gets higher due to the diode being a chip with a smaller volume and having a larger thermal resistance (see Table 6) – so after surpassing the value of about half the losses of the IGBT, the diode junction temperature surpasses that of the IGBT.

### 4.4.1 Thermal Cycling in Steady State Operation

In the previous subsection was shown the change in average losses and average temperature for different operating wind speeds (5 to 11.4 m/s) of the WT. However, the largest factor affecting the degradation and failure mechanism of interest, is the temperature swing of the cycles. The steady state analysis can be used to analyse the link between the input speed of the WT and the range of the temperature cycles in steady-state, i.e. cycles caused by AC frequency cycling.

Particularly the question of interest is to what extent the AC frequency junction temperature cycling changes with changing wind speeds. To answer this question, the cycle counting algorithm can be applied to the junction temperature waveforms obtained for steady-state WT operation with different wind speeds. After counting the cycles in the temperature waveforms, the results can be shown in histograms such as in Figure 4.16 and Figure 4.17, where the counted cycles for steady-state operation with 5 m/s and 11 m/s wind input are compared. The histograms represent bar plots of number of counted cycles in 50 minutes of operation, put in bins depending on the range of each of these cycles. The most thermally stressed part of each converter is used: Figure 4.16 shows the counted cycles in the GSC IGBT, and Figure 4.17 the counted cycles in the MSC diode. For both the MSC and GSC, the range of the cycles for 11 m/s is undistinguishable to the plotted case for 11.4 m/s operation which was discussed in Figure 4.14.

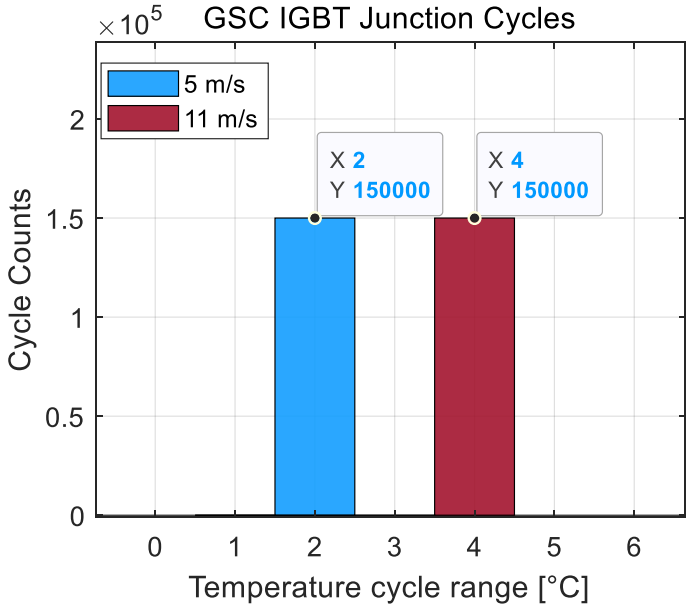


***Figure 4.16: Histogram of counted cycles against cycle range, in GSC IGBT for 5 and 11 m/s WT operation***

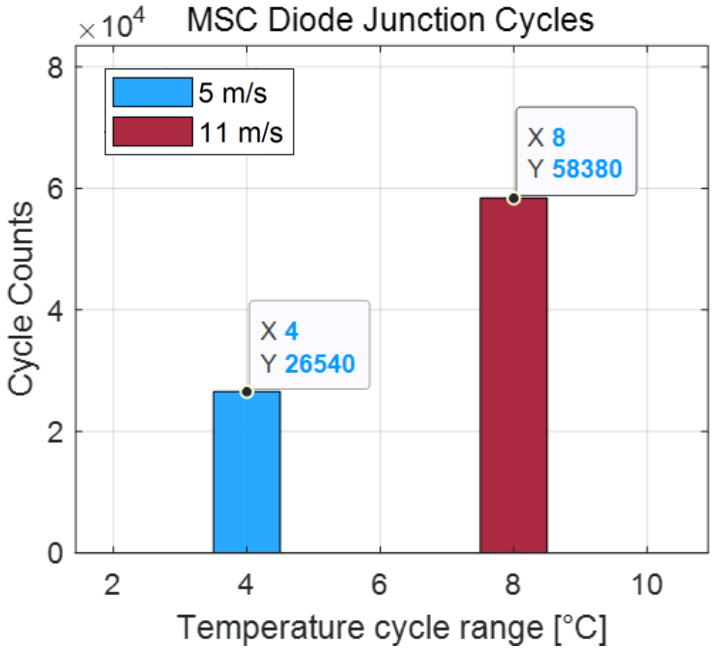


***Figure 4.17: Histogram of counted cycles against cycle range, in MSC Diode for 5 and 11 m/s WT operation***

In steady-state operation with wind speed going down to 5 m/s, as expected the cycling range reduces, because of the power output reduction. However, the extent of this change is insignificant so that it would have any effect in consumed lifetime. Especially for the GSC, even the highest cycling at 11.4 m/s is very small to have significant effect on the degradation and aging of the bond-wire. In the GSC case also can be seen that the number of counted cycles is exactly the same for 5 m/s and 11 m/s, given that the frequency stays

constant. For the MSC this is not the case, and reduced wind speed translates to reduced frequency and less cycles (see the difference in Figure 4.17).

The observation from this steady-state analysis is that the range of (steady-state) thermal cycles for different operating input speeds of the WT is in the range from 4 to 8 °C for MSC diode and 2 to 4 °C for the GSC IGBT. Consequently, all of the cycles that result from the AC frequency will be around this spectrum of temperature cycling. Additionally all these temperature cycle amplitudes are well below the border (around 20 °C in this case), above which the cycles start to meaningfully affect B10 consumed lifetime. However it should not be immediately assumed that these cycles can be neglected. Ignoring the AC frequency cycling from the start, would prevent analysing any impact that could result when aspects such as highly variable wind profile and WT control are added. The full detailed model is used for analysing the more complete operation, which involves transients and a dynamic wind profile input.

## 4.5 Highly-Variable Wind Profile

A more realistic and useful application of the approach for estimating lifetime consumption of wind turbine converters can be realised if the model is applied to a scenario where the WT operates with a highly-variable wind profile input as opposed to the constant wind speed which was considered in the previous sub-section. The highly variable mission profile is the distinctive property that makes WTs a vastly problematic application for IGBT power modules when it comes to their thermo-mechanical fatigue mechanism. The portion of wind speed profile that has been used to run the model is shown in Figure 4.18, and represents a 1 second-resolution wind measurement at an offshore WT wind turbine in the UK.

The results produced from simulating the junction temperature change of the MSC and GSC are shown in Figure 4.19 and Figure 4.20 respectively. From initial observation it can be noticed that for the MSC the diode is the chip with the higher junction temperature, as opposed to the GSC where the more thermally stressed device is the IGBT. This is in line with the observations made when considering the cycling and average temperature values in steady-state operation in subsection 4.4.

In order to quantify the lifetime consumption, the cycles in temperature waveforms from Figure 4.19 and Figure 4.20 have been counted using a rain-flow algorithm. The output of the rain-flow counting, i.e. the counted cycles can be shown in a 3D histogram as in Figure 4.21 and Figure 4.22. The x-axis is the range $\Delta T$ of counted cycles, y-axis is the mean temperature $T_m$ of the counted cycles, and z-axis is the number of counted cycles in bins and shown in a logarithmic scale.

Using the counted cycles, the consequential lifetime consumption of the IGBT module for the operating period can be calculated by evaluation against the B10 curves with the recursive approach explained in Figure 4.13 and section 4.3. The lifetime consumption, for operation of 50 minutes, is $3.5 \times 10^{-6}$ (% of $B_{10}$ lifetime) for the MSC diode and $0.1 \times 10^{-6}$ (%) for the GSC diode. For an evident comparison, the lifetime consumptions for the diode and IGBT for GSC and MSC are shown in the bar plot in Figure 4.23.

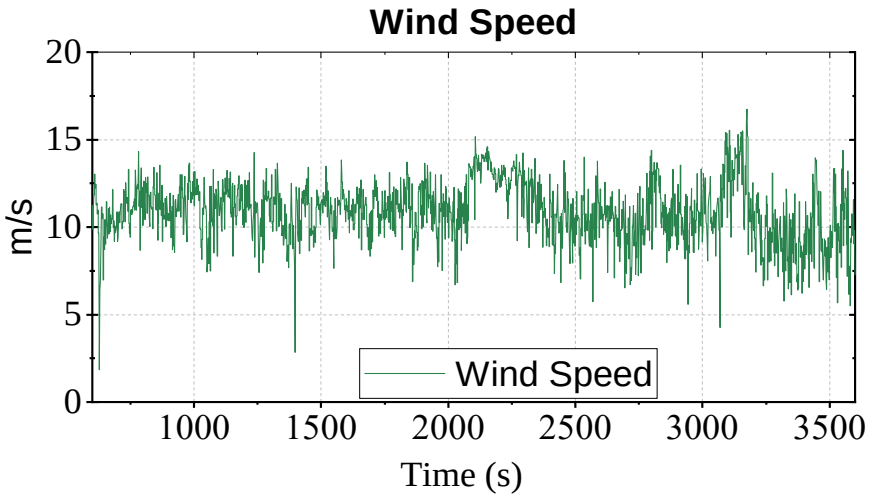


***Figure 4.18: Wind Speed Profile***

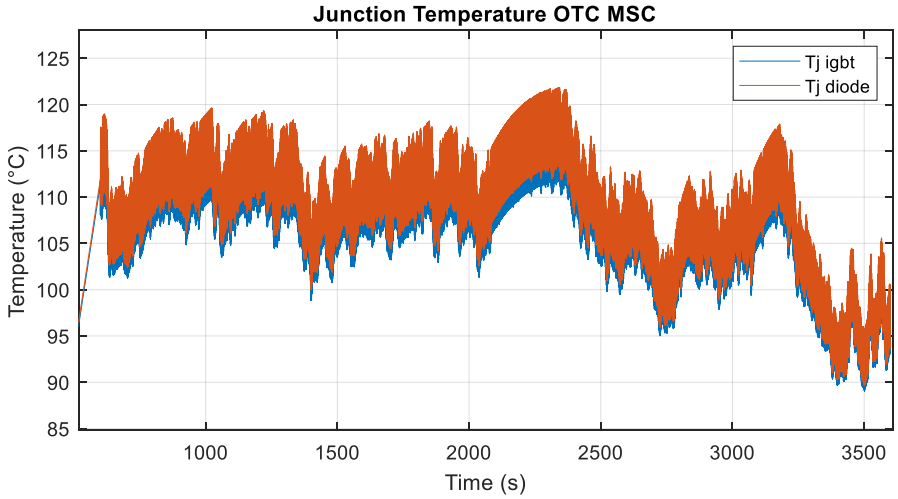


***Figure 4.19: MSC diode and IGBT junction temperature variation***

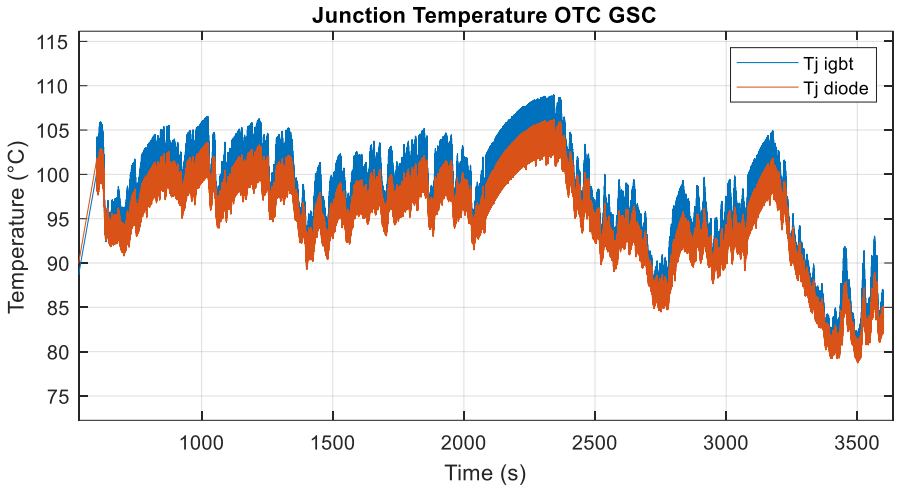


***Figure 4.20: GSC diode and IGBT junction temperature variation***

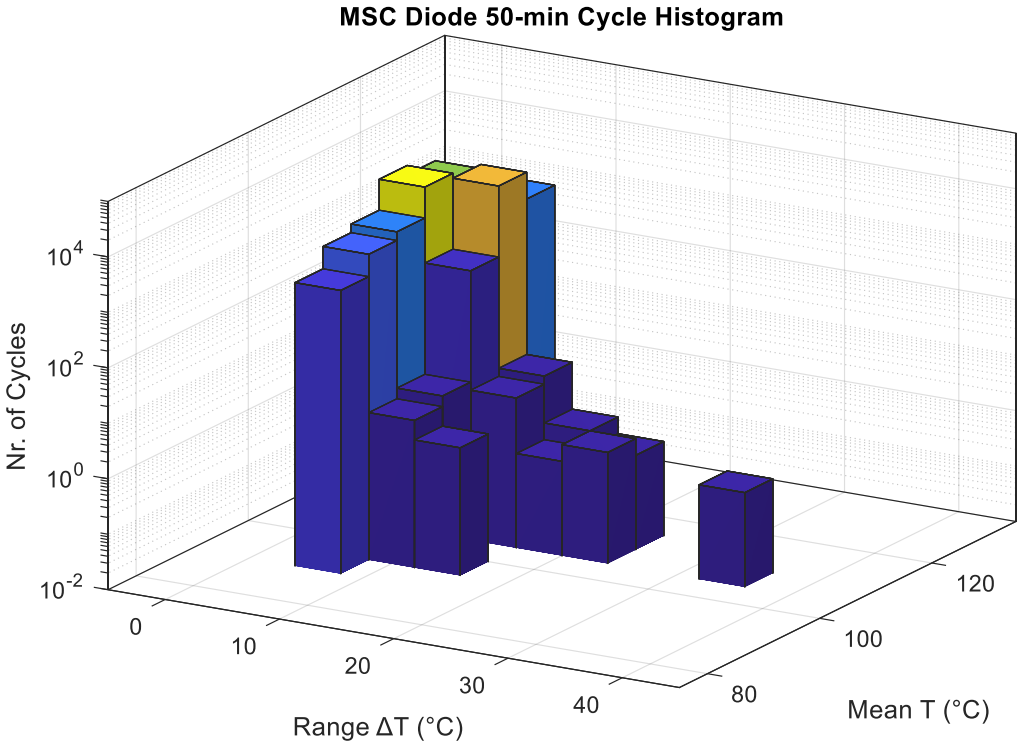


***Figure 4.21: 3D Histogram of counted cycles against cycle range in °C and cycle mean temperature in °C for diode of MSC operating for 50 minutes with wind profile shown in Figure 4.18.***

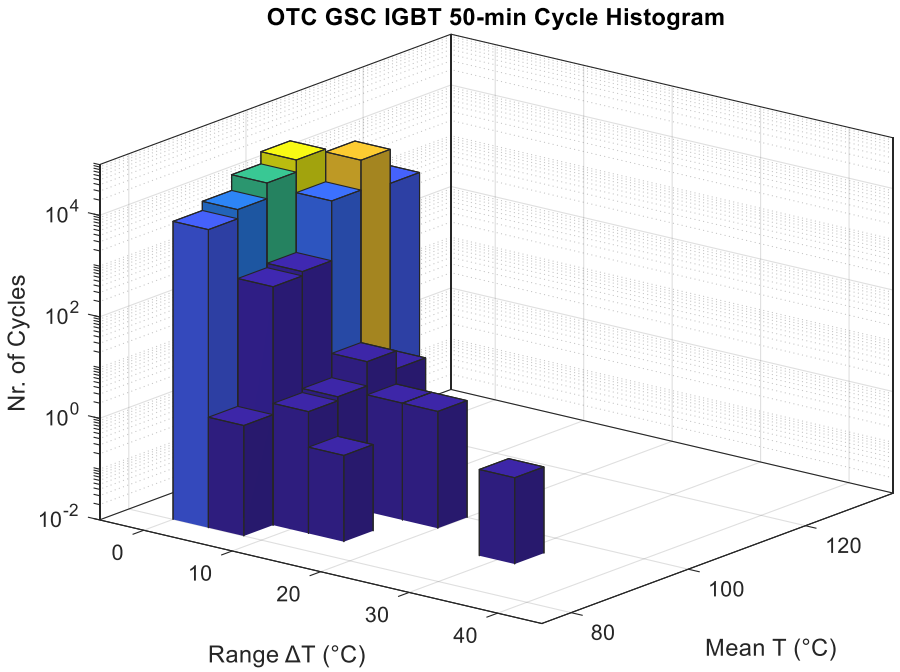


***Figure 4.22: 3D Histogram of counted cycles against cycle range in °C and cycle mean temperature in °C for IGBT of GSC operating for 50 minutes with wind profile shown in Figure 4.18.***

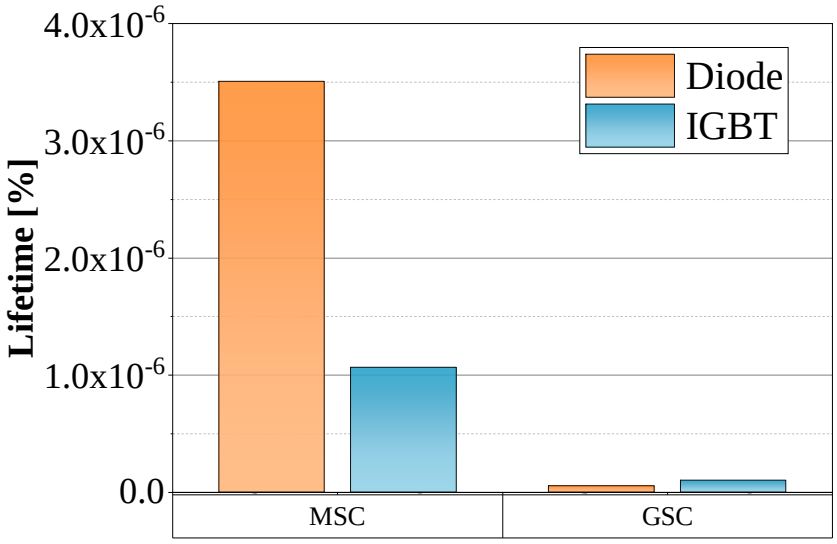


***Figure 4.23: Lifetime consumption of MSC and GSC devices for the considered 50 minute operating period***

The largest converter temperature cycling (with largest ΔT) in an operation with variable wind profile input comes from the change in wind speed and the consequential change in output power of the WT. There is a large difference in lifetime consumption between the variable-wind and steady-state analysis which is due to the disproportionate effect of cycles that have a large range ΔT – even though they are just a few in number,

their lifetime consumption effect can outweigh the effect of thousands of small cycles. This effect is described by the logarithmic shape of the B10 curves. Furthermore, this effect has an explanation and comes from the physics of failure, where for very small temperature cycling, the thermomechanical expansion effect is not only so small that it can be neglected, but also it is likely to be mostly elastic and not contribute at all to accumulated wear-out and aging.

## 4.6 Summary

This chapter describes in detail the second and third layers of the lifetime estimation methodology: the layer containing the losses and thermal models, and the layer undertaking the lifetime evaluation. The nature of the considered failure mechanism and the resulting failure mode bond wire lift-off was described. The analytical equations to estimate the conduction and switching (reverse recovery) losses as well as the construction of the thermal network from the datasheet information were described. The method of evaluating the consumed lifetime using counted junction temperature cycles and $B_{10}$ lifetime strength information was described.

Thermal stress and lifetime were evaluated for steady-state operation for different constant speeds of the input wind profile. Finally, thermal stress and lifetime was evaluated for a variable (realistic) wind profile input. One conclusion observed from the simulations is that the thermal stress and lifetime consumption is much higher on the MSC than the GSC.

# 5 Lifetime Evaluation of the WT Converter Considering Control Transients and Grid Requirements

In this chapter, the methodology for evaluation of thermal stress and lifetime consumption is applied to compare the impact of different control scenarios of the WT generator and the MSC and GSC converters. This comparison is undertaken using a high resolution wind profile input for the WT operational model. The results of the comparison show valuable information on the aspects that cause the most thermal stress and lifetime consumption on the converter. One of the main conclusions coming from the comparison is that dynamic transients related to the wind profile input and wind turbine operation, can highly affect the converter lifetime, and therefore have to be accounted for in lifetime prediction models in order to have useful and accurate lifetime assessment.

## 5.1 WT MPPT Torque Control

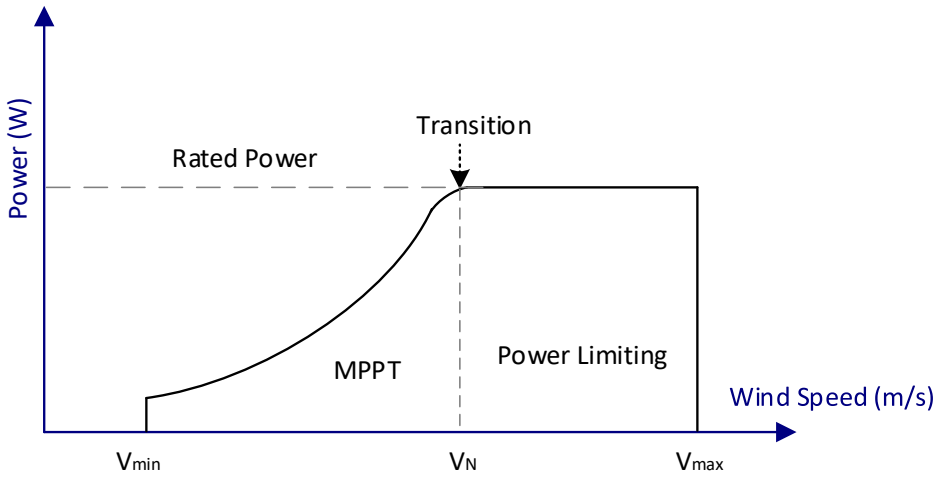


***Figure 5.1: Typical WT power curve***

The WT power curve can be divided in different regions of operation and is shown in Figure 5.1, where $V_{min}$ is the cut-in wind speed, $V_N$ is the rated speed, and $V_{max}$ is the cut-off speed. The WT is normally turned off for speeds below $V_{min}$ and above $V_{max}$ while it is operated at a constant power output in the Power Limiting region above $V_N$. In the second region, between $V_{min}$ and $V_N$ the so-called Maximum Power Point Tracking (MPPT) control is applied for most efficient power conversion from the wind. In this chapter are compared the lifetime consumptions and thermal stress effect of three different designs of

this MPPT control, which are shown in Figure 5.2. Each of the three controls is described in the next few subsections. These three controls have been chosen given that they are some of the most widely used for WT MPPT application in the literature and in industry [92], [128].

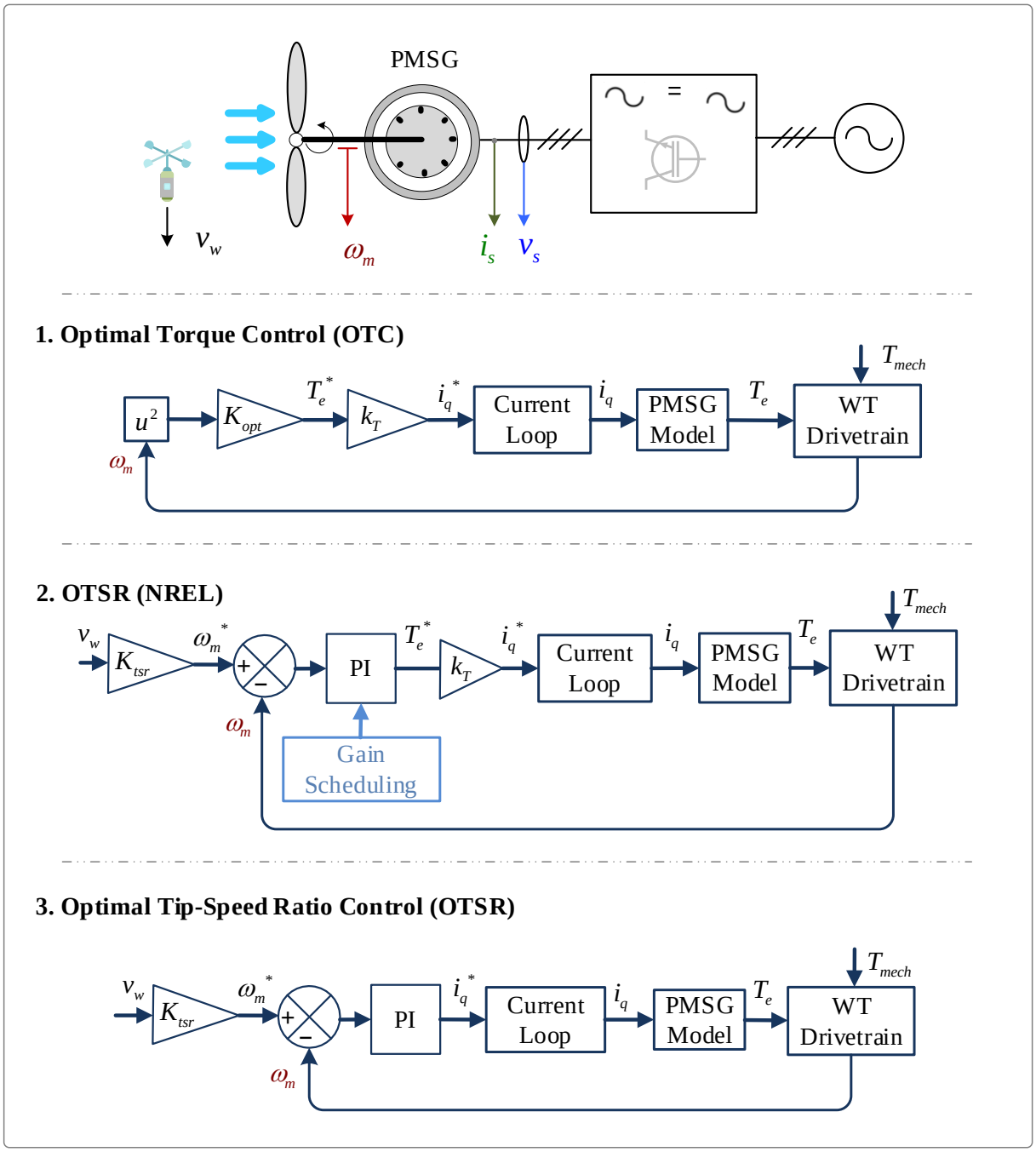


***Figure 5.2: MPPT control strategies***

### 5.1.1 Optimal Torque Control

This is the control proposed in the original NREL publication from where the WT that has been applied in this thesis was adapted [92]. It is called Optimal Torque Control (OTC) and this optimal torque is realised using an effective control which adjusts the electrical torque reference depending on the measured mechanical speed of the WT rotor. The relationship between the two quantities is derived from the aerodynamic torque equation and is given in (5.1) and (5.2). The OTC state feedback block diagram as applied here is shown as the first option in Figure 5.2.

$$T_e = K_{opt} \cdot \omega_g{}^2 \tag{5.1}$$

$$K_{opt} = \frac{\pi \rho R^5 C_p}{2\lambda^3} \tag{5.2}$$

This OTC works in a way that the reference electrical torque is set to be equal to the calculated mechanical torque of the turbine as the measured rotor speed changes. Given that the electrical and mechanical torque are set to be equal and counteract each other, according to the swing equation (5.3) - (5.5), these torques balance each other at the shaft and steady-state is achieved. The rotor speed is measured and acts as a feedback loop to reach steady-state and cancel any mismatch between the calculated electrical torque and the mechanical torque of the turbine resulting from the wind input.

$$J_w \frac{d\omega_w}{dt} = T_w - k_{wg}\theta_{wg} - d_{wg}\frac{d\theta_{wg}}{dt} \tag{5.3}$$

$$J_g \frac{d\omega_{gm}}{dt} = k_{wg}\theta_{wg} + d_{wg}\frac{d\theta_{wg}}{dt} - T_g \tag{5.4}$$

$$\frac{d\theta_{wg}}{dt} = \omega_w - \omega_{gm} \tag{5.5}$$

The problem with this OTC control is that there is no flexibility in controlling the response characteristics of the WT which depend on the drivetrain inertia. Additionally, in practice $K_{opt}$ cannot be calculated with total accuracy so there can be a significant error in the maximum power point tracking.

### 5.1.2 Optimal Tip Speed Ratio (NREL version)

In another publication [128], several years later after the first one, NREL suggested an improved OTSR control for their baseline 5 MW turbine, in order to match with more modern requirements and industry standards. This updated control tracks the maximum power point curve by ensuring optimal tip-speed ratio and is shown as the second option in Figure 5.2. The measured feedback quantity of this control is the rotor mechanical speed – the same as in OTC. However, in this case there is also a control flexibility of this speed achieved by a PI controller in the loop. This controller adjusts the torque reference for the inner current loop according to the error between the reference rotor speed and the measured rotor speed of the mechanical shaft. The reference mechanical speed is calculated using the measured wind speed hitting the WT blades and the optimal tip-speed ratio given in equation (5.6). In this way, the tip-speed ratio is being held at its optimal value for any changing speed, and MPPT control is achieved.

$$\lambda_{opt} = \frac{l \cdot \omega_m}{v_{wind}} \tag{5.6}$$

For a more advanced PI control implementation, NREL have applied gain scheduling for the controller, to ensure the desired response is consistent at any input wind speed. For calculation of the gain scheduling dependence, advanced simulations using NREL's OpenFAST aero-hydro-servo-elastic software [129] have been run. This dependence has been provided for users to apply the gain scheduling using analytical expressions. Here we have applied the gain scheduling and the PI control with response characteristics corresponding to a bandwidth frequency $f = 0.05\ Hz$ and a damping factor of $\zeta = 1$.

### 5.1.3 Optimal Tip-Speed Ratio Control (OTSR)

This is a version of the OTSR control which can be applied by using second order approximation and no gain scheduling. It is essentially a less complex version of the NREL OTSR and its design is shown as the 3rd option in Figure 5.2 [130]. The transfer function and the expressions for calculating the $K_i$ and $K_p$ parameters are given in (5.7) to (5.9), while their derivation is given in Appendix 9.4.

$$\frac{\omega_e^*(s)}{\omega_e(s)} \approx (2^{nd}\, order) \approx \frac{K_i \cdot \frac{3}{2}\frac{{p_p}^2}{J_{tot}}\psi_{PM}}{s^2 + s\cdot\left(\frac{B_{tot}}{J_{tot}} + K_p\frac{3}{2}\frac{{p_p}^2}{J_{tot}}\psi_{PM}\right) + K_i \cdot \frac{3}{2}\frac{{p_p}^2}{J_{tot}}\psi_{PM}} \tag{5.7}$$

$$K_i = \frac{{\omega_n}^2 \cdot J_{tot}}{{p_p}^2 \cdot \psi_{PM}} \cdot \frac{2}{3} \tag{5.8}$$

$$K_p = \frac{\left(2\xi\omega_n - \frac{B_{tot}}{J_{tot}}\right)}{\frac{3}{2}\frac{{p_p}^2}{J_{tot}}\psi_{PM}} \tag{5.9}$$

## 5.2 Response of the Three Controls

Both OTSR controls were tuned to a matching bandwidth $f = 0.05\ Hz$ and damping factor $\zeta = 1$ . The OTC transient response is governed by the drivetrain inertia and is not controllable. The response of the three controls, for a step change of WT wind speed input from 9 to 10 m/s is shown in Figure 5.3. Please note that the OTSR controls have been tuned to respond quicker than the OTC and when imposing this quick change in rotor speed, there is a transient decrease in the electromagnetic torque of the generator (which is breaking torque).

In Figure 5.3 can be noticed that the OTC controlled WT responds to the wind change more slowly than the other two OTSR controls. The steady-state is reached roughly at the same time because it is led by the system intertias. However, OTSR controls get close (> 90 %) to the final steady-state value more quickly than the OTC, according to their tuned response time. This shorter response time comes with a certain overshoot in rotor speed. More importantly, the quicker response is on account of having a larger torque swing manifested in the shaft, as seen in Figure 5.3. This large torque swing can potentially be problematic and undesirable for the reliability of the mechanical drivetrain, so further adjustments and tuning might be needed, but they are outside the focus of the work here.

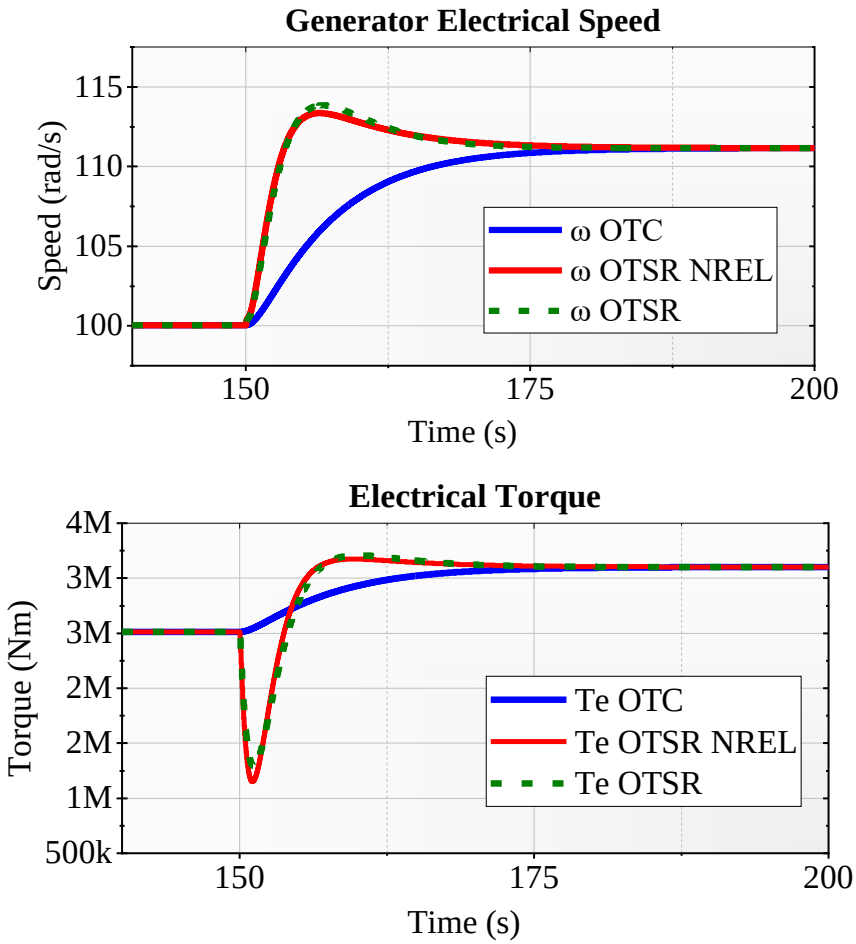


***Figure 5.3: Generator speed step response for wind speed change of 9 to 10 m/s for the three different MPPT control implementations***

## 5.3 Variable Wind Profile and Different Generator Control

A more realistic operation scenario is taken into consideration if the WT model is simulated with a highly variable wind speed input. The used wind profile (1 hour) is shown in Figure 5.4 and is a time-series 1-second resolution data which has been measured at an offshore wind turbine site in the UK. The change in generator electrical speed in this one hour operation for the three control strategies explained in the previous subsection, OTC, OTSR-NREL, and OTSR, is shown in Figure 5.5. The change of some operational quantities including collective pitch of the turbine blades, generator electrical speed, and generator electrical power, are shown in Figure 5.6 (for a clarity, focused to only 30s).

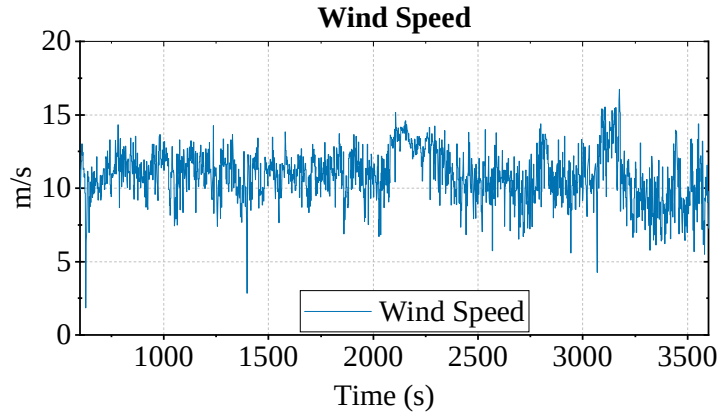


***Figure 5.4: Highly variable wind profile in an offshore site in the UK (November 2018)***

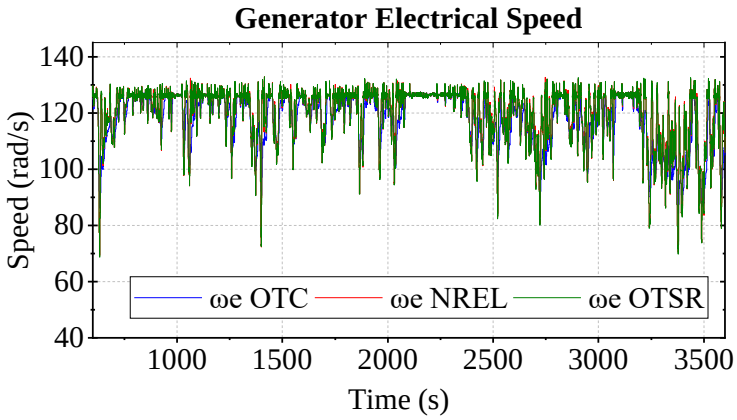


***Figure 5.5: Generator speed change for the variable wind profile.***

## 5.4 Temperature Cycling and Thermal Stress Comparison for the Different Controls

The comparison between the three controls of the WT generator is undertaken in terms of evaluating the difference in thermal stress and consumed lifetime in the converter. This is done by applying the lifetime estimation methodology. The thermal and losses parts of the methodology are used to simulate the junction temperature change as shown in Figure 5.7 where the MSC OTC junction temperature is considered. However, comparing the thermal stress using these time series waveforms does not result in a set of data that allows for obvious evaluation. A better comparison results if the next step, thermal cycle counting using the rain-flow algorithm, is also applied.

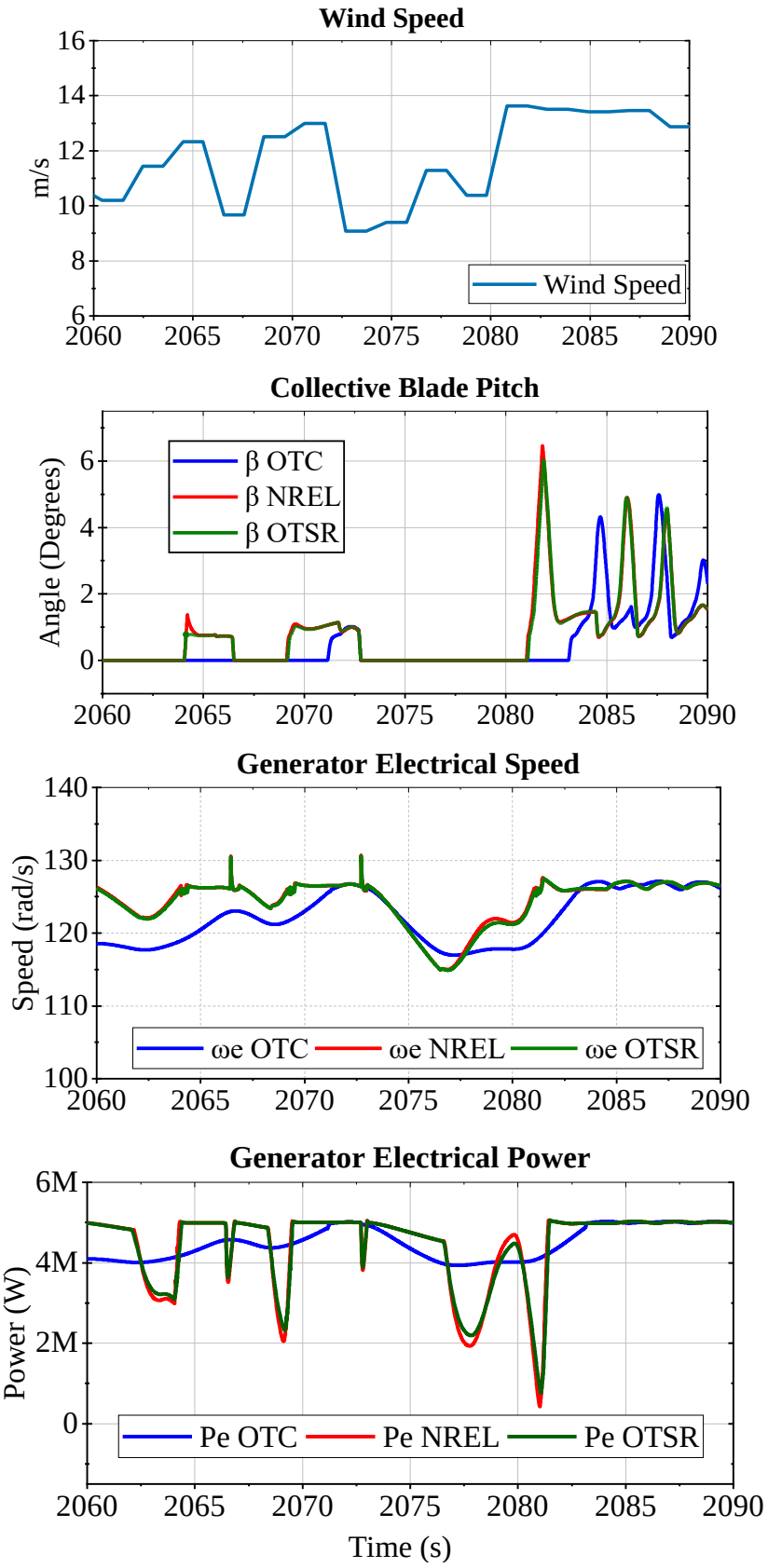


***Figure 5.6: Wind turbine response for the variable wind profile (magnified to show 30s for clarity)***

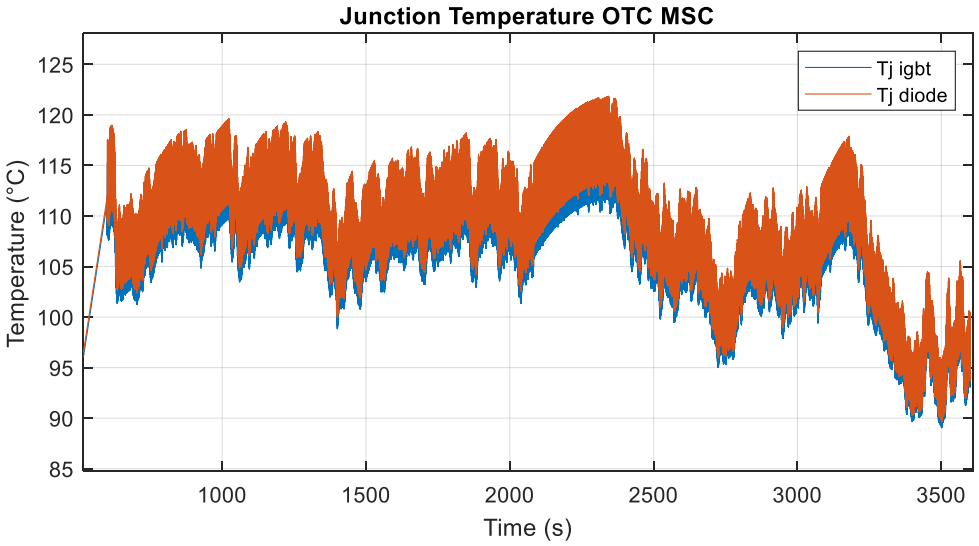


***Figure 5.7: MSC diode and IGBT junction temperature variation for OTC control***

### 5.4.1 Comparison of Thermal Stress Using Counted Junction Temperature Cycles

For the case study in this chapter, a range of comparisons can be made, for combinations between the three different controls, the MSC or GSC, and the diode and IGBT chips. The number of such combinations to compare can be high, thus the most interesting comparisons out of which useful conclusions can be drawn are shown and discussed in this subsection. The comparisons are made by showing histograms of the counted cycles which represent the accumulated thermal stress on the diode and IGBT chips and hence on the bond-wire.

In Figure 5.8 is shown the comparison of counted thermal cycles between the diode of GSC and MSC, when the WT generator is controlled with OTSR method. It is clear that over almost all the spectrum of temperature range, the MSC diode is more thermally stressed and has cycles with larger temperature swing. This conclusion coincides with the observations made in steady-state analysis in chapter 4. The AC frequency cycles – that are present both in steady-state and variable wind (transient) operation – will be concentrated around the two histogram peaks and their distribution in the histogram changes only marginally with changing wind input (shown in Chapter 4 and in Figure 4.16 and Figure 4.17). It is evident in Figure 5.8 that a large portion of the difference in thermal stress between the MSC and GSC is because of cycles that are outside of that AC frequency cycling. Even though the highest number of cycles (the histogram peaks) are AC cycles and outnumber by a large extent the other cycles, because of the non-linearity of the

phenomenon, even a few cycles with significantly larger temperature range (to the right of the histogram peak), outweigh the lifetime impact of tens of thousands of cycles with lower amplitude [131]. This is because a large portion of the thermo-mechanical effect of these small cycles is elastic, therefore the accumulated degradation (plastic part) of the bond-wire connection is minor [67].

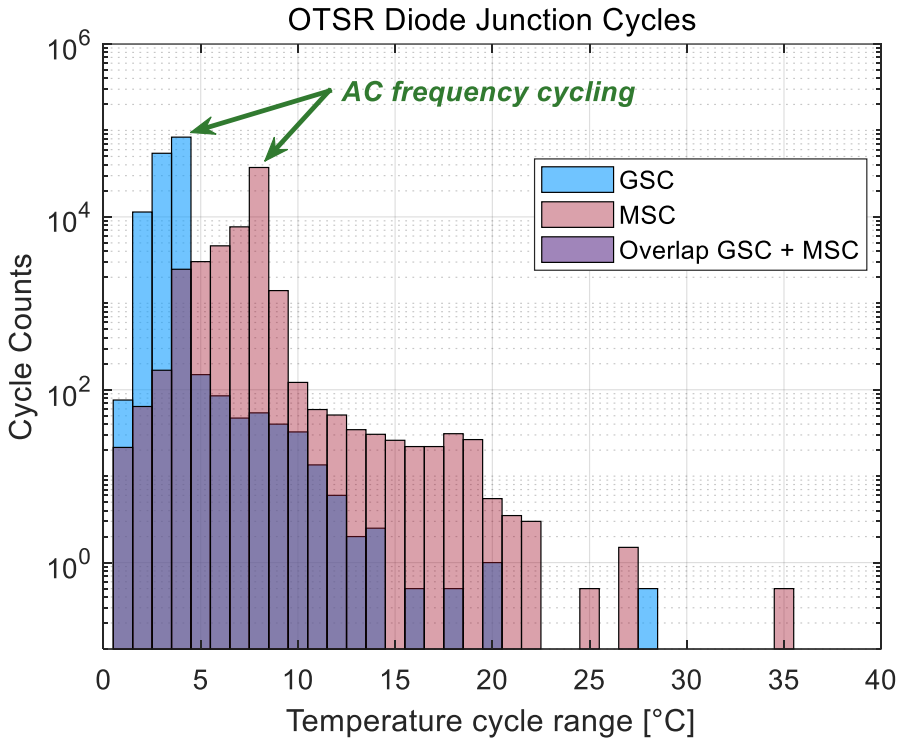


***Figure 5.8: OTSR, diode cycle count histogram GSC vs MSC (range)***

An additional parameter that impacts the stress apart from the swing range, is the mean temperature of the counted cycles. The histograms of the counted cycles against their mean temperature for the same GSC vs MSC comparison from Figure 5.8 are shown in Figure 5.9. It can be seen that even on this basis, the MSC diode cycles have a larger mean temperature. In essence, as seen from the shift of the whole histogram compared to the GSC, this mean temperature difference is reflected in the same way for all the cycles and can also be recognized from observing the steady state cycling only. However, in Figure 5.9 is also apparent the large difference in total number of cycles between the GSC and the MSC, where the former has a substantially larger number of counted cycles, mainly because the AC grid frequency is more than two times larger than the rated frequency of the generator stator current.

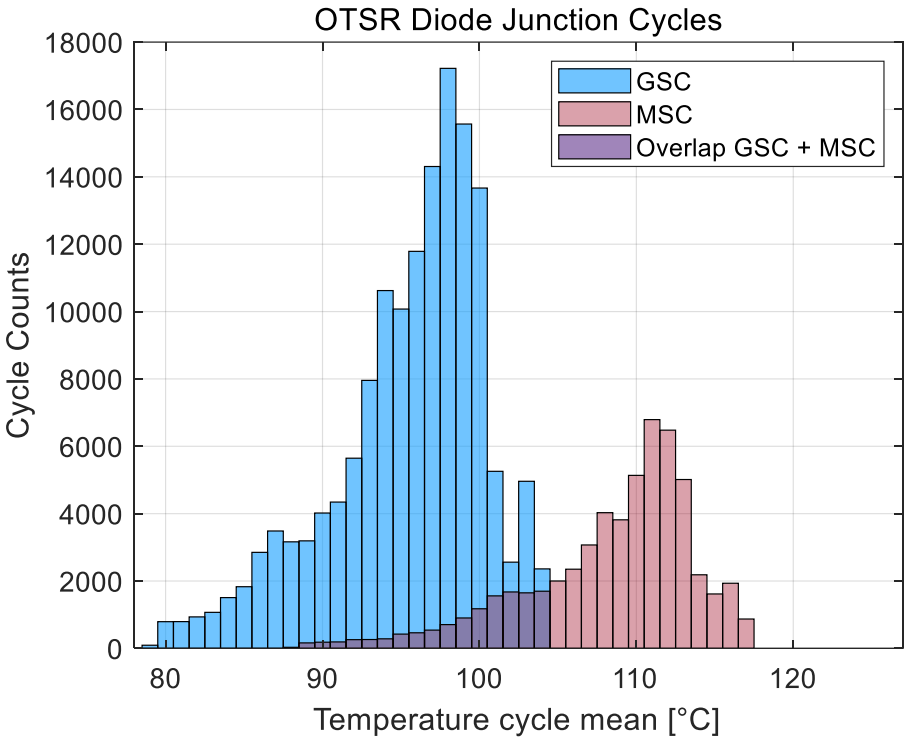


***Figure 5.9: OTSR, diode cycle count histogram GSC vs MSC (mean)***

Another comparison that is interesting to be shown using the cycle histograms is between two different control strategies. In Figure 5.10 and Figure 5.11 are shown histogram comparisons (cycle range and mean respectively) between OTC and OTSR control for MSC diode junction cycles. In Figure 5.10, first it can be seen that there is a significant overlap at the range of cycles where the AC frequency cycling is concentrated – at and around the peak of the histograms at 8 °C. The overlap of these cycles is because they are barely affected by the change in the torque control of the generator, and these cycles are dependent mainly from the AC frequency and the transfer of current between the IGBT and antiparallel diode, which remain unchanged.

Another aspect that requires attention in the comparison in Figure 5.10 between the OTC and OTSR, is the fact that these controls differ only in the transient response, while in steady-state they are anticipated to reach the same value (see Figure 5.3). This observation gives two important suggestions:

a) Any difference in thermal stress and lifetime that is observed in the control comparisons is because of the different transient response of these controls.

b) If the difference in a) is significant, then lifetime estimation methods need to find a way to take into consideration the transient operation of the system in order to be complete, accurate, and provide useful lifetime calculations.

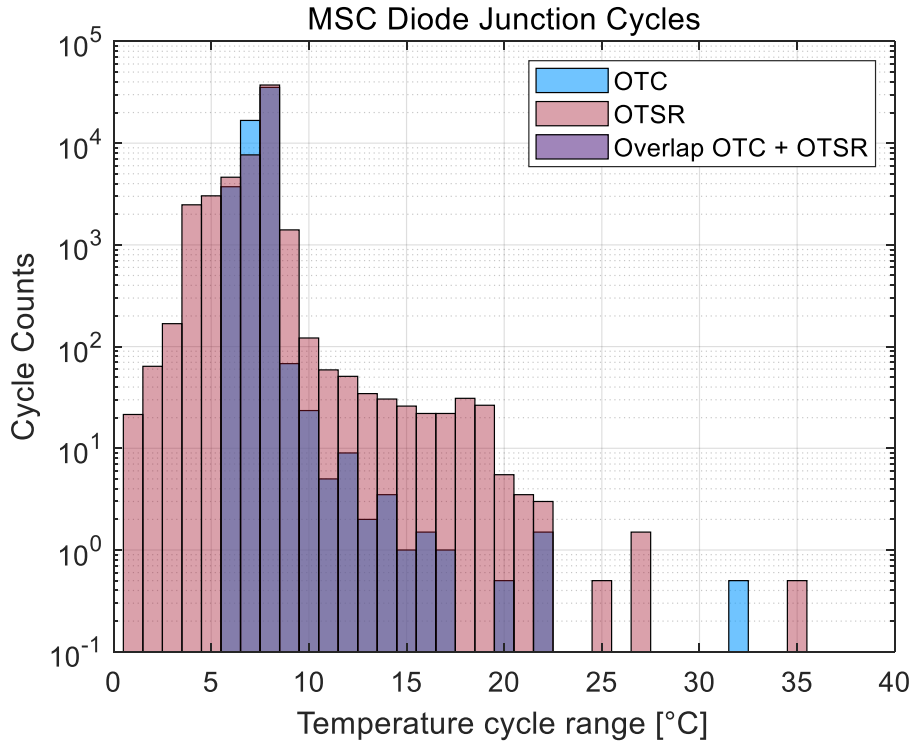


***Figure 5.10: MSC, diode cycle range histogram OTC vs OTSR (range)***

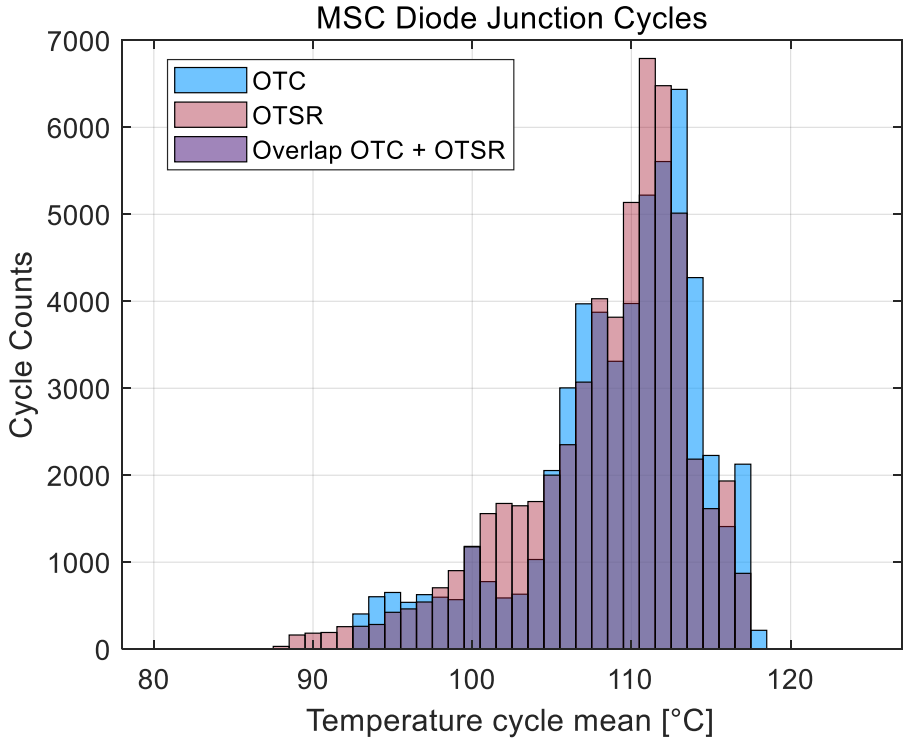


***Figure 5.11: MSC, diode cycle range histogram OTC vs OTSR (mean)***

The difference between the OTC and OTSR thermal stress cycles as observed in Figure 5.10 is substantial, with the exception of cycles with a range around the steady-state (histogram peaks) – how important this difference is will be evaluated more precisely using the lifetime consumption after which the significance of the difference and the suggestion b) from the paragraph above will be reviewed.

Another difference that can be seen in Figure 5.10 is that for OTSR control there is a presence of some smaller cycles, down to 1 °C. This is because of the quicker response of the OTSR which can pick up some of the higher frequency changes in the wind input, while the slow response of the OTC filters out the same changes.

For the same comparison from Figure 5.10, MSC diode OTC vs OTSR, in Figure 5.11 is shown the distribution of the counted cycles against their mean temperature. In this case, the distribution of the OTC and OTSR cycles against mean temperature in general is more similar, apart from some difference in the number of cycles in particular bins still being present. No obvious conclusion can be noticed in this comparison.

It was identified from steady-state that the most stressed chip on the MSC side is the diode, while on the GSC it is the IGBT. Therefore, comparing the most thermally stressed chips from each converter is another comparison that can be of interest. Such a comparison is shown in Figure 5.12 and Figure 5.13 for the case of OTSR control. As expected, these histograms confirm that the MSC diode is more thermally stressed.

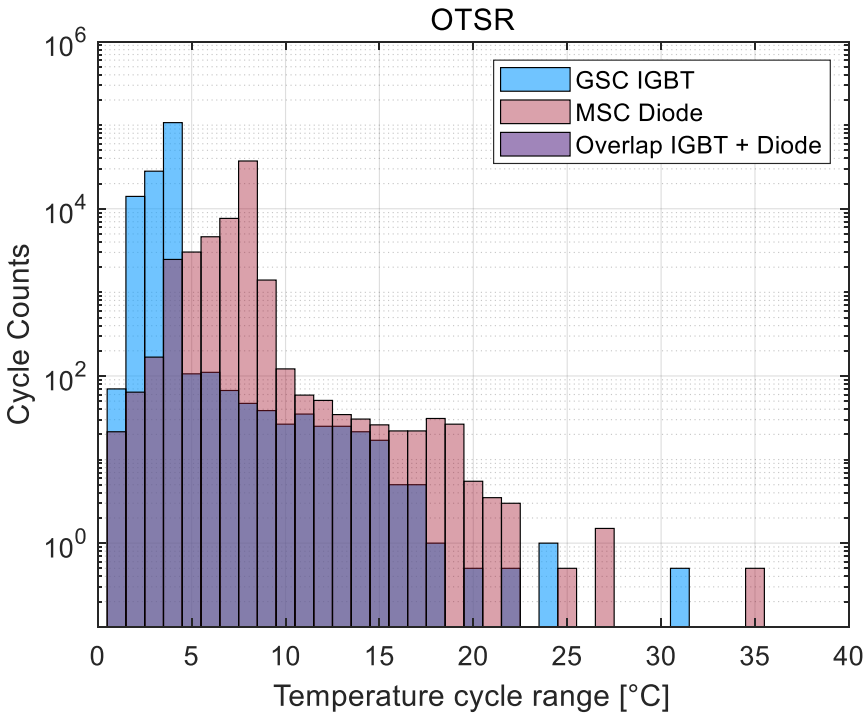


***Figure 5.12: OTSR, cycle count histogram of most thermally stressed chips, GSC IGBT vs MSC Diode (range)***

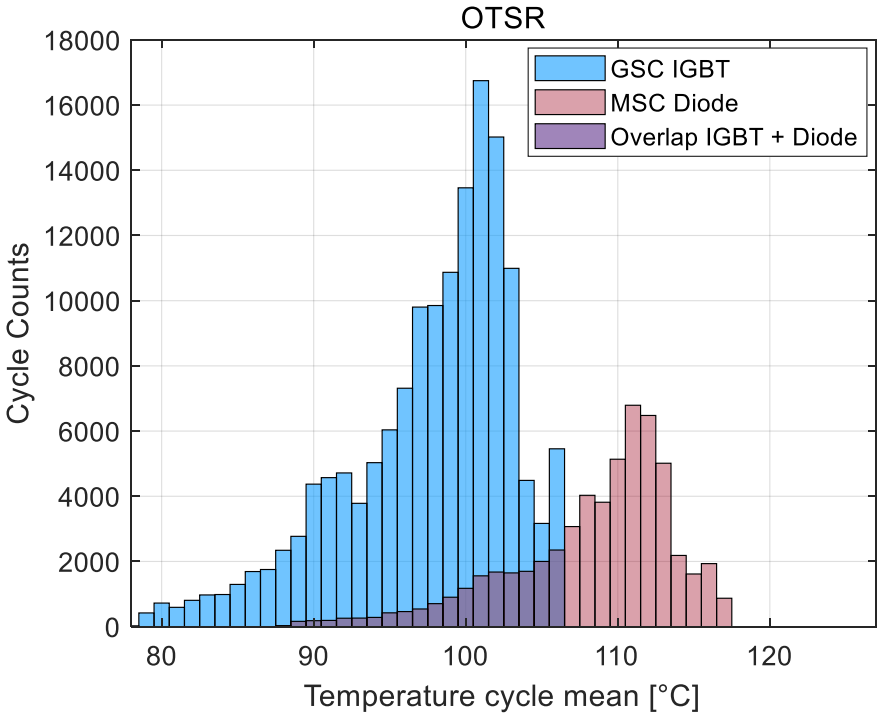


***Figure 5.13: OTSR, cycle count histogram of most thermally stressed chips, GSC IGBT vs MSC Diode (mean)***

### 5.4.2 Comparison of Estimated Lifetime Consumption

The thermal stress in the previous sub-section was observed based on the histogram comparison of the counted cycles. However, while using such means of comparison, it is difficult to come to any quantitative lifetime evaluation of all considered scenarios. Therefore, adding the final layer of the lifetime evaluation method provides an opportunity for easier and more precise comparison.

The estimated lifetime consumption for 50 minutes of operation with the highly variable wind profile and for the different chips and torque control strategies is shown in Figure 5.14. The consumed lifetime is shown in percent of nominal ($B_{10}$) lifetime. Given that the operation is for only 50 minutes – limited by the computational burden of the detailed model – these lifetime calculations are more suitable if used as a proxy for comparing relative lifetime between each other, rather than to assess the absolute lifetime of the converter. The accurate absolute lifetime calculation would require consideration of other relevant aspects that come with analysing longer timeframes such as the seasonal change in mission profile. Additionally, the relative comparison means useful conclusions can be made from the comparison regardless of any bias or inaccuracy of the lifetime calculation because of scarcity of data and information.

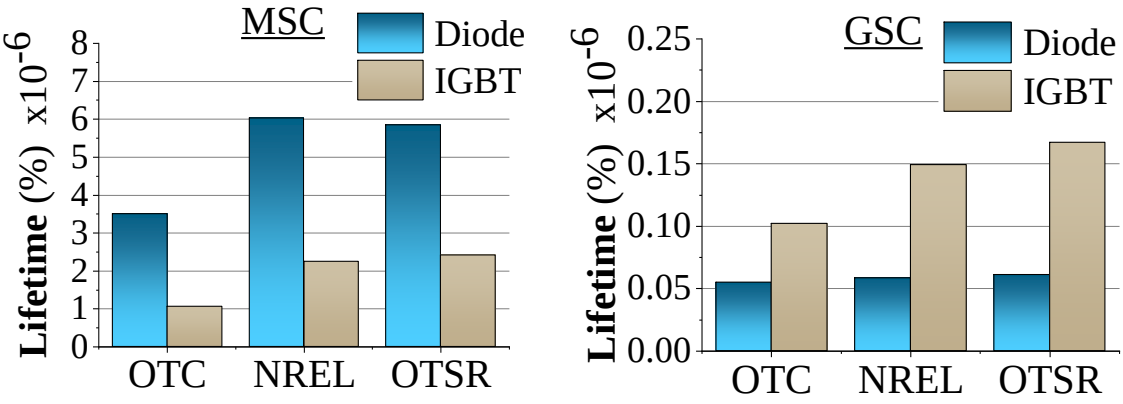


***Figure 5.14: Comparison of the lifetime consumption of both chips in MSC and GSC and for all three different controls (for operation of 50mins)***

From the overall observation of the calculated lifetimes in Figure 5.14 can be seen that when translated to lifetime consumption, the difference in thermal stress that was observed qualitatively previously, is translated in the MSC having more than 10 times larger lifetime consumption than the GSC. The MSC diode is still the most stressed chip, especially in the NREL and OTSR controls.

Another interesting factor is the difference in lifetime consumption between the different controls. The lifetime difference for the MSC diode between operations with OTC and the other two OTSR controls is almost 100%. This large difference is interesting because the controls differ only in terms of their transients, and have the same steady-state output. Normally, lifetime estimation models have modelled the WT operation with a high degree of approximation, and do not take into account these transient control aspects at all. For improving the accuracy of the lifetime evaluation based on thermal cycling, suggestions such as more detailed thermal networks have been considered [75]. However, as seen from the results here the WT operational aspects and transients resulting from the control design have a large impact, and their omission can mean a large over- or under-estimation of the lifetime. Therefore, large improvements of converter lifetime models can be made while focusing on the first layer (WT model) of the approach and while paying attention to prioritise the most important factors, including the transients.

## 5.5 Lifetime Evaluation with Reactive Power Control of Grid Side Converter

Depending on the configuration and the requirements of the wind farm, there may be additional factors affecting the operation of the GSC as well as the WT integration to the grid. In the results in the previous subsection, the grid model was assumed to be 'stiff' with unchanging voltage and frequency and no additional requirement of reactive power or frequency support from the WT was needed. This scenario might represent an offshore wind farm where the wind farm array voltage is regulated by the offshore MMC HVDC converter. However, depending on the configuration and wind farm layout, it is not uncommon for the WF operators to demand additional requirements from WTs, such as reactive power compensation [132]. Additionally, it is highly likely that the WTs would need to provide reactive power for the wind farm array. In this subsection is discussed how this additional requirement of reactive power can affect the thermal stress and lifetime of the converter.

In the previous analysis in this chapter the operation was with no reactive power transfer between the grid and the inverter (GSC). The phasor diagram for that operation is shown in Figure 5.15 a), where unity power factor connection with grid is realized i.e. $\cos\theta = 1$, where $\theta$ is the angle between grid voltage $V_G$ and the current flowing to the grid $I_G$. In this sub-section, the other scenarios with reactive power flow between the GSC and

the grid are considered. The corresponding phasor diagrams for these cases are shown in Figure 5.15 b) and c), for reactive power flow from inverter to the grid and from the grid to the inverter, respectively. $V_{inv}$ is the voltage at the inverter terminals, $V_L$ is the voltage drop across the inductance element L which represents the total inductance of the connection between the inverter and the grid, $V_G$ is the grid voltage, $\delta$ is the angle between $V_{inv}$ and $V_G$, $I_G$ is the current flowing between the inverter and the grid, $I_P$ is the component of the grid current $I_G$ that is in phase with $V_G$, and $I_Q$ is the component of the grid current that lags the grid current by 90 degrees. Component $I_Q$ of the current is responsible for the reactive power in the system. If $I_Q$ is lagging $V_G$ and $I_P$ by 90 degrees as in Figure 5.15 b), the reactive power is positive flowing from the GSC to grid and $|V_{inv}| > |V_G|$; while, when $I_Q$ is leading $V_G$ and $I_P$ by 90 degrees as in Figure 5.15 c), then reactive power is flowing from the grid to the inverter and $|V_{inv}| < |V_G|$.

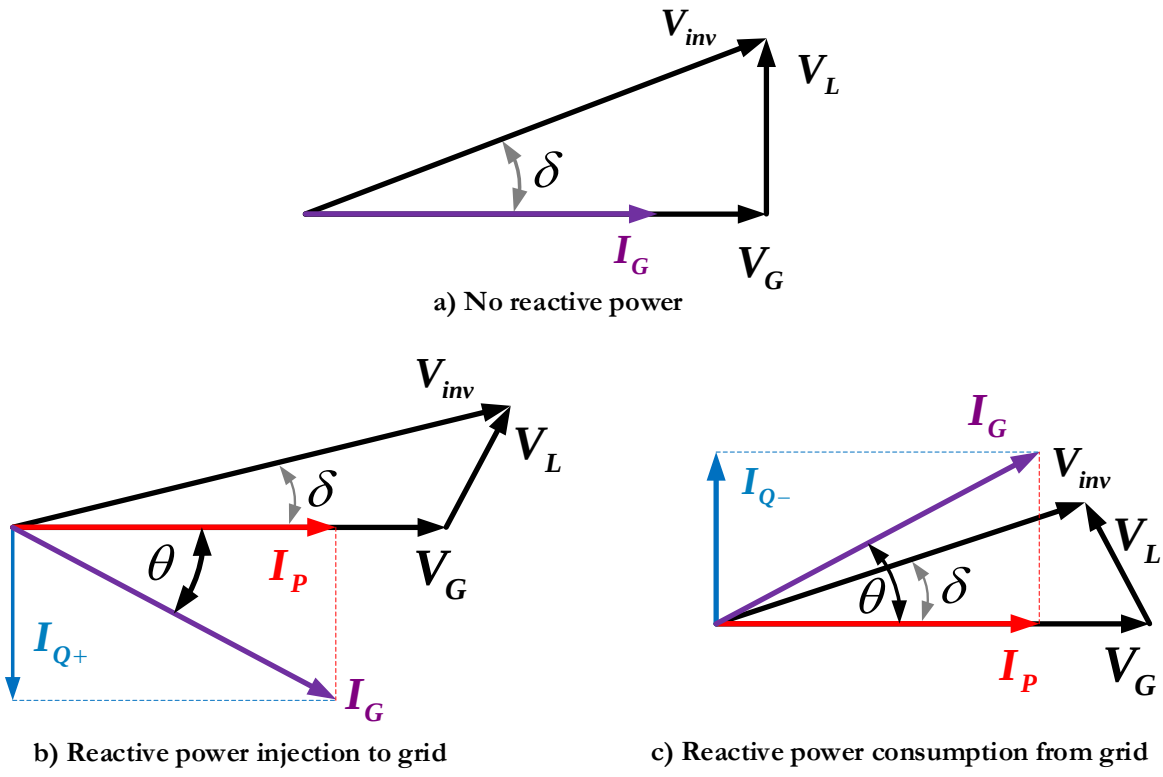


***Figure 5.15: Phasor diagram of GSC operation for a) No reactive power flow; b) Reactive power injection to grid from inverter; c) Reactive power consumption from grid to inverter***

As seen from the phasor diagrams, the flow of reactive power, compared to no reactive power operation, means a phase shift as well as an increase in magnitude for the resulting current flowing through the converter to the grid. This change for the current $I_G$ is directly

reflected in the losses and the temperature cycling of the converter IGBT phase modules, which is the focus of interest of this study.

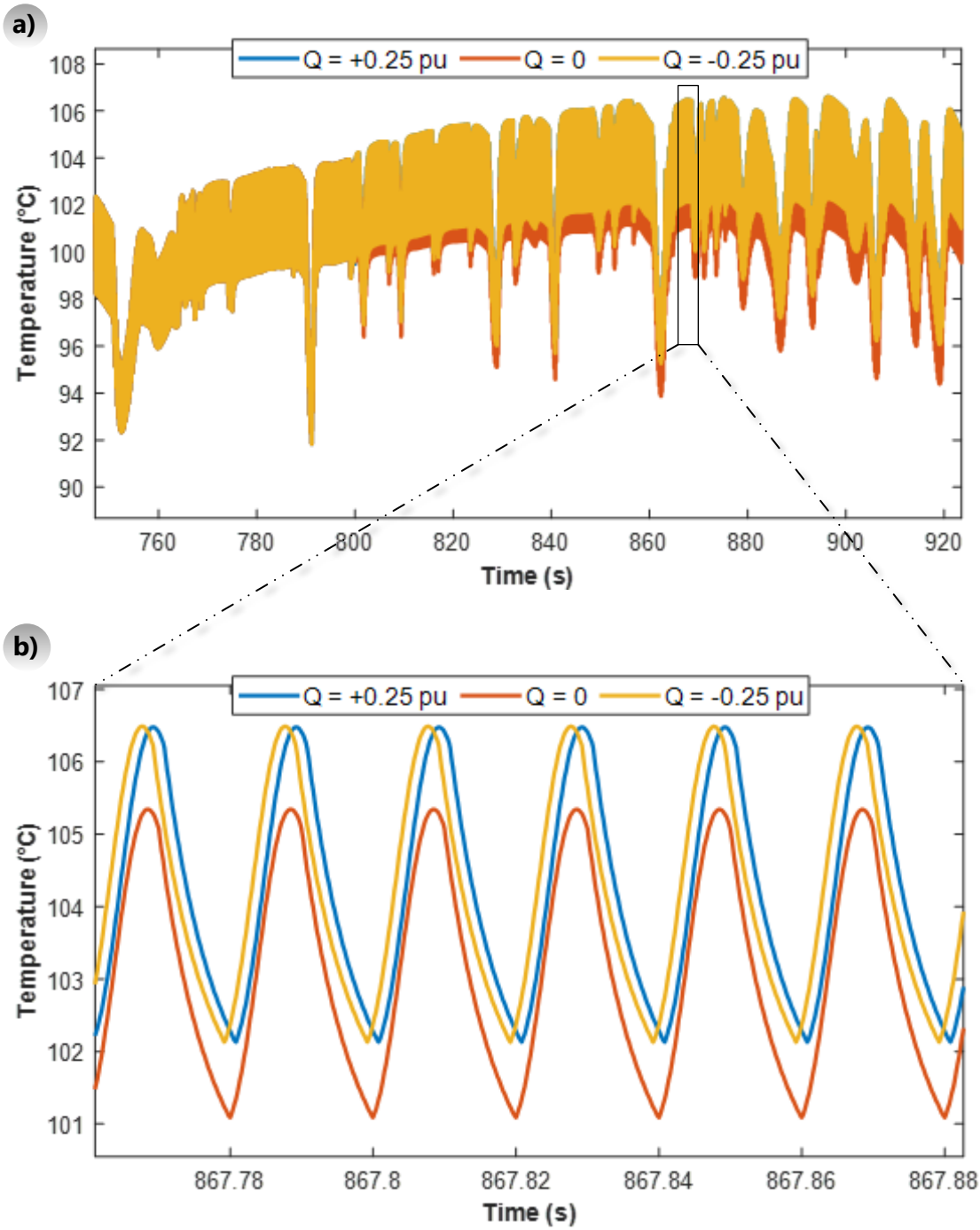


***Figure 5.16: Junction temperature change of GSC IGBT for variable wind operation. At t = 800s step increase from zero to ±0.25 pu of reactive power transfer between GSC and grid***

In Figure 5.16 is shown the GSC IGBT junction temperature cycling when reactive power of 0.25 pu is injected/consumed to/from grid, starting from t = 800s – additional to the previously observed scenario with no reactive power consumption. From Figure 5.16 a)

can be seen how after the change in reactive power t = 800 s, the average junction temperature of the IGBT increases compared to the case with Q = 0. This increase is due to the increase in magnitude of the current. We are considering two cases with a positive and negative reactive power injection of equal magnitude 0.25 pu. The reactive power values of +/- 0.25 pu, which correspond to a power factor of around 0.97 for rated WT active power generation, were chosen arbitrarily; but represent an order of magnitude of reactive power capability that is expected from commercial wind turbines [50]. The effect of both these cases on the magnitude of the resulting current is effectively the same, therefore the increase in the average cycling temperature in Figure 5.16 is effectively the same when the GSC is injecting and consuming reactive power – this is more clear in the magnified plot in b), where it is apparent that the blue and yellow waveforms cycle around the same mean temperature. This suggests that as far as the average temperature rise in the thermal loading of the converter is concerned, only the magnitude – which contributes to an increase of the total conducted current through the converter – is significant, and not the direction of the reactive power. In general, the direction may be significant for converter losses at higher reactive power flows and for other network impedances, since the inverter voltage varies slightly with reactive power direction and this can have an impact on current and losses. The case here however suggests that this effect may be moderate.

In Figure 5.15 is also illustrated the other effect of the reactive power: the resulting phase shift of the current as a consequence of the increased reactive power flow. In this case the direction of the reactive power is important as seen from comparing phasor diagrams in Figure 5.15 b) and c). In these phasors, a positive flow of reactive power Q (and current $I_{Q+}$ contributing to positive reactive power) is defined from the GSC to the grid, while negative Q is from grid to GSC. With these assumed directions, a positive reactive power flow makes the current $I_G$ lag behind the voltage output of GSC (inductive mode), while a negative power flow makes $I_G$ lead $V_{inv}$ (capacitive mode). It should be noted here that for option a) in Figure 5.15, the GSC is still operating marginally in inductive mode to supply for the low voltage drop $V_L$ across the connecting inductance while unity power factor ($\cos\theta = 1$) of the grid connection is enabled. The phase shift in the current is directly reflected in the conduction of the IGBT and the diode in a phase module, and consequently in the thermal loading and junction temperature. This effect can be clearly seen in Figure 5.16 b), where corresponding to the phasor diagrams from Figure

5.15, the junction temperature cycling accordingly has a leading or lagging phase compared to the case with Q = 0, depending on the direction of the reactive power flow.

From the discussion and observation of the temperature cycling waveform was seen that the difference between the cases with inductive and capacitive reactive power transfer was a phase shift of the cycling waveform which corresponds to the phase shift in the current at the considered phase leg of the converter. Other characteristics of interest, including the rise in average temperature as well as the range of the temperature cycling seemed identical between the inductive and capacitive mode. This similarity of the average temperature and the range of cycles can be confirmed by applying the rain-flow algorithm. This comparison has been undertaken and the resulting range and mean cycle histograms have been confirmed to be matching – shown in Appendix 9.5. Thus, in Figure 5.17 and Figure 5.18 is shown the comparison between the scenarios with Q = 0 and Q = + 0.25 pu, keeping in mind that the histograms of the latter are identical with the Q = - 0.25 pu scenario.

The histograms in Figure 5.17 show that the reactive power flow contribution to the change in temperature cycles of AC frequency (around histogram peak of 5 °C) is insignificant. However, in the histogram comparison can be seen that a noticeable difference is present in the other cycles, mainly with a larger range. According to the results, when there is a reactive power flow of 0.25 pu from the GSC to the grid, the range of the large temperature cycles in the IGBT is lower than in the case of unity power factor operation. These larger cycles are mostly a result of the wind input change and the fluctuation of the real power generated from the WT. The constant reactive power output of 0.25 pu that is added contributes to a share of the total converter power loading which is reflected to losses and thermal loading for the IGBT module. Therefore, the fluctuation of the active power resulting from the wind change becomes a lesser share of the total power module thermal loading compared to the scenario with $\cos \theta = 1$. For this reason, the same real power fluctuation coming from the WT generator, results in smaller temperature swings of the IGBT power module when there is an additional supply of reactive power.

From the histograms in Figure 5.18 can be confirmed the observation that although the reactive power transfer diminishes the range of the thermal cycles, it increases the absolute average junction temperature of the observed cycling. This increase is consistent for all

cycles including the smaller AC frequency cycles (peak of histogram) – different from the comparison of cycling range where these cycles did not encounter much difference compared to Q = 0 operation.

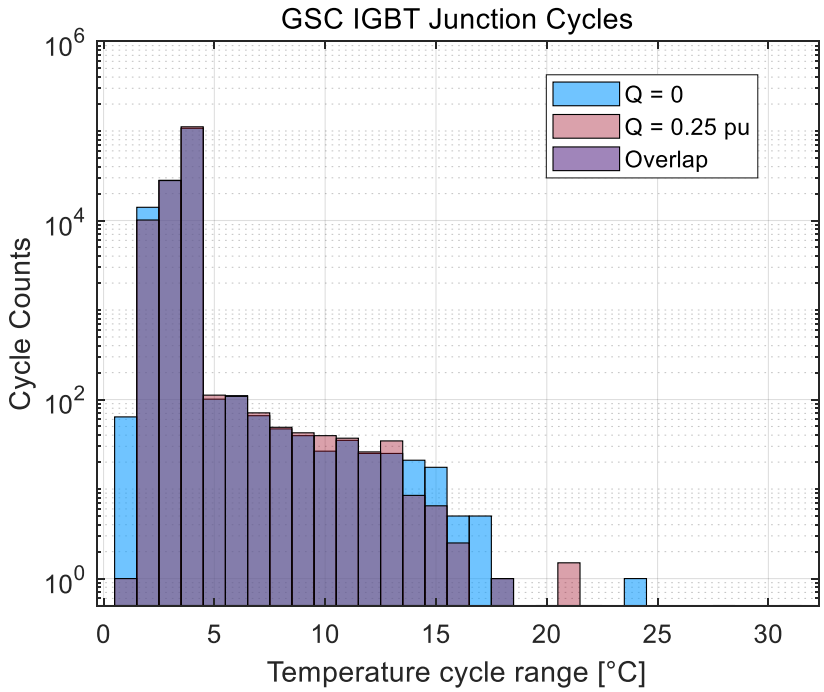


***Figure 5.17: Cycle count histogram of GSC IGBT OTSR: comparison between Q = 0 (unity power factor) and Q = 0.25 pu (lagging power factor) operation (range)***

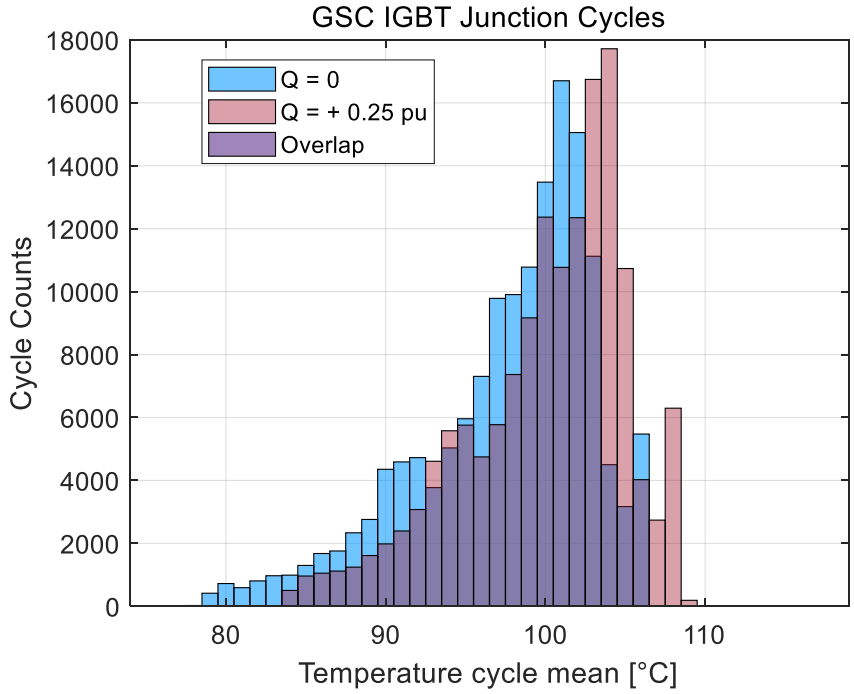


***Figure 5.18: Cycle count histogram of GSC IGBT OTSR: comparison between Q = 0 (unity power factor) and Q = 0.25 pu (lagging power factor) operation (mean)***

Finally, the comparison between the basic cos $\theta = 1$ and the other two scenarios with a leading and lagging power factor can be undertaken in terms of consumed lifetime. The results of the GSC IGBT lifetime for the considered 50 minutes operation with highly variable wind profile and when the WT is controlled using the OTSR control are plotted in Figure 5.19. These results confirm the previous conclusions made from observing the temperature cycling and the thermal stress, where because of the effect that reactive power transfer has on reducing the range $\Delta T$ of the larger cycles, it results in less aging and fatigue of the IGBT module. This is true even though there is an increase in the absolute value of IGBT losses and mean junction temperature $T_m$, since $\Delta T$ has a larger effect on degradation than $T_m$. The direction of the reactive power flow makes no significant difference in consumed lifetime.

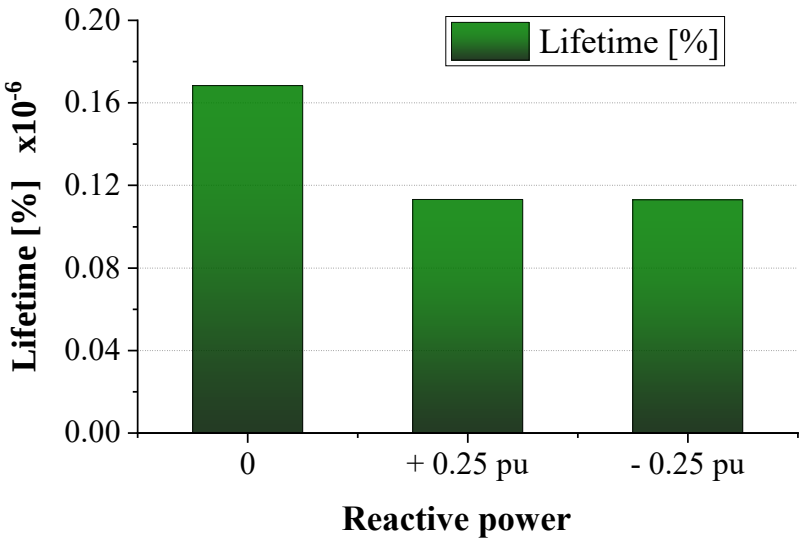


***Figure 5.19: Lifetime consumption comparison – reactive power flow for OTSR GSC IGBT***

## 5.6 Summary

In this chapter the thermal stress and lifetime estimation methodology developed in previous chapters was applied to a range of scenarios with different control setup when the WT is operating under variable mission profile. Initially, the lifetime evaluation methodology was applied to assess the difference in thermal loading and lifetime consumption between three different control strategies of the WT generator. An optimal torque control (OTC) strategy which proportionally adjusts the rotor torque for changing shaft speed was compared against two other more complicated optimal tip speed ratio (OTSR) methods which apply PI feedback control and can be tuned for quicker response.

After applying the complete methodology it was observed that in terms of converter reliability, the smoother OTC control is the most optimal design choice and best control option. It was also observed that the calculated thermal stress and lifetime consumption can have a substantial difference when two controls with different transient response characteristics are compared. This large difference suggests that transient cycling has a significant effect on the lifetime consumption. However, it should be additionally noted that the OTSR methods could be tuned to have a slower response which would be closer to that of the OTC – such an analysis additionally depends on other drivetrain design choices and could be further investigated. It was concluded that in order to provide useful and accurate assessment, lifetime evaluation models need to include higher detail in the WT operational side and account for the operational transients.

Finally, additional to the comparison between different control methods on the generator side of the WT, the effect of the reactive power control for the grid side converter on the converter lifetime consumption and thermal stress was also considered and simulated. It was observed that reactive power flow, regardless of the direction, can reduce the range of the thermal cycles which are a consequence of the real power fluctuation, and therefore the resulting lifetime consumption is also reduced. Adding reactive power injection or consumption however increases the absolute (average) junction temperature, so attention needs to be paid to not thermally overload the converter above the maximally allowed junction temperature.

# 6 Model Order Reduction: Converter Lifetime Estimation for Longer WT Operation Periods

In the previous chapters a detailed methodology for evaluation of lifetime consumption in IGBT modules in WT converters was developed. Various analyses were undertaken using this model. A detailed mission profile was used to define the WT operation in the analysed cases. The high level of detail that was included, allowed changes and transients of different frequency and magnitude to be observed. This established an approach that allows modelling the failure mechanism of interest while evaluating a wider range of factors which may affect the thermal degradation of IGBT modules. However, one downside of the highly detailed analysis is the difficulty of implementation and the computational burden of the simulation model which limits the practical time-length of the WT operation (wind speed profile) that can be analysed.

In order to reduce the computational burden and the complexity of the simulation model, an optimisation of the simulation and a model order reduction approach are necessary. Reducing the computational complexity in the simulation built in this thesis is necessary for running the lifetime analysis for longer WT operational time. Additionally, if the methodology would operate in real time as a digital twin concept of the WT, the computational cost needs to be most optimal. The possibilities of undertaking this model order reduction at different parts of the lifetime estimation methodology are considered in this chapter. A further reason for simplifying the methodology, is to make the model more convenient to parametrise and apply in different operational WTs. Different options for the model simplification are first discussed below. Then the lifetime consumption and accuracy for a number of reduced models based on these options is assessed. In the end, for a chosen reduced model which has an acceptable accuracy, the lifetime consumption analysis is undertaken for a longer WT operating period: a 24 hour period of measured wind speed data at a UK offshore site.

## 6.1 Contribution of Different Cycles to Total Consumed Lifetime

For one of the torque control strategies considered in Chapter 5 (NREL control), the junction temperature cycles in the MSC Diode for one hour operation (as analysed in

Chapter 5) are shown in Figure 6.1. The contribution to the lifetime consumption that was caused by these cycles is shown in Figure 6.2 and Figure 6.3. The distribution of the percentage of consumed lifetime that is contributed by cycles with different ranges and different average temperatures is depicted. It can be observed that the lifetime effect of the cycles of different range ΔT is not distributed proportionally to the absolute number of observed cycles: a small number of cycles which have a larger ΔT contribute to a disproportionally larger amount of lifetime consumption compared to the much larger number of cycles with a lower ΔT [131].

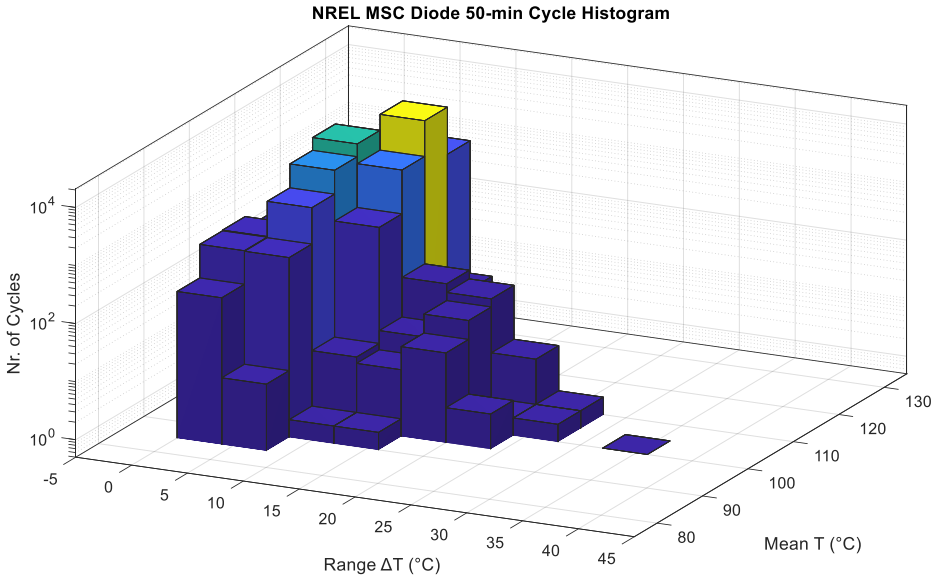


***Figure 6.1: Histogram of counted cycles against cycle temperature range ΔT and mean $T_m$***

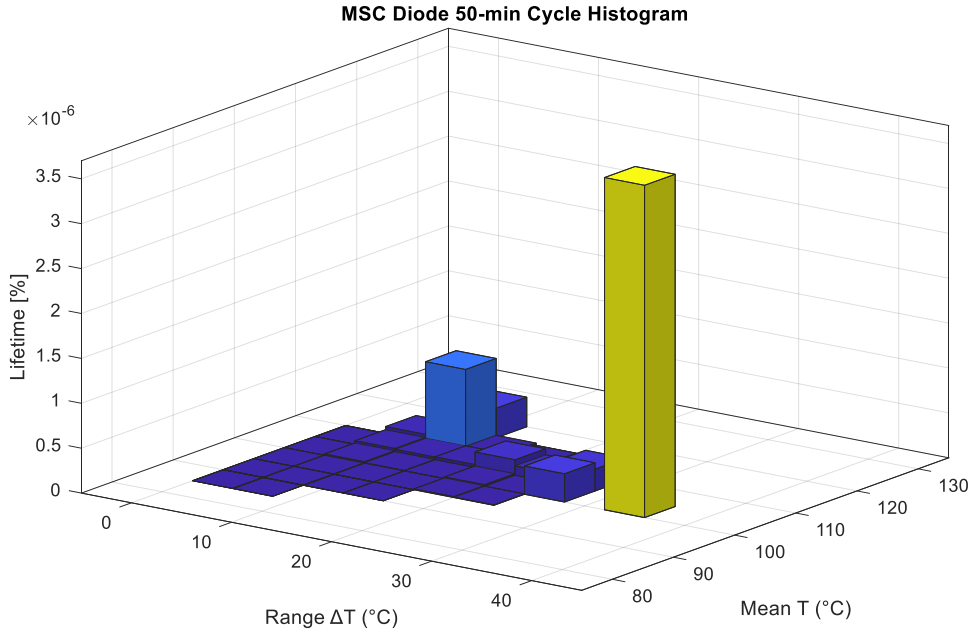

***Figure 6.2: Histogram showing the lifetime consumption contribution by the cycles with different $\Delta T$ and $T_m$.***

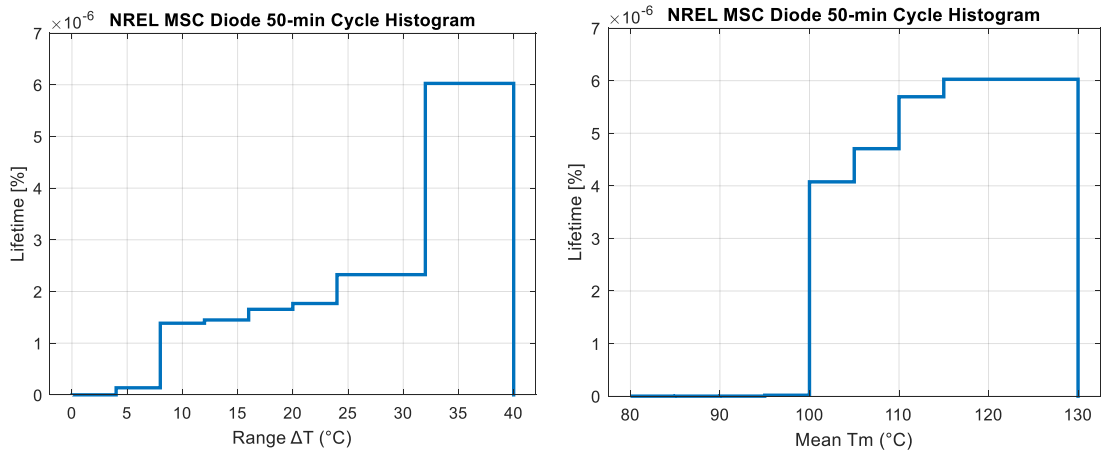


***Figure 6.3: Cumulative lifetime contribution of cycles with different $\Delta T$ (left) and $T_m$ (right)***

From Figure 6.2 can be seen that for the analysed period, the lifetime is dominated by two bins of the histogram, with a certain temperature range $\Delta T$ and temperature mean $T_m$. Thus, the major contributors (cycles) to the shown (specific) lifetime consumption can be visually identified in the results of the analysis given through the histogram representation. And if the effect of the other 'minor' cycles is subtracted, the calculated lifetime would still be within a reasonable accuracy for the intended study. However, running the full detailed analysis and then ignoring part of the results is not really beneficial from a modelling point of view and does not give any reduction of the complexity or effort.

It would be beneficial if we could simplify the actual WT and the thermal model (Chapters 3 and 4 respectively) so that the cycles that dominate in the contribution to the total lifetime consumption are simulated or closely approximated while the others are not. This would have been a more straightforward task if each of the produced cycles seen in the histogram Figure 6.1, could be linked to a particular dynamic of the WT and converter model. This is frequently undertaken is other systems where a particular effect is due to a specific frequency range. However, this is not the case here where lifetime is produced by a large temperature change which is not necessarily part of a cyclic phenomenon. In the case examined in the WT every produced cycle in the junction temperature of the chips is a result of the interaction of all included factors starting from the wind profile up to and including the details in the loss calculation of the semiconductor devices. Therefore, the model order reduction needs to be done much more carefully and by undertaking a

thorough analysis before adding an acceptable degree of approximation for the simulated dynamics.

For the sake of simplification, the condensed analysis in the rest of this chapter is reduced to analysing the MSC only. This simplification is done given that in all of the analyses in the previous chapters, it was shown that the MSC is more thermally stressed than the GSC – therefore it is reasonably prioritized as an indicator for the thermal degradation of the entire converter.

It is expected that any simplification and reduction on the WT and converter thermal models, will result in a change on the simulated thermal stress of the IGBT module and therefore the final result of the methodology i.e. the calculated lifetime. The goal of this chapter is to consider how much of this reduction and simplification of the model can be made without getting results that are too inconsistent or have a large error compared to the most detailed model that was applied in the previous chapters. The actual purpose in doing this is to be able to simulate WT operation for a longer time period in which the converter lifetime will be evaluated with optimal processing capability and memory.

## 6.2 Complexity and Detail of the Converter Losses and Thermal Model

### 6.2.1 Losses and Temperature Simulation – Average and Instantaneous Losses

As explained in previous chapters, correctly building and applying the losses model using the equations requires attention to the VSC operation, starting from the current directions and the duty ratio variation. In Chapter 4, the loss equations for the diode and the IGBT were derived. The instantaneous losses were calculated (equation (6.1) for conduction losses). From the instantaneous losses, and while considering the operational properties of the VSC, the expression for the average losses was also derived as in (6.2). The equations for averaged losses are averaged over one AC cycle of conduction. A similar expression is derived for the average switching losses as given in (6.3).

$$P_{con}(i_c, T_j) = \overbrace{(k_0 + k_1 \cdot T_j)}^{V_{CE0}(T_j)} \cdot i_c + \overbrace{(m_0 + m_1 \cdot T_j)}^{r_{CE}(T_j)} \cdot i_c^2 \tag{6.1}$$

$$P_{\text{av, cond}}\left(T_j\right)=\frac{1}{2}\left(V_{\text{CE0}}\left(T_j\right)\cdot\frac{\hat{\text{I}}_{\text{c}}}{\pi}+r_{\text{CE0}}\left(T_j\right)\cdot\frac{\hat{\text{I}}_{\text{c}}^{\,2}}{4}\right)+$$
$$+m\cdot\cos\varphi\cdot\left(V_{\text{CE0}}\left(T_j\right)\cdot\frac{\hat{\text{I}}_{\text{c}}}{8}+\frac{1}{3\pi}\cdot r_{\text{CE0}}\left(T_j\right)\cdot\hat{\text{I}}_{\text{c}}^{\,2}\right) \quad (6.2)$$

$$P_{sw,avg}=f_{sw}\cdot E_{sw,avg}\cdot\left(\frac{V_{cc}}{V_{cc}^{ref}}\right)^{K_{v1}}\cdot\left(1+K_{T,sw}\cdot\left(T_j-T_j^{ref}\right)\right) \quad (6.3)$$

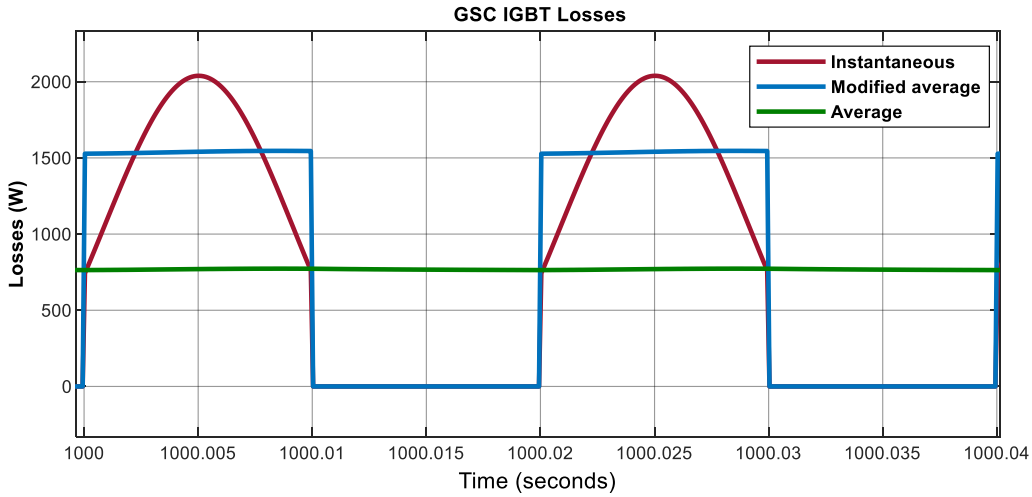


***Figure 6.4: Inverter operation IGBT losses***

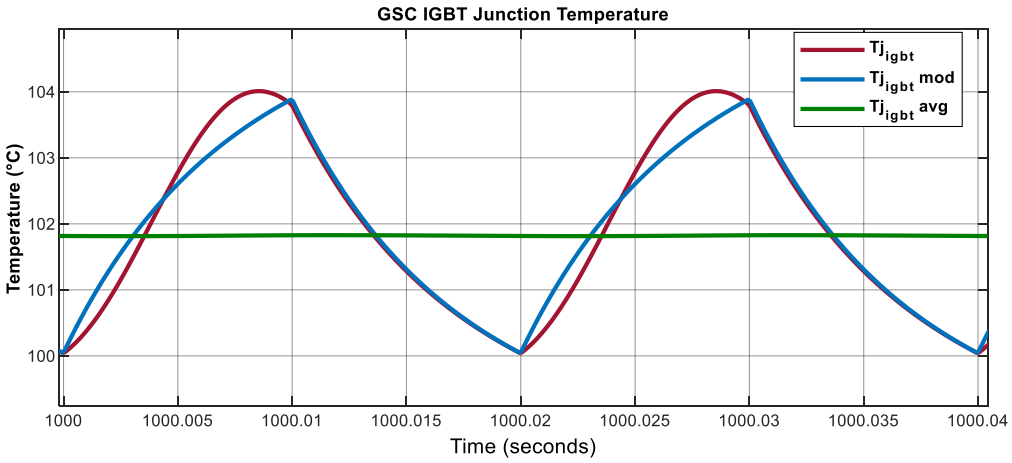


***Figure 6.5: Inverter operation IGBT junction temperature***

In a time-series simulation, these two different analytical models for instantaneous and average losses give the results shown in Figure 6.4, where the IGBT total (conduction + switching) losses are shown for the inverter operation: the red waveform is the instantaneous calculated losses, while the green waveform are the average losses calculated

using (6.2) and (6.3). The corresponding junction temperature waveforms simulated using these losses are shown in Figure 6.5.

The averaged losses appear convenient because of their simpler calculation. They completely ignore the direction of current and the cycling change of losses coming from the change of conduction between the diode and IGBT. As a result, when average losses are used to simulate the junction temperature, the AC frequency cycling is completely filtered out as shown in Figure 6.5 green waveform. If this meant that only the AC frequency cycles were ignored in the evaluation, the effect on lifetime calculation (for the converter design here) would have been minor – as seen in the analysis in other chapters, these do not cause a significant part of the damage. However, such averaging of losses also results in a reduction of the magnitude of the other temperature swings that are a product of the simulated dynamic transients during WT operation. In some way using the average losses reduces the resolution with which the losses variation is modelled, and therefore some of the transients are missed or inaccurately modelled. And these transients can be large and are responsible for most of the lifetime damage.

One way to modify the average losses for enabling to simulate the fast frequency junction temperature cycling has been suggested in [133] and [123], with the modified average losses. These losses were also included in Figure 6.4 and their resulting junction temperature in Figure 6.5, with the blue waveform, annotated as ‘Modified average’ losses. They are named as ‘modified’ compared to the average losses, because of how they account for the time (percentage of the full AC period) of conduction for the particular IGBT (or diode) switch: they have a value of zero when the current through the IGBT is zero and is flowing through the antiparallel diode (or lower IGBT); and a value of two times the average losses ($2 \times P_{avg}$) for the instants when the particular IGBT is conducting. The simplification of the modified average losses compared to the instantaneous losses is that the modified average losses can be calculated knowing the AC waveform frequency and load power factor, and not the actual waveforms for the current and the duty ratio. The simplification is more significant if the AC frequency is fairly constant, such as the case for the GSC in our system. The same method can be applied for the antiparallel diode accounting for the complementary conduction i.e. in the other part of the waveform period when the current flows the other direction.

If the different losses representation are used as the heat source generator in the thermal network (Figure 6.6), a thermal change with different dynamics is simulated as shown in Figure 6.5. Again it can be noted that applying the average analytical loss model for the device provides a junction temperature calculation (green waveform) which reduces the accuracy while completely ignoring the AC frequency cycling of the junction temperature. This cycling can be of interest in some analysis, such as when assessing the reliability and thermal fatigue of the semiconductor module. Meanwhile, the junction temperature cycling that is simulated using the modified average losses, closely and acceptably matches the cycling simulated by the most detailed (instantaneous) model, and could possibly be used to create a less detailed representation that satisfies the requirements for the intended analysis.

The crucial aspect to notice is that the model reduction that results when applying the averaged and modified average losses in the lifetime calculation methodology is not very beneficial for the time-series simulation used in the lifetime estimation approach. This is because simulating the full time-series temperature change is necessary for observing the thermal cycling. The modified average losses as a calculation are simpler for implementation but do not really reduce the computational complexity since all the current and voltage waveform parameters are still needed (amplitude, frequency, modulation index, power factor). The average losses are analytically simpler but significantly reduce the accuracy of the calculation as it will be seen later in this chapter when comparing the lifetime results. Therefore, although when the goal is calculation of losses, the average and modified average loss calculations from the provided references can offer a level of simplification, for the thermal stress and lifetime calculation methodology as developed here they do not offer a worthwhile improvement in the simulation, when compared to applying the full instantaneous losses calculation.

### 6.2.2 Model Order Reduction of the Thermal Network

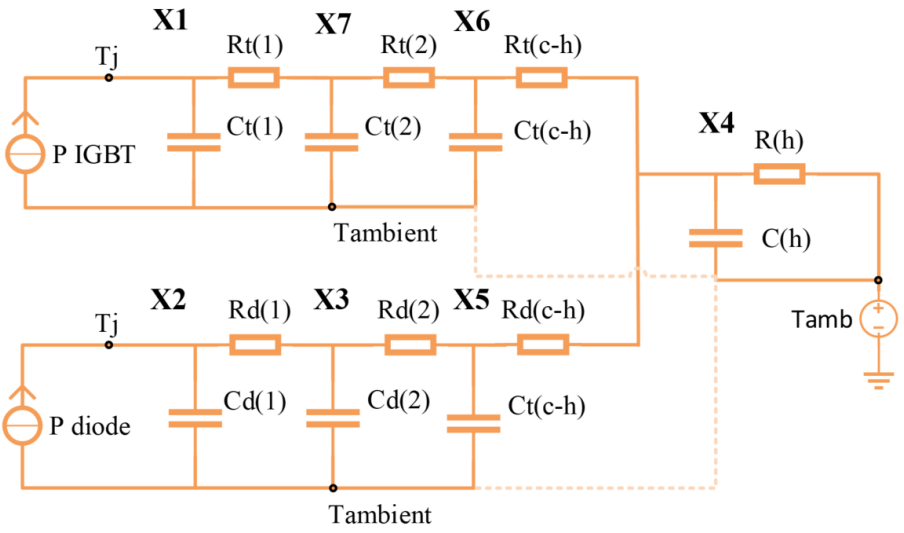


***Figure 6.6: Cauer thermal network for a single-chip IGBT module connected to a heatsink***

The thermal network of the IGBT power module given in Figure 6.6 (explained in Chapter 4) can be represented as a two-input two-output Linear Time Invariant (LTI) system. The two inputs are the time-series values of losses in the IGBT and diode while the two outputs are the IGBT and diode junction temperatures. The matrix form equations that describe this system are given with (6.4).

$$\begin{bmatrix} T_{j\_diode} \\ T_{j\_IGBT} \end{bmatrix} = \begin{bmatrix} G_{11} & G_{12} \\ G_{21} & G_{22} \end{bmatrix} \begin{bmatrix} P_{loss\_diode} \\ P_{loss\_IGBT} \end{bmatrix} \tag{6.4}$$

Where $G_{12}$ and $G_{21}$ are transfer functions of the form in (6.5) and $G_{11}$ and $G_{22}$ are of the form given in (6.6).

$$TF_1 = \frac{k_1}{a_1 s^7 + a_2 s^6 + a_3 s^5 + a_4 s^4 + a_5 s^3 + a_6 s^2 + a_7 s + a_8} \tag{6.5}$$

$$TF_2 = \frac{n_1 s^6 + n_2 s^5 + n_3 s^4 + n_4 s^3 + n_5 s^2 + n_6 s + n_7}{d_1 s^7 + d_2 s^6 + d_3 s^5 + d_4 s^4 + d_5 s^3 + d_6 s^2 + d_7 s + d_8} \tag{6.6}$$

Alternatively to the transfer function, the system can be represented as state-space model or zero-pole-gain. The state space model is considered for the plant with seven (x) states, two (y) outputs, and two (u) inputs as shown in equation (6.7). Where values for A, B, C and D matrixes are given below in equations (6.8).

$$\begin{aligned} \dot{x} &= Ax + Bu \\ y &= Cx + Du \end{aligned} \tag{6.7}$$

The junction temperature simulation when running the SIMULINK model with the full thermal network from Figure 6.6 and with representation of the thermal network state-space model from (6.7) has been compared. The response is identical for all frequencies, apart from a small difference which is likely coming from the rounding error of the parameters in the state-space matrices.

The state-space or transfer function representations are reduced and more convenient to implement in the methodology than the full thermal network. Such representation is also convenient for transferring the simulation to other software that does not support thermal network analysis. Furthermore, having the system represented in a state-space mathematical form, allows for reducing the model to lower orders i.e. reducing the number of states which for the studied IGBT module is seven ($x_1$ to $x_7$). Seven states are linked to the seven pairs of thermal resistance and capacitance elements in the thermal network as depicted from X1 to X7 in Figure 6.6.

$$\boldsymbol{A} = \begin{bmatrix} & \boldsymbol{x_1} & \boldsymbol{x_2} & \boldsymbol{x_3} & \boldsymbol{x_4} & \boldsymbol{x_5} & \boldsymbol{x_6} & \boldsymbol{x_7} \\ \boldsymbol{x_1} & \mathbf{-147.9} & \mathbf{0} & \mathbf{0} & \mathbf{0} & \mathbf{0} & \mathbf{0} & \mathbf{147.9} \\ \boldsymbol{x_2} & \mathbf{0} & \mathbf{-148.4} & \mathbf{148.4} & \mathbf{0} & \mathbf{0} & \mathbf{0} & \mathbf{0} \\ \boldsymbol{x_3} & \mathbf{0} & \mathbf{22.09} & \mathbf{-30.12} & \mathbf{0} & \mathbf{8.029} & \mathbf{0} & \mathbf{0} \\ \boldsymbol{x_4} & \mathbf{0} & \mathbf{0} & \mathbf{0} & \mathbf{-0.0725} & \mathbf{0.02083} & \mathbf{0.04167} & \mathbf{0} \\ \boldsymbol{x_5} & \mathbf{0} & \mathbf{0} & \mathbf{1029} & \mathbf{1000} & \mathbf{-2029} & \mathbf{0} & \mathbf{0} \\ \boldsymbol{x_6} & \mathbf{0} & \mathbf{0} & \mathbf{0} & \mathbf{1000} & \mathbf{0} & \mathbf{-2025} & \mathbf{1025} \\ \boldsymbol{x_7} & \mathbf{22.26} & \mathbf{0} & \mathbf{0} & \mathbf{0} & \mathbf{0} & \mathbf{7.666} & \mathbf{-29.93} \end{bmatrix}$$

$$\boldsymbol{B} = \begin{bmatrix} & \boldsymbol{u_1} & \boldsymbol{u_2} \\ \boldsymbol{x_1} & \mathbf{0} & \mathbf{0.5964} \\ \boldsymbol{x_2} & \mathbf{1.258} & \mathbf{0} \\ \boldsymbol{x_3} & \mathbf{0} & \mathbf{0} \\ \boldsymbol{x_4} & \mathbf{0} & \mathbf{0} \\ \boldsymbol{x_5} & \mathbf{0} & \mathbf{0} \\ \boldsymbol{x_6} & \mathbf{0} & \mathbf{0} \\ \boldsymbol{x_7} & \mathbf{0} & \mathbf{0} \end{bmatrix} \quad \boldsymbol{C} = \begin{bmatrix} & \boldsymbol{x_1} & \boldsymbol{x_2} & \boldsymbol{x_3} & \boldsymbol{x_4} & \boldsymbol{x_5} & \boldsymbol{x_6} & \boldsymbol{x_7} \\ \boldsymbol{y_1} & \mathbf{1} & \mathbf{0} & \mathbf{0} & \mathbf{0} & \mathbf{0} & \mathbf{0} & \mathbf{0} \\ \boldsymbol{y_2} & \mathbf{0} & \mathbf{1} & \mathbf{0} & \mathbf{0} & \mathbf{0} & \mathbf{0} & \mathbf{0} \end{bmatrix}$$

$$\boldsymbol{D} = \begin{bmatrix} & \boldsymbol{u_1} & \boldsymbol{u_2} \\ \boldsymbol{y_1} & \mathbf{0} & \mathbf{0} \\ \boldsymbol{y_2} & \mathbf{0} & \mathbf{0} \end{bmatrix} \tag{6.8}$$

The model order reduction is done using MATLAB control system tools. In this process, Hankel Singular Values which define the “energy” contained in each state of the system are used. The representation of the Hankel values for the seven state model is shown Figure 6.7. It can be seen that the absolute “energy” in the last two states is too small and negligible. The reduction of the state-space model has been made by eliminating two and four of the least dominant terms for deriving a five and a three order state-space system respectively. The comparison of thermal cycling with arbitrary periodic losses for the full network and the LTI system with seven, five and three states is shown in Figure 6.8. From this can be seen that the reduced five order TF can represent the dynamic changes with high accuracy while the three order-system includes some inaccuracy, which for different frequencies and when calculating the lifetime, could be compounded to a large error.

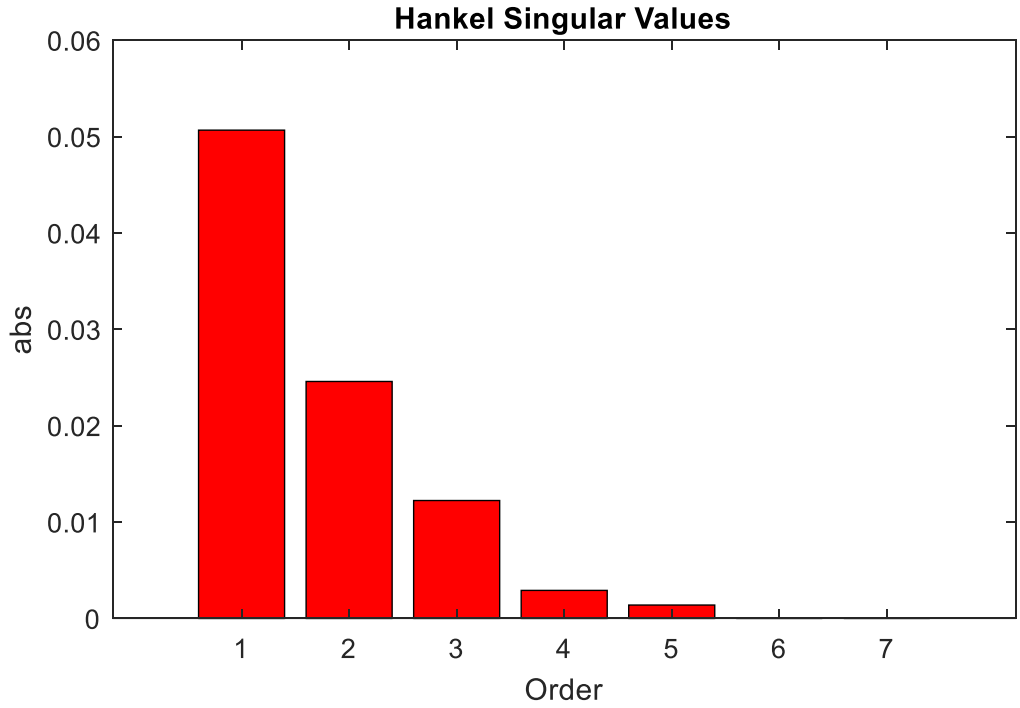


***Figure 6.7: Hankel singular values for the full (seven state) state-space representation of the IGBT module thermal network***

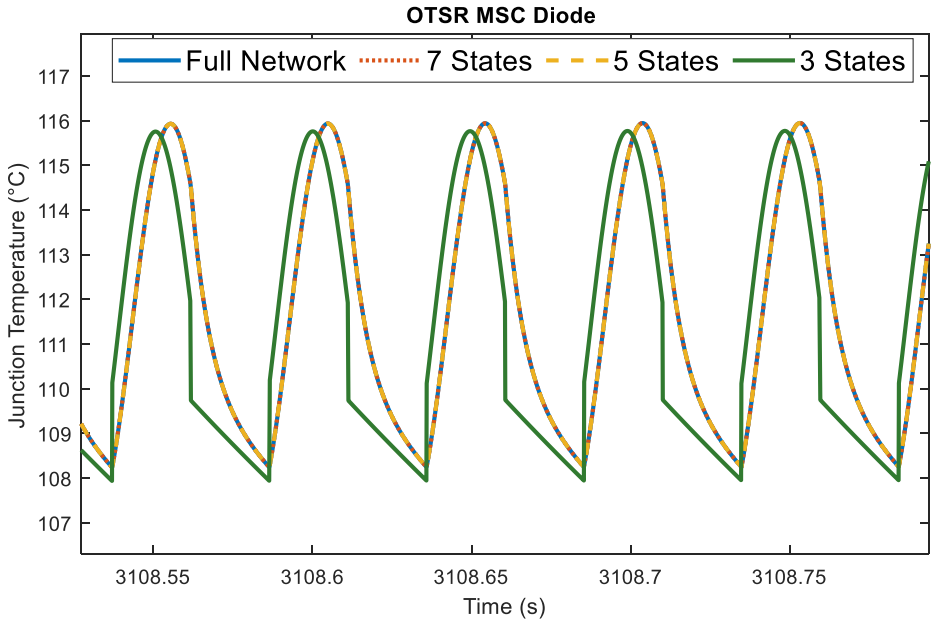


***Figure 6.8: Thermal cycling with full network and seven, five, and three state-space model. (The full, seven, and five state traces are on top of each other)***

In Figure 6.8 the comparison for the isolated (without the mission profile defined by the WT) response of the different thermal network representations is shown. For a further analysis of the results, the scenario when the thermal network has as an input the losses defined by the mission profile of the WT system is also considered. The histograms of counted cycles for this scenario are shown in Figure 6.9 and Figure 6.10 where the state-space models with seven and five states are compared. It can be seen that the counted cycles closely match.

The seven and five state model represent the full thermal network with high accuracy, while the three states model ignores some of the cycles. The lifetime estimations corresponding to counted cycles in the histograms above are given in Figure 6.11. At this level, the TFs with reduced number of states do not offer reduced simulation speed compared to the seven state model. Nonetheless, the LTI transfer function system representation is a simplification in terms of ease of parametrization and compactness of the model as compared to the full thermal network representation. It should be noted that the thermal network for other IGBT modules might be represented with a higher number of thermal RC elements and therefore the resulting TF might have more than seven states.

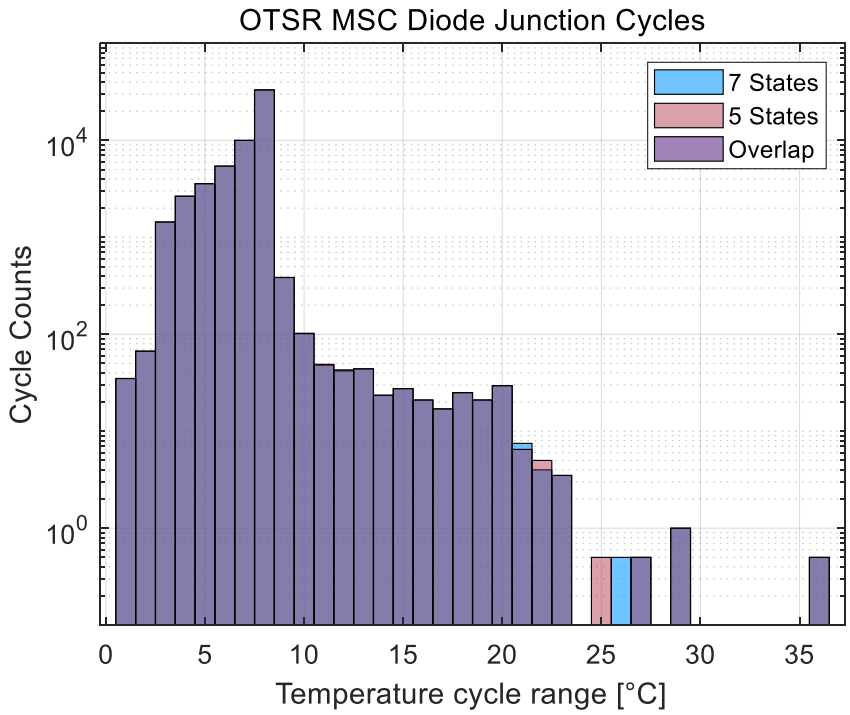


***Figure 6.9: Cycle range histogram comparison between seven and five state-space thermal model for OTSR controlled WT and for MSC diode junction temperature***

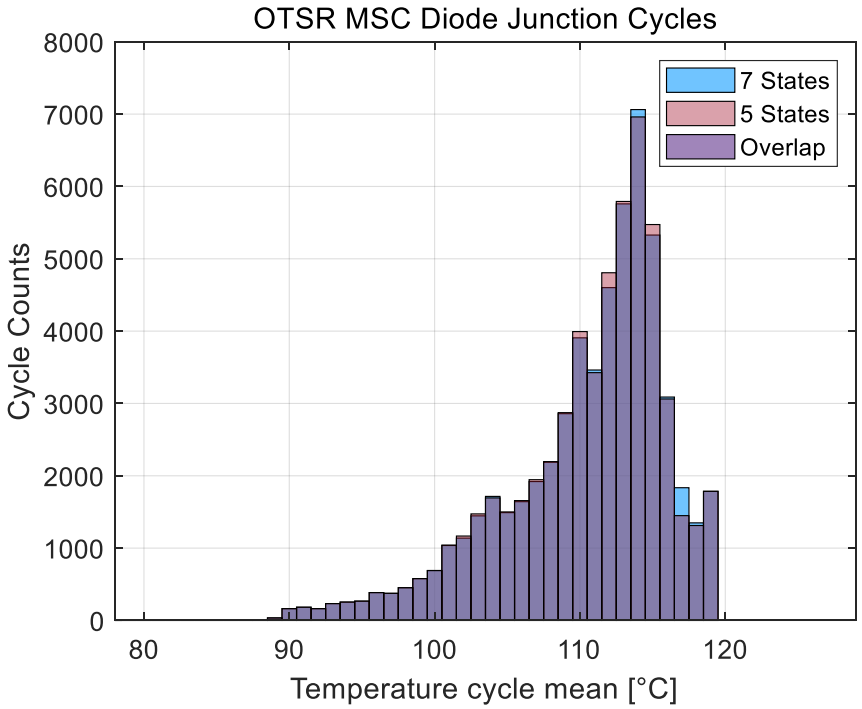


***Figure 6.10: Cycle mean histogram comparison between seven and five state-space thermal model for OTSR controlled WT and for MSC diode junction temperature***

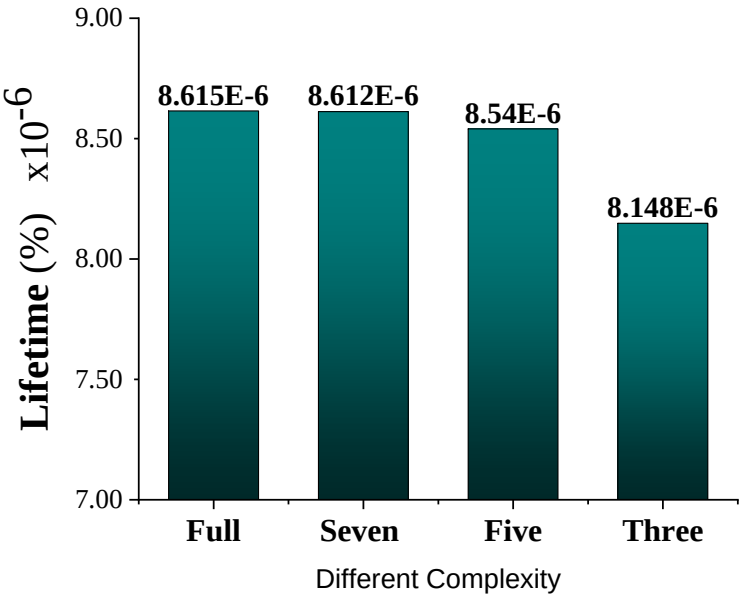


***Figure 6.11: Lifetime comparison between different state-space thermal models***

## 6.3 Fully Reduced WT Model – Look-up Table of Wind Speed vs Device Losses

Part of the approach undertaken in this chapter is to simplify the WT operational layer as well as the converter thermal stress layer at the expense of not simulating some of the transients that are present in the fully-detailed approach. As an initial observation, let us look at the issue from the other end of the continuum, where the model is reduced by omitting almost all if its details that contribute to the simulation of the transients present in the full analysis. We can call this model a fully reduced WT operational model. The fully reduced model does not simulate the operational transients which were the primary focus in this thesis. Similar reduced models have been used in some of the other lifetime estimation approaches previously as was covered in the literature review in Chapter 2.

The fully reduced model is shown in Figure 6.12 and uses a lookup table to relate the wind speed change to the power losses in the WT converter (and in the studied IGBT module). The lookup table was constructed using the fully detailed model from the previous chapter while running the WT in steady-state at different wind speed inputs. The lookup table dependency for the MSC and GSC is shown in Figure 6.13.

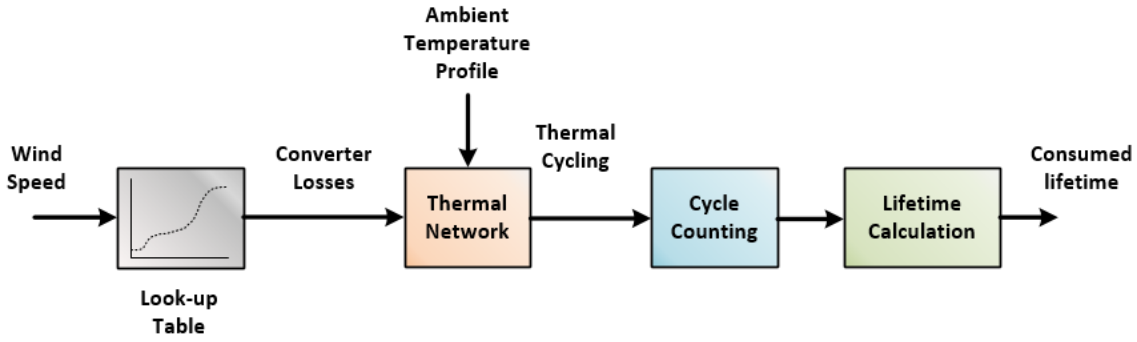


*Figure 6.12: 'Fully reduced' lifetime estimation model*

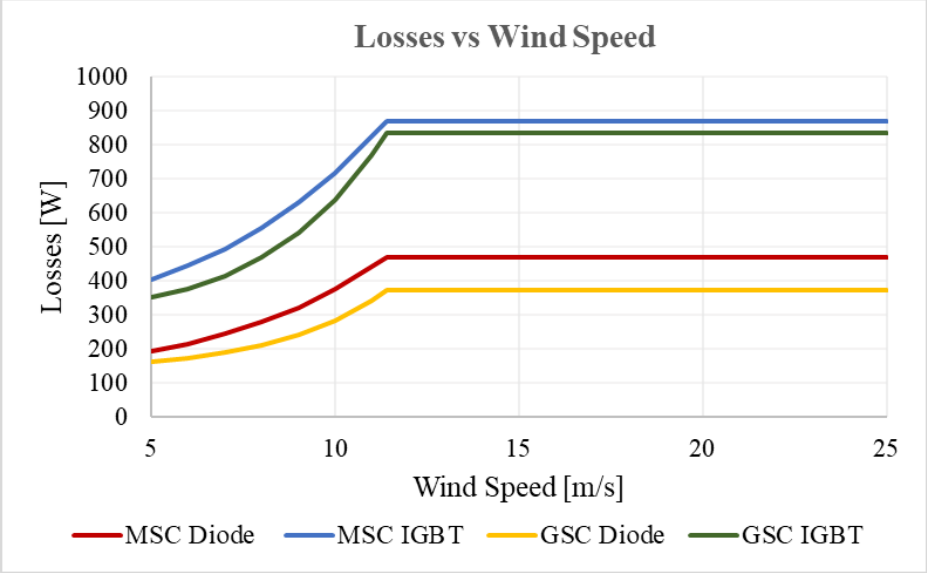


*Figure 6.13: Losses vs wind speed look-up table (steady state losses)*

When the fully reduced model is used to evaluate the lifetime consumption during WT operation with one hour of variable wind data, the counted thermal cycles compare to the full model as shown in Figure 6.14 and Figure 6.15. The fully-reduced (in the figures 'Simplified') model is based on steady-state losses and does not account for whether OTSR or OTC torque control is applied for the generator. This makes it unable to account for the transients which were previously shown to be highly important. The comparison of the histograms of counted cycles between the fully-reduced and the full model where the OTSR control is applied confirms the large mismatch.

The comparison can also be quantified in terms of consumed lifetime. This is shown in Figure 6.17, where the fully reduced model is annotated as 'Reduced' (equivalent to 'Simplified' in Figure 6.14). It can be seen that the fully reduced model gives a lifetime underestimation of more than one order of magnitude.

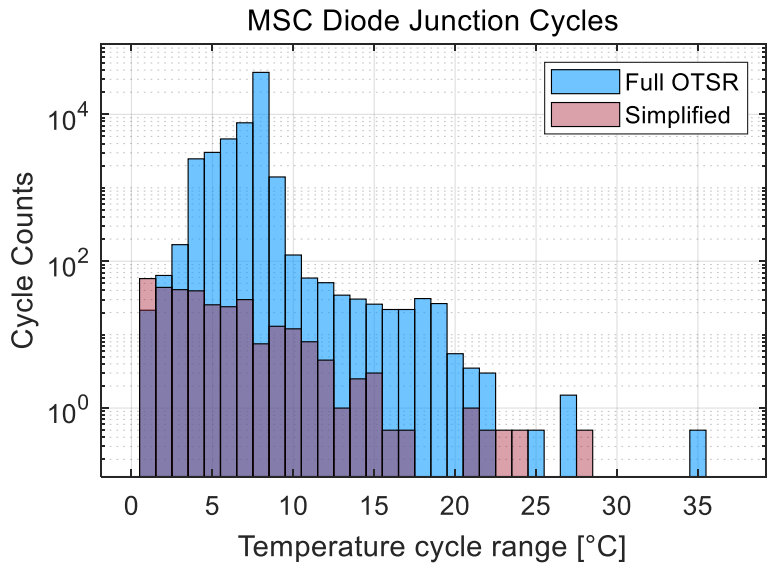


***Figure 6.14: Full model vs Fully Reduced (Simplified)***

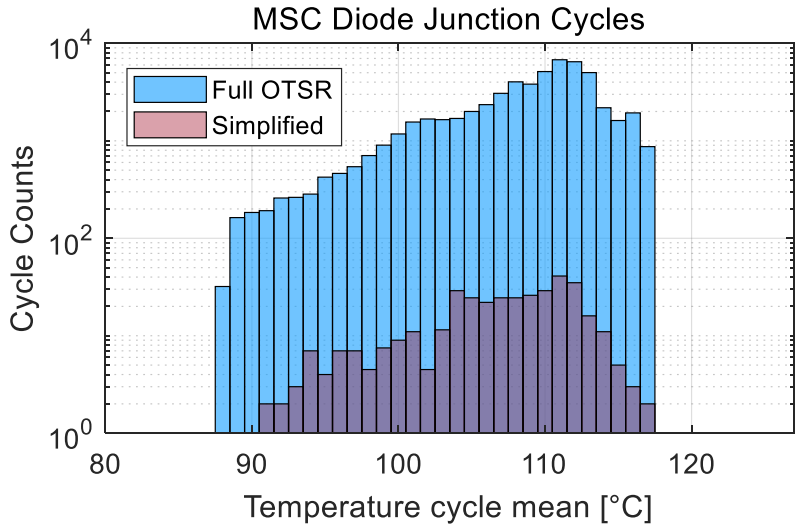


***Figure 6.15: Full model vs Fully Reduced (Simplified)***

Additionally Figure 6.17 gives the lifetime consumption for when average losses are used to model the thermal cycling. This is the modelling that was depicted with the green waveform in Figure 6.4 and Figure 6.5. If the WT is run with the full OTSR model and the same one hour wind profile, the temperature waveform difference between using the instantaneous and average losses is shown in Figure 6.16. This confirms that in addition to neglecting the steady-state high frequency cycles, using the average waveform also reduces the amplitude of the cycles that are registered for the temperature large swings. Consequently, the lifetime that would be modelled with the average losses as shown in Figure 6.17 is more than an order of magnitude underestimated.

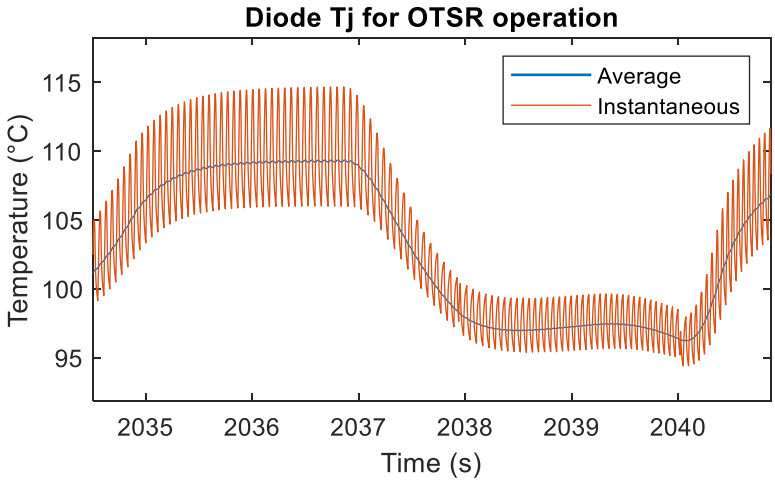


***Figure 6.16: Diode junction temperature simulated using instantaneous (full) versus averaged (reduced) model of losses for WT operation with a specific wind speed profile***

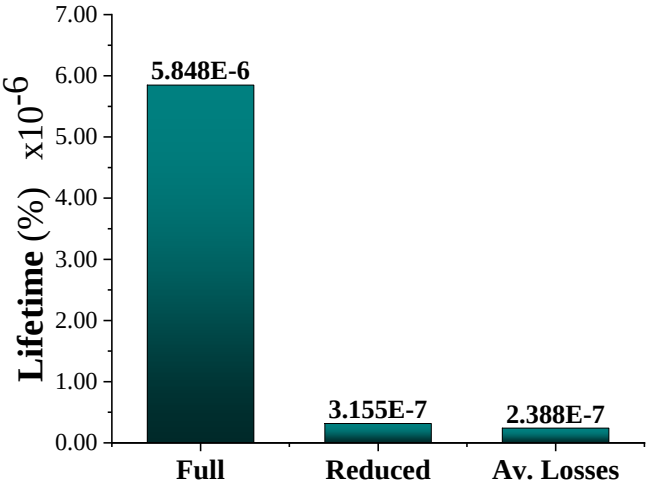


***Figure 6.17: Lifetime for WT operation with a specific wind speed profile: comparison between the full simulated WT and converter operation (Full), the fully reduced model (Reduced), and the case where the WT operation is simulated fully but the losses are calculated using the averaged model (Av. Losses)***

## 6.4 Model Order Reduction of the Detailed WT Operational Model

### 6.4.1 Converter Current Loop

The fastest control loop in both the MSC and GSC models is the current loop, which is included for both the d and q axis currents. This loop for the MSC in the previous chapters was tuned to respond with a natural frequency (≈ bandwidth) of 10 Hz, while the GSC with 450 Hz. Given the relatively high value of this bandwidth compared to the observed thermal cycling frequency in the converter module, some of the transients in this loop can be approximated without losing much of the useful information in the thermal model.

In Chapter 5 it was seen that the most important transients which cause the majority of the thermal stress are from the torque response and Maximum Power Point Tracking (MPPT) of the WT generator during wind speed changes. Relative to those dynamics, the current loop is fast enough (4-10 times faster) to not have any interference with the MPPT control and the WT power generation. As a consequence, the dynamics of the PI loop could be approximated (neglected) by assuming the current loop output perfectly tracks the input set-point (steady-state value) as shown in Figure 6.18. In other words we are assuming the fastest possible current controller, also known as 'dead-beat' controller from discrete time control theory. This is an approximation and ignores the fact that the current control loop has to be slower than the inner voltage synthesis loop.

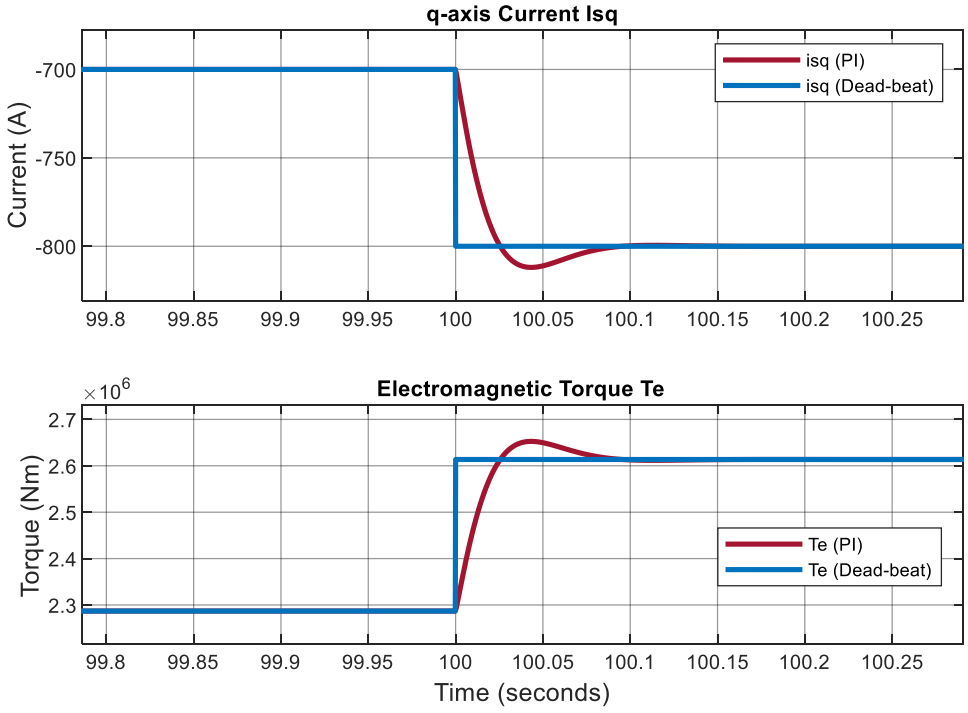


***Figure 6.18: Dead-beat current control isq_set = isq***

If the current loops are neglected, then the current change is assumed to be instantaneous. The full voltage equations can be written as in (6.9) and (6.10).

$$v_{sd} = R_s i_{sd} + L_{sd}\frac{di_{sd}}{dt} - \omega_{gen}{}^{e} L_{sq} i_{sq} \tag{6.9}$$

$$v_{sq} = R_s i_{sq} + L_{sq}\frac{di_{sq}}{dt} + \omega_{gen}{}^{e} L_{sd} i_{sd} + \omega_{gen}{}^{e}\Psi_{PM} \tag{6.10}$$

Knowing that $i_{sd} = 0$, (6.9) and (6.10) for steady-state when the derivative of current is zero, can be simplified to:

$$v_{sd} = -\omega_{gen}{}^{e} L_{sq} i_{sq} \tag{6.11}$$

$$v_{sq} = R_s i_{sq} + \omega_{gen}{}^{e} \Psi_{PM} \tag{6.12}$$

For the current control loops in Figure 6.18, when they are a part of the WT operational model and the step change is at the input wind speed (instead of the current set-point), there is an additional delay in transferring this wind speed change to the current loop. This delay comes from the turbine mechanics, inertia, as well as some sensor delays that have been included in the simulation as first order transfer functions. This means that the current set-point during WT operation varies depending on the dynamics of the WT response and the applied torque control of the generator. For Optimal Torque Control (OTC) (see Chapter 5), this change in set-point is limited by the slower dynamics of the WT and generator so that no transients of the current loop can be observed. In that case, the response between the PI controlled current and the simplified representation is identical.

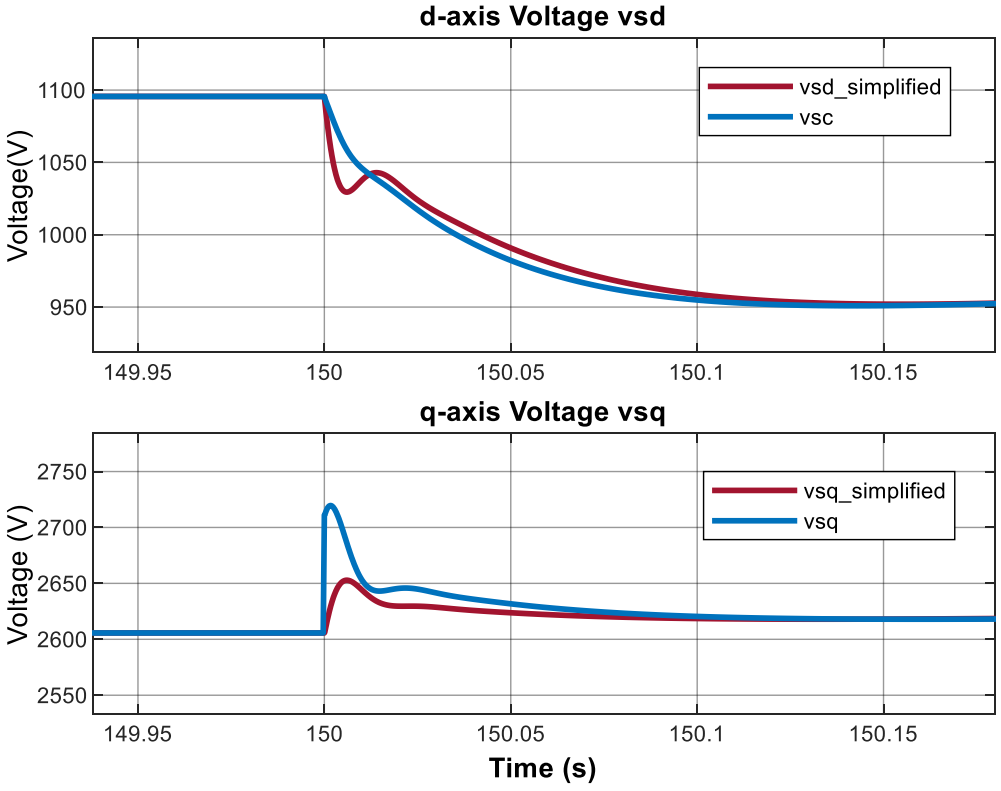


***Figure 6.19: Comparison of voltage change between the full model with PI current loop (blue waveform) and the simplified model with dead-beat current loop (red waveform)***

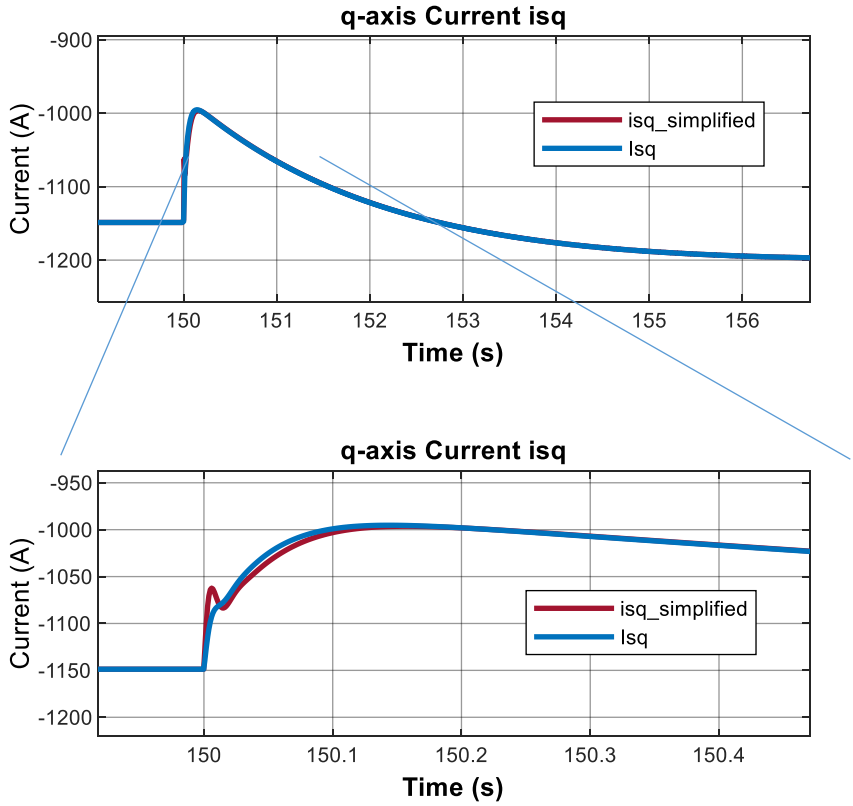


***Figure 6.20: Comparison of q-axis current change between the full model with PI current loop (blue waveform) and the simplified model with dead-beat current loop (red waveform)***

The difference in simulated operation between the full and simplified current loop operation with OTSR control of the WT generator is shown in Figure 6.19 and Figure 6.20, where dq voltages and currents are shown respectively.

The simplifications made so far allow for a faster and less computationally intensive simulation. First of all, in the most detailed model, the fastest loop was the inner current loop of the GSC with 450 Hz. In this chapter it was decided to focus the analysis on the MSC thermal stress where the fastest inner current loop has been tuned with a natural frequency (≈ bandwidth) of 10 Hz – an order of magnitude lower than the GSC. Just with this redefinition of the analysis, the simulation time step can be increased accordingly.

In Figure 6.21 is shown the q-axis stator current in the WT and converter operational model for the fully-detailed (MSC) and the reduced (omitted current loop and increased time-step). This figure shows that the simulated current with a slightly simplified model is very close to the one simulated with the original full model. In the next sub-section, more such reduced models are analysed and evaluated in terms of simulation speed and accuracy.

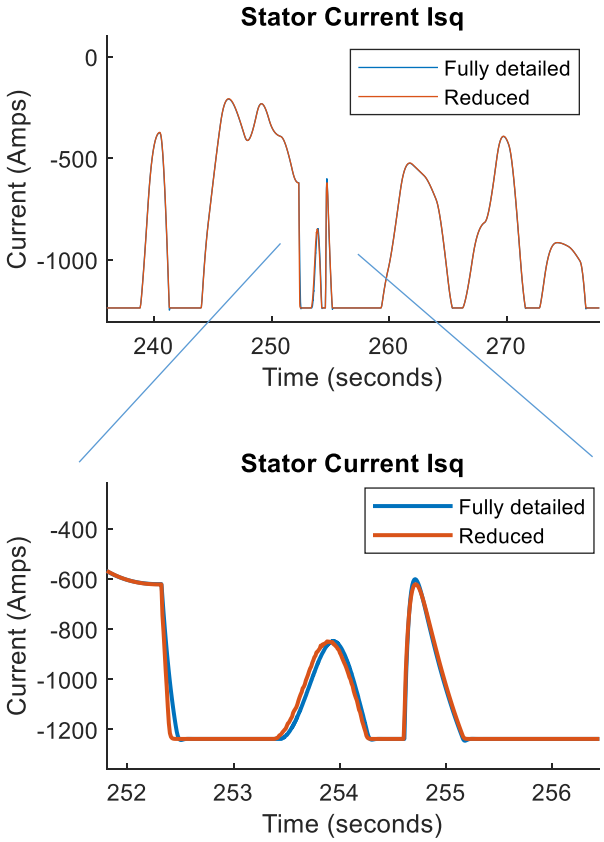


***Figure 6.21: Comparison of the current q-axis waveforms between the fully detailed model and a reduced model with no PI current loop and increased simulation time-step.***

## 6.5 Reduced Models

Table 9 gives the features and simulation runtime for the full optimized model and eleven versions of simplified models. The simplified models are derived from the full case while changing some of the features as given in the table. The full optimized model was built using the original model used in previous chapters with some optimizations within the Simulink framework: simulating only the quantities of interest, not using MATLAB functions in the model, reducing the number of scopes, merging the WT operational and converter thermal models in a single simulation, and so on.

In Table 9 the reduced models are named as SIMPLIFIED1 to SIMPLIFIED11. The features that are changed in each consecutive simplified model are annotated using orange font colour. The features that are included in Table 9 are (in order from left to right): type of solver, the explicitly entered maximum time-step of the simulation, the PI current loop (included or not), the sampling of the obtained junction temperature, the number of states in the state-space model representing the thermal network, the feedback of junction

temperature in the calculation of losses (included or not). The elapsed simulation time that each model takes to run thermal evaluation for one hour of WT operation with the same wind speed profile is given in the final column in Table 9.

***Table 9: Reduced models with their changed features and their impact in the runtime of simulating 1h of WT operation***

| | FEATURES | | | | | | |
|---|---|---|---|---|---|---|---|
| **Model** | **Solver** | **Max Time Step** | **PI Current Loop** | **Tj Sampling (s)** | **Thermal network # of states** | **Losses Tj Feedback** | **1h simulation runtime (average out of 3)** |
| **FULL Optimised** | ODE45 | 1.0E-04 | ✓ | inherited (-1) | 7 | ✓ | 7:49 min |
| **SIMPLIFIED1** | **ODE23t** | 1.0E-04 | ✓ | inherited (-1) | 7 | ✓ | 9 min ↗ |
| **SIMPLIFIED2** | ODE45 | **1.0E-03** | ✓ | inherited (-1) | 7 | ✓ | 3:13 min ↘ |
| **SIMPLIFIED3** | ODE45 | 1.0E-03 | ✗ | inherited (-1) | 7 | ✓ | 3:08 min ↘ |
| **SIMPLIFIED4** | ODE45 | 1.0E-03 | ✗ | **0.01** | 7 | ✓ | 02:27 min ↘ |
| **SIMPLIFIED5** | ODE23t | 1.0E-03 | ✗ | 0.01 | 7 | ✓ | 50 sec ↘ |
| **SIMPLIFIED6** | ODE23t | 1.0E-03 | ✗ | 0.01 | **5** | ✓ | 9:16 min ↗ |
| **SIMPLIFIED7** | ODE23t | 1.0E-03 | ✗ | 0.01 | **3** | ✓ | 7:42min ↘ |
| **SIMPLIFIED8** | ODE23t | 1.0E-03 | ✗ | 0.01 | 7 | ✗ | 49 sec ↘ |
| **SIMPLIFIED9** | ODE23t | **5.0E-03** | ✗ | 0.01 | 7 | ✗ | 33 sec ↘ |
| **SIMPLIFIED10** | ODE23t | 1.0E-03 | ✗ | **0.1** | 7 | ✓ | 44 sec ↘ |
| **SIMPLIFIED11** | ODE23t | 1.0E-03 | ✗ | **1** | 7 | ✓ | 43 sec ↘ |

The different simplified models in Table 9 were chosen to represent different model order reduction stages that can be performed as identified when building the detailed simulation. The features of the PI current loop and the number of states of the thermal network were described in detail earlier in this chapter. The junction temperature sampling and the time step of the simulation are related to the resolution of the time-series solution. Depending on other features, the problem and the way that the simulation solver obtains the solution can be impacted. For this reason, when changing some of the features, the problem defined by the Ordinary Differential Equations (ODEs) can become stiff and then changing from a non-stiff solver (ODE45) to a stiff solver (ODE23t) could provide a more efficient simulation.

The Diode MSC lifetime consumption for all the models of Table 9 has been calculated and shown in Table 10 where the simplified models are shortly annotated as S1 to S11. The ‘diode MSC’ lifetime consumption for 1 hour operation was evaluated using the lifetime estimation methodology and is shown in the ‘1 hour DIODE’ column. In the

second column this lifetime has been analytically extrapolated to the yearly consumed value – with the ambiguous assumption that the lifetime consumption would be the same for all the other hours of the year. In the third column is given the error in percent between the lifetime calculation for the simplified models and the FULL model (first row of the table). The 1 hour consumed lifetimes from Table 10 have been plotted in Figure 6.22.

***Table 10: Evaluated MSC lifetime consumption for the different models from Table 9 running the WT simulation with a specific one-hour highly variable wind speed profile with OTSR control method of the generator***

| | LIFETIME [%] | | |
|---|---|---|---|
| MODEL | 1 hour DIODE | Yearly extrapolated | Error compared to FULL (%) |
| FULL | 6.14E-06 | 6.28E-02 | 0 |
| S1 | 5.83E-06 | 5.96E-02 | -5.07% |
| S2 | 6.12E-06 | 6.25E-02 | -0.35% |
| S3 | 5.55E-06 | 5.67E-02 | -9.63% |
| S4 | 5.16E-06 | 5.28E-02 | -15.95% |
| S5 | 5.53E-06 | 5.65E-02 | -9.97% |
| S6 | 5.30E-06 | 5.42E-02 | -13.72% |
| S7 | 6.56E-06 | 6.70E-02 | +6.81% |
| S8 | 3.47E-06 | 3.55E-02 | -43.45% |
| S9 | 3.25E-06 | 3.32E-02 | -47.07% |
| S10 | 4.02E-06 | 4.1E-2 | -34.52% |
| S11 | 3.26E-06 | 3.33E-2 | -46.92% |

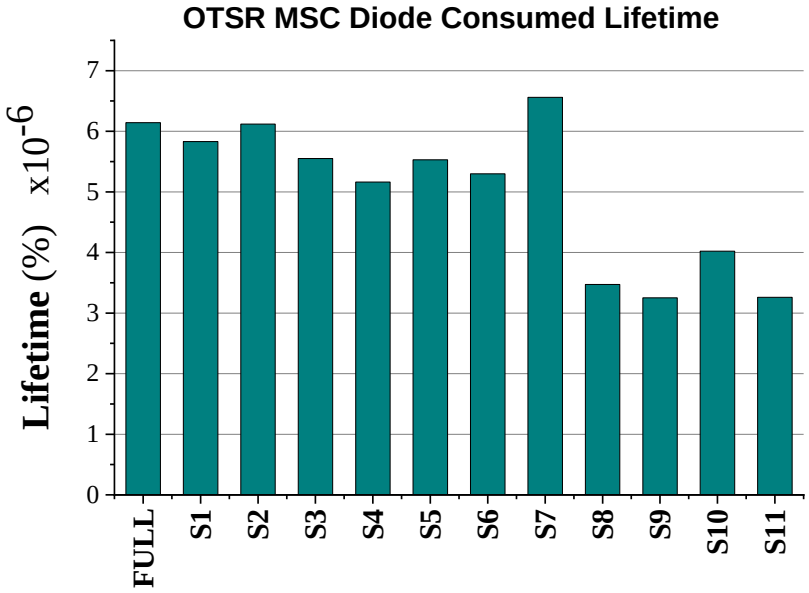


Figure 6.22: Evaluated MSC lifetime consumption for the different models – plotting of results from Table 10.

When the Ordinary Differential Equations (ODEs) of a problem are such that they force the solver to perform a very large number of small steps (smaller than the interval of integration) even in regions where the solution curve is smooth, these are called stiff ODE problems [134]. Stiffness depends on the differential equation, the initial conditions, and the numerical method. Applying stiff solver methods to such problems means they will do more work per step and therefore can take bigger steps. This makes them more efficient in solving the ODEs. In the comparison here we show the impact that the choice of two different solvers can have on the lifetime estimation model. Further detail to this analysis can be included if as part of the problem the different aspects of numerical solutions of ODEs are included.

Two different Simulink solvers are considered and included in Table 9. One is the default ODE45 (Dormand-Prince) which is recommended by MATLAB to be used as a first try for most problems [135]. This is a one-step solver which needs the solution at the preceding time point. The other considered solver is also a one-step solver ODE23t (Modified Stiff/Trapezoidal). This solver is efficient and is recommended to be used for moderately stiff problems [135]. From the elapsed simulation time for the different simplified models it can be seen that the modified stiff ODE23t solver can reduce simulation time and offer a more efficient solution. But this improvement does not come for all models. It can be noticed that if the model detail is such that it includes the converter inner current loops, the problem is not stiff and in that case applying the ODE23t solver actually makes the solution of ODEs less efficient and increases the simulation time (see difference between FULL Optimised and SIMPLIFIED1 models in Table 9). If the current PI loop is excluded and approximated as explained earlier, then the rapid (10 Hz) dynamics are not modelled and the moderately stiff solver can reach a solution more efficiently. This is noticed when the solver is changed from SIMPLIFIED4 to SIMPLIFIED5 and the simulation time is reduced by more than 50%. And there is actually no negative effect on the accuracy of the lifetime evaluation when the solver is changed – the error of SIMPLIFIED4 is actually higher and this is because the non-stiff solver ODE45 is applied after losing some of the information of the full model when the PI current loop was omitted and the $T_j$ sampling time was increased from ‘inherited’ (from the simulation time-step that the solver takes) to ‘explicit, 0.01 seconds’.

From the other considered features, the maximum allowed time-step of the simulation is a parameter that also highly affects simulation speed, as seen when changing it for SIMPLIFIED2 (S2) and SIMPLIFIED9 (S9) models. In both these cases, the absolute increase of the error in lifetime estimation compared to the earlier version (S1 and S8 respectively) is about 5% (see Table 10), which is adequate.

It is interesting that reducing the number of states in the state-space representation of the thermal network from the full seven states to five and three states in SIMPLIFIED6 (S6) and SIMPLIFIED7 (S7) increases the simulation time and computational effort of the solver. This is because, as seen in (6.8) the seven state model state matrixes contain a lot of zero elements. When the five and three state models are created, in order to have a response that is close to the full model, there are more non-zero elements in the matrices and therefore an increased number of calculations. The lifetime estimation error is acceptable. However, it is larger for the five state than the three state system. This is most probably due to the interaction of all the different specific features: only the accuracy of the thermal state-space models on their own was explicitly shown in sub-section 6.2.2 and compared in Figure 6.11 with all the other features unchanged.

One thing that can increase simulation speed significantly for the full model is ignoring the feedback loops such as the dependence of the losses on the real-time junction temperature $T_j$. So when the problem is non-stiff, the losses Tj feedback dependency can significantly slow down the simulation and in that case it could be necessary to be omitted. However, after the problem becomes stiff and with the modified stiff solver, the difference in simulation speed introduced by omitting the Tj feedback in SIMPLIFIED8 (S8) is not worth it, considering that such a change would introduce a very large error in the lifetime calculation: underestimation of lifetime consumption by 43% (S8 in Table 10).

The last three models in Table 9 (from S9 to S11) are with increased simulation time-step and with increased sampling time of the junction temperature $T_j$ waveform. The increase of maximum simulation time-step to 5e-3 and the $T_j$ sampling time to 0.1 s and 1 s brings a small simulation speed increase, but the inaccuracy of the calculated lifetime becomes very high (Table 10).

From all the considered simplified versions with the different combinations of features, the best trade-off between simulation speed and accuracy is the model SIMPLIFED5 (S5). With this model the simulation speed was improved by more than 9 times while the error in lifetime estimation compared to the FULL model was lower than 10%. Thus, this is the chosen reduced model with which longer analysis can be attempted.

The long term analysis has been run for a 24 hour data set. After running the WT and converter thermal simulation, the counting of the cycles was undertaken and the lifetime was evaluated. This lifetime is shown in Table 11 for two different 24-hour periods with different wind profiles. The first one (15 Oct 2018) is around and below rated speed where there are a lot of power fluctuations of the WT generator. The second wind profile (30 Oct 2018) is mostly around or above rated wind speed where the WT power generation is limited to rated and therefore has less fluctuations. Because of this difference, the estimated consumed lifetime between the two is also significantly different, with the period that has a very high wind speed having lower lifetime consumption.

A comparison between the OTC and OTSR controls has also been made using the 24 hour simulation and the simplified model. These calculated lifetime consumptions are given in Table 11 and plotted in Figure 6.23. The relative difference between the two controls is not as large as it was when only one hour was analysed (see Chapter 5). Additionally it can be seen that this comparison can differ depending on the wind profile – for the high speed wind profile with low fluctuations and low lifetime consumption, it is actually the OTC that is evaluated to have a larger consumed lifetime. However please note that this consumed lifetime (for 30 Oct) is less than 50% of the one calculated for the more problematic period with large wind and power fluctuations (15 Oct).

Another thing to be noted is that the yearly extrapolated lifetime consumption from the 24 hour analysis is significantly, by one order of magnitude, higher than the ones extrapolated from the 1 hour analysis in Table 10. This suggests that the extrapolation from analysing just a small subset of the wind speed data is highly inaccurate and rough approximations should be avoided. Even the extrapolation from a 24 hour analysis to the yearly consumed lifetime will have limited accuracy. Nonetheless, such an extrapolated number from the obtained results suggests a very reliable converter with estimated lifetime of more than 100 years.

It has to be noted that one positive aspect of WTs that are installed offshore, compared to onshore ones, is that on average, wind profiles in offshore waters are usually with higher average speed and less fluctuations – this is likely to contribute to less aging from the thermal cycling mechanism which has been prioritised here. But indeed the offshore conditions are much harsher and the observed total failure rate of the converter when all the impacting factors are added is likely to be worse.

***Table 11: Consumed lifetime for an operational period of 24 hours in two different days: one with a relatively high wind speed profile and less wind speed fluctuations (15 Oct), and the other with lower wind average speed and higher fluctuations (30 Oct).***

| | 15-Oct-2018 Consumed Lifetime [%] | Yearly extrapolated [%] | 30-Oct-2018 Consumed Lifetime [%] | Yearly extrapolated [%] |
|---|---|---|---|---|
| **OTSR** | 5.33e-4 | 0.195 | 2.12e-4 | 0.077 |
| **OTC** | 5.07e-4 | 0.185 | 2.29e-4 | 0.083 |

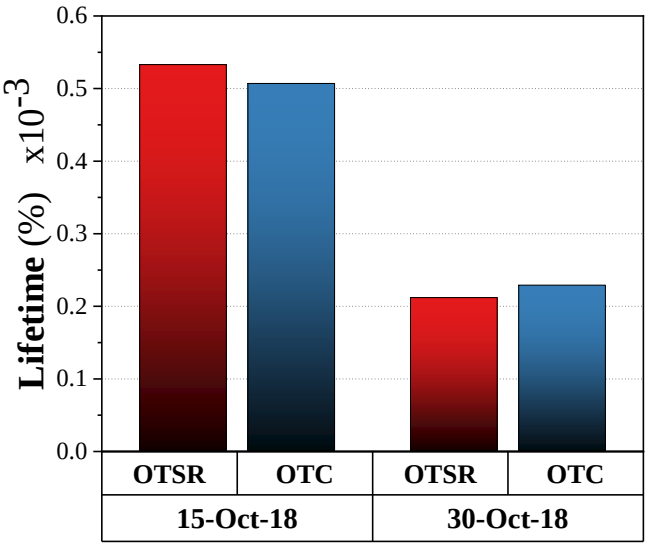


***Figure 6.23: Consumed lifetime in 24 hours with operational wind speed data for two different days in October 2018.***

## 6.6 Summary

In this chapter options for simplifying and improving the efficiency of the lifetime estimation methodology were considered, with the objective of running the analysis for longer time periods with less computational effort. Initially the counted thermal cycles were presented in a set of results that were obtained using the fully detailed model from the previous chapters. In these results it was observed that there is an evident disproportion concerning the contribution by the cycles with different temperature towards the total

consumed lifetime in an analysed period. It was pointed out that it would be beneficial to be able to reduce the detail of the simulation while still modelling the most important cycles and therefore maintaining an accurate lifetime prediction.

A model which completely disregards the dynamics and transients introduced by the different parts of the WT and converter operation was first presented. This was named a fully-reduced model. The simulation of the fully reduced model is highly efficient from the computational aspect given that the whole WT operational and losses model is replaced with a look-up table linking the wind speed and the losses in the Diode and IGBT of the power module. Although this efficient model can be used to evaluate the converter lifetime consumption for very long periods of WT operation, it was shown to have a poor accuracy and to be incomplete.

Next, to build a model that in terms of detail and computational effort lies between the fully detailed and fully reduced models, different aspects of the approach were analysed and their potential for simplification was discussed. These aspects included the level of complexity in the analytical representation of the power module losses; the analysis of the power module thermal network as a transfer function and state-space model with different number of states; and the current control loops of the converter. Additionally the simulation features such as choice of solver and simulation time-step were also considered. Combining the different considered aspects and features, several simulation models were created and were run using the same operational wind data. This allowed to show the implication that specific reductions and changes in the models had on the simulation speed and on the accuracy of the calculated lifetime.

One of the reduced (simplified) models was chosen as adequate for reducing the computational complexity and increasing simulation speed while also offering an acceptable accuracy when used for calculating the lifetime consumption. With the chosen reduced model, a 24 hour WT operation was simulated with wind speed data for two different days (24 hour periods). The thermal stress and the lifetime consumption for these two days were evaluated for two different controls of the WT generator. A discussion was made using the results from the longer (24 hour) simulation and lifetime evaluation.

# 7 Conclusion and Further Work

In this chapter, the essential contributions and outcomes of the work done in this thesis will be outlined. The importance of these contributions will be discussed in relation to current and foreseeable future developments in the wind industry. Suggestions on how the work undertaken in this thesis can be supplemented and extended by further studies are made.

In this thesis a methodology for performing lifetime estimation studies for converter modules in WT power electronic systems was developed. The methodology was built around a specific failure mechanism and failure mode: the bond-wire failure mode in IGBT modules developed through the mechanism of thermo-mechanical cycling stress accumulation. Various operational aspects of the WT were analysed from the perspective of the converter thermal stress loading and lifetime consumption using a series of case studies. A discussion on optimising and reducing the complexity of the approach was also undertaken.

The work in the thesis contributes new knowledge to the field of converter reliability by having achieved the following objectives:

- Development of a complete and thorough lifetime estimation methodology for wind turbine converters based on thermal stress of IGBT modules. This methodology considers WT operational aspects that have been overlooked by previous approaches.
- Evaluating the lifetime and thermal stress impact for different modules in the WT converters, including the modules on the Machine Side Converter (MSC) as well as on the Grid Side Converter (GSC). Additionally, the thermal stress modelling was done at the device level (IGBT and diode) for each module.
- Evaluating the lifetime and thermal stress impact of different control strategies for both the torque regulation of the generator as well as the control of reactive power transfer to the AC grid. Three different torque control strategies in the MPPT region were compared: Optimal Torque Control (OTC), and two versions of Optimal Tip Speed Ratio (OTSR) controls which were tuned to track the

MPPT faster than the OTC. Two additional scenarios with a constant reactive power injection and consumption from the grid were considered.

- In the last chapter, model order reduction of the fully detailed model was undertaken using a number of simulation criteria. The potential for reducing the simulation complexity while not losing the accuracy was assessed by creating a number of model variations. In the end a reduced model variation with acceptable accuracy was chosen for running the simulation for a longer operational time period of the WT. The same operational scenarios that were observed with the fully detailed model, were analysed with the reduced model for a longer WT operational period.

Based on the assumptions, observations, and the analyses in the chapters of the thesis, the following conclusions can be stated:

- When building lifetime assessment methodologies and modelling the thermal stress of WT converters, more attention needs to be paid to operational and control aspects of the converter and the WT.
- The most thermally stressed part of a WT BVSC comprised of IGBT power modules is the diode on the MSC. Also, on converter level in general, the MSC is more thermally stressed than the GSC.
- The dynamic transients of the torque control of the WT generator largely impact the thermal cycling stress of the converter. Using the thermal stress and lifetime consumption methodology it was shown that applying the Optimal Torque Control (OTC) results in less thermal stress and higher reliability compared to the OTSR strategies. This was true especially for the most thermally stressed converter, i.e. the MSC. However, note that there is potential to further adjust the tuning of the OTSR strategies that were used in the thesis so that the response is smoother and closer to the OTC – this would reduce the thermal stress on the converter.
- Reactive power transfer with the wind farm array grid has an impact on the converter loading of the GSC. It was shown that for the same active power injected to the grid, a constant value of reactive power transfer increases the average thermal loading (mean junction temperature) of the grid side converter, but reduces the amplitude of the thermal swings. Because the thermal swings have a higher impact on degradation than the mean junction temperature, it was observed

that an increased reactive power transfer can even lower thermal lifetime consumption.

- The mission profile and wind speed data is crucial for analysing the converter thermal stress. Direct extrapolation of consumed lifetime after analysing just an hour of operation with a particular wind speed profile to yearly predictions will contain a large error in the calculated lifetime.
- Although the approach requires including some detail that describes operational and control aspects in the WT, there is potential for reducing its complexity to analyse long time operation and so that it can be a part of a digital twin that is continuously used by the wind farm operator to monitor WT performance.

The results in this thesis showed a large impact of control aspects and parameters in the thermal stress of the converter. This leads to the suggestion that there is potential to design and include an additional operation mode in actual WTs: the reduced converter thermal stress mode. This could be used in periods when it is known that the converter can be subjected to high thermal cycling (or when it has already been subjected to a large stress and it is known that has an increased likelihood of failure), the stress can be mitigated by switching to a smoother control mode. In the example in this thesis would be to switch from an OTSR MPPT control to the OTC control.

One of the main challenges of the work in this thesis was the lack of availability of data and information. This scarcity includes the reliability data for the converter and the relevant failure mechanism. Additionally there is a lack of information on the WT electrical system configuration, such as information on the design of the converter that is installed in WT nacelles. If reliability and failure data were available, a data-based approach to the lifetime and reliability estimation could have been added, additional to the knowledge- and model-based estimation. On the other hand, having more information on the converter and WT system design can make the methodology and analysis more representative and relevant to operating turbines – at the same time more accurate because less assumptions would be included in building the operational layer of the lifetime methodology.

The first suggestions for the future work are concerned with improving the lifetime methodology regarding the challenges faced. A project that attempts to add analysis of real

operational data in order to cross-validate and expand the operational-based methodology developed here would be highly beneficial. The aim would be to combine the two so they complement each other. A machine learning algorithm could be used to combine the inputs from the thermal stress based lifetime methodology (as developed in this thesis) that would be combined with, what would in effect be a WT operational digital twin, with added failure data and condition monitoring data in order to predict converter failures. Such a combination could give results that will be very useful for the operation of WT converters as close as possible to their designed lifetime.

With more data and further development of the approach, an additional thing that can be done is add confidence intervals for the lifetime predictions. With reasonable confidence intervals, not only early failure detection and predictive maintenance can be achieved, but also operational strategies can be redefined. This can include designing strategies such as active control for increased reliability [136]. Additionally, failure detection mechanisms and health indicator evaluations can be done by building digital twins of wind turbines and comprising subsystems. The methodology developed in this thesis is aimed to ultimately be a part of such a complete digital twin which would be a digital representation of the operation of the real wind turbine and its converter. Data produced by the digital twin can be combined with the measured data from the sensors in the real WT, and by using the increased information on the turbine operation and state-of-health, fault prediction and predictive maintenance strategies can be applied [137].

Other converter topologies with more complex control can be investigated. This would require modelling their losses and thermal cycling patterns. Other failure mechanisms and failure roots have also to be further investigated. Possibilities to create modelling techniques that allow for prediction of failures that come from all the dominating root-causes of failures in WT converters need to be investigated. This includes causes such as humidity, vibration, and corrosive environments, which have an increased presence in offshore WTs.

The IGBT lifetime estimation and thermal stress model developed is rather complex and an analysis and a first try of reducing it was done in the last chapter of the thesis. There is potential for further work done in this direction and more extensive mathematical model order reduction techniques can be applied. This would be necessary especially if this model

becomes part of a larger lifetime model that considers other failure modes and ultimately comprises the full digital twin of the wind turbine. In that case, sophisticated model order reduction would need to be performed in order to minimize the computational requirements.

# 8 References

[1] Lee Joyce and Zhao Feng, “Global Wind Report 2022,” Report, Global Wind Energy Council (GWEC), 2022.

[2] Wilkinson, M., Hendriks, B., Spinato, F. et al. (7 more authors) "Methodology and results of the reliawind reliability field study." In: European Wind Energy Conference , EWEC 2010, 20-23 April 2010, Warsaw, Poland.

[3] P. Tavner, “Wind turbine systems,” in Book *Reliability of Power Electronic Converter Systems*, H. S. Chung, H. Wang, F. Blaabjerg, and M. Pecht, Eds. The Institution of Engineering and Technology, 2015, pp. 165–194.

[4] P. Tavner, *Offshore Wind Turbines*. Book, The Institution of Engineering and Technology, 2012.

[5] E. Artigao, S. Martín-Martínez, A. Honrubia-Escribano, and E. Gómez-Lázaro, “Wind turbine reliability: A comprehensive review towards effective condition monitoring development,” *Applied Energy*, vol. 228. Elsevier Ltd, pp. 1569–1583, 15-Oct-2018.

[6] V. Yaramasu, B. Wu, P. C. Sen, S. Kouro, and M. Narimani, “High-power wind energy conversion systems: State-of-the-art and emerging technologies,” *Proc. IEEE*, vol. 103, no. 5, pp. 740–788, May 2015.

[7] H. Li and Z. Chen, “Overview of different wind generator systems and their comparisons,” *IET Renew. Power Gener.*, vol. 2, no. 2, pp. 123–138, Jun. 2008.

[8] A. D. Hansen, F. Iov, F. Blaabjerg, and L. H. Hansen, “Review of Contemporary Wind Turbine Concepts and their Market Penetration,” vol. 28, no. 3, pp. 247–263, 2004.

[9] V. Akhmatov, “Analysis of dynamic behaviour of electric power systems with large amount of wind power,” Ph.D Thesis, Electrical Power Engineering, Orsted-DTU Technical University of Denmark, 2003.

[10] H. Polinder, J. A. Ferreira, B. B. Jensen, A. B. Abrahamsen, K. Atallah, and R. A. McMahon, “Trends in Wind Turbine Generator Systems,” *IEEE J. Emerg. Sel. Top. Power Electron.*, vol. 1, no. 3, pp. 174–185, Sep. 2013.

[11] “V82-1.65 MW Creating more from less.”, Technical Brochure, Vestas Wind Systems, Denmark, 2006.

[12] “The new standard for moderate wind conditions - Siemens Wind Turbine SWT-2.3-101”, Technical Brochure, Siemens Wind, Erlangen, Germany, 2009.

[13] “S88-2.1 MW TECHNICAL OVERVIEW.”, Technical Brochure, Suzlon, 2013

[14] J. Carroll, A. McDonald, and D. McMillan, “Failure rate, repair time and unscheduled O&M cost analysis of offshore wind turbines,” *Wind Energy*, vol. 19, no. 6, pp. 1107–1119, 2016.

[15] S. Pfaffel, S. Faulstich, and K. Rohrig, “Performance and reliability of wind turbines: A review,” *Energies*, vol. 10, no. 11, 2017.

[16] S. Sheng, “Report on Wind Turbine Subsystem Reliability - A Survey of Various Databases,”, Presentatio, National Renewable Energy Laboratory , 2013. Available [Online] https://www.nrel.gov/docs/fy13osti/59111.pdf [Accessed 04/07/2022]

[17] K. Branner and A. Ghadirian, “Database about blade faults,”Report, DTU Wind Energy, DTU Wind Energy E No. 00672014, December 2014

[18] B. Hahn *et al.*, “Recommended practices for wind farm data collection and reliability assessment for O&M optimization,” *Energy Procedia*, vol. 137, pp. 358–365, Oct. 2017.

[19] J. M. Pinar Pérez, F. P. García Márquez, A. Tobias, and M. Papaelias, “Wind turbine reliability analysis,” *Renew. Sustain. Energy Rev.*, vol. 23, pp. 463–472, Jul. 2013.

[20] J. Ribrant and L. M. Bertling, “Survey of Failures in Wind Power Systems With Focus on Swedish Wind Power Plants During 1997–2005,” *IEEE Trans. Energy Convers.*, vol. 22, no. 1, pp. 167–173, Mar. 2007.

[21] P. J. Tavner, H. Long, Y. Feng Bba, P. J. T. Ma, and H. Long Msc, “Early experiences with UK round 1 offshore wind farms,” *Proc. Inst. Civ. Eng.*, no. EN4, pp. 167–181, 2007.

[22] J. Carroll, A. McDonald, I. Dinwoodie, D. McMillan, M. Revie, and I. Lazakis, “Availability, operation and maintenance costs of offshore wind turbines with different drive train configurations,” *Wind Energy*, vol. 20, no. 11, pp. 361–378,

2017.

[23] “WInD-Pool.” , Project Website, Fraunhofer Institut for Energy Economics and Energy System Technology IEE, [Online]. Available: https://wind-pool.iee.fraunhofer.de/wind_pool_en/WInD-Pool/index.html. [Accessed: 10-May-2019].

[24] The Crown Estate and ORE Catapult, “System Performance, Availability and Reliability Trend Analysis-SPARTA: Portfolio review 2016,”, Report, 2017.

[25] The Crown Estate and ORE Catapult, “System Performance, Availability and Reliability Trend Analysis-SPARTA: 2017/18 Portfolio Review 2.” Report, 2019

[26] J. A. Andrawus, “Maintenance Optimisation For Wind Turbines,” PhD Thesis, The Robert Gordon University, 2008.

[27] P. J. Tavner, F. Spinato, G. J. W. Van Bussel, and E. Koutoulakos, “Reliability of Different Wind Turbine Concepts with Relevance to Offshore Application.” European Wind Energy Conference, Brussels, April 2008, URL: https://community.dur.ac.uk/supergen.wind/Phase1/docs/Tavner,%20Spinato,%20van%20Bussel,%20Koutoulakos-EWEC2008.pdf [Accessed: 03-June-2019]

[28] S. Faulstich, “Deliverable WP7 3.3, Component reliability ranking with respect to WT concept and external environmental conditions,”, Deliverable Report WP7 3.3 Condition Monitoring, 2010.

[29] Hahn, B., Durstewitz, M., Rohrig, K. (2007). Reliability of Wind Turbines. In: Peinke, J., Schaumann, P., Barth, S. (eds) Wind Energy. Springer, Berlin, Heidelberg. https://doi.org/10.1007/978-3-540-33866-6_62

[30] S. Faulstich, S. Pfaffel, P. Kühn, and P. Lyding, “Monitoring Offshore Wind Energy Use in Europe-Offshore~WMEP,” *Energy Procedia*, vol. 24, pp. 322–327, 2012.

[31] P. J. Tavner, J. Xiang, and F. Spinato, “Reliability analysis for wind turbines,” *Wind Energy*, vol. 10, no. 1, pp. 1–18, Jan. 2007.

[32] J. Ribrant, “Reliability performance and maintenance-A survey of failures in wind power systems,” MsC Thesis, KTH School of Electrical Engineering, 2005.

[33] A. Stenberg, “Analysis of wind turbine statistics in Finland,” PhD Thesis, Alto University, 2010.

[34] B. Uzunoglu, F. Amoiralis, and C. Kaidis, “Wind turbine reliability estimation for different assemblies and failure severity categories,” *IET Renew. Power Gener.*, vol. 9, no. 8, pp. 892–899, Nov. 2015.

[35] M. D. Reder, E. Gonzalez, and J. J. Melero, “Wind Turbine Failures - Tackling current Problems in Failure Data Analysis,” *J. Phys. Conf. Ser.*, vol. 753, no. 7, p. 072027, Sep. 2016.

[36] E. Gonzalez, M. Reder, and J. J. Melero, “SCADA alarms processing for wind turbine component failure detection,” *J. Phys. Conf. Ser.*, vol. 753, no. 7, p. 072019, Sep. 2016.

[37] J. B. Gayo, “Final Publishable Summary of Results of Project ReliaWind,”, Project Final Report, ReliaWind Project Nr 212966, 2011.

[38] M. Wilkinson, K. Harman, B. Hendriks, F. Spinato, and T. Van Delft, T. Garrad, G.L. Thomas, “Measuring Wind Turbine Reliability-Results of the Reliawind Project,” EWEA conference, pp. 1-8, 2011.

[39] C. Su, Y. Yang, X. Wang, and Z. Hu, “Failures analysis of wind turbines: Case study of a Chinese wind farm,” in *2016 Prognostics and System Health Management Conference (PHM-Chengdu)*, 2016, pp. 1–6.

[40] Jiangtao Chai, Guoyin An, Zhiyong Ma, and Xiaowei Sun, “A study of fault statistical analysis and maintenance policy of wind turbine system,” in *International Conference on Renewable Power Generation (RPG 2015)*, 2015, pp. 4 .-4 .

[41] Y. Lin, L. Tu, H. Liu, and W. Li, “Fault analysis of wind turbines in China,” *Renew. Sustain. Energy Rev.*, vol. 55, pp. 482–490, Mar. 2016.

[42] C. R. Bond, V. A. Peters, and A. B. Ogilvie, “Continuous Reliability Enhancement for Wind (CREW) Database: Wind Plant Reliability Benchmark,”, Report No. SAND2012-7328. Sandia National Laboratories (SNL), Albuquerque, NM, and Livermore, CA (United States), 2012.

[43] C. Carter, B. Karlson, S. Martin, and C. Westergaard, “Continuous Reliability Enhancement for Wind (CREW) Program Update,” Program Update. No. SAND-2016-3844. Sandia National Lab.(SNL-NM), Albuquerque, NM (United States), 2016.

[44] G. M. J. Herbert, S. Iniyan, and R. Goic, “Performance, reliability and failure analysis of wind farm in a developing Country,” *Renew. Energy*, vol. 35, no. 12, pp. 2739–2751, Dec. 2010.

[45] I. Dinwoodie, O.-E. V. Endrerud, M. Hofmann, R. Martin, and I. B. Sperstad, “Reference Cases for Verification of Operation and Maintenance Simulation Models for Offshore Wind Farms,” *Wind Eng.*, vol. 39, no. 1, pp. 1–14, Feb. 2015.

[46] A. Fox and C. Hill, “System Performance, Availability and Reliability Trend Analysis-SPARTA: 2018/19 Portfolio Review.” Report vol. 3, The Crown Estate and ORE Catapult, 2019.

[47] PD CLC/TS 61400-26:2017 - Wind energy generation systems. Availability for wind power stations, Technical Standard, BSI Standards Publication, 2017.

[48] “Hywind Scotland remains the UK’s best performing offshore wind farm - equinor.com.” News Article, Equinor, [Online], Available: https://www.equinor.com/en/news/20210323-hywind-scotland-uk-best-performing-offshore-wind-farm. [Accessed: 06-Jan-2022].

[49] F. Spinato, P. J. Tavner, G. J. W. van Bussel, and E. Koutoulakos, “Reliability of wind turbine subassemblies,” *IET Renew. Power Gener.*, vol. 3, no. 4, p. 387, 2009.

[50] H. S. Chung, H. Wang, F. Blaabjerg, and M. Pecht, *Reliability of Power Electronic Converter Systems - The IET*. Book, The Institution of Engineering and Technology, 2015.

[51] E. De Francesco, R. De Francesco, and E. Petritoli, “Obsolescence of the MIL-HDBK-217: A critical review,” *4th IEEE Int. Work. Metrol. AeroSpace, Metroaerosp. 2017 - Proc.*, no. February 1995, pp. 282–286, 2017.

[52] K. Fischer *et al.*, “Exploring the Causes of Power-Converter Failure in Wind Turbines based on Comprehensive Field-Data and Damage Analysis,” *Energies*, vol. 12, no. 4, 2019.

[53] K. Fischer *et al.*, “Reliability of power converters in wind turbines: Exploratory analysis of failure and operating data from a worldwide turbine fleet,” *IEEE Trans. Power Electron.*, vol. 34, no. 7, pp. 6332–6344, 2019.

[54] K. Fischer *et al.*, “Field-experience based root-cause analysis of power-converter

failure in wind turbines," *IEEE Trans. Power Electron.*, vol. 30, no. 5, pp. 2481–2492, May 2015.

[55] H. Wang and F. Blaabjerg, "Power Electronics Reliability: State of the Art and Outlook," *IEEE J. Emerg. Sel. Top. Power Electron.*, vol. 9, no. 6, pp. 6476–6493, 2021.

[56] L. Alhmoud, "Reliability Improvement for a High-Power IGBT in Wind Energy Applications," *IEEE Trans. Ind. Electron.*, vol. 65, no. 9, pp. 7129–7137, Sep. 2018.

[57] C. Busca *et al.*, "An overview of the reliability prediction related aspects of high power IGBTs in wind power applications," *Microelectron. Reliab.*, vol. 51, no. 9–11, pp. 1903–1907, Sep. 2011.

[58] K. Ma, M. Liserre, F. Blaabjerg, and T. Kerekes, "Thermal loading and lifetime estimation for power device considering mission profiles in wind power converter," *IEEE Trans. Power Electron.*, vol. 30, no. 2, pp. 590–602, 2015.

[59] D. Zhou, F. Blaabjerg, T. Franke, M. Tønnes, and M. Lau, "Comparison of Wind Power Converter Reliability with Low-Speed and Medium-Speed Permanent-Magnet Synchronous Generators," *IEEE Trans. Ind. Electron.*, vol. 62, no. 10, pp. 6575–6584, 2015.

[60] T. Lei, M. Barnes, S. Smith, S. H. Hur, A. Stock, and W. E. Leithead, "Using Improved Power Electronics Modeling and Turbine Control to Improve Wind Turbine Reliability," *IEEE Trans. Energy Convers.*, vol. 30, no. 3, pp. 1043–1051, 2015.

[61] C. Chen, V. Pickert, M. Al-Greer, C. Jia, and C. Ng, "Localization and Detection of Bond Wire Faults in Multichip IGBT Power Modules," *IEEE Trans. Power Electron.*, vol. 35, no. 8, pp. 7804–7815, 2020.

[62] A. Abuelnaga, M. Narimani, and A. S. Bahman, "A review on IGBT module failure modes and lifetime testing," *IEEE Access*, vol. 9, pp. 9643–9663, 2021.

[63] J. Falck, C. Felgemacher, A. Rojko, M. Liserre, and P. Zacharias, "Reliability of Power Electronic Systems: An industry Perspective," *IEEE Ind. Electron. Mag.*, vol. 12, no. 2, pp. 24–35, 2018.

[64] Shaoyong Yang, A. Bryant, P. Mawby, Dawei Xiang, Li Ran, and P. Tavner, "An

Industry-Based Survey of Reliability in Power Electronic Converters," *IEEE Trans. Ind. Appl.*, vol. 47, no. 3, pp. 1441–1451, May 2011.

[65] L. Yang, P. A. Agyakwa, and C. M. Johnson, "Physics-of-failure lifetime prediction models for wire bond interconnects in power electronic modules," *IEEE Trans. Device Mater. Reliab.*, vol. 13, no. 1, pp. 9–17, 2013.

[66] M. Musallam, C. Yin, C. Bailey, S. Member, and M. Johnson, "Mission Profile-Based Reliability Design and Real-Time Life Consumption Estimation in Power Electronics," *IEEE Trans. Power Electron.*, vol. 30, no. 05, pp. 2601–2613, 2015.

[67] A. Antonopoulos, S. D'Arco, M. Hernes, and D. Peftitsis, "Limitations and Guidelines for Damage Estimation Based on Lifetime Models for High-Power IGBTs in Realistic Application Conditions," *IEEE J. Emerg. Sel. Top. Power Electron.*, vol. 9, no. 3, pp. 3598–3609, 2021.

[68] H. Wang, M. Liserre, and F. Blaabjerg, "Toward Reliable Power Electronics: Challenges, Design Tools, and Opportunities," *IEEE Ind. Electron. Mag.*, vol. 7, no. 2, pp. 17–26, Jun. 2013.

[69] H. Wang *et al.*, "Transitioning to Physics-of-Failure as a Reliability Driver in Power Electronics," *IEEE J. Emerg. Sel. Top. Power Electron.*, vol. 2, no. 1, pp. 97–114, Mar. 2014.

[70] S. Ye, D. Zhou, X. Yao, and F. Blaabjerg, "Component-Level Reliability Assessment of a Direct-Drive PMSG Wind Power Converter Considering Two Terms of Thermal Cycles and the Parameter Sensitivity Analysis," *IEEE Trans. Power Electron.*, vol. 36, no. 9, pp. 10037–10050, 2021.

[71] M. Ciappa, F. Carbognani, P. Cova, and W. Fichtner, "Lifetime prediction and design of reliability tests for high-power devices in automotive applications," *IEEE Int. Reliab. Phys. Symp. Proc.*, vol. 2003-Janua, no. 4, pp. 523–528, 2003.

[72] I. F. Kovačević, U. Drofenik, and J. W. Kolar, "New physical model for lifetime estimation of power modules," *2010 Int. Power Electron. Conf. - ECCE Asia -, IPEC 2010*, pp. 2106–2114, 2010.

[73] U. Drofenik, I. Kovacevic, R. Schmidt, and J. W. Kolar, "Multi-domain simulation of transient junction temperatures and resulting stress-strain behavior of power

switches for long-term mission profiles," in *2008 11th Workshop on Control and Modeling for Power Electronics*, 2008, pp. 1–7.

[74] X. Du, J. Zhang, G. Li, H. M. Tai, P. Sun, and L. Zhou, "Lifetime estimation for IGBT modules in wind turbine power converter system considering ambient temperature," *Microelectron. Reliab.*, vol. 65, pp. 69–78, 2016.

[75] A. S. Bahman, K. Ma, and F. Blaabjerg, "A Lumped Thermal Model Including Coupling and Thermal Boundary Conditions for High-Power IGBT Modules," *IEEE Trans. Power Electron.*, vol. 33, no. 3, pp. 2518–2530, 2018.

[76] A. Mohammed *et al.*, "Distributed Thermal Monitoring of Wind Turbine Power Electronic Modules Using FBG Sensing Technology," *IEEE Sens. J.*, vol. 20, no. 17, pp. 9886–9894, Sep. 2020.

[77] U. M. Choi, K. Ma, and F. Blaabjerg, "Validation of Lifetime Prediction of IGBT Modules Based on Linear Damage Accumulation by Means of Superimposed Power Cycling Tests," *IEEE Trans. Ind. Electron.*, vol. 65, no. 4, pp. 3520–3529, Apr. 2018.

[78] C. Lalanne, Mechanical Vibration and Shock Analysis, Third Edition, Book, ISTE Ltd and John Wiley & Sons. Inc, Great Britain and the United States, May 2014.

[79] K. Ma, Marco Liserre, Frede Blaabjerg, "Reactive power influence on the thermal cycling of Multi-MW wind power inverter," *Res. Top. Wind Energy*, vol. 5, no. 2, pp. 145–157, 2015.

[80] I. Vernica, K. Ma, and F. Blaabjerg, "Optimal derating strategy of power electronics converter for maximum wind energy production with lifetime information of power devices," *IEEE J. Emerg. Sel. Top. Power Electron.*, vol. 6, no. 1, pp. 267–276, 2018.

[81] P. Lang, M. Michel, N. Wade, R. Grunbaum, and T. Larsson, "Dynamic energy storage - Field operation experience," in *IEEE Power and Energy Society General Meeting*, 2013.

[82] M. Andresen, K. Ma, G. Buticchi, J. Falck, F. Blaabjerg, and M. Liserre, "Junction Temperature Control for More Reliable Power Electronics," *IEEE Trans. Power Electron.*, vol. 33, no. 1, pp. 765–776, 2018.

[83] L. Alhmoud and B. Wang, “A review of the state-of-the-art in wind-energy reliability analysis,” *Renew. Sustain. Energy Rev.*, vol. 81, pp. 1643–1651, Jan. 2018.

[84] M. Matsuichi and T. Endo, “Fatigue of metals subjected to varying stress,”, Japan Society of Mechanical Engineers, Fukuoka, vol. 68, no. 2, pp. 37–40, 1968.

[85] ASTM E1049, “Standard practices for cycle counting in fatigue analysis,” ASTM Stand., vol. 85, no. Reapproved 2017, pp. 1–10, 2017.

[86] L. Alhmoud, “Reliability Improvement for a High-Power IGBT in Wind Energy Applications,” *IEEE Trans. Ind. Electron.*, vol. 65, no. 9, pp. 7129–7137, 2018.

[87] “Rainflow counts for fatigue analysis - MATLAB rainflow - MathWorks United Kingdom.”, MATLAB Documentation, Mathworks Help Centre, [Online]. Available: https://uk.mathworks.com/help/signal/ref/rainflow.html [Accessed: 27-Feb-2022].

[88] M. Musallam and C. M. Johnson, “An efficient implementation of the rainflow counting algorithm for life consumption estimation,” *IEEE Trans. Reliab.*, vol. 61, no. 4, pp. 978–986, 2012.

[89] Y. Zhang, H. Wang, Z. Wang, Y. Yang, and F. Blaabjerg, “Impact of lifetime model selections on the reliability prediction of IGBT modules in modular multilevel converters,” *2017 IEEE Energy Convers. Congr. Expo. ECCE 2017*, vol. 2017-January, pp. 4202–4207, Nov. 2017.

[90] N. Kaminski, Ö. Emre, and H. Samuel, “Load-cycling capability of HiPak IGBT modules,”, Application Note 5SYA 2043-04, ABB Semiconductors, Lenzburg Switzerland, 2014.

[91] M. A. Miner, “Cumulative Damage in Fatigue,” *J. Appl. Mech.*, vol. 12, no. 3, pp. A159–A164, Sep. 1945.

[92] J. Jonkman, S. Butterfield, W. Musial, and G. Scott, “Definition of a 5-MW Reference Wind Turbine for Offshore System Development,”, NREL Publication No. NREL/TP-500-38060, National Renewable Energy Laboratory, (NREL), Golden, CO (United States), 2009.

[93] R. M. M. Slot and L. Svenningsen, “Consistent direct-drive version of the NREL

5MW turbine," Proceedings of *WindEurope Hamburg, Germany (2018): 25-28* , 2018.

[94] J. Carmona-Sanchez, Z. Lin, M. Collu, M. Barnes, O. Marjanovic, and D. Cevasco, "An analysis of the impact of an advanced aero-hydro-servo-elastic model of dynamics on the generator-converter dynamics, for an offshore fixed 5MW PMSG wind turbine," Conference Proceedings, in *15th IET International Conference on AC and DC Power Transmission (ACDC 2019)*, 2019.

[95] N. A. Bhuiyan and A. McDonald, "Optimization of Offshore Direct Drive Wind Turbine Generators With Consideration of Permanent Magnet Grade and Temperature," *IEEE Trans. Energy Convers.*, vol. 34, no. 2, pp. 1105–1114, Jun. 2019.

[96] J. Zhang, M. Cheng, and Z. Chen, "A novel stator interior permanent magnet generator for direct-drive wind turbines," *IET Renew. Power Gener. Stevenage Vol. 1, Iss. 4, (Dec 2007) 203-210.*, no. 4, pp. 723–728, 2007.

[97] Siemens, "The Smart Way – HVDC PLUS – One Step Ahead," Company Publication, Siemens Power Transmission Division, Order No. E50001-G610-A102-V2-4A00, Germany, 20011.

[98] M. Annoukoubi, A. Essadki, H. Laghridat, and T. Nasser, "Comparative study between the performances of a three-level and two-level converter for a Wind Energy Conversion System," *2019 Int. Conf. Wirel. Technol. Embed. Intell. Syst. WITS 2019*, Apr. 2019.

[99] R. Melício, V. M. F. Mendes, and J. P. S. Catalão, "Power converter topologies for wind energy conversion systems: Integrated modeling, control strategy and performance simulation," *Renew. Energy*, vol. 35, no. 10, pp. 2165–2174, Oct. 2010.

[100] K. Ma, *Power Electronics for the Next Generation Wind Turbine Systems*. Book, Springer International Publishing, 2013.

[101] A. Wintrich, U. Nicolai, W. Tursky, and T. Reimann, Application Manual Power Semiconductors, Semikron, ISLE Verlag, Ilmenau, 2015.

[102] ABB, "A matter of FACTS Deliver more , high quality power," Company Report,

Vasteras Sweden, 2017.

[103] R. Lanzafame, S. Mauro, and M. Messina, “Wind turbine CFD modeling using a correlation-based transitional model,” *Renew. Energy*, vol. 52, pp. 31–39, Apr. 2013.

[104] M. M. Rezaei, H. Zohoor, and H. Haddadpour, “Aeroelastic modeling and dynamic analysis of a wind turbine rotor by considering geometric nonlinearities,” *J. Sound Vib.*, vol. 432, pp. 653–679, Oct. 2018.

[105] H. Ye, B. Yue, X. Li, and K. Strunz, “Modeling and simulation of multi-scale transients for PMSG-based wind power systems,” *Wind Energy*, vol. 20, no. 8, pp. 1349–1364, Aug. 2017.

[106] S. M. Muyeen *et al.*, “Comparative study on transient stability analysis of wind turbine generator system using different drive train models,” *IET Renew. Power Gener.*, vol. 1, no. 2, p. 131, 2007.

[107] C. J. O’Rourke, M. M. Qasim, M. R. Overlin, and J. L. Kirtley, “A Geometric Interpretation of Reference Frames and Transformations: Dq0, Clarke, and Park,” *IEEE Trans. Energy Convers.*, vol. 34, no. 4, pp. 2070–2083, Dec. 2019.

[108] D. S. Vilchis-Rodriguez, A. Ahmedi, M. Barnes, S. Shen, Z. Wang, and S. Gao, “STATCOM+BESS MODELLING AND HARMONIC ANALYSIS,” Proceedings in *The 17th International Conference on AC and DC Power Transmission (ACDC 2021)*, 2022, pp. 73–78.

[109] N. Mohan, T. M. Undeland, and W. P. Robbins, *Power Electronics Convertors, Applictions, and Design*. New York: Wiley., 2002.

[110] D. G. Holmes and T. A. Lipo, *Pulse Width Modulation for Power Converters: Principles and Practice*, vol. 1. Wiley-IEEE Press, 2003.

[111] P. Krause, O. Wasynczuk, S. Sudhoff, and S. Pekarek, *Analysis of Electric Machinery and Drive Systems*, Third. John Wiley & Sons, Inc., 2013.

[112] H. de Bellescize, “La reception synchrone,” 1932.

[113] S. Golestan, J. M. Guerrero, and J. C. Vasquez, “Three-Phase PLLs: A Review of Recent Advances,” *IEEE Transactions on Power Electronics*, vol. 32, no. 3. Institute of Electrical and Electronics Engineers Inc., pp. 1897–1907, 01-Mar-2017.

[114] C. Zhan *et al.*, “Dynamic voltage restorer based on voltage-space-vector PWM control,” *IEEE Trans. Ind. Appl.*, vol. 37, no. 6, pp. 1855–1863, Nov. 2001.

[115] X.-Q. Guo, W.-Y. Wu, and H.-R. Gu, “Phase locked loop and synchronization methods for grid-interfaced converters: a review.” Przeglad Elektrotechniczny 87.4 (2011): 182-187.

[116] M. Barnes and R. Preece, “PEET D1.1 The Power Converter,”, Internal Project Deliverable, Project: Power Electronics Enhanced Transformer (PEET), 2019.

[117] M. H. Hansen, A. Hansen, T. J. Larsen, and S. Øye, “Control design for a pitch-regulated, variable speed wind turbine,” Technical Report, U.S. Department of Energy, Office of Scientific and Technical Information (OSTI), 2005.

[118] W. Qiao and D. Lu, “A Survey on Wind Turbine Condition Monitoring and Fault Diagnosis - Part II: Signals and Signal Processing Methods,” *IEEE Trans. Ind. Electron.*, vol. 62, no. 10, pp. 6546–6557, 2015.

[119] ABB, “Datasheet for IGBT Module ABB 5SNA 0400J650100,” ABB Semicond., Datasheet, no. 5, pp. 1–9, 2016.

[120] D. Graovac and M. Pürschel, “IGBT Power Losses Calculation Using the Data - Sheet Parameters,” Application Note, Infineon, 2009.

[121] N. Rao and D. Chamund, “Calculating Power Losses in an IGBT Module,” Appllication Note AN6156-1, Dynex Semiconductors, 2014.

[122] J. W. Kolar and U. Drofenik, “A General Scheme for Calculating Switching and Conduction Losses of Power Semiconductors in Numerical Circuit Simulations of Power Electronic Systems,” *Int. Power Electron. Conf.*, 2005.

[123] B. Backlund, R. Schnell, U. Schlapbach, R. Fischer, and E. Tsyplakov, “Applying IGBTs Application Note 5SYA2053-02,”, Application Note, ABB Semiconductors, 2008.

[124] Y. C. Gerstenmaier, W. Kiffe, and G. Wachutka, “Combination of thermal subsystems modeled by rapid circuit transformation,” in *2007 13th International Workshop on Thermal Investigation of ICs and Systems (THERMINIC)*, 2007, pp. 115–120.

[125] K. Ma, N. He, M. Liserre, and F. Blaabjerg, “Frequency-Domain Thermal Modeling

and Characterization of Power Semiconductor Devices," *IEEE Trans. Power Electron.*, vol. 31, no. 10, pp. 7183–7193, 2016.

[126] SEMIKRON, P16 Heatsinks Series, Datasheet, [Online]. Available: https://www.semikron.com/products/productclasses/accessories/heatsinks/detail/p-16-pm139410pm139450.html [Accessed: 22-May2021].

[127] ABB, "SEMIS Simulation Tool Three Phase 2-level VSC with IGBT User manual 5SYA 2105," (2020) ABB Semiconductors, User Manual, [Online] Available:https://www.hitachiabbpowergrids.com/offering/productandsystem/semiconductors/semis-models/semis4 [Accessed: 18-July-2021].

[128] N. J. Abbas, A. Wright, and L. Pao, "An Update to the National Renewable Energy Laboratory Baseline Wind Turbine Controller," *J. Phys. Conf. Ser.*, vol. 1452, no. 1, pp. 1–14, 2020.

[129] "OpenFAST | Wind Research | NREL.", National Renewable Energy Laboratory, Open Source Simulation Tool - NREL Tools, [Online]. Available: https://www.nrel.gov/wind/nwtc/openfast.html [Accessed: 10-Jan-2022].

[130] A. Ahmedi, M. Barnes, V. Levi, J. Carmona Sanchez, C. Ng, and P. Mckeever, "Modelling of Wind Turbine Operation for Enhanced Power Electronics Reliability," *IEEE Trans. Energy Convers.*, 2022.

[131] Ahmedi, Arsim, M. Barnes, V. Levi, J. Carmona-Sanchez, A. Madariaga, C. Ng, and C. Jia. "Lifetime Estimation of IGBT Power Modules for Reliability Study of Wind Turbine Systems." In The 10th International Conference on Power Electronics, Machines and Drives (PEMD 2020), vol. 2020, pp. 729-734. IET, 2020.

[132] Grid Code Regulation, "GC0101 Extract of European Connection Conditions Legal Text," 08-Jan-2018. Legal Text, National Grid, [Online]. Available: https://www.nationalgrideso.com/document/104906/download. [Accessed: 04-Jan-2022].

[133] B. Backlund, R. Schnell, U. Schlapbach, R. Fischer, and E. Tsyplakov, "Applying IGBTs Application Note 5SYA 2053-04," Application Note, ABB Semiconductors, 2004.

[134] Cleve Moler, "Stiff Differential Equations - MATLAB & Simulink.", Technical

Article, Mathworks, 2003, [Online]. Available: https://uk.mathworks.com/company/newsletters/articles/stiff-differential-equations.html. [Accessed: 21-May-2022].

[135] "Solve Stiff ODEs - MATLAB & Simulink - MathWorks United Kingdom." [Online]. MATLAB Documentation, Mathworks Help Centre, Available: https://uk.mathworks.com/help/matlab/math/solve-stiff-odes.html. [Accessed: 21-May-2022].

[136] N. Requate and T. Meyer, "Active Control of the Reliability of Wind Turbines," *IFAC-PapersOnLine*, vol. 53, no. 2, pp. 12789–12796, Jan. 2020.

[137] Y. Peng, S. Zhao, and H. Wang, "A digital twin based estimation method for health indicators of DC–DC converters," IEEE Trans. Power Electron., vol. 36, no. 2, pp. 2105–2118, Feb. 2021.

# 9 Appendix

## 9.1 Integration of Conduction Losses

Relevant to section 4.2 where the losses and thermal model of the converter is described.

$$P_{\text{cond, IGBT}} = \frac{1}{T_0}\int_0^{T_0/2} V_{CE0}\cdot \hat{\mathrm{I}}_c \sin(\omega t)\cdot\tau(t)\,dt + \frac{1}{T_0}\int_0^{T_0/2} \mathrm{r_{CE}}\cdot\left(\hat{\mathrm{I}}_c \sin(\omega t)\right)^2\cdot\tau(t)dt =$$

$$= \frac{1}{T_0}\int_0^{T_0/2} V_{CE0}\cdot \hat{\mathrm{I}}_c \sin(\omega t)\cdot\frac{1}{2}\left(1+m\sin(\omega t+\phi)\right)dt + \frac{1}{T_0}\int_0^{T_0/2} \mathrm{r_{CE}}\cdot\left(\hat{\mathrm{I}}_c \sin(\omega t)\right)^2\cdot\frac{1}{2}\left(1+m\sin(\omega t+\phi)\right)dt =$$

$$= \frac{\hat{\mathrm{I}}_c\cdot V_{CE0}}{2\cdot T_0}\int_0^{T_0/2} \sin(\omega t)\cdot\left(1+m\sin(\omega t+\phi)\right)dt + \frac{\hat{\mathrm{I}}_c^{\,2}\cdot \mathrm{r_{CE}}}{2\cdot T_0}\int_0^{T_0/2} \left(\sin(\omega t)\right)^2\cdot\left(1+m\sin(\omega t+\phi)\right)dt =$$

$$= \frac{\hat{\mathrm{I}}_c\cdot V_{CE0}}{2\cdot T_0}\left[\int_0^{T_0/2} \sin(\omega t)dt + m\cdot\int_0^{T_0/2} \sin(\omega t)\cdot\sin(\omega t+\phi)\,dt\right] +$$

$$+\frac{\hat{\mathrm{I}}_c^{\,2}\cdot \mathrm{r_{CE}}}{2\cdot T_0}\left[\int_0^{T_0/2} \sin(\omega t)^2 dt + m\cdot\int_0^{T_0/2} \sin(\omega t)^2\cdot\sin(\omega t+\phi)\,dt\right]$$

The four integrals that need to be solved then are as below:

$$\int \sin(\omega t)dt = -\frac{\cos(\omega t)}{\omega} + C$$

$$\int \sin(\omega t)\cdot\sin(\omega t+\phi)dt = \frac{1}{2}t\cos\phi - \frac{\sin(\phi+2\omega t)}{4\omega} + C$$

$$\int \sin(\omega t)^2 dt = \frac{t}{2} - \frac{\sin(2\omega t)}{4\omega} + C$$

$$\int \sin(\omega t)^2\cdot\sin(\omega t+\phi)\,dt = \frac{-3\cos(\phi-\omega t) - 6\cos(\phi+\omega t) + \cos(\phi+3\omega t)}{12\omega} + C$$

Replacing $T_0 = 2\pi$ for the integration limits and $\omega = 2\,\pi f =$

$$P_{\text{av, cond}}(T_j) = \frac{1}{2}\left(V_{\text{CE0}}(T_j)\cdot\frac{\hat{\mathrm{I}}_c}{\pi} + r_{\text{CE0}}(T_j)\cdot\frac{\hat{\mathrm{I}}_c^{\,2}}{4}\right) + m\cdot\cos\phi\cdot\left(V_{\text{CE0}}(T_j)\cdot\frac{\hat{\mathrm{I}}_c}{8} + \frac{1}{3\pi}\cdot r_{\text{CE0}}(T_j)\cdot\hat{\mathrm{I}}_c^{\,2}\right)$$

## 9.2 Pitch Control Tuning

Relevant to section 3.8 which describes the control of the turbine.

***Table 12. Pitch control tuning gain scheduling***

| Wind Speed (m/s) | Rotor speed (rad/s) | Pitch angle β (degees) | $\left(\frac{\partial P}{\partial \beta}\right)$ | Kp | Ki |
|---|---|---|---|---|---|
| **11.4** | 1.267 | 0.000 | 328478 | 1713.333 | 514.000 |
| **12** | 1.267 | 0.765 | 2254986 | 249.577 | 74.873 |
| **13** | 1.267 | 1.237 | 2561397 | 219.721 | 65.916 |
| **14** | 1.267 | 1.783 | 1591620 | 353.597 | 106.079 |
| **15** | 1.267 | 2.786 | 713800 | 788.444 | 236.533 |
| **16** | 1.267 | 4.641 | 452102 | 1244.834 | 373.450 |
| **17** | 1.267 | 6.758 | 438239 | 1284.211 | 385.263 |
| **18** | 1.267 | 8.713 | 460022 | 1223.403 | 367.021 |
| **19** | 1.267 | 10.463 | 487376 | 1154.739 | 346.422 |
| **20** | 1.267 | 12.038 | 507568 | 1108.801 | 332.640 |
| **21** | 1.267 | 13.498 | 510327 | 1102.807 | 330.842 |
| **22** | 1.267 | 14.937 | 311936 | 1804.192 | 541.258 |
| **23** | 1.267 | 16.517 | 253993 | 2215.773 | 664.732 |
| **24** | 1.267 | 18.510 | 181312 | 3103.995 | 931.198 |
| **25** | 1.267 | 21.350 | 179587 | 3133.809 | 940.143 |

## 9.3 Comparison of Steady-State Losses and Temperature with SEMIS tool

MATLAB losses calculation and comparison with ABB semis online tool for a 2-level 3-phase IGBT VSC. These results are relevant and supplement the discussion in section 4.2 on the losses and thermal modelling of the converter.

| | 1 | | | 2 | | | 3 | | | 4 | | | 5 | | | 6 | | |
|---|---|---|---|---|---|---|---|---|---|---|---|---|---|---|---|---|---|---|
| **Parameter** | **MATLAB** | **Semis** | Difference | **MATLAB** | **Semis** | Difference | **MATLAB** | **Semis** | Difference | **MATLAB** | **Semis** | Difference | **MATLAB** | **Semis** | Difference | **MATLAB** | **Semis** | Difference |
| *Operation Mode* | Inverter | | | Inverter | | | Inverter | | | Inverter | | | Inverter | | | Rectifier | | |
| **Calculated Device Losses** | | | | | | | | | | | | | | | | | | |
| Switching losses IGBT 1 [W] | 488 | 492.6 | 0.93% | 386.3 | 383.1 | -0.83% | 306.36 | 308.4 | 0.66% | 423 | 425.94 | 0.69% | 1110.8 | 1117 | 0.56% | 1034.2 | 1042 | 0.75% |
| Switching losses Diode 1 [W] | 115.8 | 121.8 | 4.95% | 100.2 | 100.9 | 0.71% | 78.55 | 77.4 | -1.49% | 102.6 | 106.76 | 3.90% | 244.1 | 252.22 | 3.22% | 266.9 | 270.94 | 1.49% |
| Conduction losses IGBT 1 [W] | 416 | 414.3 | -0.41% | 261.7 | 254.4 | -2.89% | 254.78 | 260.6 | 2.23% | 341.7 | 338.91 | -0.82% | 769.4 | 761.27 | -1.07% | 240.2 | 238.47 | -0.73% |
| Conduction losses Diode 1 [W] | 33 | 31.62 | -4.36% | 22.8 | 20.93 | -8.93% | 51.91 | 53.8 | 3.51% | 47.2 | 45.8 | -3.06% | 154.3 | 154.79 | 0.32% | 465.1 | 467.76 | 0.57% |
| Combined Losses IGBT1 [W] | 904 | 906.9 | 0.32% | 648 | 637.5 | -1.65% | 561.14 | 569 | 1.38% | 764.7 | 764.85 | 0.02% | 1880.2 | 1878.3 | -0.10% | 1274.4 | 1280.47 | 0.47% |
| Combined Losses Diode1 [W] | 148.8 | 153.5 | 3.03% | 123 | 121.9 | -0.94% | 130.46 | 131.2 | 0.56% | 149.8 | 152.56 | 1.81% | 398.4 | 407.01 | 2.12% | 732 | 738.7 | 0.91% |
| Junction Temp. Avg IGBT 1 [°C] | 71.6 | 71.6 | 0.00% | 71.6 | 71.6 | 0.00% | 54.4 | 54.4 | 0.00% | 64.57 | 64.57 | 0.00% | 122.82 | 122.82 | 0.00% | 100.89 | 100.89 | 0.00% |
| Junction Temp. Avg Diode 1 [°C] | 54.77 | 54.77 | 0.00% | 54.77 | 54.77 | 0.00% | 46.11 | 46.11 | 0.00% | 51.86 | 51.86 | 0.00% | 93.42 | 93.42 | 0.00% | 106.6 | 106.6 | 0.00% |
| Converter Losses [W] | 6316.8 | 6362 | 0.71% | 4626 | 4556 | -1.54% | 4149.6 | 4201.2 | 1.23% | 5487 | 5504.46 | 0.32% | 13671.6 | 13712 | 0.29% | 12038 | 12115.02 | 0.63% |
| Losses % | 2.38% | 2.40% | 0.71% | 2.42% | 2.39% | -1.54% | 2.72% | 2.75% | 1.23% | 2.63% | 2.64% | 0.32% | 5.24% | 5.26% | 0.29% | -4.61% | -4.64% | 0.63% |
| **AC Parameters** | | | | | | | | | | | | | | | | | | |
| Real Power [kW] | | 265.1 | | | 190.9 | | | 152.7 | | | 208.5 | | | 260.9 | | | -260.9 | |
| Reactive Power [kVAR] | | 0 | | | 0 | | | 74 | | | 68.5 | | | 147.9 | | | 147.9 | |
| Phase Voltage RMS [V] | | 354 | | | 354 | | | 283 | | | 318 | | | 250 | | | 250 | |
| Phase Current RMS [A] | | 250 | | | 180 | | | 200 | | | 230 | | | 400 | | | 400 | |
| Output Frequency [Hz] | | 50 | | | 50 | | | 50 | | | 50 | | | 50 | | | 50 | |
| Power Factor | | 1 | | | 1 | | | 0.9 | | | 0.95 | | | 0.87 | | | 0.87 | |
| **DC & Control Parameters** | | | | | | | | | | | | | | | | | | |
| DC Power [kW] | | 271.5 | | | 195.4 | | | 156.9 | | | 214.1 | | | 274.6 | | | -278.8 | |
| DC Voltage [V] | | 1000 | | | 1000 | | | 1000 | | | 1000 | | | 1000 | | | 1000 | |
| Switching Frequency [Hz] | | 1500 | | | 1700 | | | 1250 | | | 1450 | | | 1750 | | | 1750 | |
| Modulation Index | | 1 | | | 1 | | | 0.8 | | | 0.9 | | | 0.707 | | | 0.707 | |

## 9.4 OTSR 2nd Order System Derivation

This appendix is relevant to section 5.1 on the torque control of the WT generator.

To tune as a 2nd order TF, using one-mass drivetrain swing equation and motor convention:

$$\frac{d}{dt}\omega_e = \frac{p_p}{J_{tot}}\left(T_e - T_m\right) - \frac{B_{tot}}{J_{tot}}\omega_e$$

$$\frac{d}{dt}\omega_e = \frac{3}{2}\frac{{p_p}^2}{J_{tot}}\psi_{PM}\cdot i_{qs} - \frac{p_p}{J_{tot}}T_m - \frac{B_{tot}}{J_{tot}}\omega_e$$

The open loop speed-to-current TF is:

$$\frac{\omega_e(s)}{i_{qs}(s)} = \frac{\frac{3}{2}\frac{{p_p}^2}{J_{tot}}\psi_{PM}}{s + \frac{B_{tot}}{J_{tot}}}$$

The closed loop TF then would be:

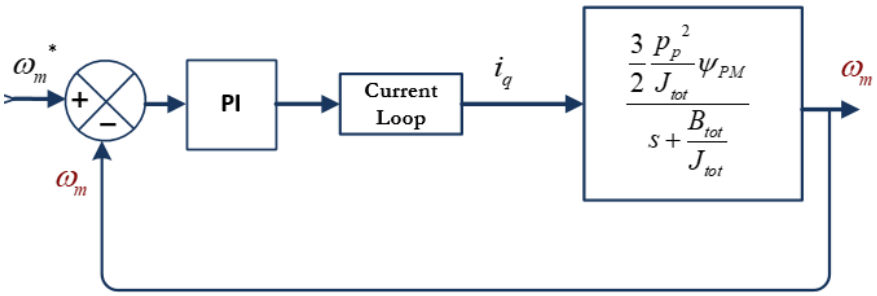


With a closed loop TF:

$$\frac{\omega_e^*(s)}{\omega_e(s)} = \frac{\left(K_p + \frac{K_i}{s}\right) \cdot \frac{\frac{3}{2}\frac{p_p^2}{J_{tot}}\psi_{PM}}{s + \frac{B_{tot}}{J_{tot}}}}{1 + \left(K_p + \frac{K_i}{s}\right) \cdot \frac{\frac{3}{2}\frac{p_p^2}{J_{tot}}\psi_{PM}}{s + \frac{B_{tot}}{J_{tot}}}}$$

$$\frac{\omega_e^*(s)}{\omega_e(s)} = \frac{\left(\frac{K_p}{K_i}s + 1\right) \cdot K_i \cdot \frac{3}{2}\frac{p_p^2}{J_{tot}}\psi_{PM}}{s^2 + s \cdot \left(\frac{B_{tot}}{J_{tot}} + K_p \frac{3}{2}\frac{p_p^2}{J_{tot}}\psi_{PM}\right) + K_i \cdot \frac{3}{2}\frac{p_p^2}{J_{tot}}\psi_{PM}} \approx$$

$$\approx \frac{K_i \cdot \frac{3}{2}\frac{p_p^2}{J_{tot}}\psi_{PM}}{s^2 + s \cdot \left(\frac{B_{tot}}{J_{tot}} + K_p \frac{3}{2}\frac{p_p^2}{J_{tot}}\psi_{PM}\right) + K_i \cdot \frac{3}{2}\frac{p_p^2}{J_{tot}}\psi_{PM}}$$

2nd order TF:

$$T(s) = \frac{\omega_n^2}{s^2 + 2\xi\omega_n \cdot s + \omega_n^2}$$

Therefore if tuning as a 2nd order TF our speed loop:

$$K_i = \frac{\omega_n^2 \cdot J_{tot}}{p_p^2 \cdot \psi_{PM}} \cdot \frac{2}{3}$$

$$K_p = \frac{\left(2\xi\omega_n - \frac{B_{tot}}{J_{tot}}\right)}{\frac{3}{2}\frac{p_p^2}{J_{tot}}\psi_{PM}}$$

## 9.5 Cycle Count Histograms for Reactive Power Injection or Consumption

Here are shown additional results (comparison) of thermal cycles between positive and negative reactive power flow to the grid. These results are relevant to the discussion in section 5.5.

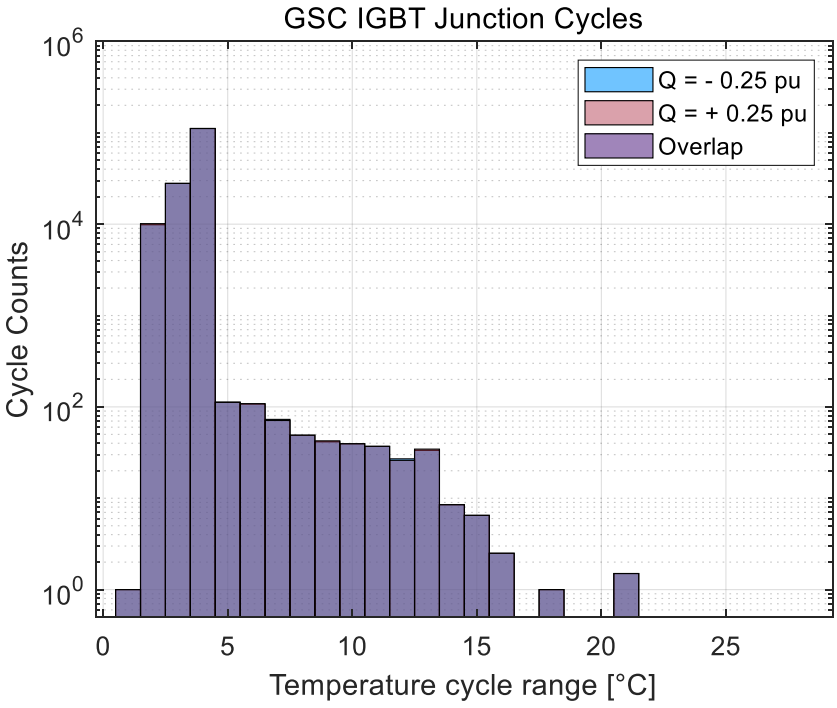


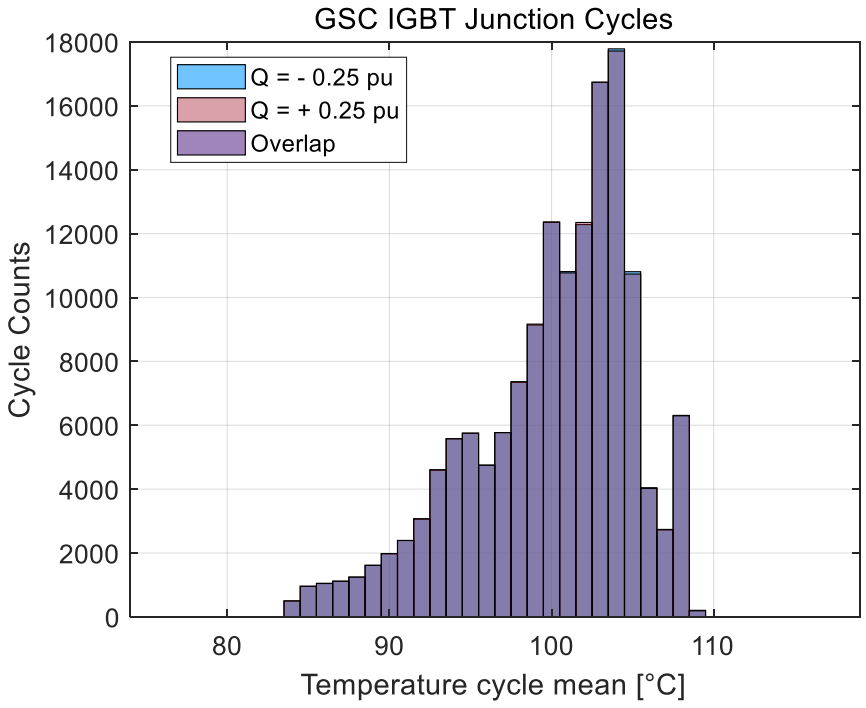

## 9.6 Matrices of Reduced-Order Thermal Models

The matrices of the reduced order thermal models with five and three states are given below. These are relevant to the discussion in Section 6.2.

**Five states reduced model:**

$$A = \begin{bmatrix} & x_1 & x_2 & x_3 & x_4 & x_5 \\ x_1 & -140.66 & 16.66 & 2.13 & 78.22 & -11.03 \\ x_2 & 16.17 & -3.20 & 12.45 & -10.32 & -5.62 \\ x_3 & 2.22 & 13.61 & -145.72 & 10.96 & 73.71 \\ x_4 & 48.65 & -6.82 & 6.80 & -31.82 & -0.007 \\ x_5 & -6.74 & -3.84 & 44.79 & -0.01 & -26.88 \end{bmatrix}$$

$$B = \begin{bmatrix} & u_1 & u_2 \\ x_1 & -1.23 & 0.09 \\ x_2 & 0.15 & 0.03 \\ x_3 & -0.18 & -0.58 \\ x_4 & 0.06 & -4.7e-5 \\ x_5 & 5.4e-4 & 0.004 \end{bmatrix} \quad C = \begin{bmatrix} & x_1 & x_2 & x_3 & x_4 & x_5 \\ y_1 & 0.15 & 0.05 & -0.98 & -7.9e-5 & 0.007 \\ y_2 & -0.98 & 0.12 & -0.14 & 0.04 & 4.3e-4 \end{bmatrix}$$

$$D = \begin{bmatrix} & u_1 & u_2 \\ y_1 & -4.8e-14 & 3.9e-10 \\ y_2 & 8.5e-10 & -4.8e-14 \end{bmatrix}$$

**Three states reduced model:**

$$A = \begin{bmatrix} & x_1 & x_2 & x_3 \\ x_1 & -0.033 & -0.293 & 0.083 \\ x_2 & -0.215 & -3.290 & -0.002 \\ x_3 & 0.166 & -5e-4 & -3.452 \end{bmatrix}$$

$$B = \begin{bmatrix} & u_1 & u_2 \\ x_1 & -0.008 & 2.59e-4 \\ x_2 & -0.021 & 0.179 \\ x_3 & -0.375 & -0.01 \end{bmatrix} \quad C = \begin{bmatrix} & x_1 & x_2 & x_3 \\ y_1 & -1e-4 & 0.454 & -0.255 \\ y_2 & -0.011 & -0.025 & -0.454 \end{bmatrix}$$

$$D = \begin{bmatrix} & u_1 & u_2 \\ y_1 & -1.73e-6 & 0.002 \\ y_2 & 0.006 & -1.7e-6 \end{bmatrix}$$